ABSTRACT

Design and Validation of New Testing Apparatus for Testing Helical Compression
Springs under Combined Axial, Shear, Torsion, and Bending Loads

Jace Dane Kelley, M.S.B.M.E

Mentor: Carolyn T. Skurla, Ph.D.

Helical compression springs are normally used to provide a linear force response
to compressive displacement. However, compression springs can be used to provide
lateral force and rotational torque responses to lateral and angular displacements. The
purpose of this thesis is to take advantage of improvements in mechanical testing
equipment to develop a testing apparatus that can mechanically test helical compression
springs under varying amounts of complex three-dimensional displacements. A testing
apparatus was constructed using a custom six axis load cell and a commercial MTS
system. The calibration and validation of the custom load cell is presented. One
compression spring was tested under different combinations of axial, shear, and torsional
displacements to validate the design of the jig. The results indicated varying levels of
interdependence between the loading modes on the spring's net force response; however,
the spring's compressive response appears to be independent of torsion and shear
displacement.

Design and Validation of New Testing Apparatus for Testing Helical Compression
Springs under Combined Axial, Shear, Torsion, and Bending Loads

by

Jace Dane Kelley, B.S.E

A Thesis

Approved by the Department of Mechanical Engineering

_____
William Jordon, Ph.D., Chairperson

Submitted to the Graduate Faculty of
Baylor University in Partial Fulfillment of the
Requirements for the Degree
of
Masters of Science in Biomedical Engineering

Approved by the Thesis Committee

_____
Carolyn T. Skurla, Ph.D., Chairperson

_____
Brian A. Garner, Ph.D.

_____
Ann E. Rushing, Ph.D.

Accepted by the Graduate School
August 2011

_____
J. Larry Lyon, Ph.D., Dean

TABLE OF CONTENTS

LIST OF FIGURES

LIST OF TABLES

NOMENCLATURE

l_0	=	Free length of spring		
l	=	Compressed length of spring		
n	=	Number of active coils		
r, D	=	Mean coil radius, mean coil diameter		
d	=	Wire diameter		
α_0	=	Wahl's compressive rigidity in unstressed state		
β_0	=	Wahl's flexural rigidity in unstressed state		
γ_0	=	Wahl's shearing rigidity in unstressed state		
G	=	Torsional or shear modulus of rigidity		
E	=	Young's modulus or tensile modulus		
I	=	Moment of Inertia		
δ	=	Axial Deflection		
P	=	Axial Load		
F	=	Transverse (Shear) Load		
M	=	Flexural Moment		
k	=	P/δ	=	Spring rate or Spring Axial Stiffness
c	=	D/d	=	Spring Index
DOF	=	Degrees of Freedom		
$3D$	=	Three-dimensional		
$NARHA$	=	The North American Riding for the Handicapped Association		
AHA	=	The American Hippotherapy Association Inc.		

FEM	=	Finite Element Method
PDE	=	Partial Differential Equation

ACKNOWLEDGMENTS

DEDICATION

To my friends and family

CHAPTER ONE

Introduction

Compression Springs

The primary purposes of a compression spring are to elastically absorb

mechanical energy, which is accomplished as the shape of the spring is changed, and to

return energy as the spring elastically returns to its initial state. By storing energy due to

geometrical changes, typical compression springs provide a linear force-response. This

response is dependent on the displacement of the spring. In other words, for every inch

of displacement, a compression spring returns a linearly increasing force in response that

is proportional to the spring rate for that particular spring. Typically, helical springs are

used to provide a linear force in response to an axial displacement from a compressive or

tensile force. The linear response of compressions springs are also used in this manner to

absorb vibrational energy when used as automotive shocks or in the case of a pogo stick

to store and return the stored energy to the user during sequential jumps.

Springs are usually designed for a single loading mode, such as bending, torsion,

compression, or tension. Springs typically do not provide an effective response to other

loading modes than their intended primary loading mode. Leaf springs, as seen in Figure

1, are typically used in vehicle suspension systems. They are designed for flexural

loading conditions and would not provide an effective spring response axially because

they are not shaped to provide a response in that direction [1].

1

Figure 1: Leaf Spring Suspension [1]

The geometric shape of helical springs allows them to provide elastic responses in other loading directions fairly effectively. When a lateral force is applied to a helical compression spring, it will deflect laterally and provide an elastic response. A helical compression spring can also provide rotational torque responses to angular displacements. A common example is seen in children's playgrounds where riding toys, such as that shown in Figure 2, are suspended above the ground by a large helical compression spring [2]. Because of the geometric shape of helical compression springs, they can be displaced laterally, axially, and angularly, and provide a force-response to these displacements. Thus, a compression spring can be used to support and react to six degree-of-freedom (DOF) movements in three dimensions. Any mechanical device that uses a compression spring to help support load on a part that moves three-dimensionally will rely on this three-dimensional response of the spring.

Figure 2: Child's Spring Rider [2]

Purpose

The purpose of this thesis is to take advantage of improvements in mechanical

testing equipment and methods to develop a new testing jig and procedure to be used for

mechanical testing of helical compression springs under varying amounts of complex

three-dimensional displacements. The new testing jig will apply various combinations

and amounts of axial, shear, and torsional displacements simultaneously or singly and

measure the helical spring's multi-axial reaction forces. In order to measure the spring's

reaction forces, a custom six axis load cell was developed. The design, manufacture, and

calibration of the load cell will be presented. The testing apparatus was constructed using

the custom six axis load cell and custom jig mounted on an MTS biaxial servo-hydraulic

mechanical testing system. One compression spring will be tested under different

combinations of axial, shear, torsional displacements to validate the design of the testing

jig and custom load cell. The results obtained from mechanical testing of the helical

compression spring will be used to investigate how various amounts of displacement or

loading may affect the three-dimensional force-response of the helical compression

spring (i.e. the compressive, flexural, and shearing rigidities of the spring).

The long term objective of this thesis is to allow the measurement of the 3D

response of a helical compression spring to complex displacements and allow the

development of a mathematical model for the 3D response of compression springs. The

results from the mechanical testing will be used to validate the mathematical model and

previous work performed Wahl describing the elementary theory for the behavior of

helical springs under single axis loading [3-7].

The initial motivation for studying the complex motion of helical compression

springs subjected to 3D displacements was the conceptual design of a saddle support

structure for a mechanical horse that simulates the complex three-dimensional movement

of a live therapy horse. The conceptual design used a Stewart platform configuration

with six helical compression springs to provide the passive supporting force of the saddle

support structure (See Figure 3). A Stewart platform design programmed to simulate the

complex three-dimensional motion of a live therapy horse's back the compression springs

would be placed under multi-axis loading and displacements. In order to properly

develop the motion control of a mechanical device utilizing compression springs in a

Stewart platform configuration a three-dimensional force-displacement model is needed.

In order to develop this mathematical model, mechanical test data from helical

compression springs under complex 3D displacements is needed.
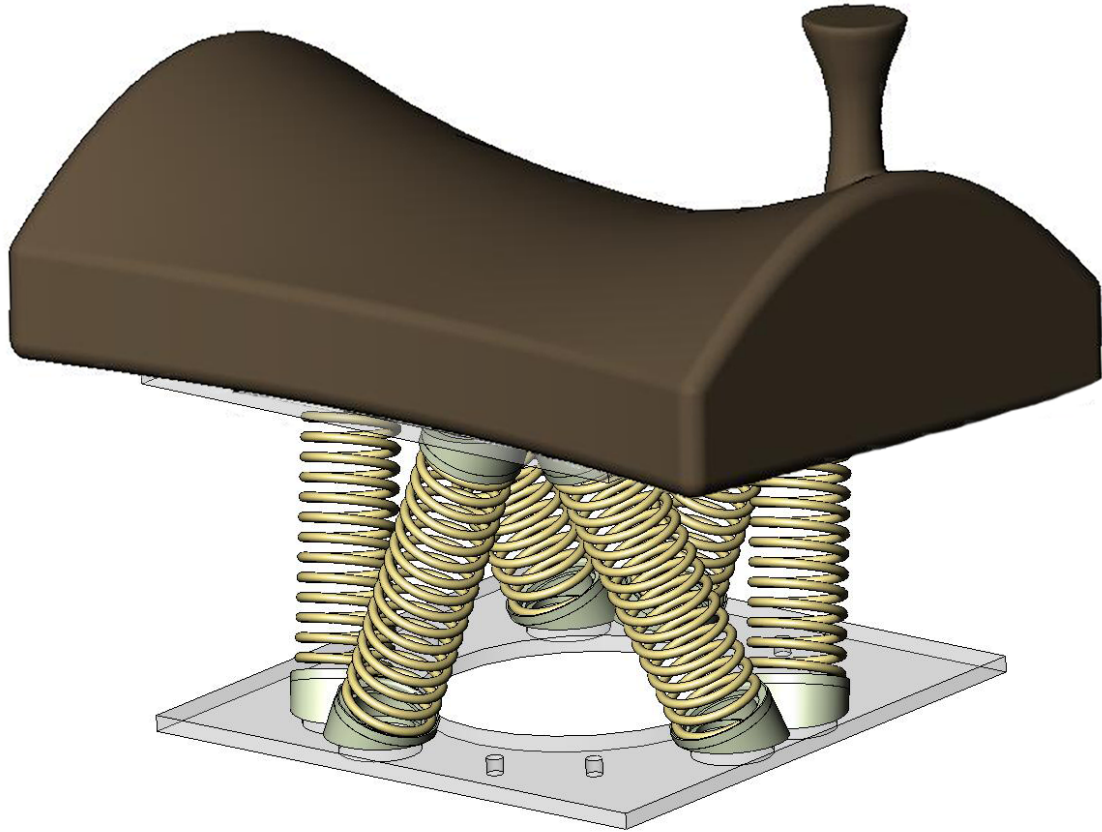
Figure 3: Stewart Platform Configuration using Helical Compression Springs as Passive Saddle Support Structure

Thesis Overview

Work completed for this thesis is presented in the following chapters. Chapter Two introduces background information on springs and the Stewart platform. Chapter Three provides detailed information regarding the motivations behind the research completed for this thesis. Chapter Four provides an overview of load cells and a detailed look into the design of the load cell built for this project. Chapter Five presents the materials and methods developed for mechanically testing helical compression springs. Chapter Six presents the results of the research completed in this thesis. These results and conclusions of the work completed for this thesis project are discussed in Chapter Seven.

CHAPTER TWO

Background

In this chapter an overview of mechanical springs and the Stewart platform will be presented. An historical overview of springs is presented first to introduce how springs are typically used and how they were developed. This is followed by a synopsis of previous work regarding the 2D behavior of helical compression springs and then a summary of additional work regarding the behavior of helical springs. The chapter concludes with a discussion of how helical compression springs have been testing under multi-axis loading conditions previously.

Mechanical Springs

A Brief Historical Overview of Springs

Since mankind first began to use the elastic characteristics of natural materials springs have technically existed, although only in the simplest form [8]. For instance a fibula, an ancient brooch, took advantage of simple spring tension in wire formed from copper to hold a person's cloak on their body [8, 9]. Spring tension was the driving force behind many ancient weapons, such as the crossbow and catapults. The development of springs, like most mechanical inventions, is limited by the materials and manufacturing processes that are available, and the clock, armament, and automotive industries provided much of the motivation behind the development of better spring designs and materials. The clock industry was one of the earliest contributors to the development and manufacturing of springs. In the 14th and 15th centuries, clockmakers began to switch

over to the use of springs rather than calibrated weights to power clocks [9]. It was

during this time period that spring shape began to be developed. Clockmakers worked to

improve the energy stored and methods to release the stored energy uniformly over a

period of time in order to improve the accuracy of the clock's timekeeping [9].

The material properties of spring material became even more important when they

were used in weapons. For instance, antiaircraft guns used spring-based mechanisms,

and initial designs had problems with spring failure due to overheating caused by rapid

fire. Chrome silicon spring wire was developed and used in World War II antiaircraft

guns to resists overheating failures [9].

The transportation industry has been a primary driver of research on spring

materials and manufacturing processes because springs are heavily used in a variety of

applications within the automotive industry. Valve springs, for example must withstand

over 100 million load cycles. The springs used for door locks and the suspension are

further examples of how springs are used in the design of a vehicle [8].

Today the applications for springs are near limitless. Springs are integral

components that provide some of the key functions of many everyday devices.

Typically, these springs go unnoticed until they fail [8]. The failure of a spring could be

insignificant or catastrophic, depending on the scenario. When the spring in the toaster or

in a pen fails, there is no immediate urgency. The pen can be replaced, and the burnt

toast removed with little effort. Consequences can be more severe when the spring that

fails is the one that provides the force to return the accelerator in a vehicle to its original

position [8]. Understanding how a spring behaves under varying conditions is important

so that the spring manufacturer can provide springs that both function correctly and do

not fail prematurely.

Axial Loading of Compression Springs

Linear compression is the most common application for compression springs. It has been studied extensively, and there are very simple and straightforward mathematical models for how the spring will respond to compressive displacements. For example, the *linear elastic spring* model predicts that the axial reaction load (P) of a spring will be equal to the product of the spring rate (k), a constant, and the axial displacement (δ), as shown in Equation 1.1.

$$P = k\delta \tag{1.1}$$

This relationship is commonly known as Hooke's law. The spring rate is the ratio of the axial force and the axial deflection as shown in Equation 1.2.

$$k = \frac{P}{\delta} \tag{1.2}$$

The spring rate value of a spring can be determined using the principles of Hooke's law by performing a mechanical test on a spring with known loads. Alternatively, the behavior of a spring can be closely approximated without running mechanical tests by using Equation 1.3 [5] that estimates the spring rate constant from the spring's geometrical and material properties. The geometrical and material properties in Equation 1.3 are: torsional or shear modulus (G), wire diameter (d), number of active spring coils (n), and mean coil radius (r).

$$k = \frac{Gd^4}{64r^3n} \tag{1.3}$$

Using Equation 1.3 to calculate an approximate value for the spring rate constant simplifies the process of predicting the spring's behavior under compression. A

compression spring's behavior under axial loads and displacements can be calculated

without the need to individually test each spring to determine the spring rate.

Multi-Axial Loading of Compression Springs

There is a need to develop a model that can calculate either the loads or

deflections of a helical compression spring in three dimensions. However, modeling the

response of a compression spring in three dimensions is much more challenging than one

that is loaded uniaxially.

Wahl evaluated the buckling and lateral loading of helical compression springs

[3]. Wahl's work also summarized the elementary buckling theory, developed by

Haringx. In order to evaluate the critical buckling load, Wahl first evaluated the

compressive, flexural, and shearing rigidities of helical springs with circular cross-

sections [3]. The equations Wahl developed to mathematically calculate a helical

compression spring's compressive (α_0), flexural (β_0), and shearing (γ_0) rigidities in an

unstressed state are shown in Equations 1.4, 1.5, and 1.6 respectively. These equations

use the spring's elastic modulus (E), moment of inertia (I) and free length (l_0) as well as

the other geometric and material properties defined previously.

$$\alpha_0 = \frac{Gd^4 l_0}{64 r^3 n} = k l_0 \tag{1.4}$$

$$\beta_0 = \frac{2 l_0 EIG}{rn\pi(2G + E)} \tag{1.5}$$

$$\gamma_0 = \frac{l_0 EI}{r^3 n\pi} \tag{1.6}$$

The compressive rigidity is the ratio of the load to deflection per unit length. Wahl's

equation for compressive rigidity (1.4) and the spring constant (1.2), can be combined

and reworked so the axial load is equal to the product of the compressive rigidity and the axial deflection divided by the spring's free length.

$$P = \alpha_0 \frac{\delta}{l_0}$$

(1.7)

The theoretical response of a helical compression spring to a flexural bending moment (*M*) (i.e. bending along the coil axis) can be estimated from the bending angle, the flexural rigidity, and the compressed length (*l*).

$$M = \beta_0 \frac{\theta}{l}$$

(1.8)

The response due to a shearing force (*F*) is described by the shearing rigidity, the coil deflection, and the free length of the spring as shown in Equation 1.9.

$$F = \gamma_0 \frac{\delta}{l_0}$$

(1.9)

Effectively Wahl described the compressive, flexural, and shearing responses of helical compression springs to axial, shear, and rotational bending forces respectively [3]. The purpose of the current research is to take advantage of improvements in mechanical testing methods to experimentally confirm Wahl's analytical results and to investigate how various amounts of displacement and loads and combinations of displacement and loads may affect the compressive, flexural, and shearing rigidities.

Additional Work on Helical Springs

Wahl provided simple, theoretical models based on the behavior of helical compression springs displaced under single loading modes by utilizing material mechanics and spring geometry [3]. Wahl's analytical models account for different loading modes individually. However, Wahl noted that helical compression springs are

10

often required to withstand lateral loads while under axial compression, as shown in Figure 4. Wahl then provided an equation to analytically evaluate the relationship between the lateral deflections of the spring with no axial load with that of the same spring with an axial load [3].
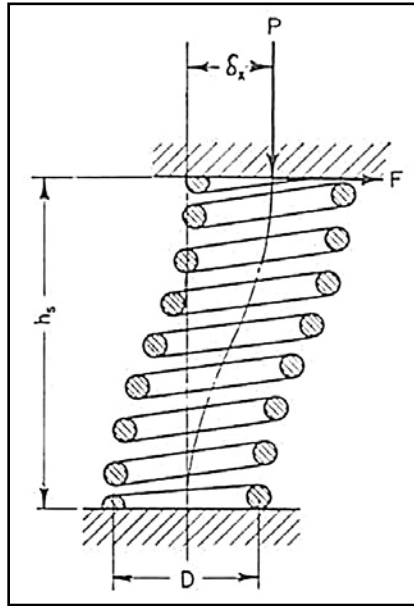
Figure 4: Spring under combined axial and lateral loading (one end fixed and other end guided) [3]

Wahl cited a series of mechanical tests on a large variety of helical compression springs performed by Burdick *et al.* [3]. Wahl further stated that the springs were loaded using combined loading, as in Figure 4. The results for lateral deflection demonstrated significant deviation between experimental and theoretical results. Wahl attributed this to imperfect clamping of the ends of the springs and stated that the results were affected by end turn effects in the spring.

Most subsequent research on helical compression springs has generally been focused on determining the buckling loads under various loading conditions [6, 10-12].

A comparison of the characteristics governing transverse stiffness of helical compression springs was performed by Vestnik Mashinostroeniya [10], who developed a modified set of equations for determining the relationship of the transverse stiffness to the transverse displacement when the spring ends are displaced in parallel. Mashinostroeniya concluded that the relationship between the transverse rigidity and displacement of helical compression springs was only effective when the loads applied to the helical springs are between 40-50% of the critical buckling load [10]. Mashinostroeniya stated that transverse stiffness of a spring increases with an increase in the axial load. This conclusion disagrees with the relationships derived by Wahl [10].

An analysis into buckling of helical compression springs that are subjected to combined torsion and axial deflection was performed by Satoh *et al.* [11] . Springs were subjected to combined torsion and axial deflection, and stated that their results showed good agreement with the theories summarized by Wahl [11].

Understanding the critical buckling load or deflection of helical compression springs is important for engineering designs that use helical springs because spring instability significantly affects the design [6]. Becker *et al.* developed partial differential equations that describe the buckling behavior of helical compression springs. By solving these equations using the transfer matrix method, buckling design charts were plotted. The plots showed that as the number of uncompressed turns of the springs coil n_0 increased, there was a convergence towards the elementary buckling theory given by Haringx, which was summarized by Wahl. G.G Chassie *et al* evaluated the buckling behavior of helical springs under combined compression and torsion about the longitudinal axis [12]. Their equations were further developed to account for torsion and solved numerically using the transfer matrix method [12]. Their results indicated that, for

12

springs with a small helix angle, the elementary theory developed by Haringx and

summarized by Wahl demonstrated good agreement with their calculated buckling curves

(See Figure 6).
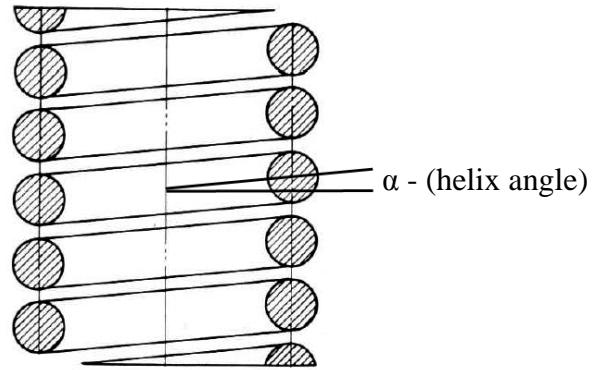
Figure 5: Spring's helix angle (Adapted from [3])
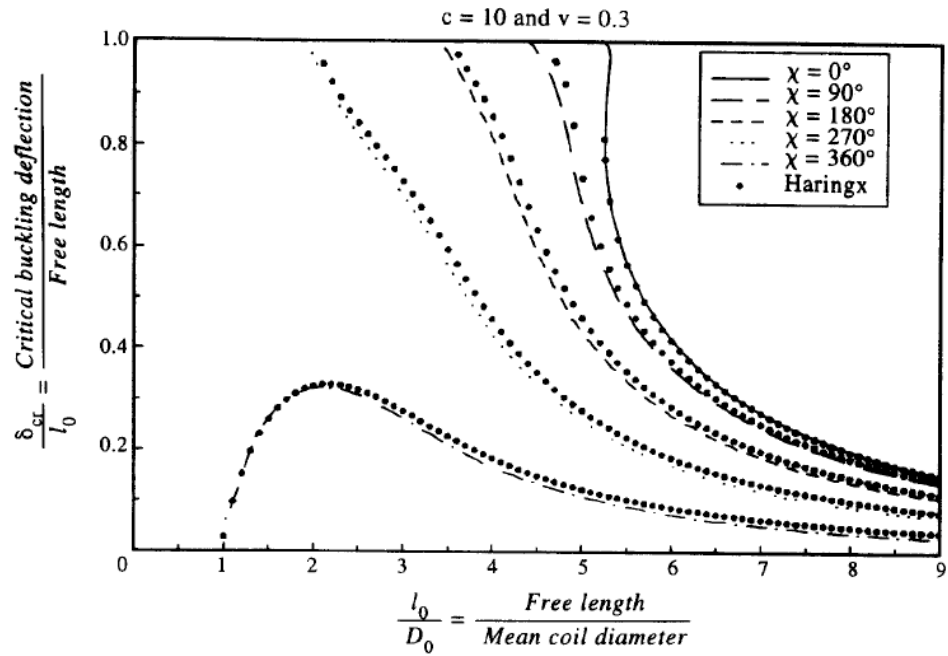
Figure 6: Buckling curves for n = 30 and Haringx formula [12]

The use of finite element analysis for predicting buckling behavior of helical

compression springs has increased. However, many commercial finite element programs

13

do not effectively allow for multi-axis loading conditions on helical springs. Tabarrok *et al.* developed a spatially curved and twisted rod element for buckling analysis. They provided a demonstrative use of the curved and twisted element by considering the buckling of helical springs [4]. Their calculations used two elements for each coil in the spring. A comparison of their buckling results with those obtained from Haringx's theory indicates that their element model yielded results close to the elementary theory for springs with small helix angles and lower critical loads than those predicted by Haringx's theory for springs with larger pitch angles (See Table 1). Springs 3 and 7 in Table 1 have larger pitch angles. The theoretical results calculated using Haringx's buckling theory (Summarized by Wahl [3]) are significantly higher than the critical buckling load predicted by the FEM used by Tabarrok *et al.* [4].

Table 1: Critical Buckling loads for Springs [4]

| Spring No. | L/D | Pitch angle (degree) | Critical loads (N) | | | |
| | | | B.C. 1 | | B.C. 2 | |
			F.E.M.	Haringx†	F.E.M.	Haringx
1	4	11.98	1313.3	1336.5		
2	5	9.04	96.50	97.32		
3	6	17.7	2024.2	2108.1	10 116.8	10 771.8
4	7.2	8.69	10 466.5	10 545.7	48 182.9	48 329.6
5	9	10.8	539.6	545.76	2345.3	2356.0
6	12	10.8	18.75	19.00	77.95	79.05
7	12	32.5	221.4	253.3	906.9	1054.1

Another finite element model for helical springs was developed by Jiang *et al.*, although this model was developed to consider only extension or torsion springs and not helical compression springs [13]. The use of finite element models and software could

prove useful in developing or validating a general model for a helical compression spring when combined with experimental validation.

Overview of Testing Setup Compared to Setup Referenced by Wahl

Wahl references the mechanical testing performed by Burdick *et al.* when discussing the combined axial and lateral loading of helical compression springs. The mechanical testing performed by Burdick *et al.* was initially performed on helical compression springs used for railway cars. Railway springs are particularly large and have high load capacities. Burdick *et al.* originally performed some testing on railway springs using a high capacity test setup shown in Figure 7 [7]. Due to the magnitude of the loads required to test these springs Burdick opted to create a simpler testing apparatus designed to test smaller springs with ground [7]. The testing apparatus used for testing the smaller springs is shown in Figure 8, and the general arrangement of the small spring testing apparatus is shown in Figure 9. Four identical springs were used in the small testing apparatus. An axial gravity load was used to displace the springs axially. The displacement was measured using four micrometer dial calipers (See Figure 9). Once the axial load was applied, a shear displacement was added. The shear displacement was actuated by rotating a turnbuckle connected to the testing apparatus. The shear displacement was measured using two micrometer dial calipers, and the shear force was measured by a spring scale connected in-line with the turnbuckle (See Figure 9).

There are several points to note about the testing setup developed by Burdick *et al.* and how the test setup used in this project should provide more accurate results. First to note is the use of micrometer dials mounted to the surface of the upper plate where the load was applied. Improvements in mechanical testing equipment have increased the

accuracy and precision of displacement measurements. The precision in the axial and torsional displacement measurements provided by the MTS machine used for this thesis work far exceeds that of dial gages. Both the method of applying the axial load and measuring the axial load is also improved due to technological developments over the past 70 years. The use of calibrated load cells that are axially centered with the crosshead which applies the axial displacement and force is significantly better than the method available to Burdick *et al.* when they performed these tests. The springs tested in this thesis are also welded to their mounting plates. This ensures that no end turn effects (laterally or rotational movement of the end coils) can affect the results of the test which is one of the possible reasons Wahl believed Burdick's results diverged from the theoretical theorems presented by Wahl.
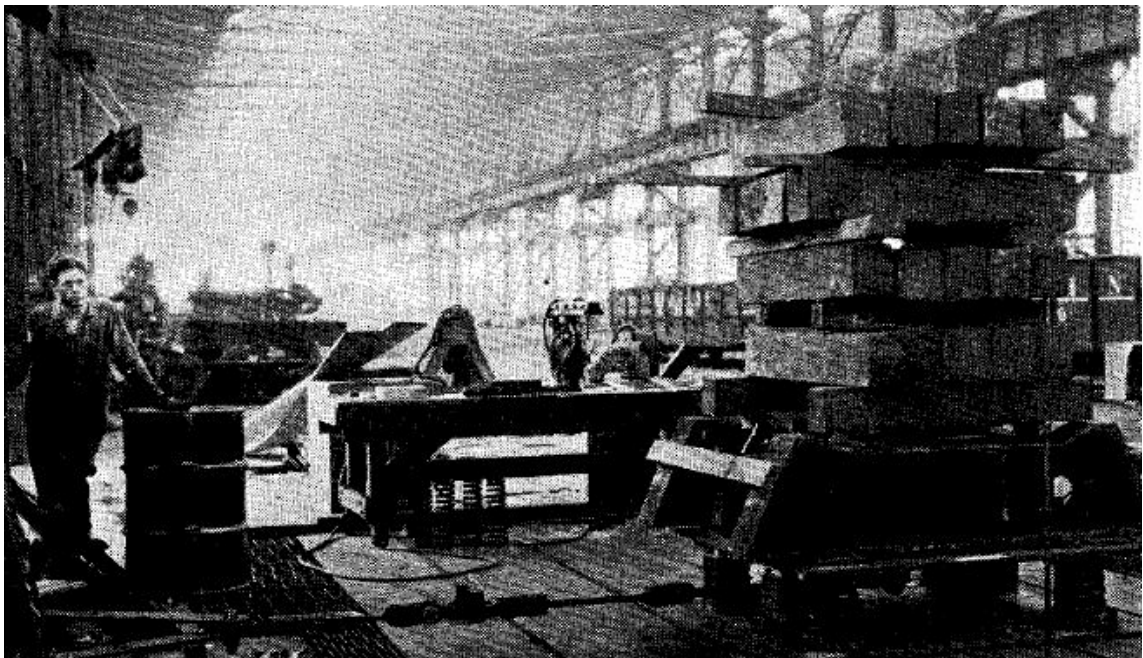
Figure 7: High Capacity Test Setup by Burdick *et al.* [7]
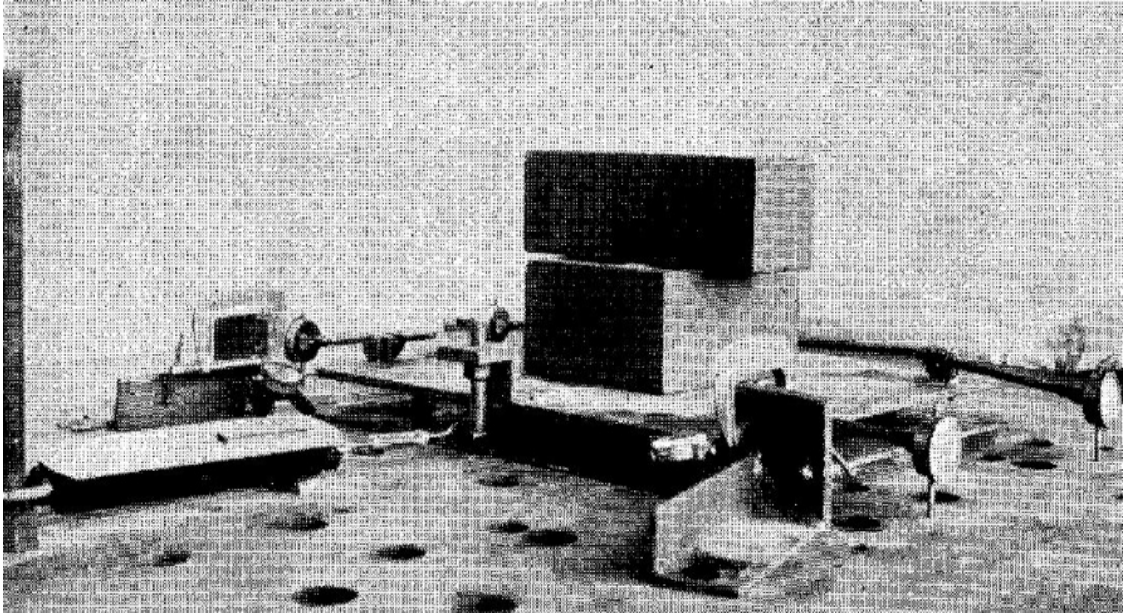
Figure 8: Small Spring Testing Apparatus by Burdick *et al.* [7]
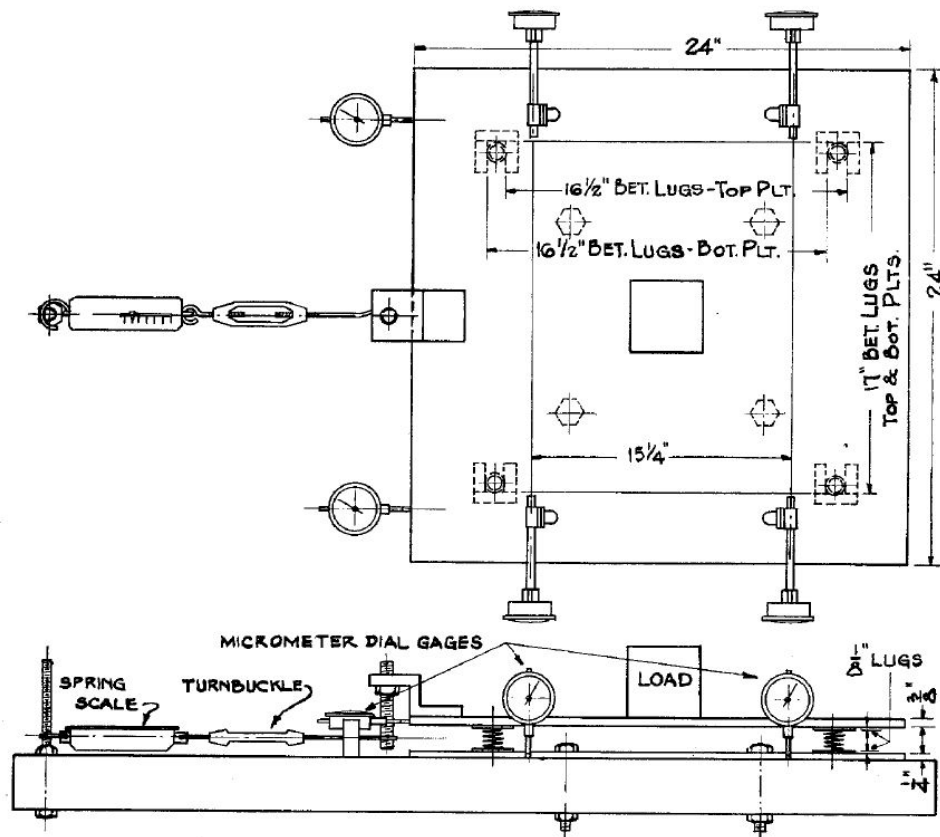
Figure 9: Small Spring Testing Arrangement by Burdick *et al.* [7]

There appears to be little mechanical testing data of helical compression springs since the testing performed by Burdick *et al.* that focused on the displacements and forces required to transversely displace springs under varying axial loads. Most work seems to be focused on recording the effects of combined loading on the axial critical buckling load. While important, these studies do not provide enough information regarding the behavior of helical compression springs under multi-axial loading conditions.

The hope is that the testing procedure and setup developed for this thesis will provide improved results over previously published results. The results obtained from the mechanical testing setup should be more precise than previous work and provide more detailed information regarding the reaction forces of helical compression springs under combined displacements.

The Stewart-Gough Platform

The need to research the complex 3D behavior of compression springs stemmed from the conceptual design of a second generation mechanical horse that used a Stewart platform with helical compression springs. Understanding what a Stewart platform is and how they operate is important considering the long term goals of this thesis. A brief general overview on the basic concept of Stewart platforms is presented in the following section. This is followed by examples of how the Stewart platform design has been used for various applications, including motion simulators.

Original Concept

The Gough-Stewart platform is a mechanical device that utilizes six parallel manipulators connected to a platform in a manner that provides control for six degrees of freedom (6DOF) in three-dimensional (3D) space. The general concept behind the

parallel manipulator known as the Stewart platform was developed by Stewart to be used

as a general motion control mechanism for flight simulators in 1965 [14, 15]. V.E.

Gough is often credited for being the first to develop a 6DOF platform structure design

and for suggesting that Stewart use six linear actuators in parallel to make Stewart's

original concept a fully parallel actuated mechanism [14]. The Stewart platform is

sometimes referred to as the Stewart-Gough platform because of Gough's original

conception and overall contribution to Stewart's design. However, since the increase in

research on the platform stemmed from Stewart's publication, it has become

commonplace to refer to this particular manipulator design as a Stewart Platform [14].

Stewart sought to develop a "six-degrees-of-motion platform capable of moving

in three linear directions and three angular directions singly or in any combination" that

could be used as a control base for flight simulators [15]. In order to develop a design

that was simple and capable of providing high performance results in a wide range of

applications Stewart developed a set of design criteria or aims. Stewart's original design

aims are shown in Table 2. After Stewart reviewed these design aims, however, he

deleted aim 5 because it was inherently incompatible with aims 2-4. Stewart states that,

"... aim 5 was abandoned in favor of achieving the other aims and thereby gaining in

structural rigidity and system response." [15]. Stewart's design aims provided the criteria

he needed to develop a platform that would be capable of a controlled six degrees of

freedom that is also controlled by a predetermined program [15].

Stewart used the design criteria in Table 2 to develop his original design concept,

shown in Figure 10. It consisted of a triangular platform. The three apex points of the

triangular platform each connected to a length-varying, controllable leg through a 3-axis

joint. Each of the three legs was connected to a base joint that consisted of two rotational

joints, one of which was controllable [14, 15].

Table 2: Stewart's Original Design Goals [15]

Design Aim	Purpose
1. The use of not more than six motors	To avoid redundancy and reduce cost
2. Each motor reacting on the foundation	To avoid interaction between motors
3. Each motor operates directly on the same load	To achieve the maximum performance for a given power source
4. High pay load/structure weight ratio	To achieve the maximum performance from power available
5. Each motor identified with one motion	Simplicity of control
6. Low friction motions	To reduce power losses and to obtain high response
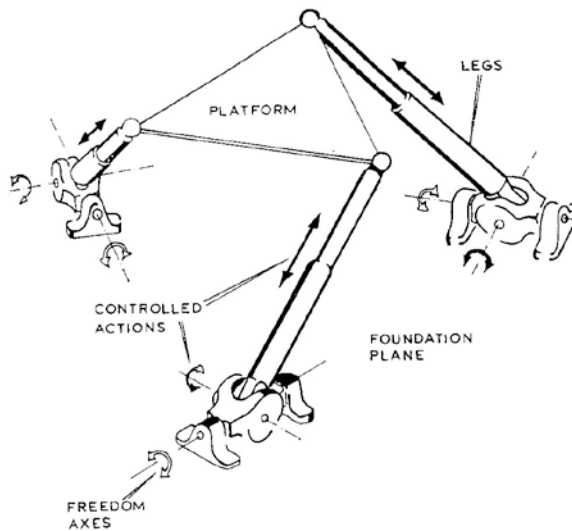
Figure 10: Stewart Platform Original Design [15]

According to Dasgupta, "The generalized Stewart platform, as it is understood today, consists of two rigid bodies (referred to as the base and the platform) connected through six extensible legs, each with spherical joints at both ends or with spherical joint at one end and with universal joint at the other" [14]. Dasgupta's description of a general Stewart platform is considered to be a completely parallel manipulator while Stewart's original design seen in Figure 10 is not truly parallel. However, the Stewart platform description given by Dasgupta is what is accepted today as the Stewart platform. Some of the more conventionally used platform arrangements, which are the 3-3, 3-6, and 6-6 configurations, are shown in Figure 11.

Type 3-3   Type 3-6   Type 6-6
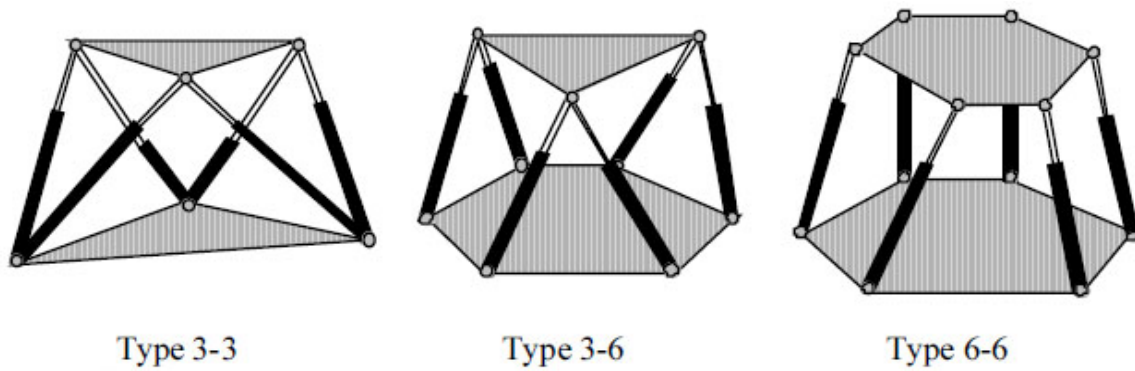
Figure 11: Common Platform Arrangements [16]

These configurations are considered to be fully parallel arrangements and differ from one another according to the configuration of the link-platform joints. For instance, the 3-3 configuration has the six links connect to both the base and platform at only three points, while the 3-6 configuration only has the link-platform joints coalesce at three points and the base joints connect independently. Most of the research regarding the Stewart platform before the 1990s was performed using the 3-3 or 3-6 arrangement [14]. The results of further research regarding the Stewart platform configurations showed that the coalescence of the spherical joints highly restricted the mobility of the manipulator.

21

This is because the coalescence of the joints limited the available workspace of the manipulator. In other words, it limited how far the platform could roll, pitch, and yaw before the legs would interfere with one another. This resulted in additional configuration designs being explored with the trend toward an arbitrary arrangement of the connection points, such as the 6-6 configuration shown in Figure 11 [14].

Today the Stewart platform is classified as a parallel manipulator in robotics, and it is often considered to be a good general representative of parallel manipulators and the distinctive features associated with them [14]. The primary roles for a parallel manipulator, such as the Stewart platform, is to provide precise positioning and to support the load, which are possible if the design criteria are focused toward the stiffness and rigidity of the manipulator [14]. These attributes of parallel manipulators allow them to be very versatile and adaptable and thus useful in many different applications. The ability of the Stewart platform to provide exceptional rigidity and positioning control are usually the primary reasons that it is chosen for a particular application. These properties provide a strong and efficient base for simulators that require a full range of motion in three dimensions. For these reasons, a Stewart platform was proposed for the next generation design of a mechanical horse.

Modern Applications of the Stewart Platform

Stewart believed that the conceptual design criteria and the beneficial attributes associated with the Stewart platform would prove useful in a variety of application. This included his original application of the platform as a motion control base for flight simulation and others applications, such as large cargo manipulation or applications within the medical industry [15]. In short, Stewart saw potential use of the Stewart

22

platform configuration for any application wherein the user needed full universal motion capabilities [15]. The Stewart platform configuration is currently used today for most full flight simulators. A Stewart platform configuration can be seen driving the three-dimensional motion of the Thales flight simulator shown in Figure 12 in a pitched position [17].

Figure 12: Thales Flight Simulator [17]

Recently, Lexus has utilized a Stewart platform configuration in conjunction with other components to develop a full-sized vehicle driving simulator [18]. The Lexus driving simulator, shown in Figure 13, couples the Stewart platform configuration with a series of connecting tracks and an additional turn-table base located inside of the visualization dome that rotates accordingly with the simulated turning. This combination

allows the Lexus simulator to realistically recreate the feeling of driving at speeds up to 186 miles per hour with a turn angle of 330 degrees. It is evident from the previous examples that the Stewart platform can be used for motion simulators that require both high load capacity and precision control in three-dimensions.

Figure 13: Lexus Full Vehicle Simulator [18]

Stewart's predictions regarding potential applications for the Stewart platform configuration were very accurate. The Stewart platform has proven useful within the medical field. Dr. J. Charles Taylor utilized a Stewart platform in the development of an external fixation system to help repair fractures, nonunions, and malunions [19]. The Taylor Spatial Frame Fixator, Figure 14, consists of two full or partial rings that act as the base and platform and six telescoping struts connected to the rings by universal joints [19].

Figure 14: Taylor Spatial Frame Fixator [19]

While Stewart's original concept included programmable simulation data, the use of the Stewart platform configuration with passive, manually controlled legs allows the Taylor Fixator be capable of correcting six axes deformities or to lengthen a limb without inducing a preload on the frame [19]. A demonstration of how the Taylor frame can be used to realign fractured bones is shown in Figure 15.
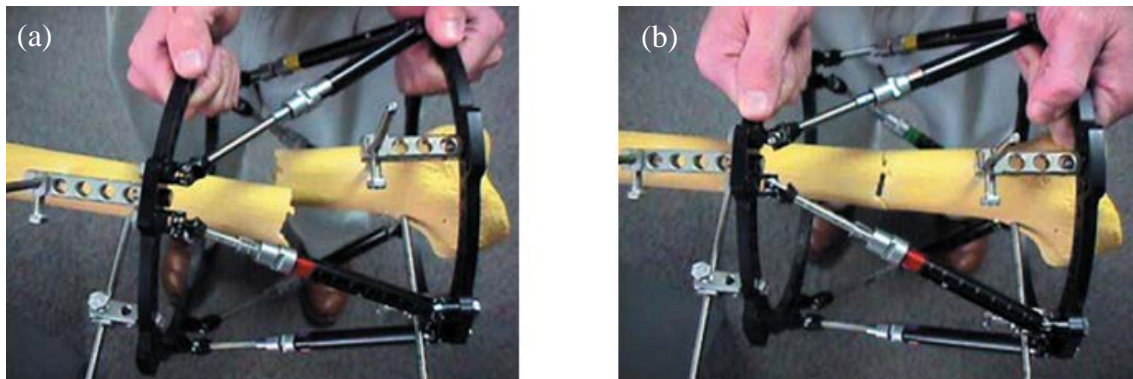
Figure 15: (a) Unaligned Bone (b) Aligned Bone [19]

This demonstration highlights the potential flexibility or range of motion of a Stewart platform design. However, while the Taylor Frame has the ability to be flexible to allow the alignment of a fractured bone, it is also capable of being extremely rigid when locked. This rigidity ensures that once the bone is set in place it stays in that position. As seen in Figure 16, the Taylor Spatial frame can be used in surgery to realign a patient's fractured leg.

Figure 16: Taylor Spatial Frame in surgery [19]

The ability of a Stewart platform to provide exceptionally precise positioning, structural rigidity, and high load capacities has led to its use for medical applications in a number of disciplines including orthopaedics, shown above, and neuroendoscopy [20, 21]. The study performed by Walper *et al.*, on the M-850 hexapod robot from Physik Instrumente (1996), showed that this particular Stewart platform based robot could

provide precise, repeatable placement of an endoscope tip that is accurate to 4.5 µm [20].

The M-850 robot, shown in Figure 17, is being tested with a phantom subject by Wapler

et al. to verify its accuracy [20].
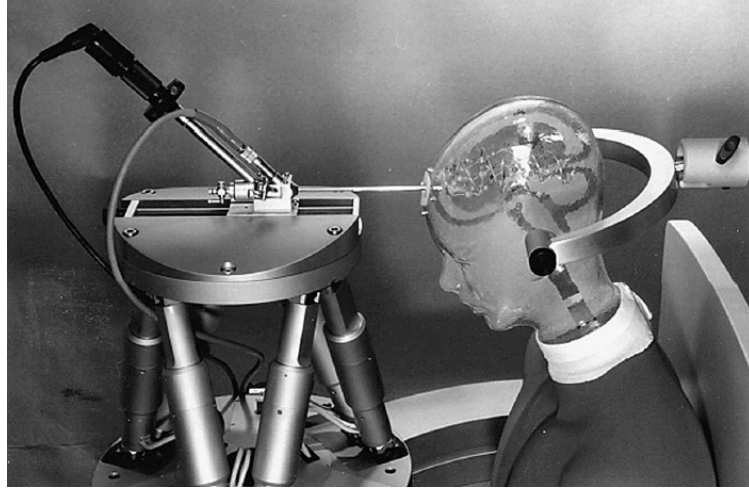
Figure 17: Stewart Platform Robot used for Precision Surgery [20]

The Stewart platform configurations may also be applicable in developing force-

torque sensors. Research into the configuration design of Stewart platform based force

sensors was undertaken by Yao *et al.* to analyze a spatially isotropic configuration of the

Stewart platform [22, 23]. An isotropic configuration of a Stewart platform sensor is

needed to provide more uniform sensitivity to external forces and to minimize relative

error in force mapping [23]. Two force-torque sensors based on the Stewart platform

were designed and analyzed by Zhenlin *et al.* [24, 25] and Dwarakanath *et al.* [24, 25].

The design developed by Dwarakanath *et al.* is shown in Figure 18. This particular

design uses a ring shaped leg that allows for an increase in the sensor's sensitivity to the

rated load [25]. A Stewart platform force sensor, such as the one described by

Dwarakanath *et al.*, could prove useful as an alternative solution to commercial six-axis

load cells when cost or use for custom applications is important.
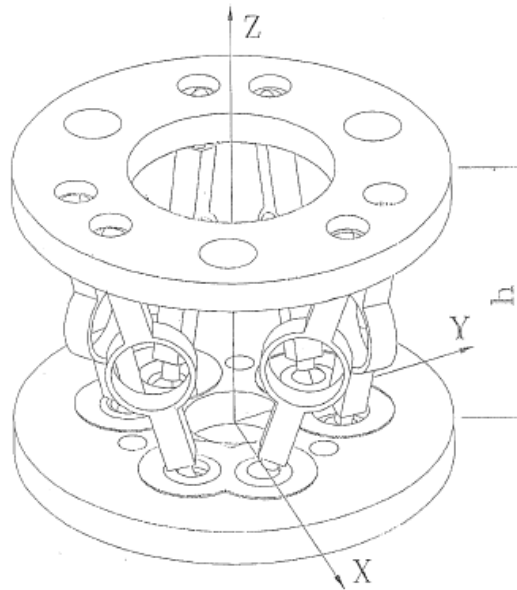
Figure 18: Stewart Platform Based Force-Torque Sensor [25]

Use of a Stewart platform configuration was proposed during the conceptual development phase of a second generation mechanical horse design at Baylor University. The concept was to utilize a passive Stewart platform configuration with six helical compression springs for the support structure of the mechanical horse. In other words, rather than utilizing linear actuators that mechanically change the length of each leg, the legs would be comprised of compression springs. The motion of the platform would then be controlled through an alternate method, such as actuated cables (See Figure 19). These cables could be actuated by a cam system as shown in Figure 20 (a) and (b). The unique design of the Stewart platform means that the use of compression springs for the legs would place the compression springs under multi-axis loading as the platform is driven in three-dimensions. To accurately define the control scheme used to drive the motion of the platform, a better understanding of compression spring reaction forces when displaced in three-dimensions is needed.

Figure 19: Second Generation Mechanical Horse Conceptual Design Prototype using Stewart Platform configuration with helical compression springs driven by cables [26]
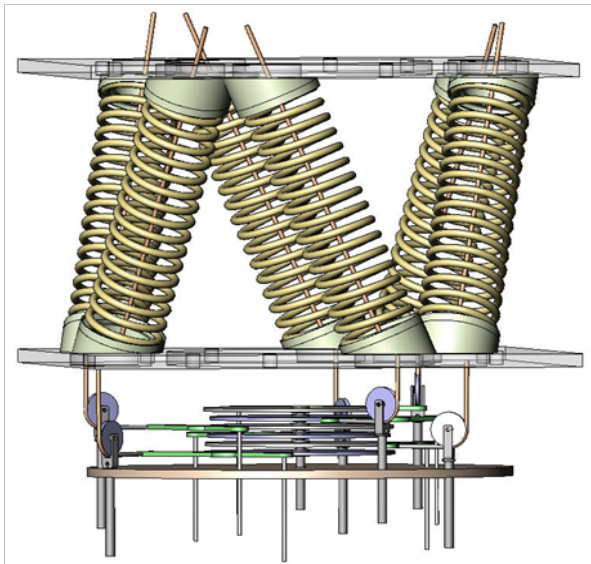
Figure 20: (a) CAD Model of Cam-Cable Driven Compression Spring Stewart Platform (b) Prototype Model of Cam-Cable Driven Design [26]

CHAPTER THREE

Motivations

Hippotherapy provides a significant amount of the motivation for the work completed in this thesis. While hippotherapy is not a primary subject matter in this thesis, the work completed regarding the behavior of compression springs was performed for the purposes of developing a model that would be used to design a control scheme for the second generation mechanical horse prototype. Thus a brief overview regarding hippotherapy is presented in this chapter to provide insight into how hippotherapy is performed and why hippotherapy research is needed. This is followed by a section covering previous devices that have been or may be used to simulate the complex 3D motion of a horse's back.

Hippotherapy

Equine Assisted Activities and Therapies

Equine Assisted Activities and Therapies (EAAT) are the equine activities and therapies that The North American Riding for the Handicapped Association (NARHA) and The American Hippotherapy Association (AHA) regulate and promote. NARHA, a nonprofit organization, was founded in 1969 with the goal to promote EAAT [27]. NARHA currently maintains over 3,500 certified instructors along with 800 member centers that provide horse-based therapies for a multitude of people each with unique needs [27]. Since the founding of NARHA, multiple forms of equine-based activities

that provide therapeutic treatments have been developed. According to NARHA's

official website, equine-based activities include:

> "*therapeutic carriage driving; interactive vaulting, which are similar to gymnastics on horseback; equine-facilitated learning and mental health, which use the horse as a cooperative partner for cognitive and behavioral therapy, usually with the participation of a licensed therapist; ground work and stable management; and NARHA Horses for Heroes, a new program that uses a variety of EAAT disciplines specifically oriented towards helping war veterans and military personnel*" [27].

These activities constitute the current curriculum list provided by NARHA for equine

assisted therapies; however, NARHA has committees that continue to refine the current

activities and to develop more activities as the EAAT industry expands [27]. One of the

EAAT categories is hippotherapy. Furthering the research of hippotherapy is the

motivation behind the current research.

A relationship has existed between humans and horses for centuries. The horse

was used as the primary means of transportation for centuries. Horses were used to help

perform physical tasks as well. Horses were used to perform heavy labor, such as

plowing. They were also fitted with armor to protect them in battle. Beyond the use of a

horse for physical tasks, there are mythological stories of the horse being a healer of man

and historical record of horses being used to rehabilitate injured people [28]. Within the

medical literature, there are reports on the benefits of horseback riding being subjectively

described by physicians and therapists dating back to the second century [29]. During the

fifth century BC, Greek and Roman soldiers injured during battle were placed back onto

their horses to help promote faster recovery. In general horses were believed to improve

the health and well-being of people [30]. Horses have been used in Germany to provide

therapeutic benefits since the 1600s, according to Riede [30].

The use of equine-assisted therapy began to receive significantly more attention from the scientific community in the 20th century. Liz Hartel of Denmark, who was physically impaired due to poliomyelitis, competed in the Olympic Grand Prix Dressage event and won the silver medal in the 1952 Olympics [27, 28, 31]. The only therapy that Hartel underwent for her recovery before competing in the dressage was horseback riding, or therapeutic riding, resulting in a spark of interest from equine and medical professionals around Europe [27, 28, 31]. Organizations began to form in Europe. These organizations started developing programs that used horseback riding for physical therapy [27, 28, 31]. One of the first organizations formed to use horseback riding for physical therapy was the Pony Riding for the Disabled Trust in England, formed in 1958. As the news of riding therapy spread to North America, the Community Association of Riding for the Disabled in Canada and the Cheff Center for the Handicapped in Michigan were founded in the 1960s [27, 28, 31]. NARHA was formed soon after and remains a prominent leader in the promotion of the education, research, and development of therapeutic riding [28]. The American Hippotherapy Association works together with NARHA to develop hippotherapy curricula and to provide the education required for therapists to become licensed to provide hippotherapy treatment. The American Hippotherapy Association started in the United States in 1987 as the Hippotherapy Curriculum Committee, which in 1992 joined NARHA. In 2004 the American Hippotherapy Association became an independent entity [32]. The AHA is primarily responsible for hippotherapy development today but remains closely affiliated with NARHA and other therapeutic riding associations.

Terminology and Common Misnomers

The terminology used within the medical community for equine-assisted activities and therapies continues to evolve. This has resulted in discrepancies among the definitions of therapeutic riding, hippotherapy, equine-facilitated learning, and other equine activities. As research into equine activities and therapies progressed, researchers worked to formulate a unified set of definitions. In 2004, Meregillano stated that the equine-assisted activities and therapies could be separated into three categories with both category specific and overlapping therapeutic benefits [28]. These three categories are hippotherapy, or medical riding; therapeutic riding, or exercise; and sport riding, or vaulting [28]. There is very little confusion regarding what activities constitute sports riding in the literature. When the definition of therapeutic riding and sport riding were first distinguished from one another, the difference was essentially defined according to the premise that with sport riding, the rider affects the horse. With therapeutic riding, the horse affects the rider [33]. The use of this particular definition might effectively separate sport riding and therapeutic riding, but it fails to distinguish between hippotherapy from therapeutic riding. Overall, sport riding, or vaulting, utilizes gymnastic-like movements on horseback and helps individuals with behavioral and emotional disabilities by working on teamwork skills, improving independence, fostering confidence, and improving social skills [27, 28].

The term "therapeutic riding" is often used as an "umbrella" term to define a number of equine activities, including hippotherapy. This usage has thus created some confusion among the medical community due to various definitions and interpretations of the term [32, 33]. Understanding the difference between therapeutic riding and hippotherapy is important. Therapeutic riding provides activities that are not purely

recreational but provide rehabilitation for people with disabilities [32, 33]. With

therapeutic riding, the patient actively participates and interacts with the horse, learns

new skills and abilities that bolster self-confidence, self-efficacy, and social skills.

Therapeutic riding provides additional benefits, such as improving coordination, balance,

and other physical abilities [27, 28, 33].

It is likely that the difficulty in developing a solid definition for hippotherapy and

therapeutic riding is partially due to the constant development of equine-based activities

over the past fifty years. In this thesis, the definitions provided by NARHA and AHA

will be used consistently to prevent confusion. According to the AHA, "when the

therapist utilizes the movement of the horse as a treatment strategy to improve

neuromuscular function, it is important to consistently use the correct terminology and

refer to it as 'hippotherapy' [32]". The motivation for the current research stems from the

original goal of understanding the complex three-dimensional behavior of compression

springs. This understanding is intended to aid in the design of a mechanical horse that

could be used as an additional tool for therapists or potentially as a substitute for the

horse all together.

Understanding Hippotherapy and its Benefits

The word *hippotherapy* is derived from the Greek *hippos*, for horse, and literally

translates as "treatment with the help of a horse" [32]. Hippotherapy is a form of

physical therapy. According to the American Hippotherapy Association, "Hippotherapy

is a physical, occupational, and speech-language therapy treatment strategy that utilizes

equine movement as part of an integrated intervention program to achieve functional

outcomes" [32]. The hippotherapy patient is passive during hippotherapy sessions and is

influenced by the environment, which is primarily the horse but can be more expansive [28, 33] It is important to stress the passive nature of the patient and the active role of the therapist and the horse. The horse in hippotherapy, is used by the therapist as a tool to provide external stimulus to the patient that will promote and enhance rehabilitation. The patient responds to this stimulus in a manner similar to that provided by the therapeutic use of a weighted medicine ball or electrical stimulation [28, 31]. AHA's definition of hippotherapy emphasizes this point:

> *"The horse influences the client rather than the client controlling the horse. The client is positioned on the horse and actively responds to his movement. The therapist directs the movement of the horse; analyzes the client's response; and adjusts the treatment accordingly. This strategy is used as part of an integrated treatment program to achieve functional outcomes"* [32].

An important misnomer is the notion of a hippotherapist because hippotherapy is provided by trained physical or occupational therapists who are often a part of a larger multidisciplinary team [32]. Hippotherapy requires a team in order to provide a safe, controlled environment for the patient. This team typically includes the horse, the horse handler, a side walker, and the therapists [28, 31, 34]. A hippotherapy horse must be extremely well trained, have a calm temperament, and have a specific gait pattern [28]. The horse's gait pattern is important because the motion transferred to the patient is changed when the gait pattern is modified. A therapy horse is a large, tall animal. Even with training, there is always some risk, but this same risk can provide a sense of accomplishment for the client. The horse handler should have strong equestrian skills and experience with therapy horses in order to ensure proper handling of the horse during the therapy sessions [31, 32]. The side walker is a person who helps assist the therapist during the sessions and provides an additional level of safety in case of any mishaps [28].

The therapist or therapists provide the treatment to the client. Multiple therapists can lead a hippotherapy session together in order to provide a well-rounded treatment plan for the patient. There could be a physical therapist, a psychologist, occupational therapist, and therapeutic riding instructor involved in the treatment of a single patient because each of these medical professions brings unique skill sets to the therapy session [28, 34]. A physical therapist works to facilitate improvements in gross motor control, and an occupational therapist works to develop the patient's fine motor control and sensory integration ability [32]. A team of therapy professionals can work together with the horse handler to change the horse's movements, the saddle, and the kind of activities the patient is directed to complete [32]. The horse is a tool in treatment. When the horse is handled properly, a team of therapists can provide behavioral, physical, and psychological goals to help rehabilitate the client [28]. Hippotherapy provides a controlled environment that takes advantage of the complex movement of a therapy horse and the patient's adaptive responses to the horse's movements. The constructive activities prescribed by the therapy team promote improvements in the posture, balance, behavior, and overall function of the patient [28, 30, 34].

Once the principles of how a hippotherapy session is performed are understood, the next step is to understand what aspects of the therapy result in the functional improvement of the patient and what the benefits of hippotherapy are in more detail. The reason for understanding these concepts and how they affect the motivation for the spring research will be discussed later. The complex three dimensional movements of the horse's back generated as the horse walks are integral to understanding many of hippotherapy's benefits.

The first systematic subjective review of the effects of riding on disability is credited to Chassaigne in 1870; he concluded that riding was helpful for patients with various neurological disorders [31]. This was based on Chassaigne's observations of improved posture, balance, and muscle control [31].

During hippotherapy the back of the horse acts as a dynamic support base for the patient to be placed on, and the movement of the horse provides a challenge for the patient that helps to develop postural strength and control and motor planning [28, 32]. The therapy horse's movement must be smooth, rhythmical, and repetitive [30-32]. When the patient sits astride and facing forward, the movement pattern generated during the horse's walking gait is transferred to the patient is biomechanically similar to the motion of the human pelvis during walking [30-33]. A therapist uses this unique aspect of the motion that the horse generates to provide controlled sensory input to the patient. This allows the patient to respond to movements that are similar to human gait patterns [29, 32]. The way a patient is placed on the horse and the activities provided for the patient while riding the horse help the therapist achieve specific functional outcomes. For instance, the therapist may choose to place the client on the horse in a variety of positions, such as facing forwards, facing backwards, sitting, prone, or side lying. Additionally, the therapist may even choose to ride with the patient in order to achieve the appropriate position for the patient [28, 31]. Figure 21 illustrates some of the different riding positions used for hippotherapy. Many of these different positions also ensure that the patient is passively reacting to the movements of the horse, and the activities are prescribed by the therapist to achieve a specific, desired response from the patient [28, 29].

It is important that the therapist understands how the motion of the horse will affect the rider and to be able to adapt to changes in the environment. In order to accomplish this, it is important that the therapist be properly trained and certified. The therapist must have enough knowledge and skill to continually read the movements of the horse. The therapist must observe how the patient is responding to the horse's movements and then make any necessary adjustments to the horse's cadence or direction or to the prescribed therapeutic activities in order to provide a positive hippotherapy session that results in the desired functional improvements in the patient [28, 31, 32, 34].
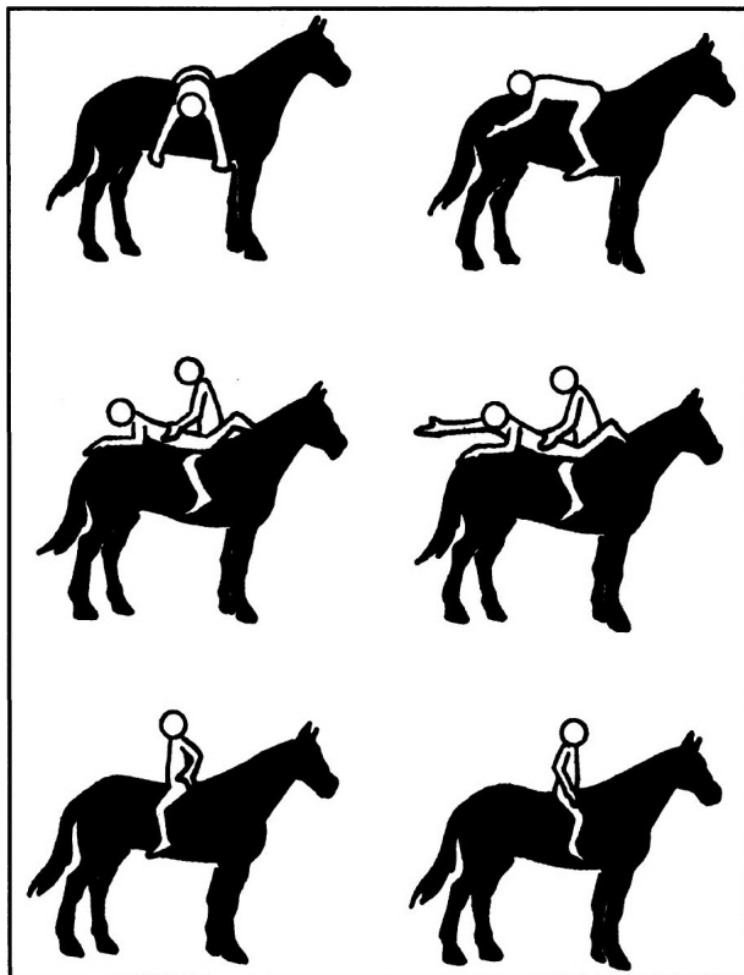
Figure 21: Various Hippotherapy Riding Positions [31]

Equine movement provides a controllable amount of vestibular, proprioceptive, tactile, and visual sensory input, that when coupled with the constant shift in the client's center of gravity, provides the patient with unique learning experiences. Many of these learning experience provided during hippotherapy are learning experiences that children without disabilities develop during normal playtime activities such as, coordination skills, respiratory control, sensory integration, and attention skills [30, 32]. In general a patient whose disability has precluded development of a rhythmic, reciprocal gait pattern is thought to acquire aspects of reciprocal movement and upright postural control through stimulation of normal balance reactions and repetitive challenges to postural coordination during hippotherapy sessions [30, 35]. Research shows that hippotherapy can provide physical, emotional, behavioral, psychological, social, cognitive, and speech benefits that traditional treatments may be unable to provide [28, 30]. These benefits occur because of the multifactorial nature of hippotherapy. For instance, emotional and psychological benefits can be gained as the patient develops a bond with the horse, a powerful animal, and from the feeling of controlled freedom as the patient rides on the horse [28, 30] . A brief listing of some of these benefits, both physical and emotional, are listed in Table 3. Improvements in the patient's postural control are gained from gait transitions during hippotherapy that provide the rider with opportunities to develop equilibrium reactions in response to the equine motion [31, 32]. Research also suggests that the warmth of the horse, which can be better transmitted to the patient by using padding instead of a saddle, provides additional benefit along with those derived strictly from the equine motion [31]. The warmth of the horse, in combination with the smooth, rhythmic movement, may help increase circulation, promote relaxation, reduce excessively high muscle tone, and stretch

out tight muscles in the patient. Many of these benefits are particularly helpful for rehabilitating children with spastic cerebral palsy [29-31].

Table 3: Summary of Hippotherapy Benefits [28]

Physical Benefits	Cognitive, Social, and Emotional Benefits
Mobilization of the pelvis, lumbar region of the spine, and hip joints	Improved self-esteem
Normalization of muscle tone	Improved confidence
Development of head and trunk postural control	Improved didactic and group interaction
Improvement of endurance, symmetry, and body awareness	Improved concentration
	Improved attention span
	Improved communication

Limitations of Hippotherapy

The availability of hippotherapy is limited. One factor that limits the availability of hippotherapy clinics are geographical restrictions. Hippotherapy centers typically require a large plot of land in order to maintain a stable for the horses to live in and enough additional land for the horses to be trained. The availability of land within most urban areas for such a facility is scarce. This means that for a patient to receive hippotherapy treatments, they must travel farther to an appropriate facility than they would for many of the more traditional therapies.

There are monetary challenges as well. The cost to acquire enough land to build both a therapy clinic and stables for the horses is not trivial. Beyond capital costs, there

are upkeep costs, such as horse feed, grooming, stable maintenance, and training for the both horse and therapist.

Obtaining and training a therapy horse is also a challenge for clinics because a therapy horse must meet specific requirements to be certified. These requirements include having a specific gait pattern during a walking cadence and being docile in environments that often are stressful and distracting with many people, including children, being around the horse at one time.

Allergies to horse dander, hay, or any other allergens commonplace in stables can prevent hippotherapy from being a treatment option for many people. Additionally, phobias, such as equinophobia, the fear of horses, and acrophobia, the fear of heights, can limit hippotherapy as a viable treatment option [28].

Performing research about the effectiveness of hippotherapy treatments to rehabilitate specific disabilities is complicated. There are difficulties in gathering data on hippotherapy and its associative benefits due to the unique individuality of each patient. Because the benefits of hippotherapy may be multi-factorial, it is difficult to discern cause and effect [30]. These factors thus make it difficult to perform a comprehensive research study on hippotherapy. For example, because the availability of hippotherapy is limited and there is generally a smaller client base for hippotherapy compared to the more traditional therapy options it is often difficult to collect data on a large enough population in order to achieve an acceptable level statistical power. Many research studies on hippotherapy supply only general observations of improvement, and such results are subjective. It is difficult to find enough patients with a particular disability to study it singularly because of the variability among patients and their disabilities.

Other factors that influence the effects of hippotherapy include the warmth of the horse and socio-psychological effects that result from the development of a relationship between the patient, the horse, and the members of the therapy team. Many of the non-physical benefits associated with hippotherapy may be due to factors that are difficult to study considering the large number of variables present in hippotherapy sessions. The physical benefits could also be significantly affected by using a live animal that provides a unique level of tactile and visual stimulus that other treatment options would not offer.

The limitations of traditional hippotherapy create a need to develop better ways of quantifying the benefits of traditional hippotherapy and options that increase the availability of hippotherapy to more people. Research into a mechanical device that can simulate hippotherapy sessions could potentially help fill both of these needs. A look into how such a mechanical device may affect the benefits of hippotherapy and an overview of some current "mechanical horses" will be discussed in the following section.

<div align="center">The Mechanical Horse</div>

The Need for a Mechanical Horse

While there has been extensive research into the therapeutic benefits of hippotherapy, there are still many factors that limit the availability of hippotherapy for use as a therapeutic treatment modality. The development of a mechanical horse could help improve the availability of hippotherapy as well as provide ways to perform research into the benefits of hippotherapy by providing a way to remove many of the variables that currently make it difficult to perform comprehensive studies. The concept of developing a mechanical substitute for horseback riding is not new. In the 1700s, Professor Samuel Theodor Qeullmalz developed a "horse machine" that was likely the first mechanical

attempt to replicate the motion of a horse [36]. Qeullmalz's device is described as a type of see-saw device that attempted to accurately mimic the effects of equestrian motion [36]. Qeullmalz studied the effects of horseback riding and noted the three dimensional motion of a horse's back [36]. According to Riede, "Qeullmalz reaches the conclusion that equitation is too expensive and it is therefore necessary to invent a machine which reproduces its effects [36]. Quellmalz's conclusion and attempt to develop a mechanical substitute shows that even in the 1700s it was becoming evident to researchers that there was a need for alternative solutions for physical exercise, including the physical exercise provided by horseback riding [36]. The next reference to a mechanical horse is seen in the work of the Swedish Dr. Gustov Zander who developed a saddle apparatus in the late 19th century that provided saddle movements similar to the pitching of an airplane to be used for exercising balance and with vibrations to be beneficial to the tonicity of one's internal organs [36, 37]. Dr. Zander's mechanical horse, shown in Figure 22, was used in the Titanic's fitness room [38].

Figure 22: Dr. Zander's Horse Exercise Machine [37]

According to Zander, "Vibrations of 180 oscillations a minute stimulate the nervous system in a congenial and beneficial way" [36]. According to research done by Reide, the back of a horse during a walking or trotting gait oscillates at a frequency around 180 oscillations per minute [36]. The development of a mechanical substitute for horseback riding could benefit hippotherapy. The designs of Professor Qeullmalz and Dr. Zander are only two examples of mechanical devices designed to replicate horseback riding motion for medical benefits. Today there are quite a few modern design concepts and commercial products that are designed to take advantage of horseback riding movement, and some of these designs will be discussed in the next section.

Current Options

Today there are a number of commercially available mechanical horse devices. Many of these commercial horse riding simulators have been developed for use as core exercise machines that help the user to improve core body strength and balance. Other simulators were developed to help train people how to ride a horse properly in a more controlled environment or to help equestrians train without a horse [39]. Today some therapists utilize a mechanism called the *Equicizer*, shown in Figure 23, as a precursor training device to hippotherapy on a live horse.

The *Equicizer* can help children who are not completely confident on a live horse and children who do not have enough postural balance control to ride on a live horse to develop the necessary skills in a control environment. The *Equicizer* was developed by former jockey Frank Lovato, Jr. who originally designed the *Equicizer* to rehabilitate himself after fracturing his leg in a riding accident [39]. While the *Equicizer* is used as a

tool to help prepare for patients for hippotherapy sessions, it does not replicate the

movements of a live therapy horse.

Figure 23: Equicizer [39]

There are other commercial mechanical horses that, like Dr. Zander's mechanical

horse, are marketed as exercise machines. One of these products is the OSIM *iGallop*, an

exercise machine that is supposed to mimic riding a horse and help build muscle tone and

lose weight. There is also the *Panasonic Joba Horseback Riding Machine*, the *Human*

touch iJoy Twist, and the *Human touch iJoy Ride*. These four mechanical horse

simulators are shown in Figure 24.

Figure 24: Commercial Simulators (a) Joba [40] (b) iJoy Ride [41] (C) iJoy Twist [41] (d) iGallop [40]

These core exercise machines do not accurately simulate the three-dimensional motion of a live horse. The motions are generally smaller in amplitude than the motion seen from a live horse. A study comparing the motion of the *Panasonic Joba* and the *OSIM iGallop*'s compared to that of three therapy horses was performed by Garner [40]. The study utilized a motion capture system to analyze the motion of the *Joba* and *iGallop* and to compare their motion to three live horses used for hippotherapy. Garner concluded that the motion patterns of the *Joba* and *iGallop* have some similarities to the

motion of the three horses, but there are significant differences [40]. The motion of the

Joba was similar to that of the three horses, but the magnitudes were substantially larger,

and the twist angle was out of phase. For the *iGallop* the rotation angles were smaller,

and the list and twist motions were repeated twice per gait cycle compared to the three

horses used in the study. For all four of the devices shown in Figure 24 the size of the

seat is significantly smaller than the back of a horse as well. Further studies are needed

on the other commercially available mechanical simulators before any significant claims

to their ability to replicate the motion of live horses can be made.

The development of a mechanical horse that can provide complete three-

dimensional, variable, repetitive, and rhythmic motion that is exactly identical to the

motion of a live therapeutic horse could provide further research possibilities into the

effects of hippotherapy and increase the accessibility of hippotherapy treatment.

Mr. Ed I

A mechanical horse that was designed to reproduce the complex three-

dimensional motion of a live therapy horse was developed at Baylor University. This

first generation mechanical horse, termed Mr. Ed (Figure 25), was developed during the

2009 spring semester at Baylor University by senior engineering students for their senior

capstone design course. The design used motion capture data recorded from a live

therapeutic horse from a local hippotherapy center for its target motion specification.

Additional design requirements provided for the students are provided in Appendix B.

Figure 25: First Generation Mechanical Horse, Mr. Ed

(a)

(b)

(c)

(d)

(e)

(f)
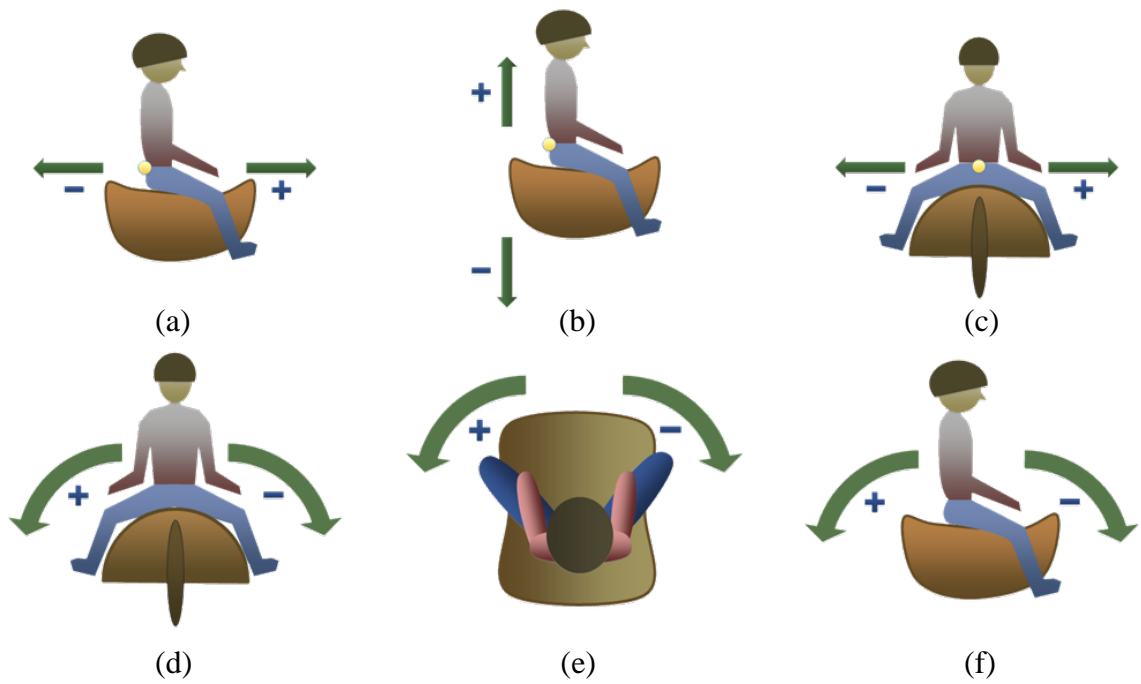
Figure 26: (a) X-Translation (b) Y-Translation (c) Z-Translation (d) X-Rotation (e) Y-Rotation (f) Z-Rotation [40]

Motion analysis was performed on the first generation mechanical horse, and the results were compared to the data from the target therapy horse. The results shown in Figure 27 and Figure 28, indicate that the motion generated by the mechanical horse was similar to that of the therapy horse, but was not an exact match. The translational movement (see Figure 26) of the mechanical horse was larger in amplitude in the z-direction and out of phase in the x-direction, as seen in Figure 27.
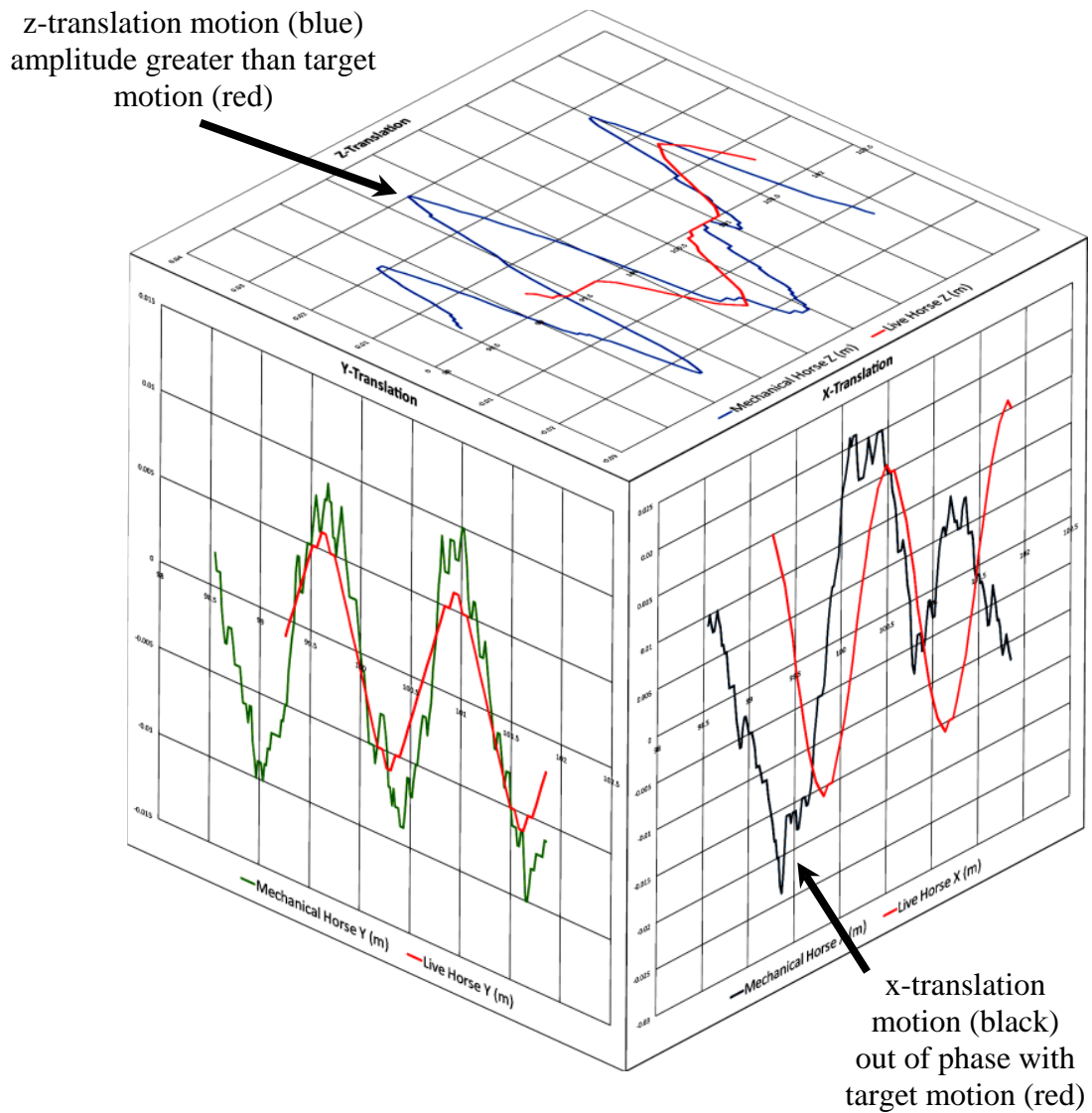
Figure 27: X, Y & Z Translations of Mechanical Horse vs. Live Horse [42]

z-rotation (blue) amplitude
greater than target motion (red)
and out of phase

y-rotation (green)
amplitude greater than
targer motion (red) and
out of phase
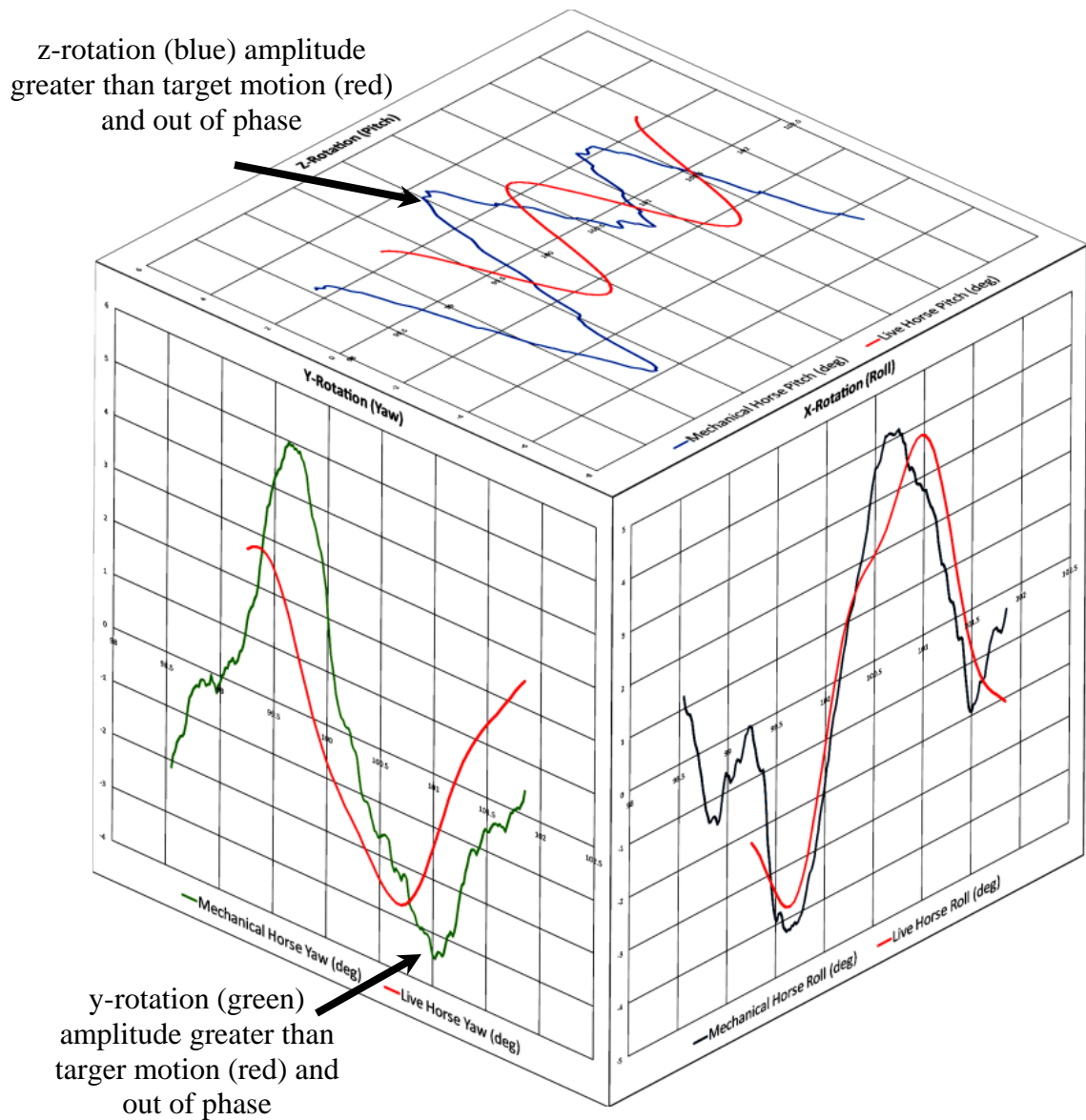
Figure 28: X, Y & Z Rotations of Mechanical Horse vs. Live Horse [42]

The rotational amplitude in the z-direction and the y-direction were larger than the

target motion and the z-direction rotation was out of phase (See Figure 28).

There were limitations to the first generation mechanical horse that need to be

resolved. First, the user load specification was not met, largely because a large moment

was placed on the rear spherical four-bar mechanism when tested under simulated user

loads. The moment placed on the back spherical four-bar became large enough to place

the back spherical mechanism into a technical singularity with respect to the mechanical

horse design. When this occurred, the mechanical horse locked up, and the back

spherical mechanism had to be manually moved out of its improper position. Second, the

motion of the mechanical horse did not match the target motion. The larger magnitudes,

phase misalignments, and unwanted joint laxity resulted in an overall motion and feel that

was choppy, rough, and noisy. However, the first mechanical horse was by no means a

failure. The first generation mechanical horse design provided insight into the process of

designing such a complex mechanical device that will prove useful when the second

generation design is developed.

The first prototype required complex and difficult to manufacture components

that are not suitable for larger production numbers. The next mechanical horse design

needs to provide a better match to the target motion data, increase the user load capacity,

improve manufacturability, and provide a means to easily change the motion from one

pattern to another. The design concepts for the second mechanical horse prototype

provide much of the motivation behind researching the behavior of a compression spring

under multi-axis loading. The reason for researching the behavior of compression

springs under complex loading scenarios is primarily motivated by the concept of using a

Stewart platform configuration coupled with compression springs forming a passive

structure whose motion could then be controlled in many different ways. For instance, a

cable system could be driven by cams as shown in Chapter 2 in Figure 20 (a) and (b).

CHAPTER FOUR

The Multi-Axis Load Cell

A load cell needed to be developed to measure the 3D response of the helical compression spring when displaced in three-dimensions. The following chapter provides detailed information regarding what load cells are, how they operate, and typical applications of load cells. This chapter concludes with a discussion of the custom load cell developed for this thesis and a description of the process used to calibrate and validate the load cell.

Load Cell Basics

What is a Load Cell?

Load cells provide researchers with valuable data about the forces an object is experiencing. These forces may be induced for quality assurance testing or product development, or the forces may be the result of the service conditions during use. Before load cells were developed, force was measured with mechanical level scales and spring scales, which can provide good accuracy if properly maintained. However, it can be cumbersome to calibrate and maintain spring scales. The development of the load cell expanded the ability to measure loads in a variety of applications and fields. At the research or educational level, load cells are used heavily for materials testing. Materials testing can range from simple loading of basic materials, such as steel and aluminum bar or rod stock, to complex loading of composite materials such as musculoskeletal tissues.

A load cell acts as a transducer, a device that converts one form of energy into another form of energy.

There are multiple types of load cells, and they differ from one another primarily in two ways: according to 1) the type of output signal the load cell provides and 2) the particular type of load they are designed to measure [43]. There are three main mechanically based load cell types, and each has certain advantages and disadvantages (See Table 4). However there are other types of load cells that are not mechanically based. The three mechanical based cells are the hydraulic load cell, the pneumatic load cell, and the strain gage load cell. Both the hydraulic and pneumatic load cells are mechanical force-balance devices, while the strain gage load cell converts strain into an electrical output [43]. Hydraulic load cells utilize a piston head that compresses a liquid that is confined inside a chamber with a fixed volume to induce a pressure increase [43]. The pressure increase provides an output reading that is linear and can be easily read [43].

The hydraulic load cells are able to handle extremely high loads along with dynamic loading. Since there is no need for electronic components, the cells are ideal for both remote and hazardous areas [44]. Some of the disadvantages of hydraulic load cells are that they are expensive, complex, and limited in accuracy to about 0.25% of FS (Full-Scale – Entire Load Range). A hydraulic load cell rated to five million pounds has at best an error of ±12,500 pounds. For a particular application an error range of 12,500 pounds may be ok, but for smaller load applications, a high capacity hydraulic load cell would not be used.

Pneumatic load cells utilize multiple chambers, allowing for increased accuracy compared to hydraulic cells, and are used often in areas that require a certain level of

sterility [43]. Pneumatic cells are inherently safe due to insensitivity to temperature changes and explosions. However, pneumatic cells respond slowly and are not effective under dynamic loading. Pneumatic load cells also require both clean and dry air to operate, so location can be limited without the use of an additional air filtration system [43].

Table 4: Types of Load Cells (Adapted from [43])

Type	Load Range (lbs)	Accuracy (FS)	Apps	Strengths	Weaknesses
Mechanical Load Cells (Non Strain Gage Based)					
Hydraulic Load Cells	≤ 10,000,000	0.25%	Tanks, bins & hoppers Hazardous areas	Takes high impacts Insensitive to temperature	Expensive Complex
Pneumatic Load Cells	Wide	High	Food industry Hazardous areas	Intrinsically safe, Contains no fluids	Slow response Requires Clean, dry air
Mechanical Load Cells (Strain Gage Based)					
Bending Beam Load Cells	10-5000	0.03%	Tanks, platform scales	Low cost. Simple construction	Strain gages are exposed, require protection
Shear Beam Load Cells	10-5000	0.03%	Tanks, platform scales, off-center loads	High side load rejection Better sealing & protection	
Canister Load Cells	≤ 500,000	0.05%	Truck, tank, track, & hopper scales	Handles load movements	No horizontal load protection
Ring / Pancake Load Cells	5-500,000		Tanks, bins, scales	All stainless steel	No load movement allowed
Button /Washer Load Cells	0-50,000 0-200	1%	Small Scales	Small & Inexpensive	Loads must be centered. No load movement permitted

Strain gage load cells are the most commonly used cell today. As technology has improved, the cost of this load cell type has been reduced and the accuracy has been increased. Currently strain gage load cells are accurate to around 0.03% of their FS value. Strain gage cells utilize the change in resistance as wire gages are strained to provide an electrical output. These gages are bonded to the load cell structure. Typically four strain gages are used to improve the strain sensitivity and to provide temperature compensation [44, 45].

Components of a Strain Gage Load Cell

The strain gage load cell is the dominate load cell type in industry because it is versatile, accurate, and not overly complex. A strain gage load cell is basically composed of three parts, which work together to accurately measure externally applied forces.

The first component is the load cell structure, which includes the type of base material used and the geometric design. The material and geometric design of the structure are typically selected based on the load limit and the loading mode that the cell will be used to measure. The design and structure of the load cell determines the maximum calibrated load that the cell should operate under. Exceeding this load may cause damage to the load cell, most likely due to plastic deformation of the load cell structure or damage to the strain gage-structure interface. The structure for a strain gage load cell is typically metallic (e.g. steel or aluminum), and is designed to be sensitive to specific load conditions, such as bending, shear, or compression and tension. The material properties of metals provide an ideal medium for strain gage load cells because they can be machined easily. Strain gages bond well to metallic surfaces. Metals typically have good thermal properties, which is beneficial because the structure acts as a

heat sink and removes heat generated by current flowing through the strain gages. Most load cells are designed to measure only one loading condition at a time, but there are load cells that are designed to measure multiple loading conditions. Typically an increase in the number of loading modes causes both an increase in the cost and complexity of the load cell.

The second primary component of a strain gage load cell is the strain gage or gages. The strain gage's electrical resistance changes as gage is elastically deformed. A strain gage acts as a variable resistor, providing a change in electrical resistance. The change in electrical resistance depends on the amount of mechanical strain the gage is under. A strain gage is bonded to the load cell structure, the substrate, so that the strain gage experiences the amount of same strain as the substrate. For a strain gage, it is the change in wire geometry that affects the electrical properties. When the wire is elongated due to strain, the wire length increases, and the wire radius decreases. These dimensional changes cause an increase in electrical resistance. Conversely, when compressed the wire length decreases, and the wire radius increases and causes a decrease in electrical resistance. By design, strain gages are developed to provide high sensitivity to very small strains. As seen in Figure 29, the wire of the strain gage is formed into a zigzag pattern [46]. This zigzag pattern creates an increased sensitivity to strain by amplifying the strain-induced change in resistance. The sensitivity of a strain gage to mechanical strain can be adjusted by changing the number of zigzags. The greater the number of zigzags in the overall pattern, the higher the sensitivity to mechanical strain. The strain sensitivity is improved because the change in resistance is amplified by the total amount of wire length. As the total length of wire in the pattern increases, the more the resistance is affected by geometric changes in the wire induced by the strain.
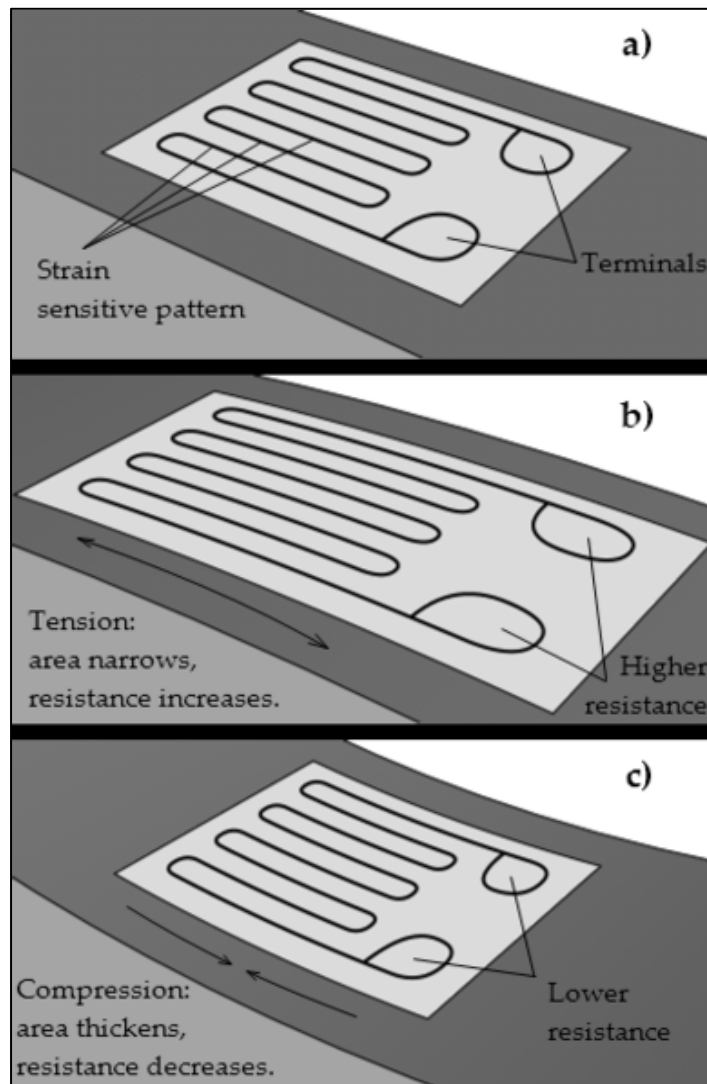
Figure 29: Generalized Strain Gage [46]

Constantan alloy or Isoelastic alloy wire is commonly used for the strain gage

wire material due to their mechanical and thermal properties [45, 47]. Constantan wire is

good when the operating conditions of the load cell are not extreme and temperature

compensation is needed. It is the most commonly used strain gage wire and is not

expensive [47]. Isoelastic wire is usually selected for applications that involve cyclic

loads or when a high signal-to-noise ratio is needed and the environment temperature is

well controlled. The strain sensitive foil wire pattern is placed onto a polyimide matrix backing, allowing the strain gage to be attached to the load cell structure. The polyimide backing is used because it is relatively flexible, which allows for mounting to surfaces with varying curvatures. For special applications, epoxy and glass fiber epoxy matrices can also be used, but these backing are more brittle and difficult to mount [47]. The strain applied to the load cell is transferred to the strain gage via a strong adhesive that provides a strong mechanical connection between the gage's matrix and the load cell structure.

Foil gages are not the only type of strain gages, but they are the most commonly used because they provide the largest selection of gage patterns. Some foil gage patterns can be seen in Figure 30. The rectangular and delta rosettes (i.e. a set of three gages on one polyimide backing) shown in Figure 30 are useful for applications where the principle stresses need to be investigated and the principle axes are unknown. The linear gage pattern is more suited for applications where only one strain direction needs to be investigated or cost is a factor. Gage patterns with more than one gage, such as rosette patterns, are typically more expensive than linear gages.

Figure 30: Rectangular and Delta Rosettes and a Linear Gage Pattern [45]

Semiconductor strain gages are an alternative to foil gages. They are very small and have large gage factors. Capacitive strain gages, another alternative, are very mechanically rugged and do not require protection [48]. Semiconductor strain gages or

piezoelectric gages are expensive because they are small in size and have large gage factors. Because piezoelectric strain gages are so small, they are often used for applications in robotics.

The Wheatstone bridge is the last primary component of a strain gage based load cell. The Wheatstone bridge, developed by Sir Charles Wheatstone in 1843, provides the means to measure very small changes in electrical resistance as a strain gage is elastically deformed [43, 44]. The measured change in resistance is converted into a voltage difference via the Wheatstone bridge, and this voltage difference is correlated back to the strain by the gage factor (GF) of a strain gage. The four legs of a Wheatstone bridge for a strain gage based load cell are usually comprised of four strain gages to provide maximum sensitivity. For a simple bending loading scenario, two of the gages would be placed under tension and the other two would be under compression, as shown in Figure 31.
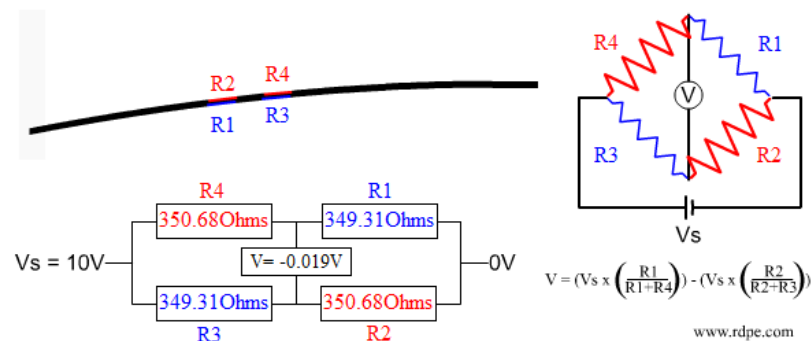

Figure 31: Example of Wheatstone bridge during bending [49]

When correctly placed into a Wheatstone bridge configuration, the four gages display an additive effect providing increased sensitivity to strain. Slight misalignments in the strain gages on opposite sides of the beam in bending can be negated The bending

setup of both the strain gages mounted to the specimen and their placement in the

Wheatstone configuration for four different loading modes are shown in Figure 31 and
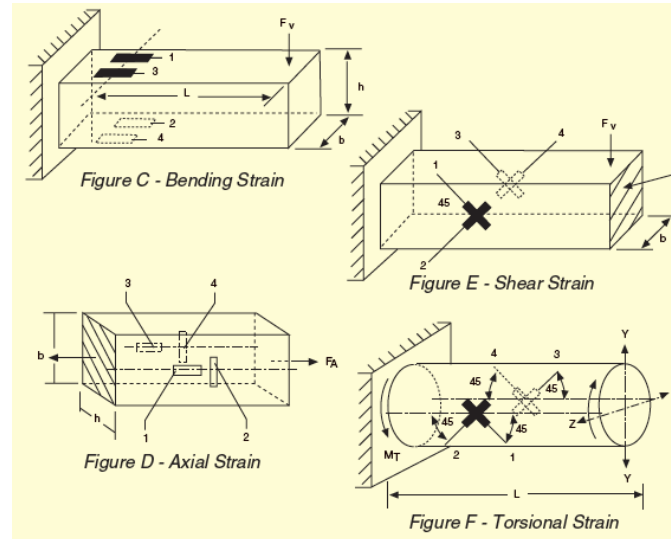
Figure 32.

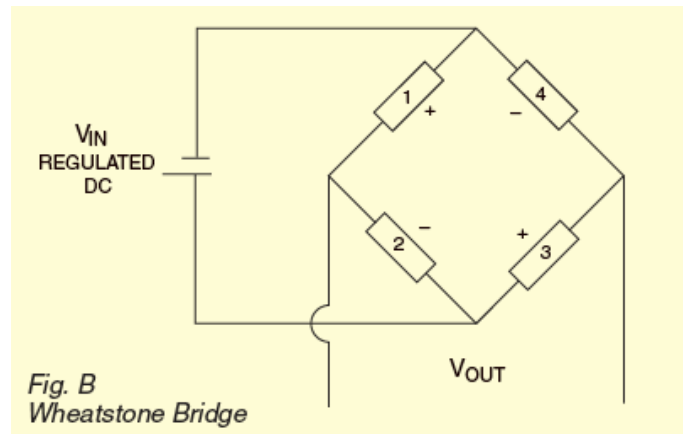Figure 32: Strain Gage Configurations for different loading modes [44]

Figure 33: General Wheatstone bridge Configuration   [44]

As shown in Figure 33, the gages opposite one another will add to each other, and the

adjacent gages will subtract from another. So gages 1 and 3 are in tension, which under

typical sign conventions make them positive, and gages 2 and 4 are in compression, or

negative. This is true for each loading mode shown in Figure 33 with the exception of the torsional loading mode. The torsional loading mode in Figure 33 has gages 2 and 4 in tension and gages 1 and 3 in compression. It could also be said that the axial, shear, and bending examples demonstrate a positive loading direction, while the torsional example demonstrates a negative loading direction considering the configuration of the four gages. Using four strain gages in this manner thus increases the sensitivity and improves the overall accuracy of the load cell. The axial load gage setup uses two gages placed along the width of the specimen rather than the length to account for Poisson's effect and to improve the accuracy of reading the axial strain.

To summarize, strain gage based load cells consist of the load cell structure, strain gages, and the Wheatstone bridge. A load cell provides a measurement of strain due to applied forces by utilizing the mechanics of each component in the load cell. First a load is applied to the load cell structure or a specimen with strain gages properly installed onto the surface. The applied load causes the load cell's structure to deform and strain. The strain is then transferred mechanically to the strain gages that are wired into a Wheatstone bridge configuration. The strain transferred to the strain gages deforms the strain gage wire and changes the gage's electrical resistance. The electrical resistance change is converted to a change in voltage by the Wheatstone bridge. From the voltage change, the user can calculate how much load, or force, was applied to the load cell.

Applications of Load Cells

Material testing was mentioned previously as one possible application of load cells. However, load cells are used in a variety of industries for many different applications. For example, load cells are used for railroad car scales, food packaging,

automotive testing, and suspension bridge load monitoring. To monitor the loads in a

suspension bridge's cables and the general user load of the bridge, load cells can be

placed in-line with the suspension cables of a bridge and underneath in the support

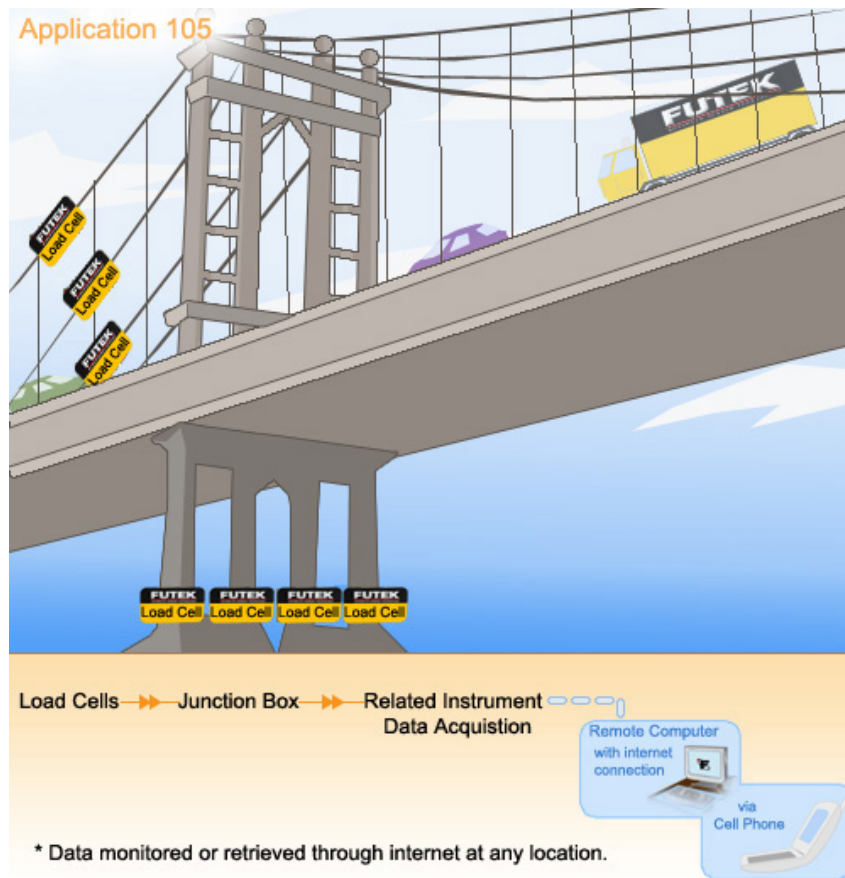columns of the bridge, as shown in Figure 34.

Figure 34: Load Cell App, Suspension Bridge [50]

These load cells allow engineers to monitor variations in the load due to changing

traffic conditions and weather changes [50]. The data from these load cells could later be

used to help determine times for bridge maintenance or as design criteria data for future

bridges.

The use of load cells for production lines is demonstrated in Figure 35 where load cells are used to monitor product bin loads. By monitoring the loads of each bin individually, the manufacturer can ensure that the proper amount of product is distributed into the packaging below. These are just a few more examples of how load cells are used in both industry and research today.
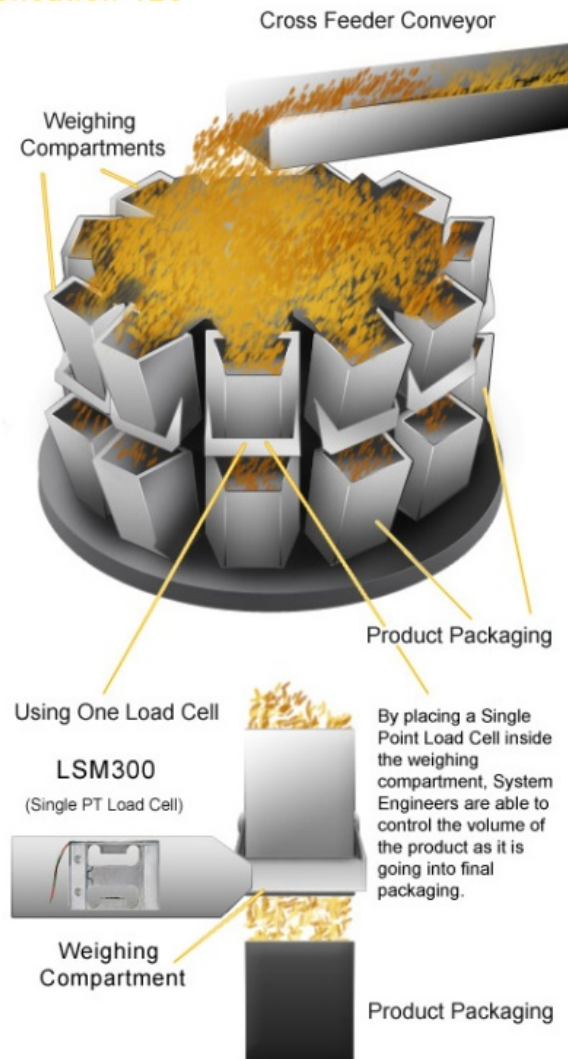
Figure 35: Load Cell App, Food Packaging [50]

Design and Construction

For this research project, a load cell was required to accurately measure the forces in a helical spring under multi-axial loading conditions a load cell. Most load cells only provide single mode measurements, such as axial (i.e. tension/compression) or torsional loads. A load cell that could collect load data from all six degrees of freedom or axes was needed in order to measure all loading modes for a compression spring under complex loading. Simultaneously measuring all six axes would allow a thorough evaluation of Wahl's helical spring stiffness equations and future development of a three dimensional model of the compression spring's force-displacement behavior. Budget limitations prohibited the purchase of a commercial six DOF load cell. Research into alternative solutions indicated that it was possible to build a custom load cell that could be tuned to meet specific requirements for a significantly lower cost.

Dr. Joseph Bracci, a professor of structural engineering at Texas A&M, had previously published a paper describing the design and construction of a multi-axis load cell for measuring forces in reinforced concrete frame structures [51]. Dr. Bracci's load cell was a strain gage based cell that could measure axial compression and tension, and both shear and moment forces in the x and y axes. In other words this particular load cell could measure a total of three loading modes, on its 5 axes. The fourth loading mode, torsion, was not included in the design. The design specifications of Dr. Bracci's load cell were ±40 kips, ±5 kips, and ±40 kip-in for the axial, shear, and bending moment load capacities, respectively [51]. These specifications greatly exceeded the load range needed for analyzing typical helical springs. From the basic design concepts in Dr.

Bracci's report a down-sized design was developed using SolidWorks (SolidWorks 2010 SP4.0, Dassault Systems SolidWorks Corporation, Delaware, MA). The Solid Works CAD model for the load cell's base structure and the actual load cell structure after fabrication are shown in Figure 36, and the specific dimensions of the load cell design are provided in Appendix K.
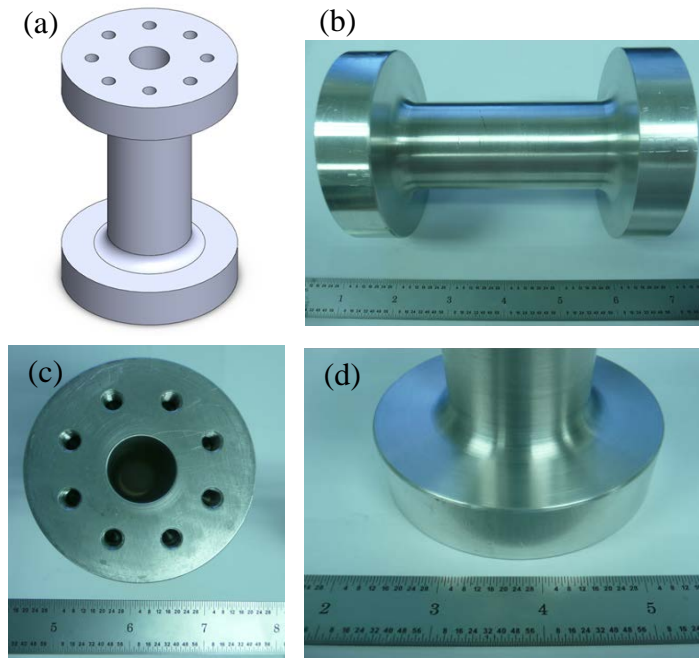

Figure 36: Load Cell Structure (a) CAD Model (b-d) Fabricated Load Cell (Detailed dimensions in Appendix K)

The material chosen for the load cell design was 6061 aluminum and was purchased from McMaster-Carr (Los Angeles, CA). Aluminum was chosen for its mechanical properties, machinability, and thermal properties. Aluminum has good thermal conductivity. This means that the load cell's aluminum structure provides both the substrate that transfers the strain to the strain gages and helps remove heat generated by the strain gages. Changes in temperature can affect the output of the gages and induce error into the measurements. The geometric dimensions of the load cell, such as the wall

thickness, tube radius, and height, were calculated specifically to provide safe strain limits in response to expected load ranges under which the load cell would be utilized. The specific dimensions of the load cell are provided in Appendix K. Yield strength of the aluminum is 10,000 ksi. The safe working axial, moment, shear, and torsion load capacity ratings for this load cell are 4 kips, 1 kip-in, 2 kips, and 2 kip-in, respectively.

The load cell structure was fabricated from 3.5 inch diameter rod stock of 6061 round stock aluminum. Two load cell structures were machined, but only one was instrumented. The second load cell structure was used as a dummy cell to pretest calibration tests and to be coupled with the actual load cell during shear and bending calibration. The dummy specimen needed to be identical to the actual load cell in order to assure that during calibration tests the stress would be uniform across both the dummy cell and the load cell.

The structure of the load cell and the dummy cell were turned on a lathe (See Figure 37 (a)). Once the aluminum was turned down to the proper dimensions, the load cell's mounting holes were drilled and tapped using a CNC mill (See Figure 37 (b)).

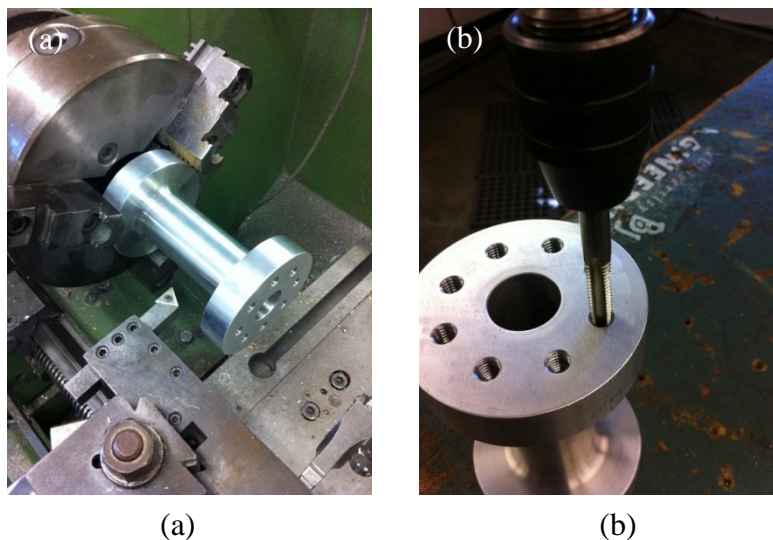(a)   (b)

Figure 37: (a) Load Cell in Lathe (b) Load cell being tapped for mounting to MTS system

These mounting holes allow the load cell and the dummy load cell to be mounted to custom mounting plates, shown in Figure 38. The mounting plates are used to mount the load cell and dummy cell securely to the MTS testing equipment. After all the mounting holes were tapped, the load cell was mounted in the lathe again, and the strain gage mounting surface was cleaned and lightly sanded with a fine grit sand paper to prepare the surface for installation of the strain gages.

Figure 38: Custom Mounting Plate

Once the load cell structure was completed and the surface was initially cleaned and prepared, additional surface preparation was performed to ensure removal of any oils or other contaminants. The surface was properly sanded to facilitate a strong interfacial bond between the load cell's surface and the backing of the strain gages. A detailed procedure for building the custom load cell is provided in Appendix A. Alignment marks were carefully scribed onto the load cell. Care was taken to ensure the alignment marks would not induce any stress concentrations that would affect the strain. These alignment markers were used to align the strain gages both vertically and horizontally on all four sides of the load cell. Placement of the alignment markers may be completed before or

after the final surface preparation; however, if this step is performed before the surface preparation, care must be taken that the marks are still visible after the surface is cleaned. If the alignment marks are scribed after surface preparation, extreme care should be taken to prevent any oil or contaminants from getting on the surface. Oils and contaminants on the gage mounting surface weaken the bond interface and prevent the proper transfer of strain from the bulk material to the strain gages.

The strain gages used for this load cell design were general purpose linear gages (CEA-06-125UW-350, Vishay Micro-Measurements Precision Group, Inc, Malvern, PA) and rosette gages (CEA-06-125UR-350, Vishay Micro-Measurements Precision Group, Inc, Malvern, PA). The gage length of these gages was 0.125 inches with a strain range of ±5% for a range of ±0.00625 inches. This distance is beyond the elastic range of the load cell material. The complete specifications of these strain gages are provided in Appendix C.

The instructions provided in Appendix E explain in detail the process of preparing and installing the strain gages. Each strain gage was positioned carefully onto the load cell's surface so the strain gage alignment marks are aligned with the appropriate scribe marks on the cell. The back of each gage was then coated with M-Bond 600 adhesive (Visay Micro-Measurements Group, Inc, Malvern, PA). The gages were installed in sets of two, with one gage on the opposing surface of the load cell. This allowed the two gages to be properly clamped into position. The adhesive was cured for one hour at 350 °F in a furnace. The furnace was cold when the load cell and strain gages being installed were placed inside as specified in the M-Bond 600 instructions (See Appendix E). The load cell was placed in a cold furnace and brought up to temperature to prevent bubble formation. If bubbles form beneath the gage they cause measurement errors and weaken

the bond interface. A rectangular rosette gage that was properly mounted to the load cell surface is shown in Figure 39. The adhesive that was squeezed out from underneath the gage during the clamping process can be seen clearly. Care was taken to that ensure any surface area where additional gages were to be mounted later was masked off with tape to prevent contamination. A strain gage will not properly bond to the substrate if the surface is contaminated with previously cured adhesive.
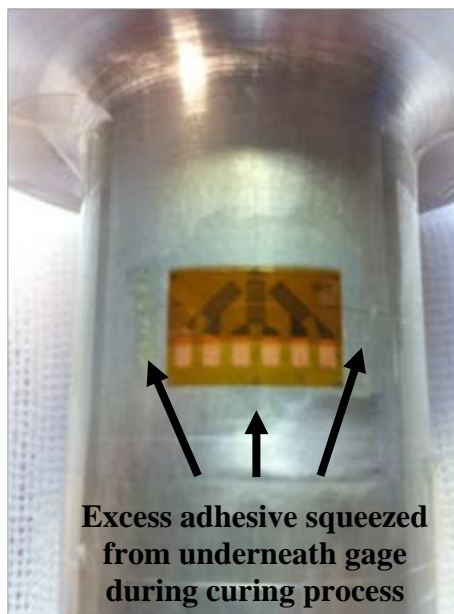

Figure 39: Rectangular rosette gage properly mounted to surface.

The installation steps outlined in Appendix A were repeated until all twenty gages were mounted onto the load cell (five gages per side). The total number of gages per side of the load cell is nine. There are two rosette gages that contain three strain gages each and three linear gages per side. There are a total thirty-six of strain gages mounted to the load cell. Figure 40 shows the arrangement of the strain gages on the load cell after installation. Figure 41 shows how the strain gages are identified and labeled in the Wheatstone bridge circuit diagrams (See Appendix J).

T: Outer rosette gages used in torsion bridge

X: Outer rosette gages used for shear bridge; Inner gage is part of axial bridge

V: Linear gage used in axial bridge

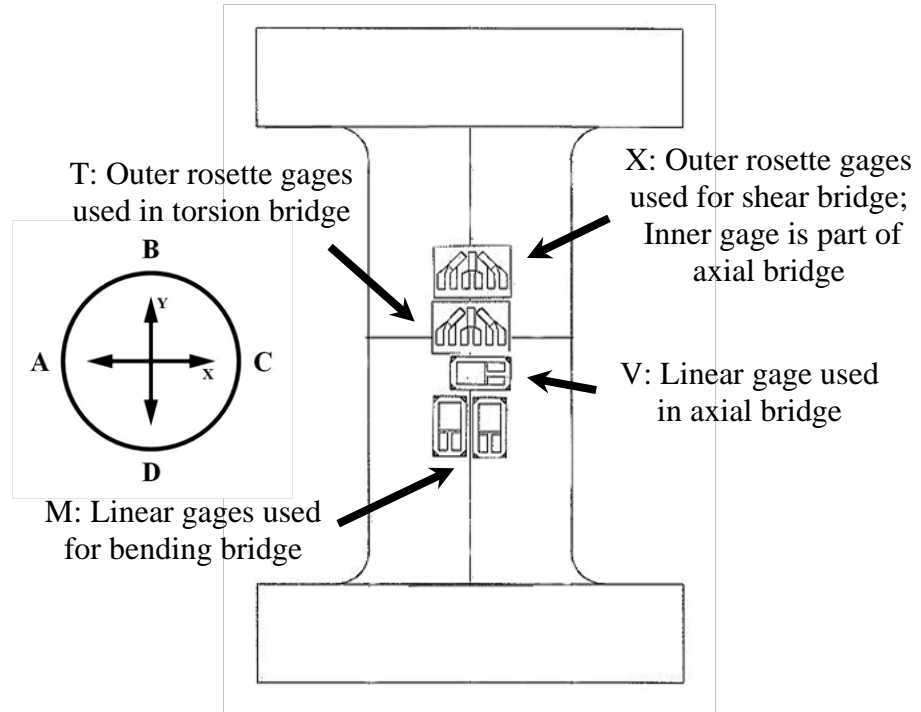M: Linear gages used for bending bridge

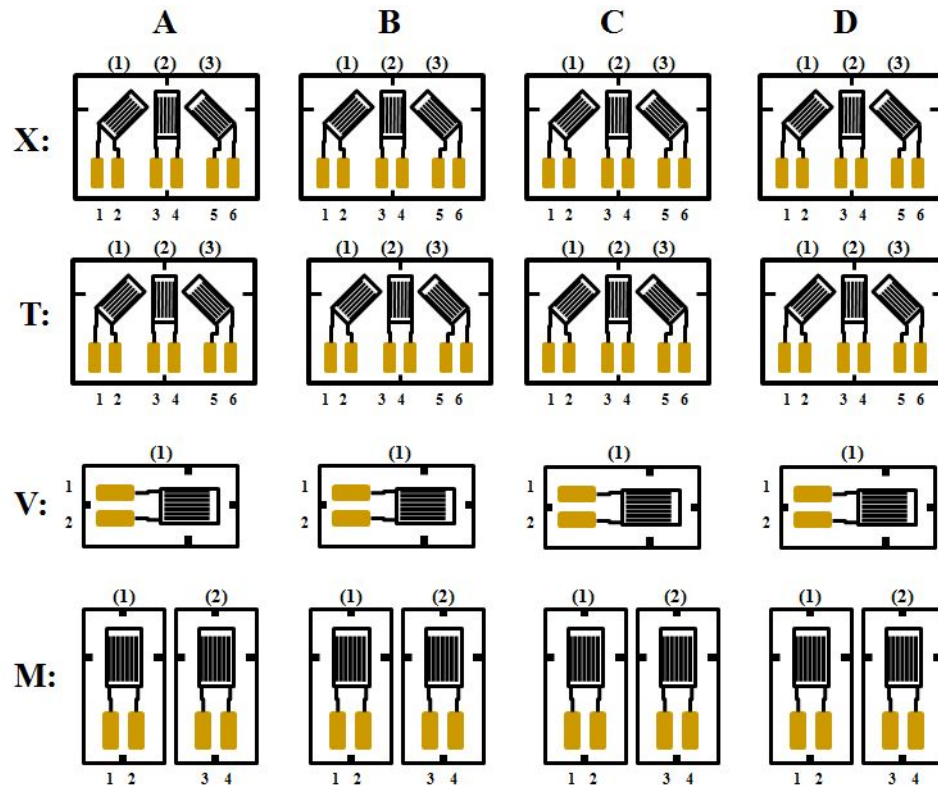Figure 40: Load Cell Axis Arrangement and Strain Gage Position Layout

Figure 41: Strain Gage Installation Layout and Wheatstone bridge Label Identifiers

Next the strain gages were wired into a Wheatstone bridge setup. The wire used was standard 26 gauge solid tinned copper wire with PVC coating (Fry's Electronics, Memphis, TN). The solder used was Vishay 361A-20R solder, purchased from Vishay Micro-Measurements Inc. (Malvern, PA). The wires were carefully labeled and color coded according to detailed, color-coded wiring diagrams. The X-axis shear Wheatstone bridge circuit diagram is shown in Figure 42 as an example of these wiring diagrams. The full set is provided in Appendix J. The excitation wires, signal wires, and both lead wires from each strain gage in the bridge are labeled and color coded. The wire labels for the strain gages correspond to the row, column, and appropriate numerical identifier are shown in Figure 41.
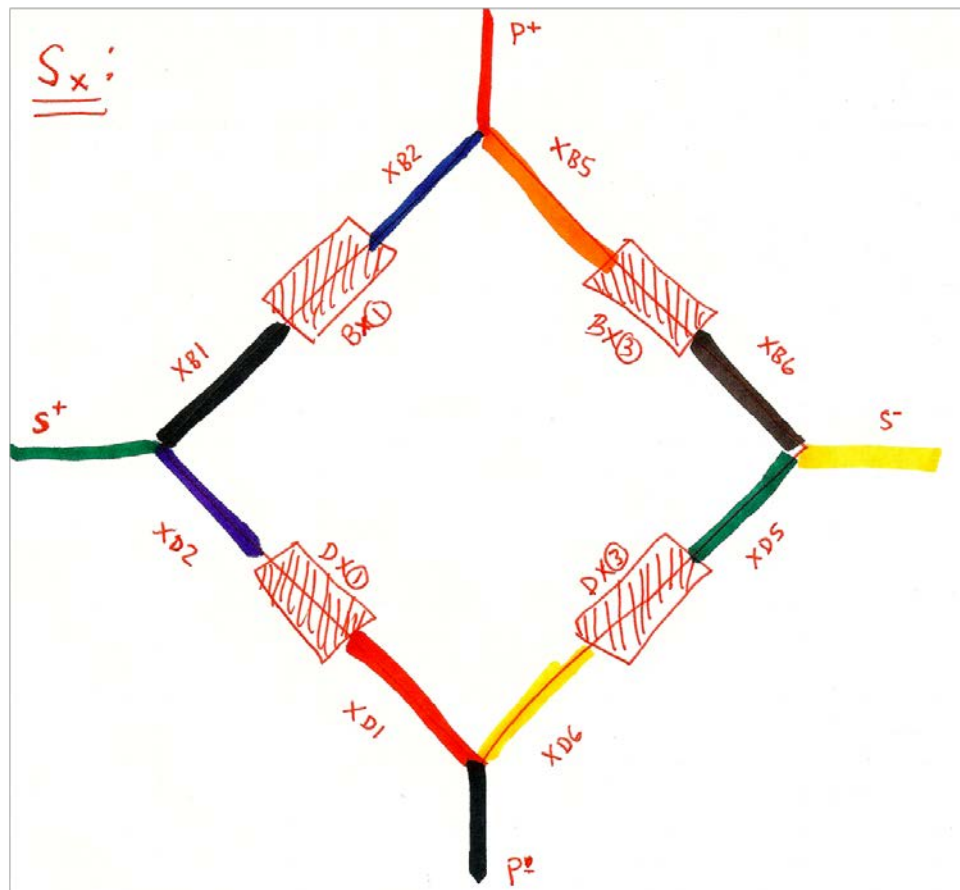

Figure 42: X-axis Shear Wheatstone bridge circuit diagram, color coded and labeled

The result of the initial soldering of the wires directly to the strain gages on the load cell is shown in Figure 43 (a). The wiring process is only half completed at this point. To keep the wires in order, wire management was necessary. Once all of the wires were successfully soldered to the strain gages, they were bundled to one side of the load cell as shown in Figure 43 (b) and (c). The wires were all cut and maintained at the same length to minimize any changes in resistance across the length of the wire. Figure 43 (b) shows the wires color coded, labeled, and positioned together on one side of the load cell. The arrows in Figure 43 (c) show the zip-ties used to manage the wires by bundling them together. The zip-ties also provide mechanical stability of the solder connections by preventing the wires from moving at the soldered ends.
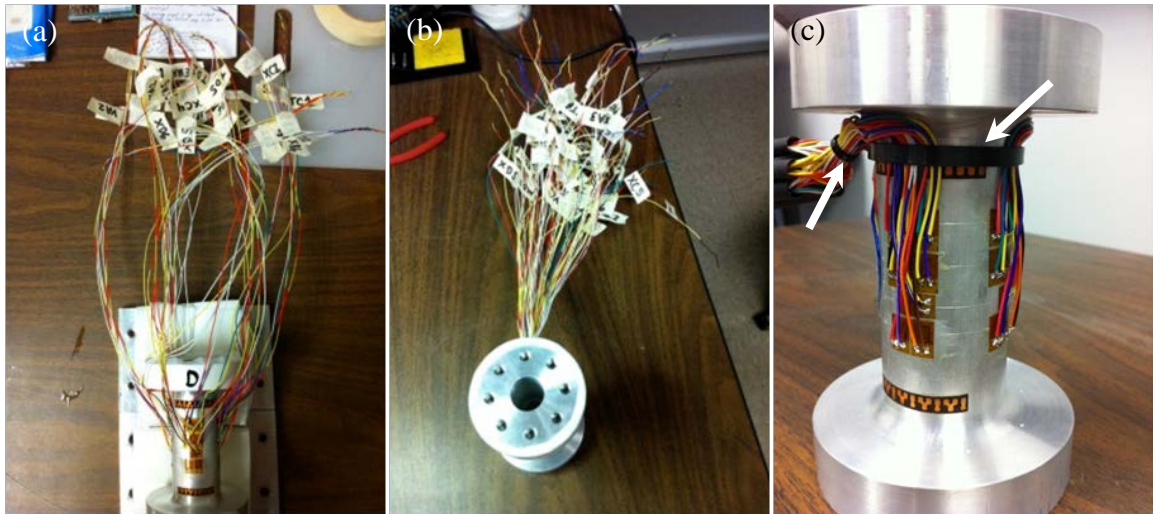

Figure 43: (a) Wires being soldered and labeled (b) Wires bundled (c) Wires bundled, close-up

The wires were organized into separate bundles according to which Wheatstone bridge group they belonged (i.e. grouped by loading mode and axis). The wires were placed into double-walled heat shrink tubing to provide a stiff, protective, mechanically

sound housing for the wires as shown in Figure 44. The heat shrink also provided wire management. At this point there were only six wire bundles to keep track of.

Figure 44: Wired Bundled and Protected by Double-Walled Heat Shrink

For the shear and moment load channels, there were eight wires. For the axial and torsion channels, there were sixteen wires each because of how the Wheatstone bridges for these two load channel were configured (See Appendix J). There were eight wires for the shear and moment load channels because there were two wires soldered to each strain gage (4 in all). Once these eight wires are connected properly, there are only four wires left. These four wires were the two excitation leads and the two signal output leads seen in a standard Wheatstone bridge configuration.

To help keep the wires organized and to ease the process of connecting all eight to sixteen wires for each load channel, a custom circuit board, shown in Figure 45 (a), was designed. The custom circuit board was constructed using a standard circuit board milling system (ProtoMat S62, LPKF Laser & Electronics, Wilsonville, OR). The wires

coming from the load cell were then soldered to the custom connecting circuit board

andgrouped by load channel (See Figure 45 (b)). A detailed and color coded circuit

diagram that maps the wires for each load channel on the connecting board is provided in

Appendix J. The final four wires (two excitation wires and two signal wires) for each

load channel were then soldered to the other side of the connecting board (See Figure 45

(c)). At this point there were only twenty-four wires to manage. The excitation and

signal wires for each load channel (4 per channel) were then placed into single-walled

heat shrink tubing to provide a flexible, protective, mechanically sound housing for the
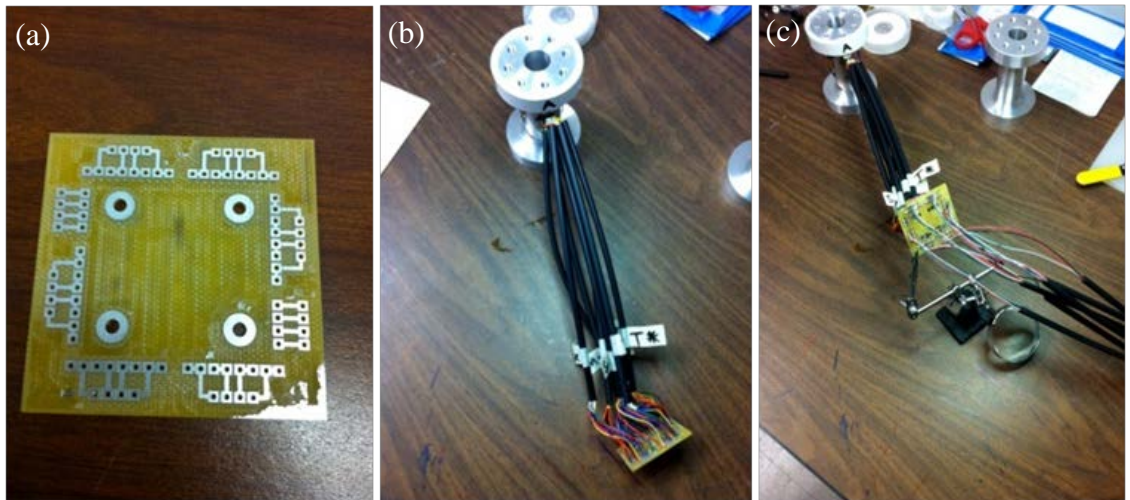
wires as shown in Figure 45 (c).

Figure 45: (a) Custom Wheatstone Circuit Connector Board (b) Wires Connected to
Wheatstone Circuit Board (c) Excitation and Signal Wires wired to Wheatstone Circuit
Board

Once the wiring was completed, the two input and two output wires for each

Wheatstone bridge were soldered and enclosed into a standard 9-pin D-sub connector

(L&M Electronics, Waco, TX). The 9-pin D-sub connectors were wired to be compatible

with the Vishay Model 5100B Scanner's strain gages cards. The D-sub pin configuration

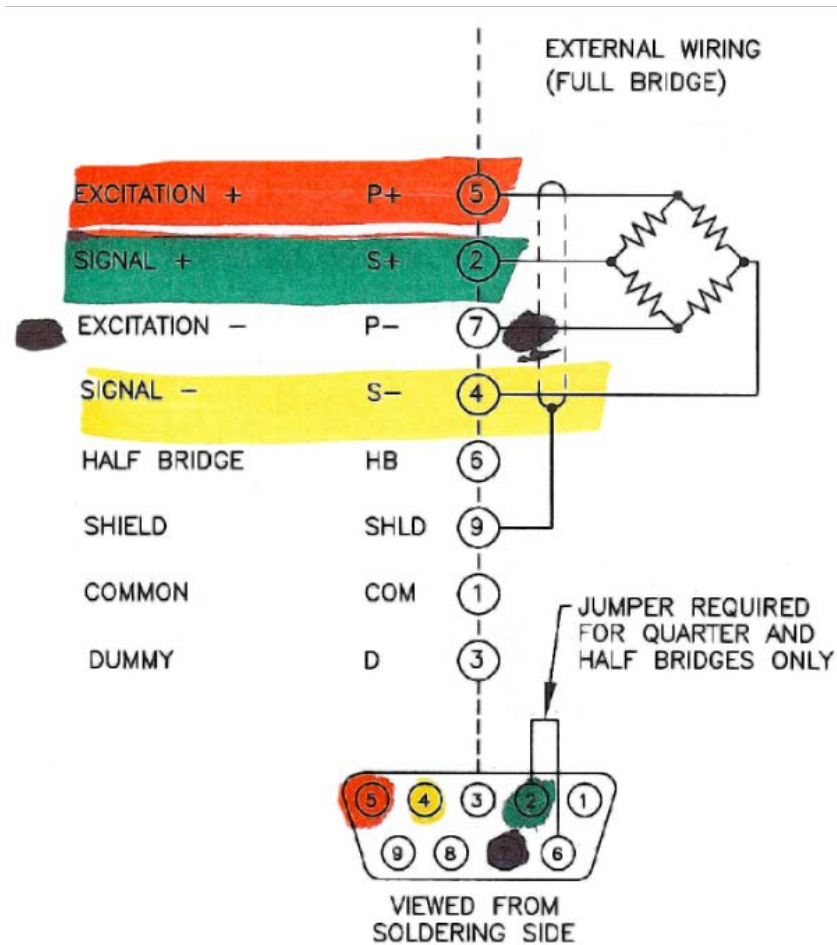for the Vishay 5100B Scanner is shown in Figure 46.

Figure 46: Vishay 5100B Scanner D-Sub Pin Configuration [52]

The internal wiring of the D-sub housing is shown in Figure 47 (a), and the final

result of the wiring, heat shrink tubing, and D-sub connections is shown in Figure 47 (b).

Since all six Wheatstone bridges were full bridges, there was no need to use the dummy

resistors supplied internally by the 5100B Scanner. Therefore, the four connecting wires

per load channel were wired directly into the D-sub connectors that provide quick and

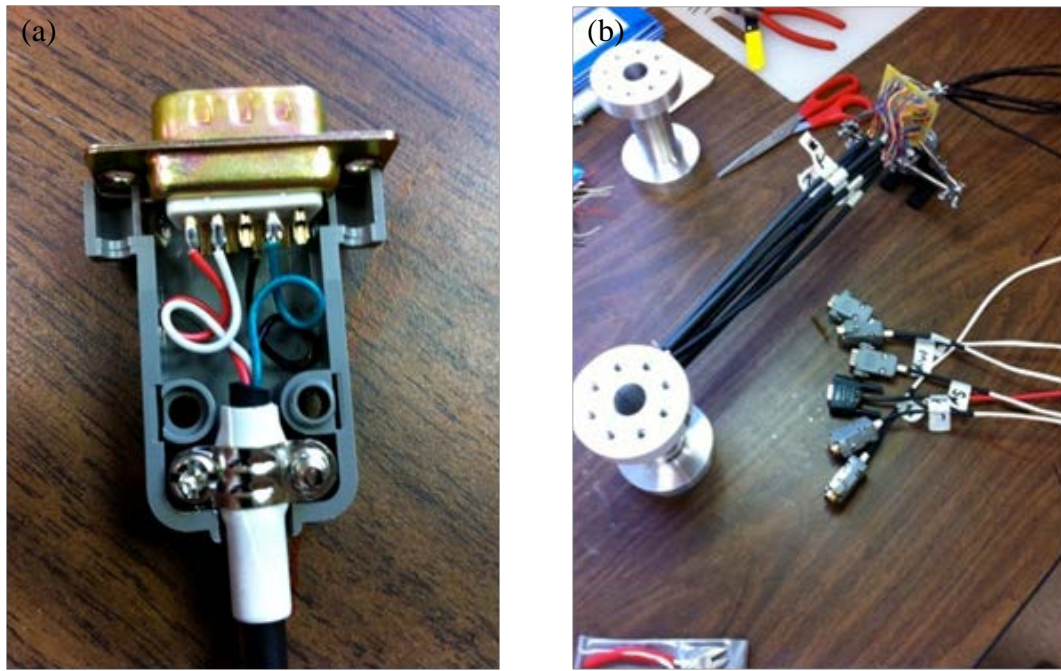secure connections to the scanner's strain gage cards.

Figure 47: (a) D-Sub Connection Casing with Wiring Shown (b) Load Cell Completely Wired with D-sub connectors

Before testing the load cell, a voltmeter was used to confirm that the wires were correctly connected. The 9-pin D-sub connectors were connected to the Vishay Model 5100B Scanner (Vishay Micro-Measurements Precision Group, Inc., Malvern, PA). that is controlled with Vishay's Strain Smart software (StrainSmart ver. 4.20, Vishay Micro-Measurements, Malvern, PA). At this point the load cell construction was completed. The process of calibrating the 6 Cell (the custom load cell) is explained in the following section.

Load Cell Calibration

The load cell was calibrated for each loading mode (i.e. axial, torsion, shear in the x-axis, shear in the y-axis, bending moment about x-axis, bending moment about y-axis) The setup of for each calibration is provided in Figure 48.
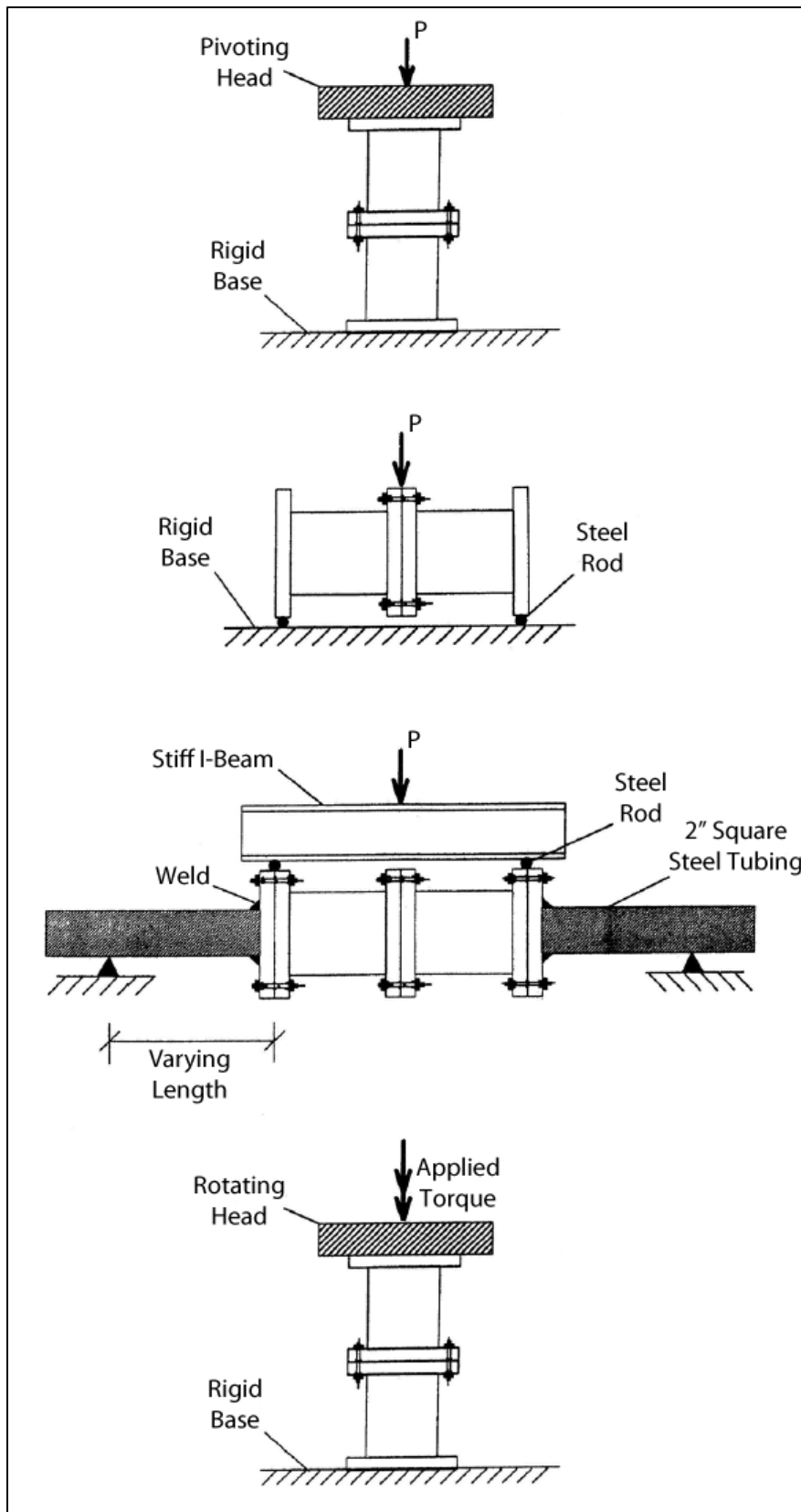
Figure 48: Load Cell Calibration Setup [51]

The axial setup with the compression platen head ensured that the load was distributed evenly over the load cell. The setup for the shear calibration was a simple three point bending test. This calibration setup required the load cell to be bolted to the dummy cell and, when loaded correctly, results in a constant shear force across the load cell. During the shear calibrations, a moment was also induced that varied linearly along the length of the load cell. The bending calibration utilized a four point bending test that ensured a constant bending moment without shear. The final calibration was torsion. The load cell was mounted securely and a torque was applied about the central vertical axis. For the axial and torsion calibrations, the strain gage load cell was not bolted in line with the dummy cell because it was not necessary to ensure even loading across the cell or to create the proper test load scenario. The base fixtures for the shear and bending tests are shown in Figure 49. These fixtures were bolted rigidly and centered with respect to the MTS crosshead to the base of the MTS machine used for the shear and bending calibrations. The complete setup for the shear and bending calibrations can be seen in Figure 50 (a) and (b) respectively.

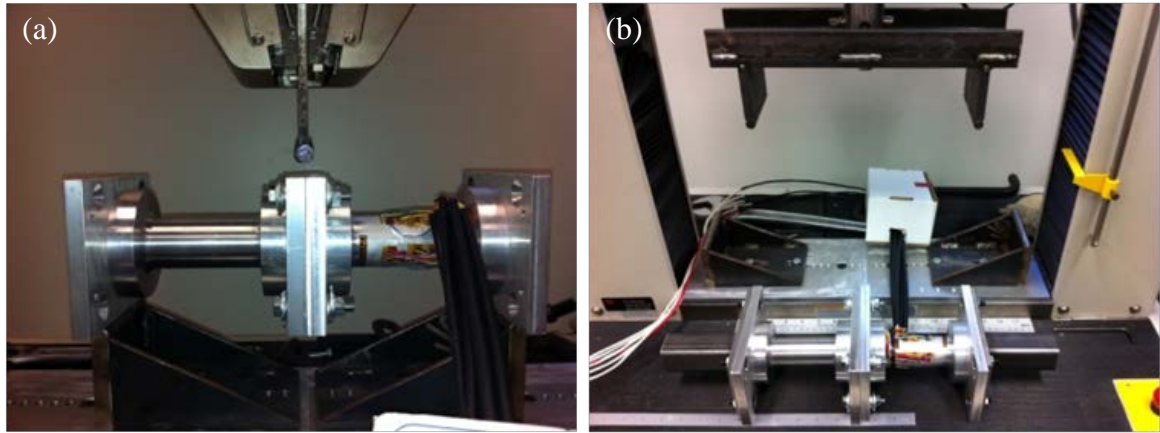Figure 49: Shear and Bending Calibration Test Base Fixtures

Figure 50: (a) Shear Calibration Setup (b) Bending Calibration Setup

Before each calibration trial, the base fixtures and the load cells were checked to ensure they were in the proper positions and level so that the load would be applied evenly during each test. This was particularly important during the four-point bending test used to calibrate for bending. If one side of the load cell-dummy cell setup was loaded before the other, a shear force would develop and cause increased error in the calibration results.

During each calibration the load cell was connected to the Strain Smart strain gage cards and the millivolts to volts (mV/V) reading for each Wheatstone bridge (load channel) was aquired. The load cell was then calibrated to the chosen maximum load using the appropriate test setup on a MTS machine that had a calibrated load cell. The shear and bending calibration tests were performed on the MTS QTest/100 (MTS Systems Corporation, Eden Prairie, MN). The shear and bending calibration tests required the MTS load cell to be positioned above the 6 Cell, and enough workspace to setup both the three-point and four-point bending tests. The MTS QTest/100 workspace was large enough to accommodate both the three-point and four-point bending tests, and the load cell was positioned above the 6 Cell. The torsion calibration test was performed

on the MTS 858 Mini Bionix II (MTS Systems Corporation, Eden Prairie, MN) because it was capable of applying torsional displacements. The axial calibration was completed with the MTS 858 Mini Bionix II also because it had the compression platen attachment.

The mV/V readings collected from each load channel were then plotted against the calibrated load from the MTS machine. Each calibration curve was collected multiple times. This provided enough calibration data for statistical analysis. Linear regression analysis was performed using SAS (ver 9.2, SAS Institute, Inc., Cary, NC). The formula for the linear curve, correlation coefficient, and 95% confidence intervals were calculated and plotted. The correlation curve was used to calibrate each load channel in the Strain Smart software. Each load channel was programmed as an individual force transducer in Strain Smart. The calibration curve for each load channel was entered into the load calibration section of the force transducer setup file. The 95% confidence interval provides the error of the load cell for each axis. Using the calibrated curve data ensured repeatability in load measurements when the 6 Cell (custom load cell) was used. The calibrated correlation curves for each load channel and samples of the calibration data are provided in Appendix L. After the load cell was calibrated in Strain Smart, all tests performed using the transducer setup file provided direct force measurements instead of Wheatstone mV/V raw data.

CHAPTER FIVE

Materials and Methods

Testing Apparatus

To test helical compression springs under multiple loading conditions, a custom testing apparatus needed to be developed. Ideally, by using the custom load cell (6 Cell) that can measure loads for all 6 DOF and a custom apparatus, the springs could be placed under complex loads. Complex loads are a combination of axial compression, transverse shear, axial torsion, and one or both axial moments. Such a complex level of loading makes it difficult to design a proper testing apparatus or testing procedure. For the purposes of evaluating Wahl's equations as thoroughly as possible, a custom testing apparatus was designed and built. The custom testing apparatus was intended to allow variable amounts of axial compression, transverse shear, and axial torsion to be applied to the compression springs either singularly or in combination. A Solid Works CAD model of the testing apparatus design is shown in Figure 51.
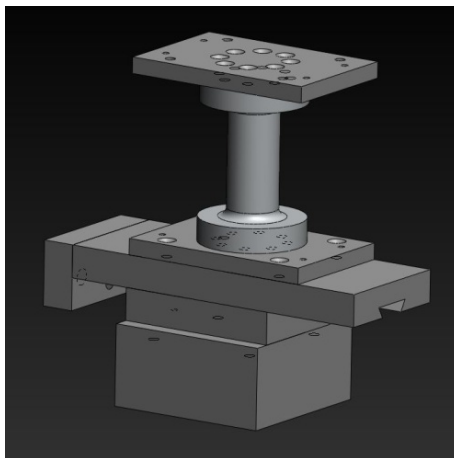

Figure 51: CAD Model of Custom Testing Assembly

A custom dovetail slide base, seen in Figure 52 (a) , and a dovetail slide, seen in Figure 52 (b), were designed to allow the helical spring to be displaced laterally to generate a transverse shear load. Detailed drawings for the dovetail slide and base are available in Appendix K.

The shear displacement is longitudinal (i.e. perpendicular to the spring's coil axis) and is applied manually. A threaded rod was mounted parallel with the dovetail slide as shown in Figure 52 (a). When the threaded rod is rotated, the dovetail slide is actuated linearly and applies a shear displacement. A precision ruler mounted to the side of the dovetail base allows the shear displacement to be measured.
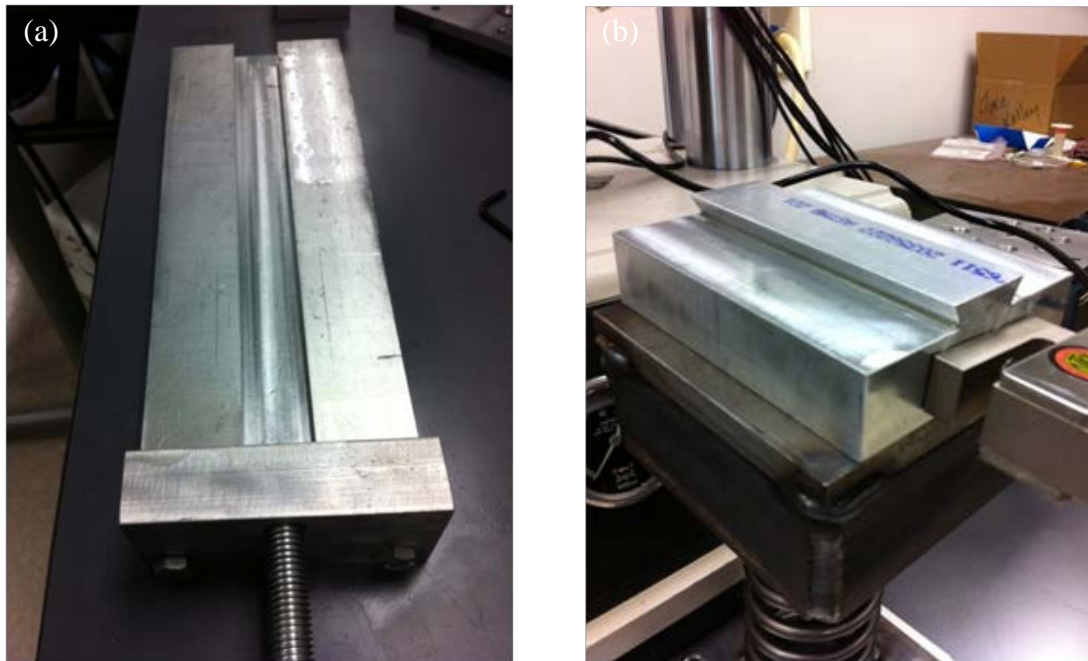

Figure 52: (a) Dovetail Base (b) Dovetail Slide mounted to spring (Dimensioned drawings in Appendix K)

The dovetail slide and base were designed to allow a load cell (S–Cell) to be mounted in-line, between the dovetail slide and threaded rod (See Figure 53 (a). The S–Cell (See Figure 53 (b)) was used to measure the pure transverse shear. A compressive

force was generated when a shear displacement was applied. The S–Cell measured the compressive load (i.e. the pure shear load). The S–Cell was a BSA-500lb S-type load cell (Transcell Technology Inc., Buffalo Grove, IL). The manufacturer's specifications for the S–Cell are provided in Appendix D.
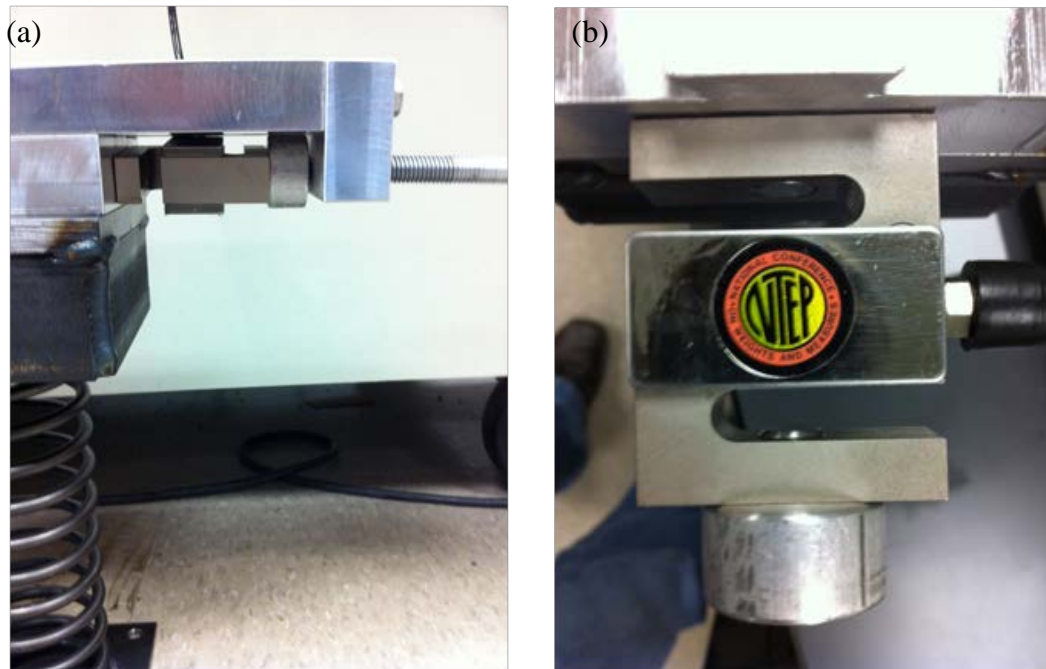
Figure 53: (a) Mounted view of S-Load Cell being used in-line with dovetail slide (b) Close-up view of S Cell

Once the spring is loaded in shear, an axial compression can be applied directly to the helical spring by the MTS 858 Mini Bionix II mechanical testing machine. A torsion load could also be applied, either separately or in combination with the compression load. Once the load or displacement was applied, the reaction forces from the spring were measured by the 6 Cell. The compressive and torsional loads were also measured by the MTS load cell. The testing apparatus included two custom fixture plates that allowed the 6 Cell to be mounted firmly to the MTS actuator at the top and the dovetail base at the bottom. The fixture plates (shown in Figure 38 in Chapter 4) and the design

specifications are provided in Appendix K. The testing apparatus during testing is shown

in Figure 54. In particular, Figure 54 (a) shows a close-up side view of the testing

apparatus with a spring laterally displaced 1.5 inches perpendicular to its coil axis

combined with axial compression. Figure 54 (b) shows the overall test setup and Figure

54 (c) shows a close-up of the 6 Cell mounted to the dovetail base. Each segment of the

testing apparatus was connected to the next rigidly using 5/16"-18 flat head socket

machine screws (Fastenal, Winona, MN). The only location where movement was

allowed during testing was along the length of the dovetail slide. Once shear

displacement was applied, the dovetail slide could still move. It was not rigid. The MTS

axial and rotational displacements are rigid once placed. This meant that once the

displacement is applied, the crosshead would not allow free movement. Two test

specimen jigs (the black steel boxes in Figure 54) were designed to mount the

compression springs in the correct position in the MTS machine. Design drawings for

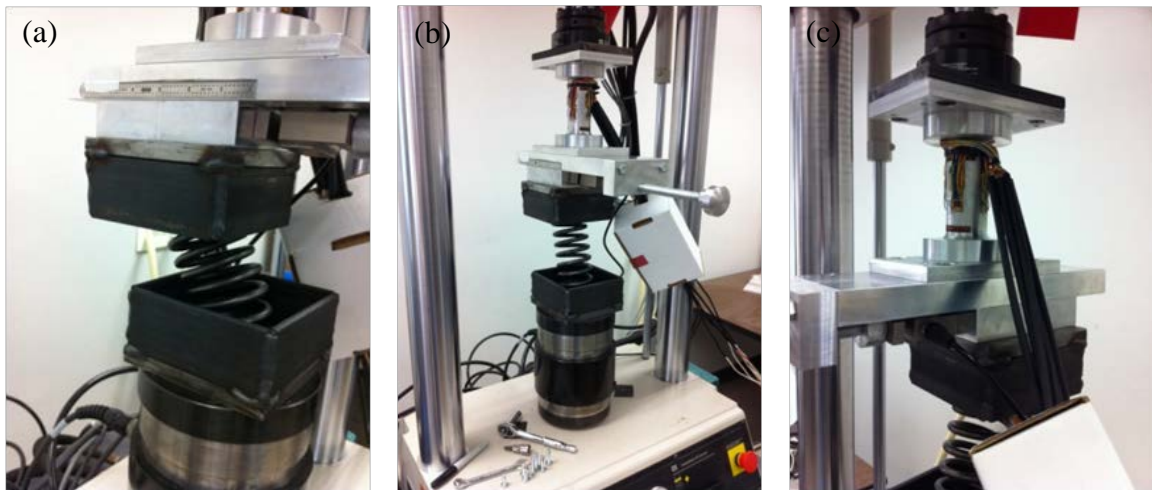the entire testing apparatus are provided in Appendix K.

Figure 54: (a) Testing Apparatus Side View with 1.5 in shear displacement during
compression testing (b) Full view of test setup mounted on MTS (c) Close up view of the
6 Cell – dovetail interface

For this project the compression springs were to be tested without any end coil turning effects being induced. To accomplish this, the springs were carefully welded onto steel plates that were rigidly mounted to the MTS test setup with machine screws. A compression spring welded to a mounting plate is shown in Figure 55 (a). The compression springs were welded so that one of the ground end coils (Indicated by the arrow in Figure 55 (b)) was centered on the mounting plate. This allowed consistent positioning of each spring during testing. The springs were then mounted for each test so that a positive torsion resulted in unwinding and negative torsion resulted in winding of the spring's coil. A spring with a rate of 104.3 lbs/inch was purchased from McMaster-Carr (Santa Fe Springs, CA). This spring was referenced as spring K104.
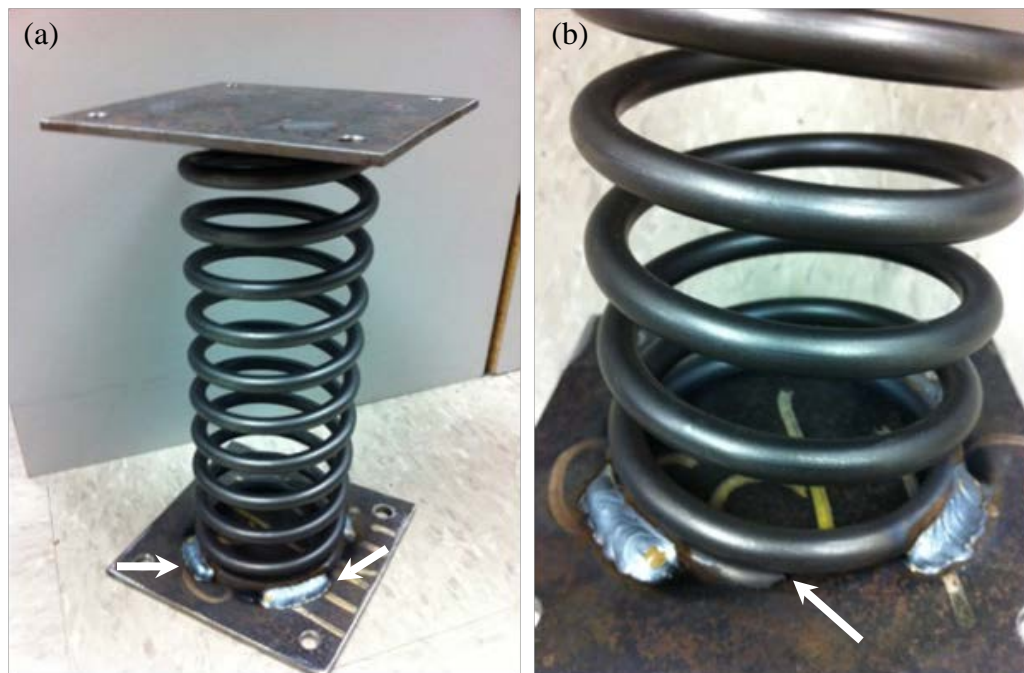

Figure 55: (a) Spring welded (welds indicated by arrows) to mounting plates (b) Close-up view of spring mounted showing ground spring end centered on the plate

Testing Procedure

Stage I and Stage II

The testing procedure was programmed using the MTS TestStar Station

Manager's (Ver. 3.3B 1205, MTS Systems Corporation, Eden Prairie, MN) multipurpose

testware application. The testing procedure consisted of two stages, each with two parts:

one that applied a torsional displacement in the unwinding direction and one with a

torsional displacement in the winding direction. Stage I was completely autonomous

once started, but Stage II had to be paused for changes in shear displacement to be

manually applied.

Levels of Displacement

For compression, the full displacement went from 0.0 to -3.6 inches. The full

torsional displacement used was 20 degrees in the unwinding direction and -20 degrees in

the winding direction. Both the axial and torsional displacements were fully automated.

Application of axial or torsional displacement occurred over 30 seconds at a constant

rate. The preloading and unloading phases were all completed over 10 seconds. The

shear displacement was manually applied from 0 to 1.5 inches. Since the shear

displacement was applied manually, the time to apply the shear displacement varied.

There were multiple levels of displacement applied for each loading mode too. Axial

compression was performed in increments of 0.9 inches, the torsional rotation was

applied in increments of 5 degrees, and shear displacement was applied in increments

0.375 inches. The protocol for part 1 of the Stage I testing is provided in Table 1. The

angular displacement applied in part 1 was positive direction and in part 2 the negative

direction.

Table 5: Stage I Test Protocol for Unwinding Torque (i.e. Part 1, Unwinding torque)

Stage I Test Protocol

- Pure Compression
    - Apply 3.6 in. compressive displacement at constant rate over 30 sec.
- Return to zero displacement
    - Constant rate over 10 sec (rate applies to all "return to zero displacement" segments).
- Pure Torsion
    - Apply 20° angular displacement at constant rate over 30 sec.
- Return to zero displacement
- Combined Mode Displacement
    - Apply 3.6 in compressive displacement at constant rate over 30 sec.
    - Simultaneously apply 20° angular displacement at constant rate over 30 sec.
- Return to zero displacement
- C1 - Combined Mode Displacement
    - Apply 0.9 in compressive displacement at constant rate over 10 sec, and Hold.
    - Then apply 20° angular displacement at constant rate over 30 sec.
- Return to zero displacement
- C2 - Combined Mode Displacement
    - Apply 1.8 in compressive displacement at constant rate over 10 sec, and Hold.
    - Then apply 20° angular displacement at constant rate over 30 sec.
- Return to zero displacement
- C3 - Combined Mode Displacement
    - Apply 2.7 in compressive displacement at constant rate over 10 sec, and Hold.
    - Then apply 20° angular displacement at constant rate over 30 sec.
- Return to zero displacement
- C4 - Combined Mode Displacement
    - Apply 3.6 in compressive displacement at constant rate over 10 sec, and Hold.
    - Then apply 20° angular displacement at constant rate over 30 sec.
- Return to zero displacement
- T1 - Combined Mode Displacement
    - Apply 5° angular displacement at constant rate over 10 sec, and Hold.
    - Then apply 3.6 in compressive displacement at a constant rate over 30 sec.
- Return to zero displacement
- T2 - Combined Mode Displacement
    - Apply 10° angular displacement at constant rate over 10 sec, and Hold.
    - Then apply 3.6 in compressive displacement at a constant rate over 30 sec.
- Return to zero displacement
- T3 - Combined Mode Displacement
    - Apply 15° angular displacement at constant rate over 10 sec, and Hold.
    - Then apply 3.6 in compressive displacement at a constant rate over 30 sec.
- Return to zero displacement
- T4 - Combined Mode Displacement
    - Apply 20° angular displacement at constant rate over 10 sec, and Hold.
    - Then apply 3.6 in compressive displacement at a constant rate over 30 sec.
- Return to zero displacement

Table 6: Stage II Test Protocol for Unwinding Torque (i.e. Part 1, Unwinding torque)

Stage II Test Protocol

Shear Level 1 (0.375 inches of shear displacement applied)

- Pure Compression
  - Apply 3.6 in. compressive displacement at constant rate over 30 sec.
- Return to zero displacement
  - Constant rate over 10 sec (rate applies to all "return to zero displacement" segments).
- Pure Torsion
  - Apply 20° angular displacement at constant rate over 30 sec.
- Return to zero displacement
- Combined Mode Displacement
  - Apply 3.6 in compressive displacement at constant rate over 30 sec.
  - Simultaneously apply 20° angular displacement at constant rate over 30 sec.
- Return to zero displacement

Shear Level 2 (0.750 inches of shear displacement applied)

- Pure Compression
  - Apply 3.6 in. compressive displacement at constant rate over 30 sec.
- Return to zero displacement
  - Constant rate over 10 sec (rate applies to all "return to zero displacement" segments).
- Pure Torsion
  - Apply 20° angular displacement at constant rate over 30 sec.
- Return to zero displacement
- Combined Mode Displacement
  - Apply 3.6 in compressive displacement at constant rate over 30 sec.
  - Simultaneously apply 20° angular displacement at constant rate over 30 sec.
- Return to zero displacement

Shear Level 3 (1.125 inches of shear displacement applied)

- Pure Compression
  - Apply 3.6 in. compressive displacement at constant rate over 30 sec.
- Return to zero displacement
  - Constant rate over 10 sec (rate applies to all "return to zero displacement" segments).
- Pure Torsion
  - Apply 20° angular displacement at constant rate over 30 sec.
- Return to zero displacement
- Combined Mode Displacement
  - Apply 3.6 in compressive displacement at constant rate over 30 sec.
  - Simultaneously apply 20° angular displacement at constant rate over 30 sec.
- Return to zero displacement

Shear Level 4 (1.50 inches of shear displacement applied)

- Pure Compression
  - Apply 3.6 in. compressive displacement at constant rate over 30 sec.
- Return to zero displacement
  - Constant rate over 10 sec (rate applies to all "return to zero displacement" segments).
- Pure Torsion
  - Apply 20° angular displacement at constant rate over 30 sec.
- Return to zero displacement
- Combined Mode Displacement
  - Apply 3.6 in compressive displacement at constant rate over 30 sec.

Test Protocol Outline and Load Axes

The test protocols are summarized schematically for Stage I in Figure 57 and for Stage II in Figure 58. The protocol schematics for Stage I and Stage II all color coded. Test initialization and data collection is shown in brown. Loading phases are shown in green, unloading in dark blue, and preloading in light blue. Each test segment of Stage I and Stage II are outlined with unique colors and are referenced to in order from left to right numerically. There were a total 30 test phases in Stage I and 24 phases in Stage II. A detailed overview of the test procedure used when testing the compression springs is provided in Appendix I. The axes of the load cell and the testing apparatus are shown in Figure 56.

Figure 56: Axes of Custom Load Cell and Testing Apparatus

Figure 57: Stage I Protocol Flow Chart

Program Start

Live Graphs Displayed

User Actived Sync Signal

Data Collection Starts on Sync

User Shear Curve (? sec)

Activate S Curve Complete GUI

Program Paused

UnTorque (10 sec)

Torque at S1 (30 sec)

UnCompress (10 secs)

Compression at S1 (30 secs)

Program Resume

Second User Sync Signal

Move to Shear 1 Position

Compress & Torque at S1 (30 sec)

UnCompress & UnTorque (10 sec)

Program Pause

Move to Shear 2 Position

Third User Sync Signal

Program Resume

Compression at S2 (30 secs)

Move to Shear 3 Position

Program Pause

UnCompress & UnTorque (10 sec)

Compress & Torque at S2 (30 sec)

UnTorque (10 sec)

Torque at S2 (30 sec)

UnCompress (10 secs)

Fourth User Sync Signal

Program Resume

Compression at S3 (30 secs)

UnCompress (10 secs)

Torque at S3 (30 sec)

UnTorque (10 sec)

Compress & Torque at S3 (30 sec)

UnCompress (10 secs)

Compression at S4 (30 secs)

Program Resume

Fifth User Sync Signal

Move to Shear 4 Position

Program Pause

UnCompress & UnTorque (10 sec)

Torque at S4 (30 sec)

UnTorque (10 sec)

Compress & Torque at S4 (30 sec)

UnCompress & UnTorque (10 sec)

Program END

Collect Data for Analysis

Figure 58: Stage II Protocol Flow Chart

CHAPTER SIX

Results

Data Collection and Data Reduction

The following sections discuss the data reduction process used to get the final

results that will be presented in this chapter and discussed in Chapter 7. There were two

data acquisition (DAQ) systems: the Strain Smart and the MTS. The data acquisition for

the 6 Cell and the S-cell on the shear jig was performed using the Strain Smart system.

Data was collected on both DAQ systems on every channel every one-tenth second.

A total of eight channels were collected by the Strain Smart DAQ system: the 6

Cell (six channels), the S-cell, and the synchronization signal. Multiple measurements

were collected per channel: the calibrated load values, the A/D counts, the A/D counts

un-zeroed, and the milli-volts per volt measurements from the Wheatstone bridge. The

sync signal was programmed differently from the load cell transducer channels. Because

the sync signal was not a load cell or a strain gage, the measured values are only nominal

readings. The value of the sync signal is only important when the measured value goes

off-scale (-9999999) in the StrainSmart program indicating that the sync signal was

activated (See Table 7, IDs 48-50). The synchronization signal was sent to both data

acquisition systems simultaneously at the beginning of each test procedure. This signal

was used to define the start of the procedure and for the purpose of merging the two raw

data files during data reduction. An example of 19 records of the raw data output from

Strain Smart is presented in Table 7 for the sync signal data and the calibrated data from

the S-Cell.

A total of 14 channels were collected by the MTS DAQ system: axial displacement, axial load, time, axial displacement absolute error, axial force absolute error, aux input 1, running time, axial output, axial segment count, torsional torque, torsional angle, torsional segment count, torsional torque absolute error, and torsional angle absolute error. An example of the raw data output from the MTS data acquisition system is presented in Table 8. The aux input 1 channel was the synchronization input channel for the MTS system. The MTS DAQ system measured the sync signal at 1.611 volts when activated (See Table 8).

Within the MTS data are segment counters for the axial and torsional controls. The segment counters change each time there is a change in the primary control between axial displacement and torsional angle. These segment counters served as markers in combination with the sync signal for aligning and merging the Strain Smart data with the MTS data.

Both the Strain Smart and MTS data acquisition processes collected more information than was needed for this project. The excess data was collected because it included raw data measurements that may be needed for troubleshooting any errors in the data. The excess data needed to be removed to make it faster and easier to analyze the results from the spring tests. A data merge program was written in SAS (ver. 9.2, SAS Institute, Cary, NC). The data merge program first stripped out excess data (e.g. data collected by the StrainSmart system while the MTS system DAQ was paused), then synchronized and merged the remaining data from the MTS and Strain Smart DAQ systems and saved the combined data into a single file.

Table 7: Example of Strain Smart raw data from Spring K104 Stage I Test

Assignment:		Sync Signal on Channel 1	Sync Signal on Channel 1	Sync Signal on Channel 1	Sync Signal on Channel 1	Shear Cell by Transcell 500 lbs on Channel 10
Reduction Method:		Strain	A/D Counts	A/D Counts Unzeroed	Millivolt per volt	Calibrated Values
ID	Seconds Elapsed	[01] Strain	[01] A/D Counts	[01] A/D Counts Unzeroed	[01] Millivolts Per volt	[10] lbf
38	3.71	-18.1927	-37	-44	-0.00925	-0.00942
39	3.81	-18.6844	-38	-45	-0.0095	0.112858
40	3.91	-17.701	-36	-43	-0.009	0.0721
41	4.01	-18.1927	-37	-44	-0.00925	0.0721
42	4.11	-18.6844	-38	-45	-0.0095	0.0721
43	4.21	-19.176	-39	-46	-0.00975	0.031343
44	4.31	-18.6844	-38	-45	-0.0095	0.0721
45	4.41	-18.6844	-38	-45	-0.0095	-0.00942
46	4.51	-19.176	-39	-46	-0.00975	0.031343
47	4.61	-835.197	-1700	-1707	-0.425	0.031343
48	4.71	-9999999	-9999999	-9999999	-9999999	0.031343
49	4.81	-9999999	-9999999	-9999999	-9999999	-0.00942
50	4.91	-9999999	-9999999	-9999999	-9999999	0.031343
51	5.01	-1072.24	-2183	-2190	-0.54575	0.031343
52	5.11	560.8549	1140	1133	0.285	-0.2132
53	5.21	-75.2249	-153	-160	-0.03825	-0.45775
54	5.31	118.5144	241	234	0.06025	-1.02835
55	5.41	43.76345	89	82	0.02225	-1.51744
56	5.51	59.99132	122	115	0.0305	-2.04729

Table 8: Example of MTS raw data from Spring K104 Stage I Test

Axial Displacement	Axial Force	Time	Axial Displacement Absolute Error	Axial Force Absolute Error	Aux Input 1	Running Time	Axial Output	Axial Segment Count	Torsional Torque	Torsional Angle	Torsional Segment Count
in	lbf	Sec	in	lbf	V	Sec	V	segments	in-lbf	deg	segments
-0.005	-0.459	12.742	0.007	0	1.611	12.718	-0.254	0	0.334	0.002	0
-0.017	-1.896	12.843	0.006	0	1.611	12.818	-0.254	0	-0.152	0.001	0
-0.030	-3.003	12.943	0.006	0	0.025	12.918	-0.251	0	-0.417	0.001	0
-0.042	-4.151	13.043	0.006	0	-0.009	13.018	-0.250	0	-0.138	-0.007	0
-0.054	-5.698	13.143	0.006	0	-0.009	13.118	-0.250	0	-0.265	0.010	0
-0.066	-6.900	13.243	0.006	0	-0.009	13.218	-0.251	0	-0.556	0.003	0
-0.078	-8.224	13.343	0.006	0	-0.008	13.318	-0.250	0	-0.458	0.004	0
-0.091	-9.520	13.443	0.005	0	-0.008	13.418	-0.249	0	-0.156	-0.003	0
-0.103	-10.680	13.543	0.005	0	-0.008	13.519	-0.246	0	-0.510	0.001	0
-0.115	-12.001	13.643	0.005	0	-0.007	13.619	-0.247	0	-0.290	0.005	0
-0.127	-13.262	13.743	0.005	0	-0.007	13.719	-0.245	0	-0.349	0.005	0

Experimental Results

The results from the calibration process are presented in the following section first, followed by the results from the validation process of the 6 Cell. The results from the Stage II testing procedure performed on one compression spring under combined loading are presented last.

6-Cell Load Calibration

Linear regression analysis was performed on the 6-Cell and the S-Cell calibration data using SAS. A linear model relationship between the force (e.g. lbs for the axial calibration) versus the millivolts-to-volts (mV2V) output from the 6-Cell channel being calibrated and a 95% confidence interval on that model were calculated and plotted. With the exception of the bending about the y-axis calibration plot the 95% confidence intervals cannot be seen because they lie within the bounds of the experimental data.

The resulting linear models served as calibration curves and were then used to calibrate each load axis in the Strain Smart software so that output collected from experimental trials would be presented in the appropriate load units for each channel. The 95% confidence interval provides the upper and lower error bounds of each calibration curve. The results obtained from the regression analyses are summarized in Table 9. These results also include the root mean square error (RMSE) for each calibration curve. The RMSE values for each load axis can be used as a general value for the load error for each load channel [53].

On each figure, the linear model for the calibration curve is printed at the upper left corner above the plot. The R-square, adjusted R-square, and root mean square error

(RMSE) are printed below the number of records (N) outside the upper right corner of the plot.

The 6-Cell calibration curves are presented for axial (Figure 59), torsional (Figure 60), shear in the x-direction (Figure 61), shear in the y-direction (Figure 62), bending about the x-axis (Figure 63), and bending about the y-axis (Figure 64) load channels. The S-Cell calibration curve is presented in Figure 65.

Table 9: Calibration and Validation of Load Cell Statistical Analysis Summary

Calibration	Correlation Coefficient	P-Value	RMSE	Slope	Intercept
6 Cell Axial Load	0.9992	< 0.0001	3.747 lbs	-9370.7	-0.7796
6 Cell Torsion Load	0.9978	< 0.0001	10.169 in-lbs	2247.5	1.222
6 Cell Shear X Load	0.9998	< 0.0001	2.0253 lbs	-4900.2	-1.1879
6 Cell Shear Y Load	0.9999	< 0.0001	1.5141 lbs	-7886.3	-0.0117
6 Cell Moment X Load	0.9998	< 0.0001	7.0189* in-lbs	3456.78*	-3.2319*
6 Cell Moment Y Load	0.9987	< 0.0001	17.3873* in-lbs	3374.18*	1.5782*
Transverse S Cell Axial Load	0.9998	< 0.0001	2.4358 lbs	163.06	0.0721
MTS vs. 6 Cell Axial Loads	0.9987	< 0.0001	4.6386 lbs	1.0225	0.5839
MTS vs. 6 Cell Torsion Loads	0.9991	< 0.0001	0.6267 lbs	1.0001	0.8997

* - Denotes values that differ from previous plots. These values have been multiplied by the moment arm of 3.5 inches to correctly obtain the calibration curve in units of in-lbs.

The statistical results of the calibration tests are summarized in the first seven entries of Table 9. The P values indicate that each calibration test is statistically highly significant. The correlation coefficients, which are near unity, indicate that the fitted

linear models, (i.e. the calibration curves), account for nearly all variability in the

calibration data. In other words the calibration curves are fitted well with the data and

are strong models. The values seen in Table 9 for the slope and intercept of the X and Y

moments are corrected values that take into account the moment arm and differ from the

slope and intercept values presented in Figure 63 and Figure 64. This is because the

calibration analysis only accounted for the applied load during the test. The applied load

is not the same as the applied moment. For a four-point bending test the load applied and

measured needs to be multiplied by the moment arm. The moment arm for the

calibration of the moments about the x- and y-axes on the 6 Cell the moment arm was 3.5

inches.

6-Cell Validation

The load data from the stage I testing of the K104 compression spring was used to

validate the axial and torsional calibration of the 6 Cell. The experimental setup used to

test the compression springs provided redundant data for the axial and torsional loads

from the 6 Cell and the MTS load cell. As a result the axial and torsional load readings

from the MTS load cell that was professionally manufactured and calibrated were used as

a reference to validate the calibration of the 6 Cell. The validation of the axial load is

presented in Figure 66. Strong correlation between the MTS and 6 Cell force readings is

indicated by a slope close to unity. As presented in either Figure 66 or Table 9 the slope

was 1.0225, and the correlation coefficient was near unity. The correlation was highly

statistically significant. The validation of the torsional load is presented in Figure 67.

The slope of the linear model of the torsional load data from the 6-Cell versus the MTS

load cell was 1.0001. Table 9 also provides the statistical summary for the torsional

validation test. It is shown that the P value for the torsional validation test is less than 0.0001; therefore, the correlation is highly statistically significant.

Figures 59 through 67 which show the calibration results are presented below. On each figure, the linear model for the calibration curve is printed at the upper left corner above the plot. The R-square, adjusted R-square, and root mean square error (RMSE) are printed below the number of records (N) outside the upper right corner of the plot.
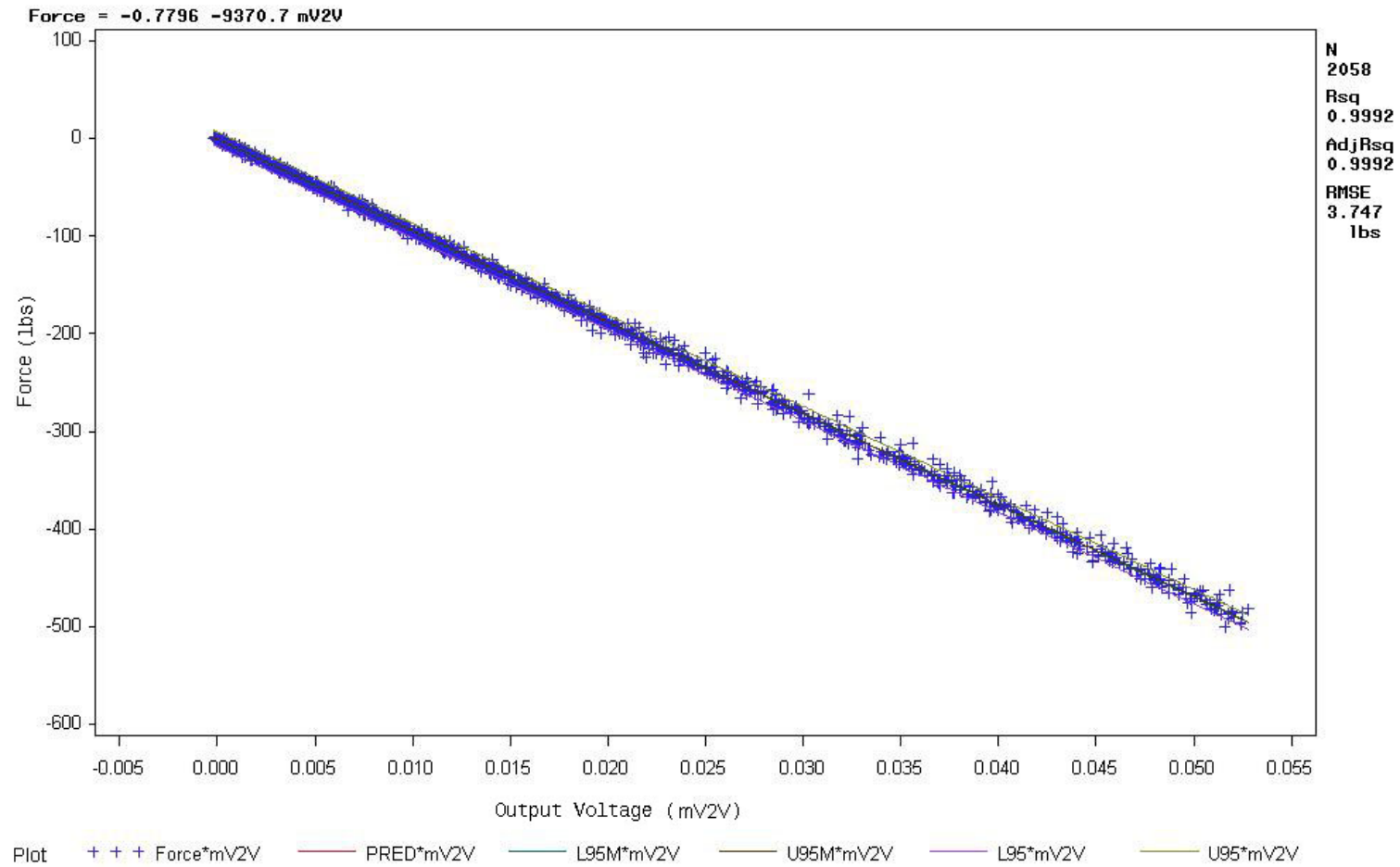
Figure 59: 6 Cell Axial Load Calibration Curve
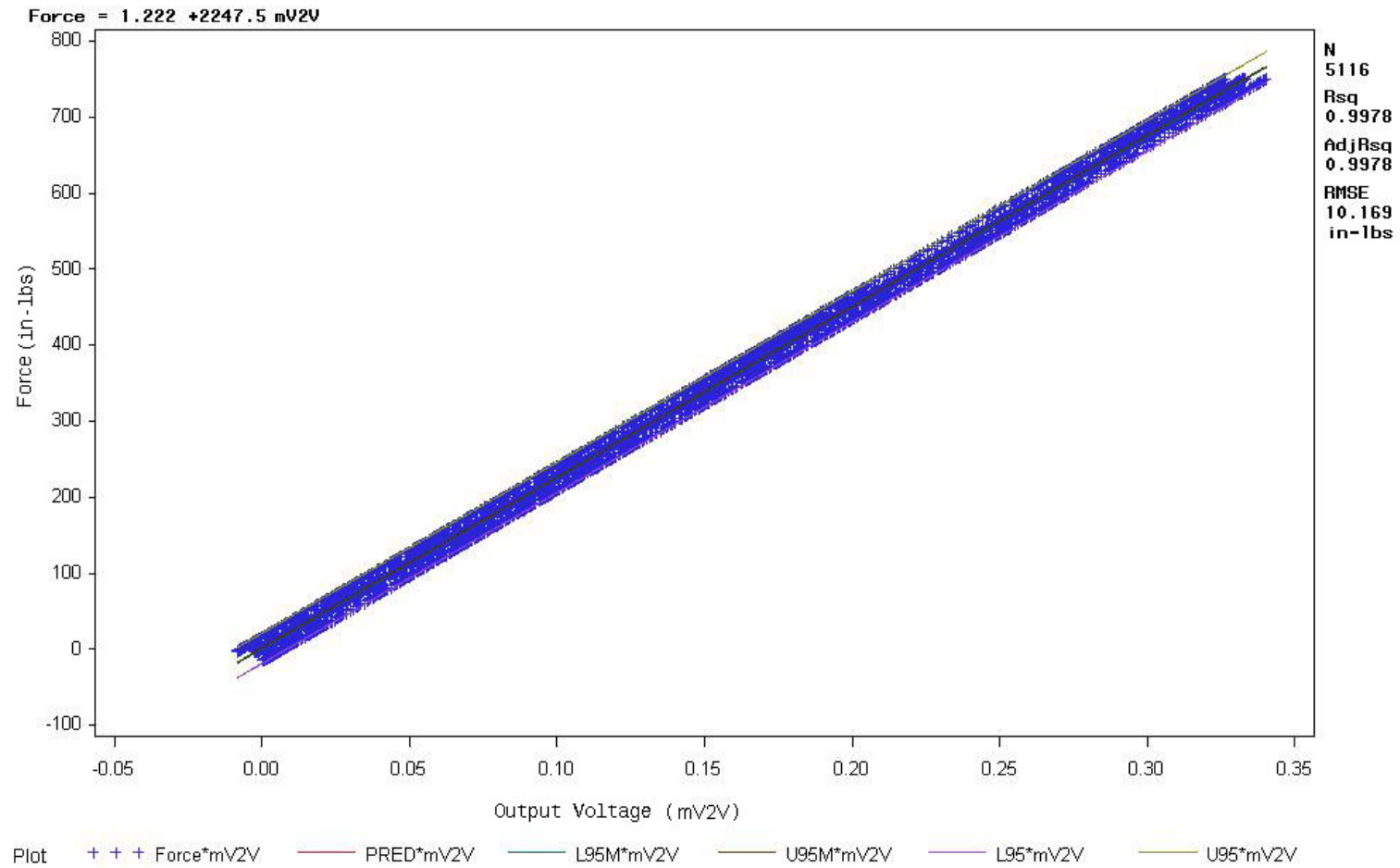
Figure 60: 6 Cell Torsion Load Calibration Curve
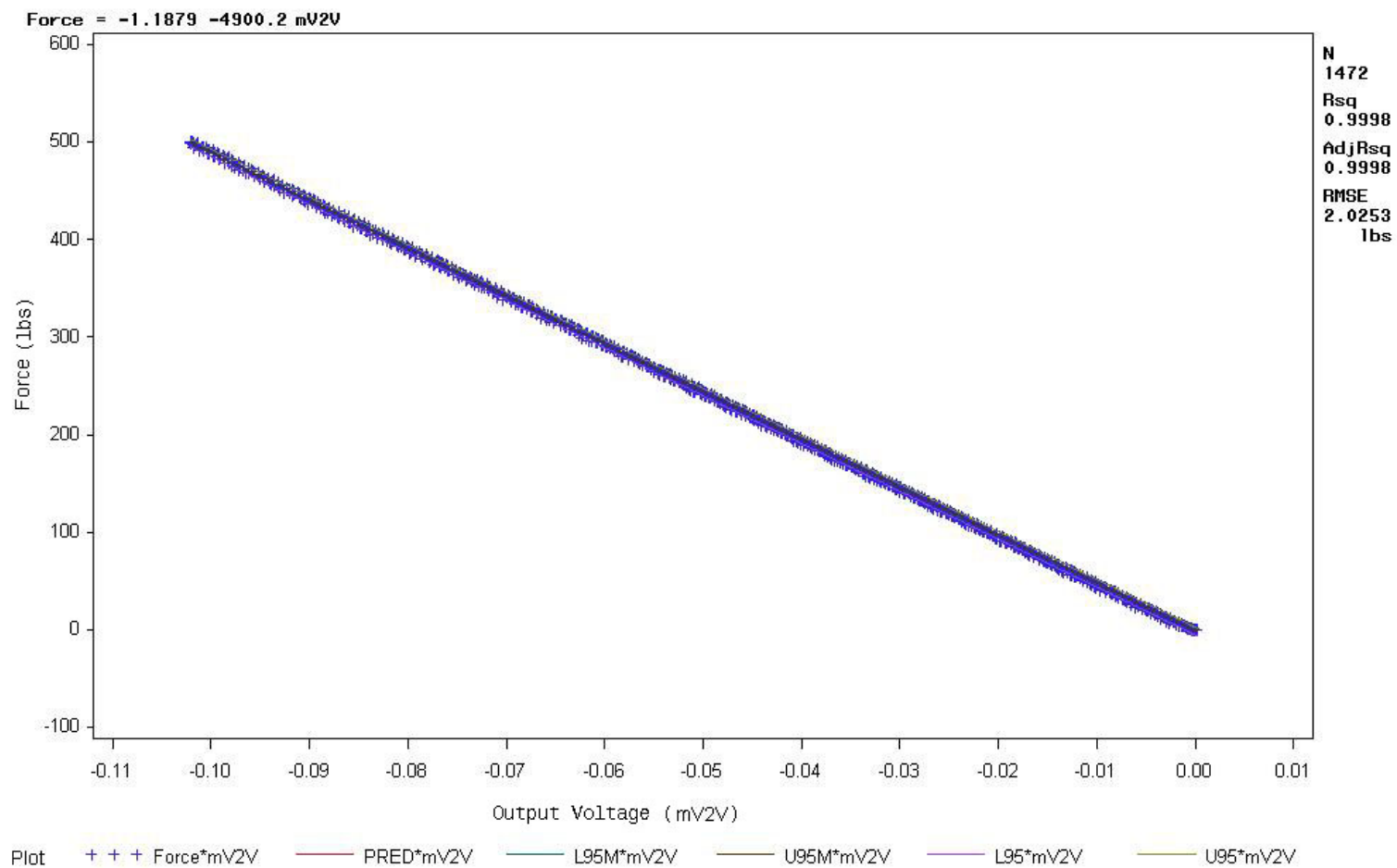
Figure 61: 6 Cell Shear x-axis Load Calibration Curve
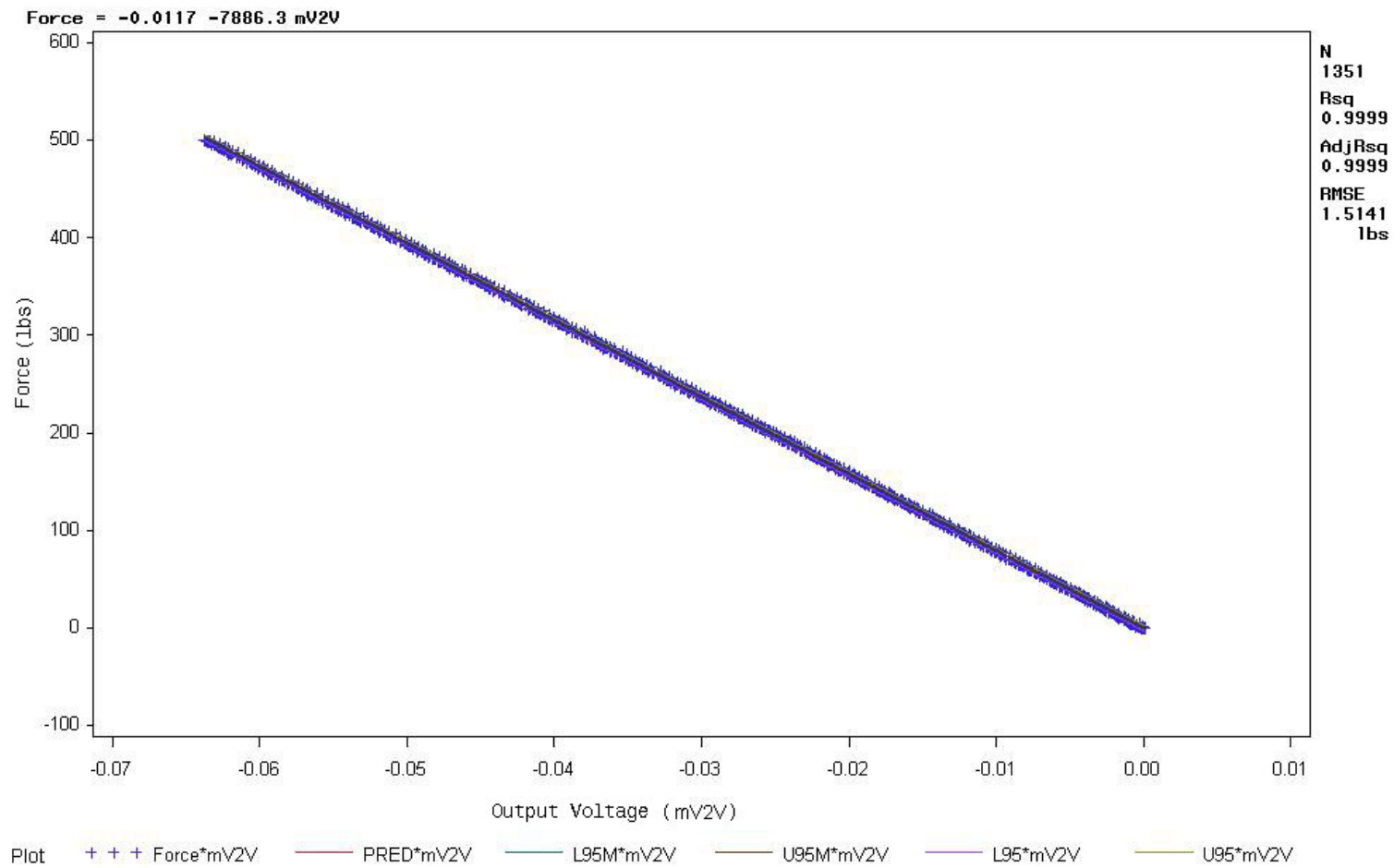
Figure 62: 6 Cell Shear y-axis Load Calibration Curve
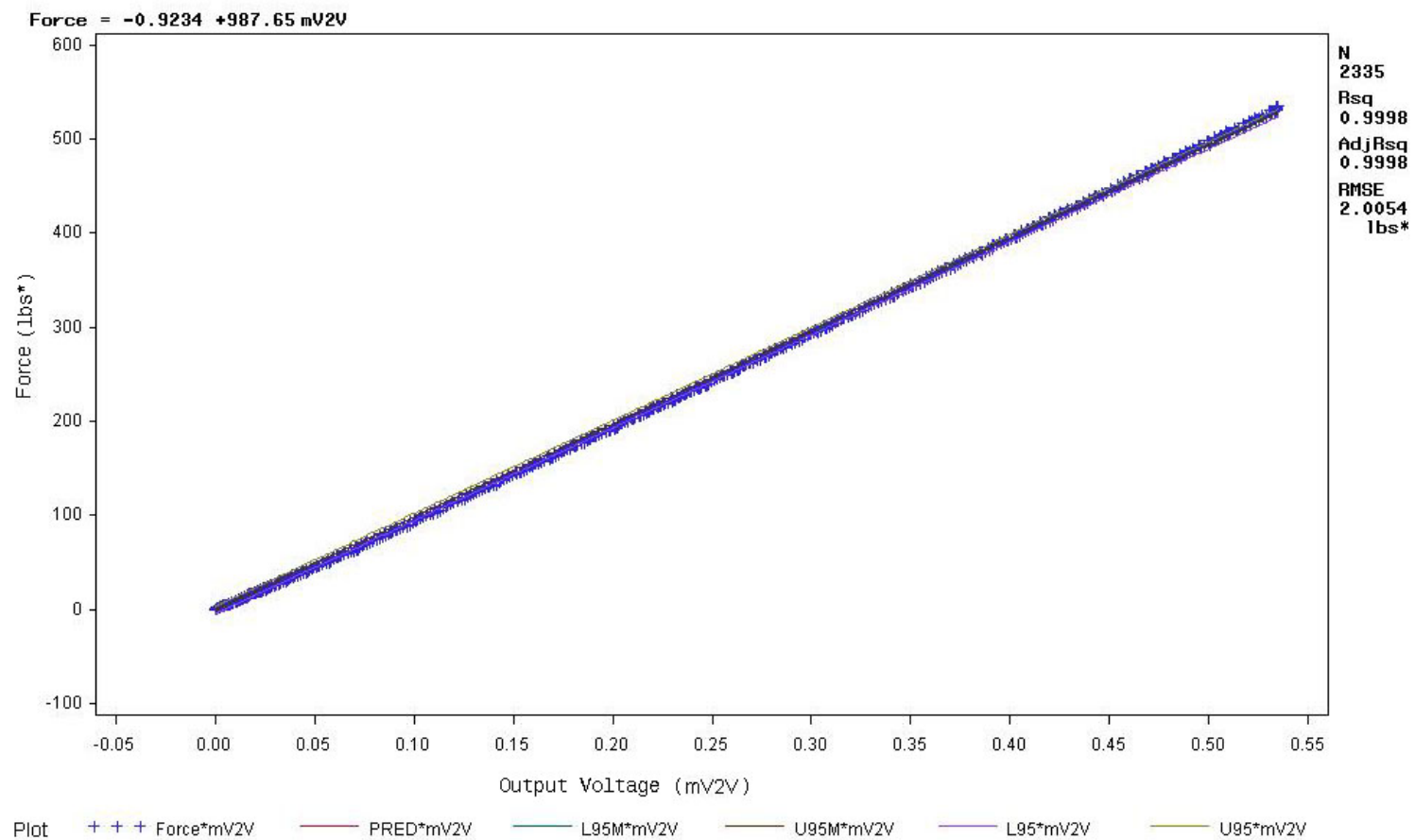
Figure 63: 6 Cell Bending about the x-axis Load Calibration Curve (* Denotes raw values without moment arm of 3.5 inches applied)
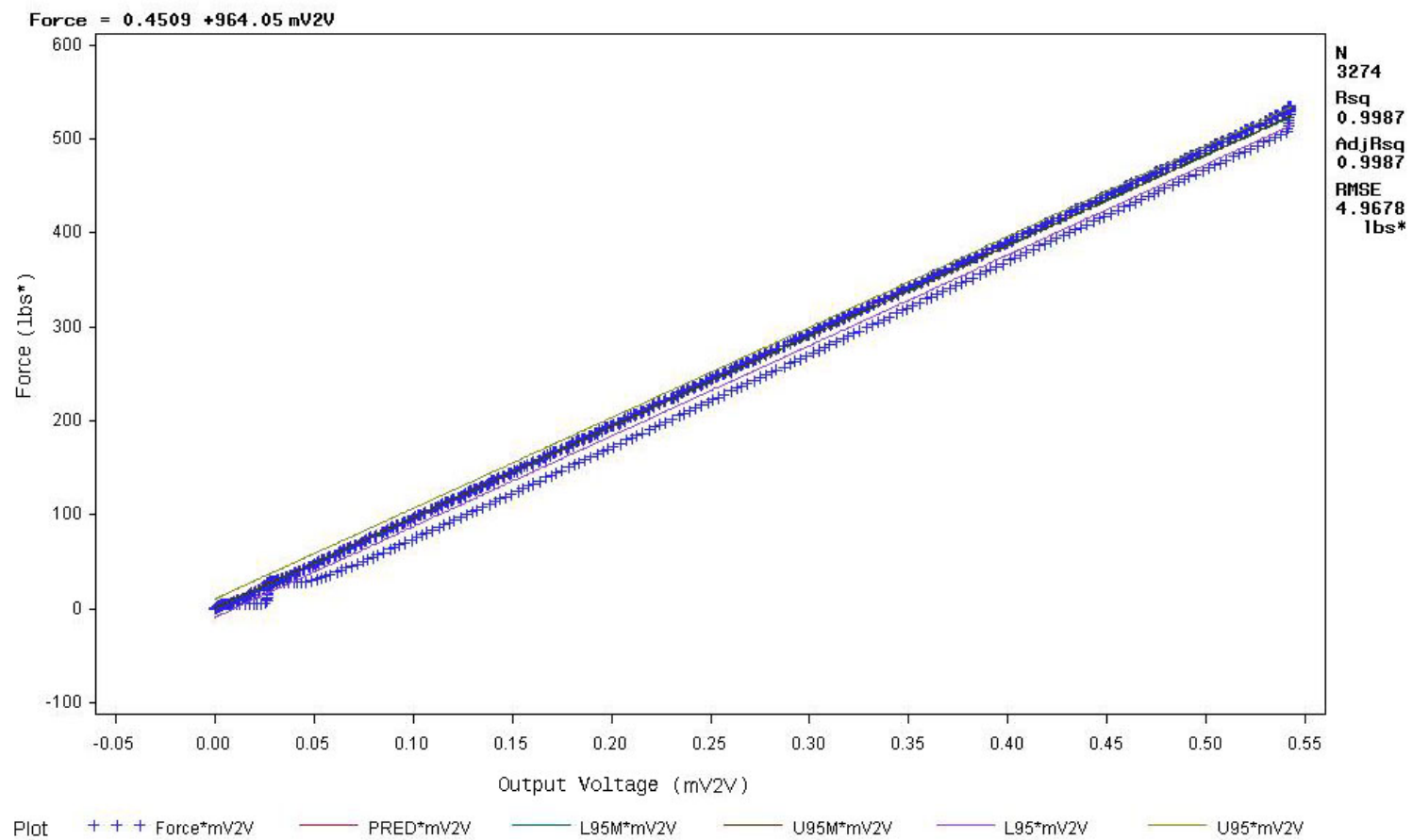
Figure 64: 6 Cell Bending about the y-axis Load Calibration Curve (* Denotes raw values without moment arm of 3.5 inches applied)

S Load Cell Calibration

Force = 0.0721 +163.03 mV2V

N
1702

Rsq
0.9998

AdjRsq
0.9998

RMSE
2.4358
lbs

Plot   + + + Force*mV2V   —— PRED*mV2V   —— L95M*mV2V   —— U95M*mV2V   —— L95*mV2V   —— U95*mV2V
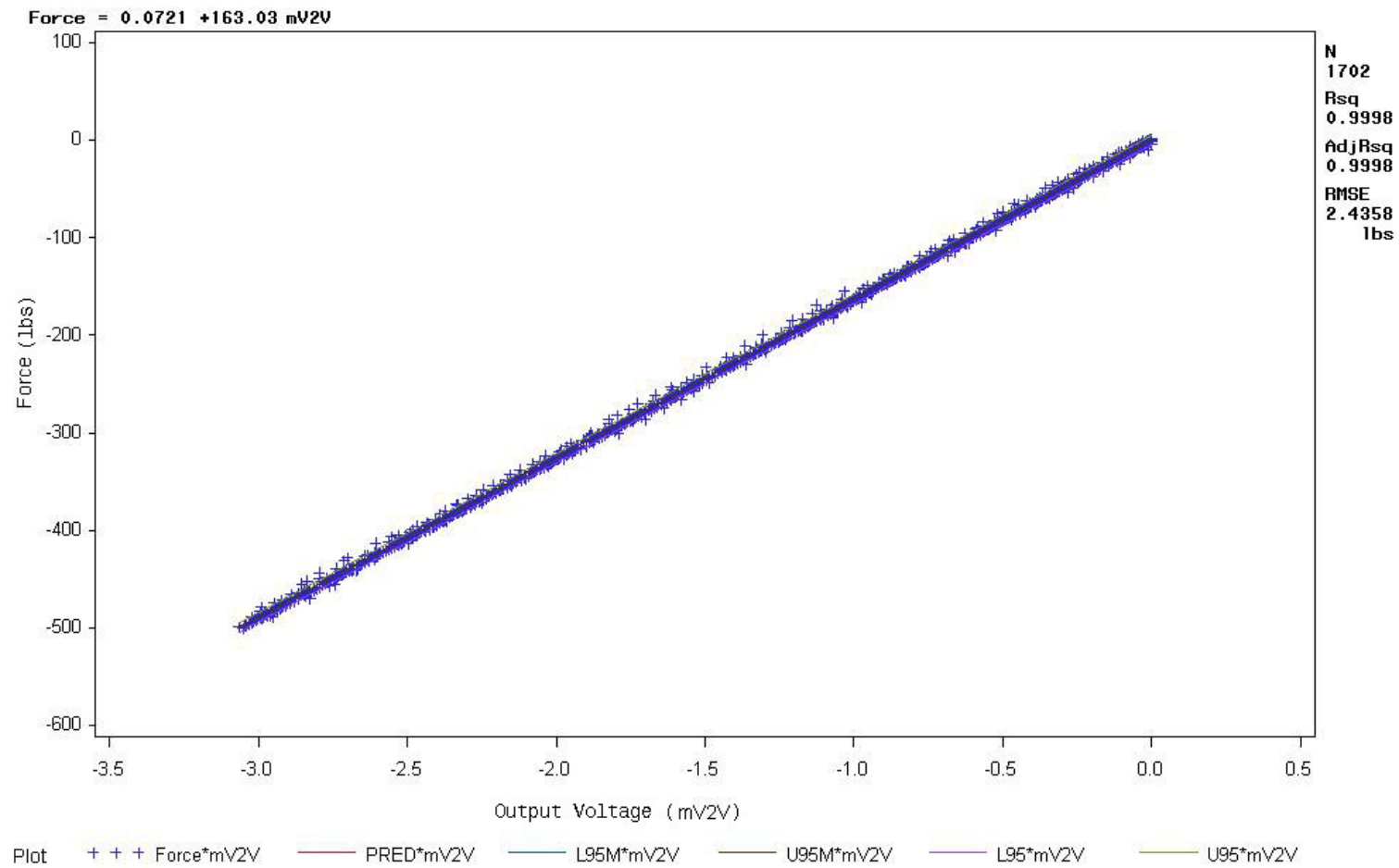
Figure 65: Transverse S Cell Axial Load Calibration Curve
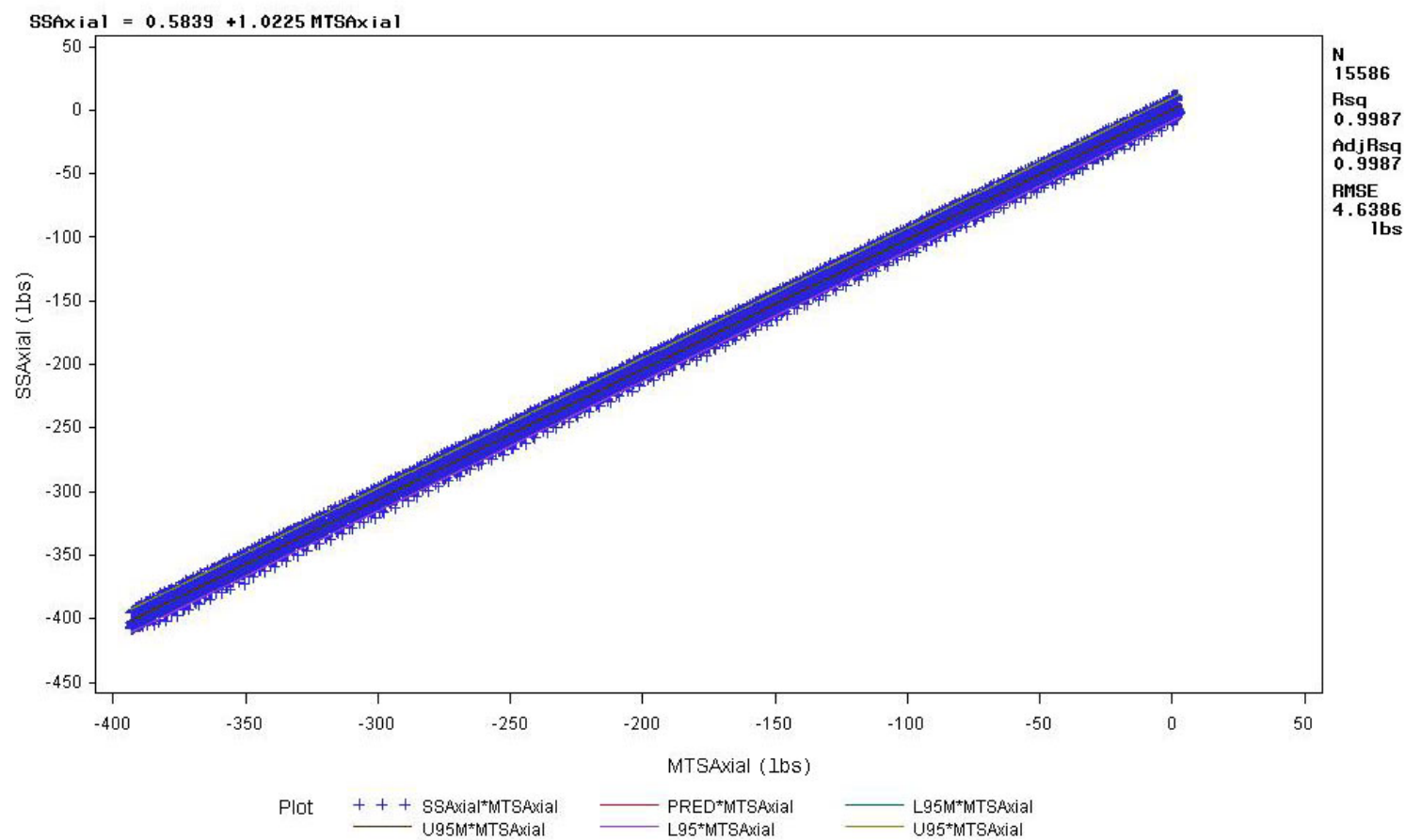
Figure 66: 6 Cell Axial Load Validation Curve from Stage I Test on K104 Spring
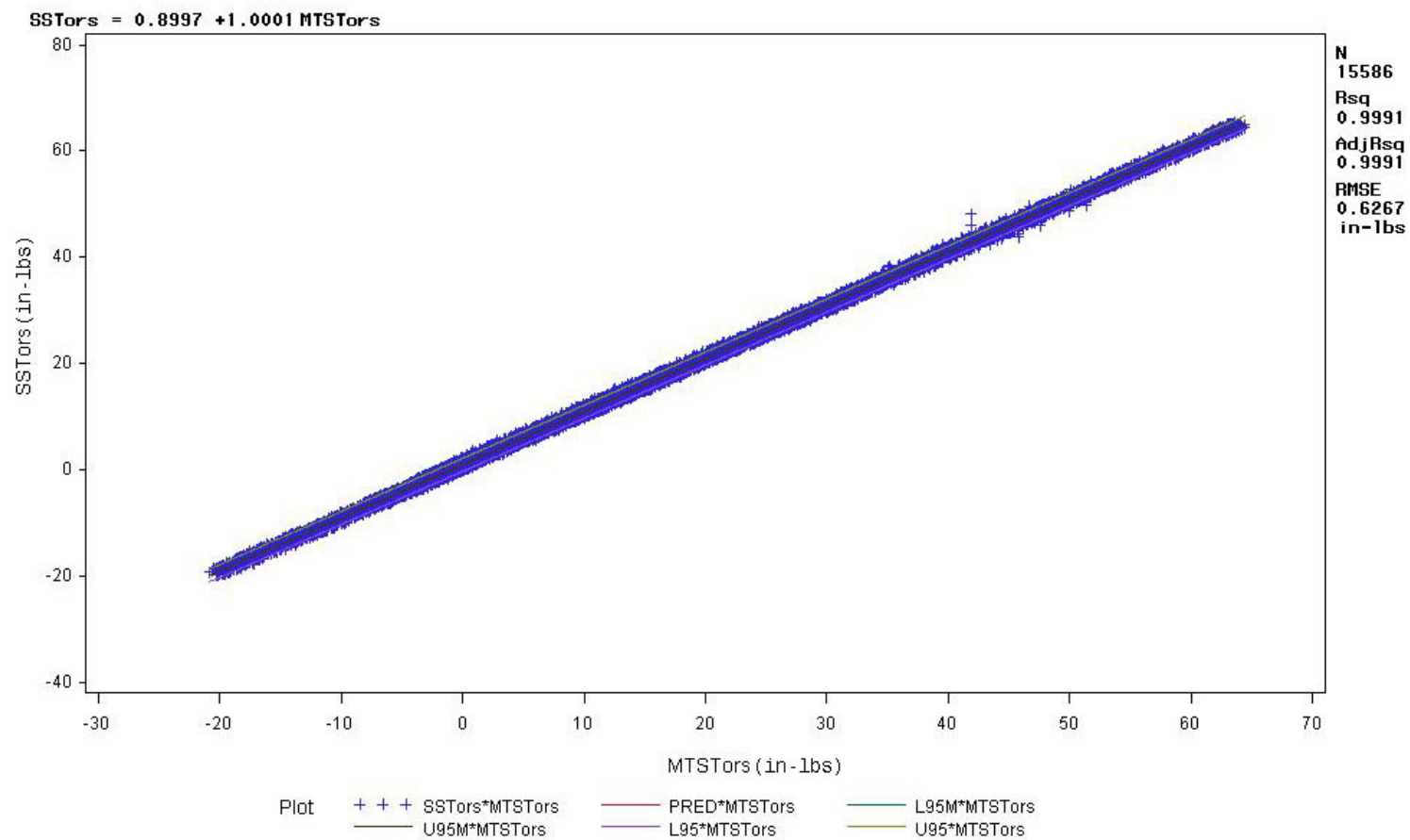
Figure 67: 6 Cell Torsional Load Validation Curve from Stage I Test on K104 Spring

Validation of Testing Procedure and Testing Jig

In this section, the evaluation of the testing procedure and testing jig are presented. The testing jig that was developed for this thesis was designed to provide a means to test compression springs under combined loads. In order to provide results that would be statistically significant it is necessary that both the testing procedure and test jig provide results that are repeatable. Repeated measures analysis was performed using SAS, and the Type III Fixed Effects results are presented.

Each analysis consists of three Stage I test trails on a single spring (the K104 spring). All three trails, the entire test, are presented on each plot. The trail number and color is printed below the x-axis label (record number). The y-axis is the force measured by the load cell during each test trial. The plots in Figure 68 through Figure 76 present the unwinding portion of the testing procedure (Part 1). The repeated measures analysis results are presented for the MTS axial channel (Figure 68), 6-Cell axial (Figure 69), MTS torsional (Figure 70), 6-Cell torsional (Figure 71), S-Cell pure shear (Figure 72), 6-Cell shear in the x-direction (Figure 73), 6-Cell shear in the y-direction (Figure 74), 6-Cell moment about the x-axis (Figure 75), and 6-Cell moment about the y-axis (Figure 76).

These results provide a means to evaluate the repeatability in one spring's response under combined loading. The mean of the three load measurement values at a particular point in time was used to normalize the results. The difference between the three trials values and the mean load at that point in time was calculated for each test. Repeated measures were calculated using the normalized data. If the load variance along the testing procedure, when compared with the mean value, is not significant, then the testing procedure and the response from the spring were inferred to be repeatable. The

109

results for all nine repeated measures tests indicated that there was not a statistical

significance among the variances in the load measurements. The repeated measures

analysis results for the part 2 (winding torque) Stage I tests, which also demonstrate

repeatability, are provided in Appendix L.

Figures 68 through 76 showing the repeated measures results are presented below.

On each figure, the y-axis displays the amount of force measured during the test. The

measurements recorded are shown on the x-axis (record number). Below the x-axis the

color legend for each of the three trials is provided.
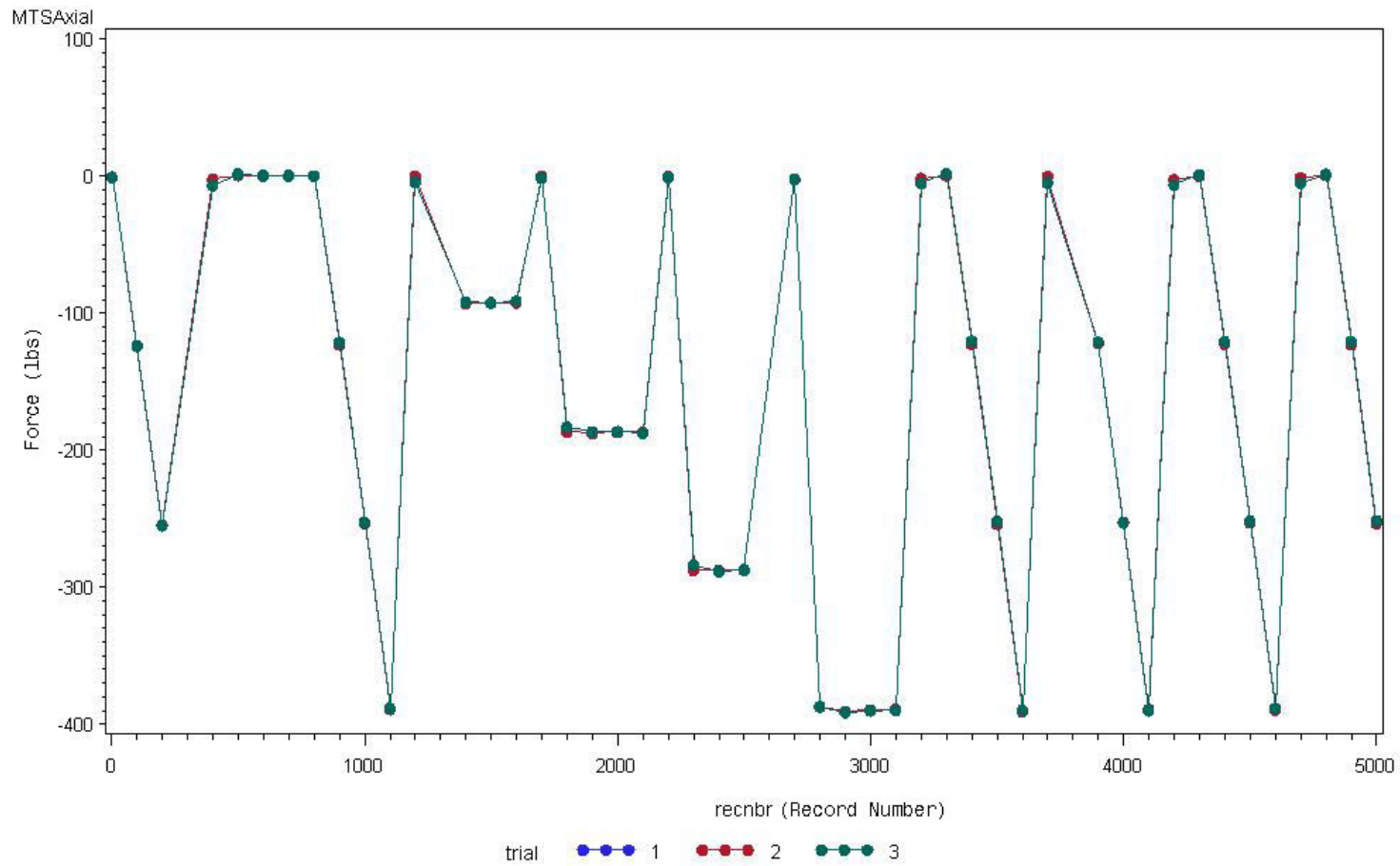
Figure 68: MTS Axial Load Repeated Measures Analysis on Three Stage I Part 1 Trials on Spring K104
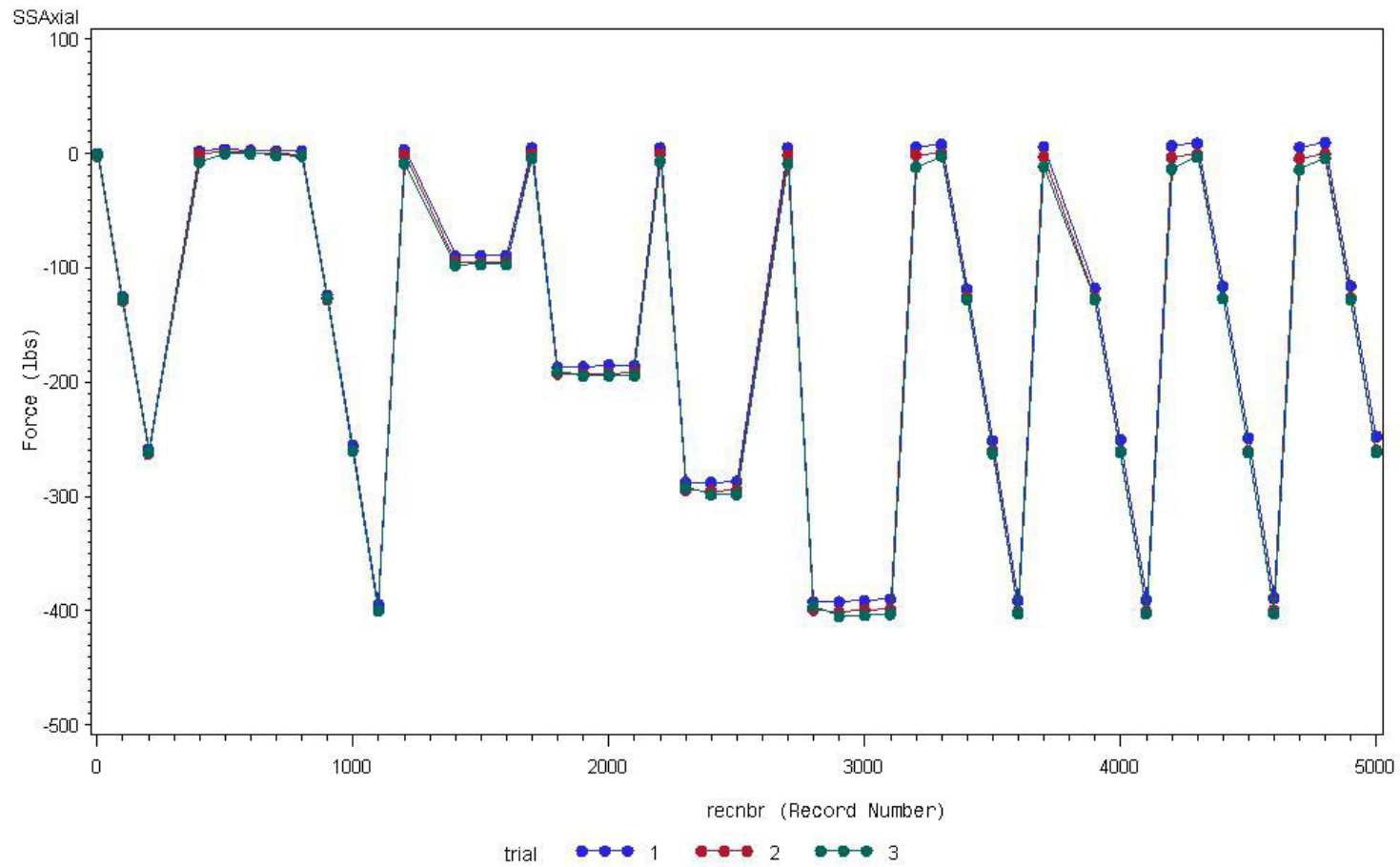
Figure 69: 6 Cell Axial Load Repeated Measures Analysis on Three Stage I Part 1 Trials on Spring K104
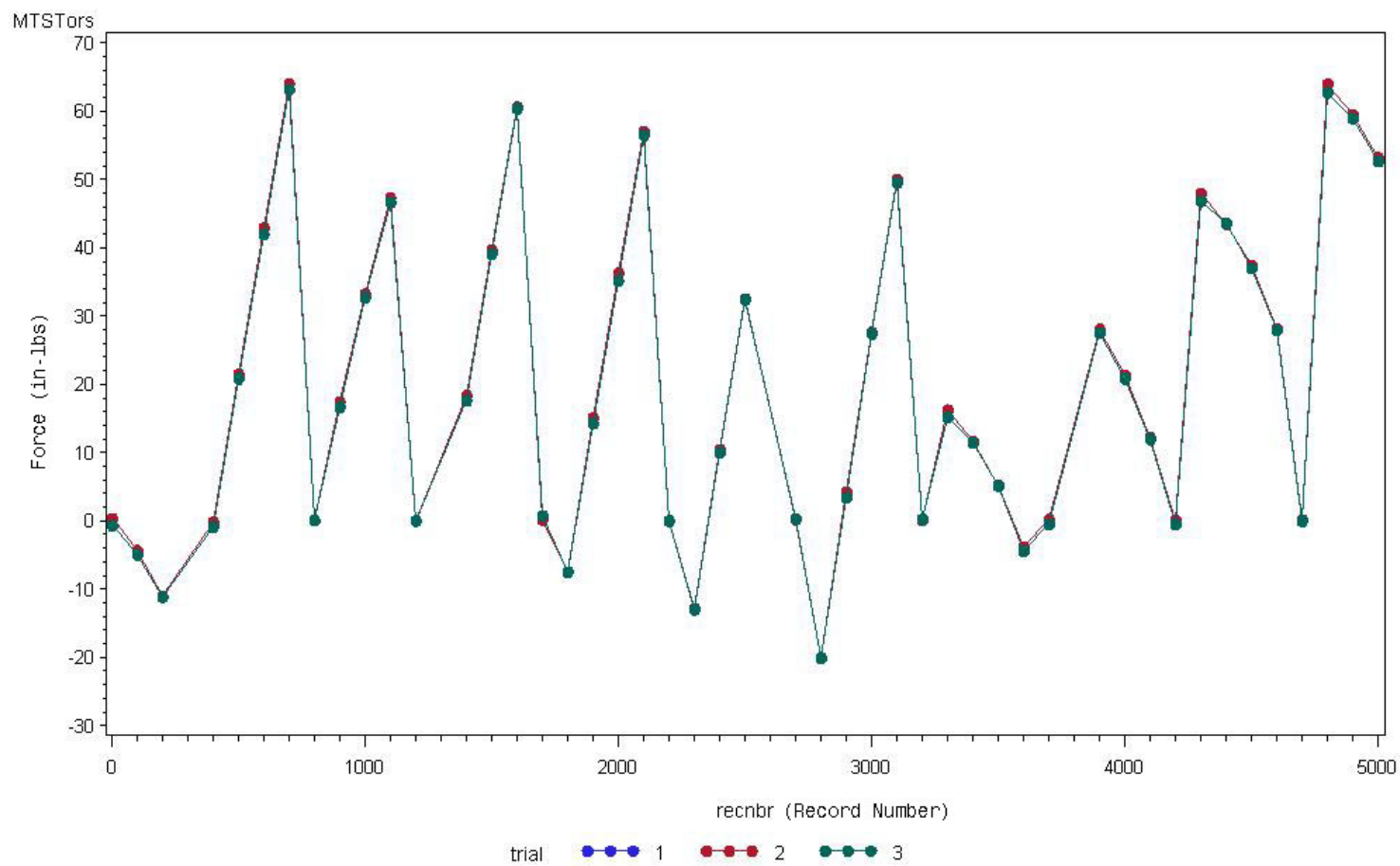
Figure 70: MTS Torsional Load Repeated Measures Analysis on Three Stage I Part 1 Trials on Spring K104
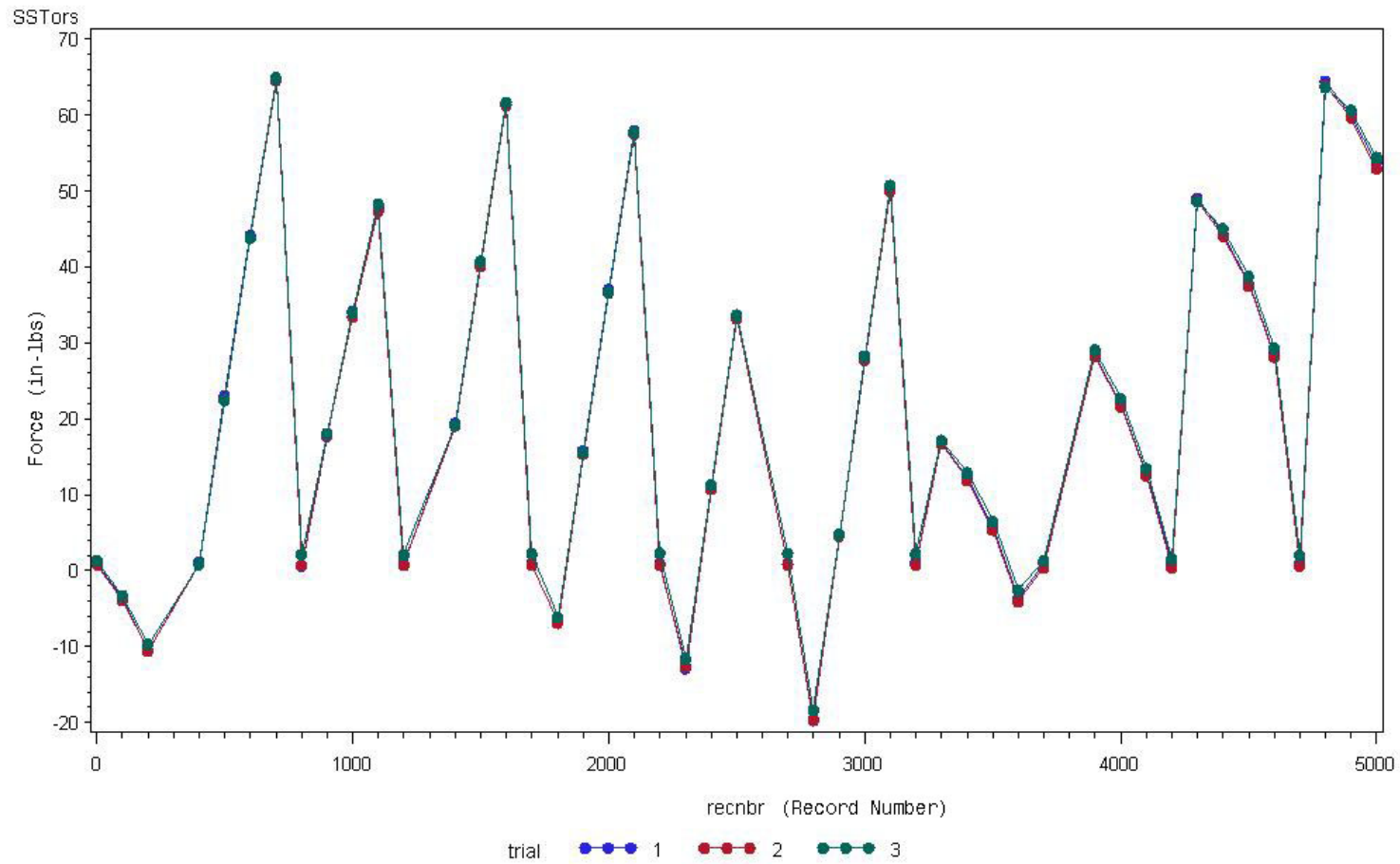
Figure 71: 6 Cell Torsional Load Repeated Measures Analysis on Three Stage I Part 1 Trials on Spring K104
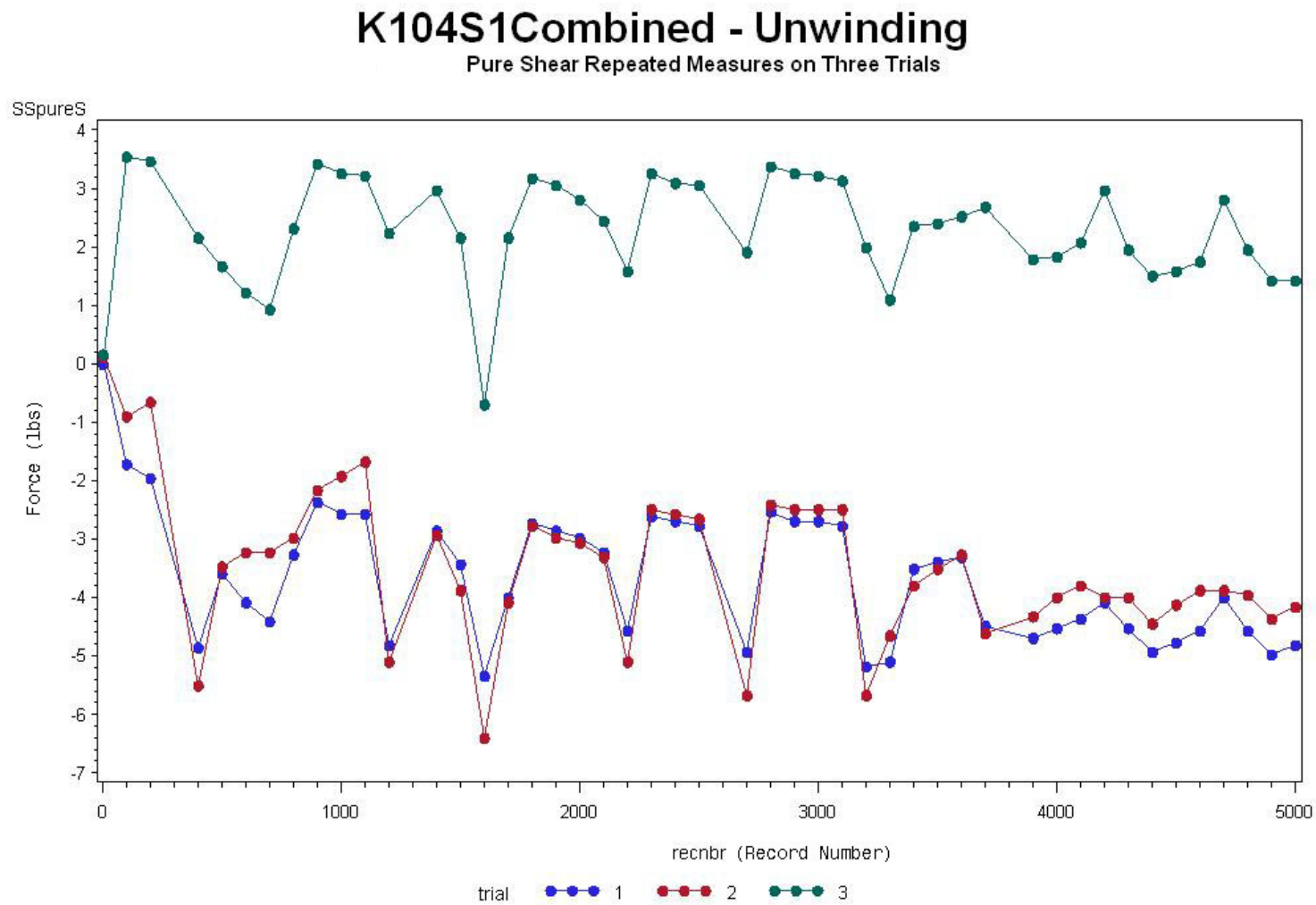
Figure 72: S-Cell Pure Shear Load Repeated Measures Analysis on Three Stage I Part 1 Trials on Spring K104
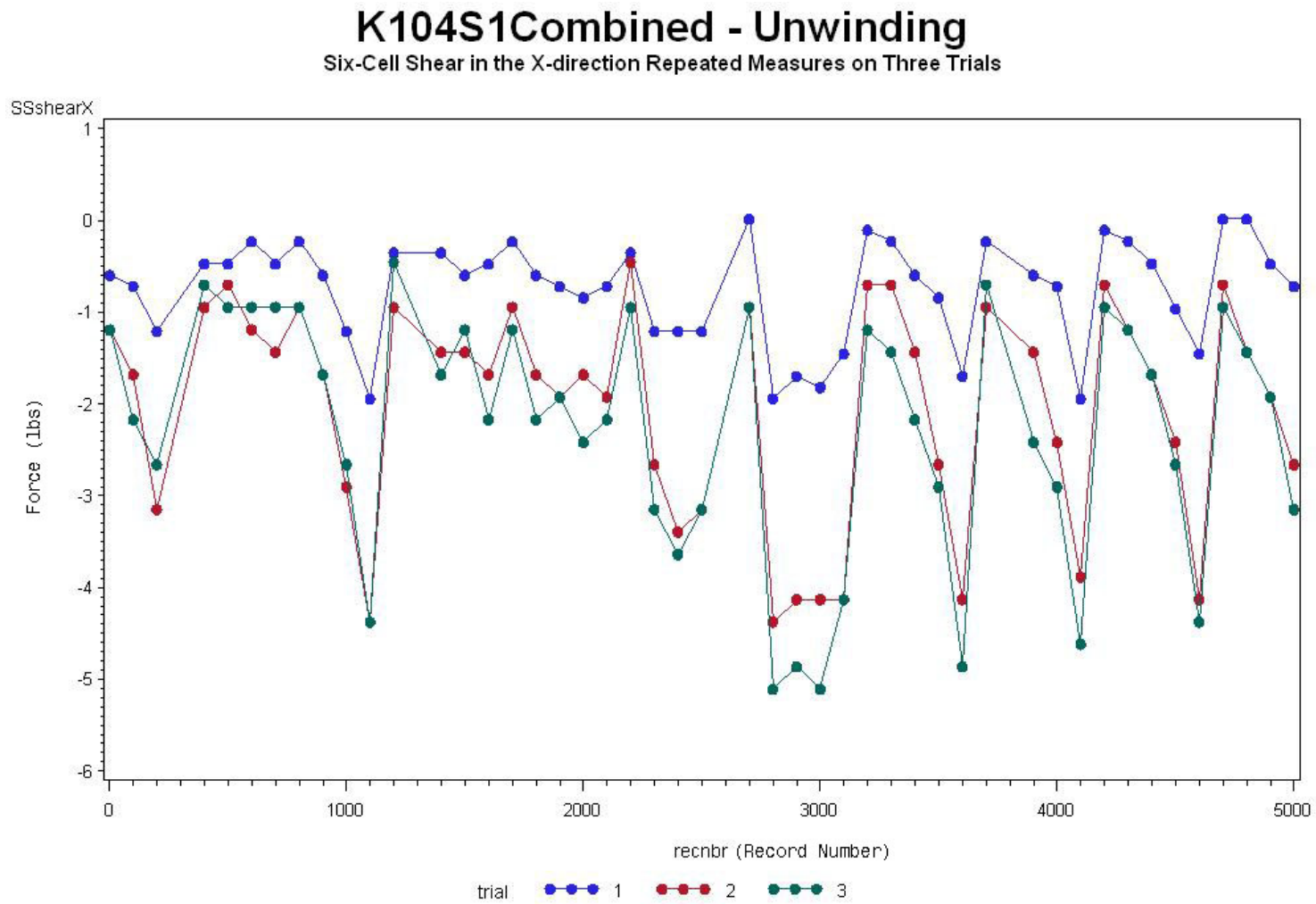
Figure 73: 6 Cell Shear X Load Repeated Measures Analysis on Three Stage I Part 1 Trials on Spring K104
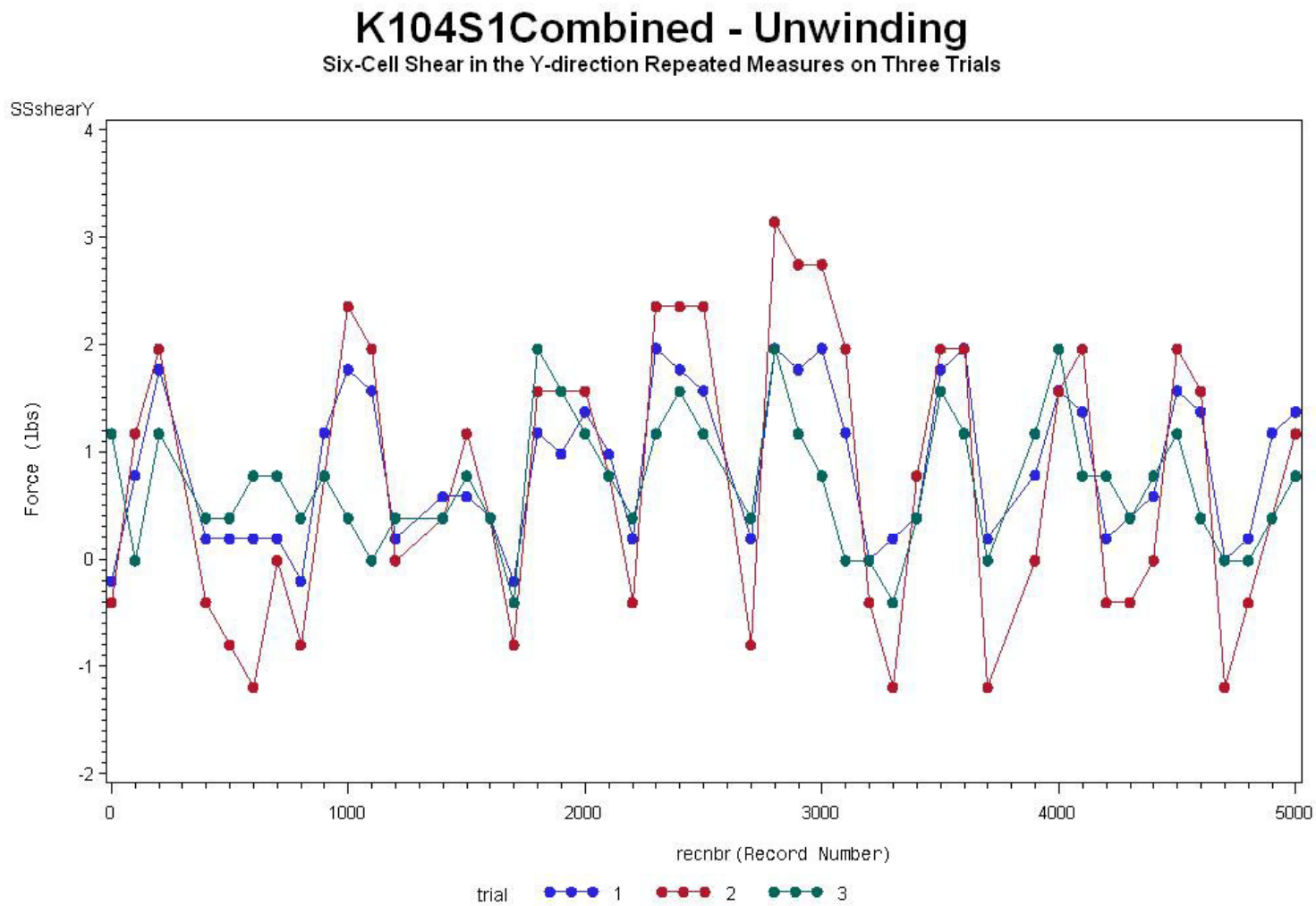
Figure 74: 6 Cell Shear Y Load Repeated Measures Analysis on Three Stage I Part 1 Trials on Spring K104
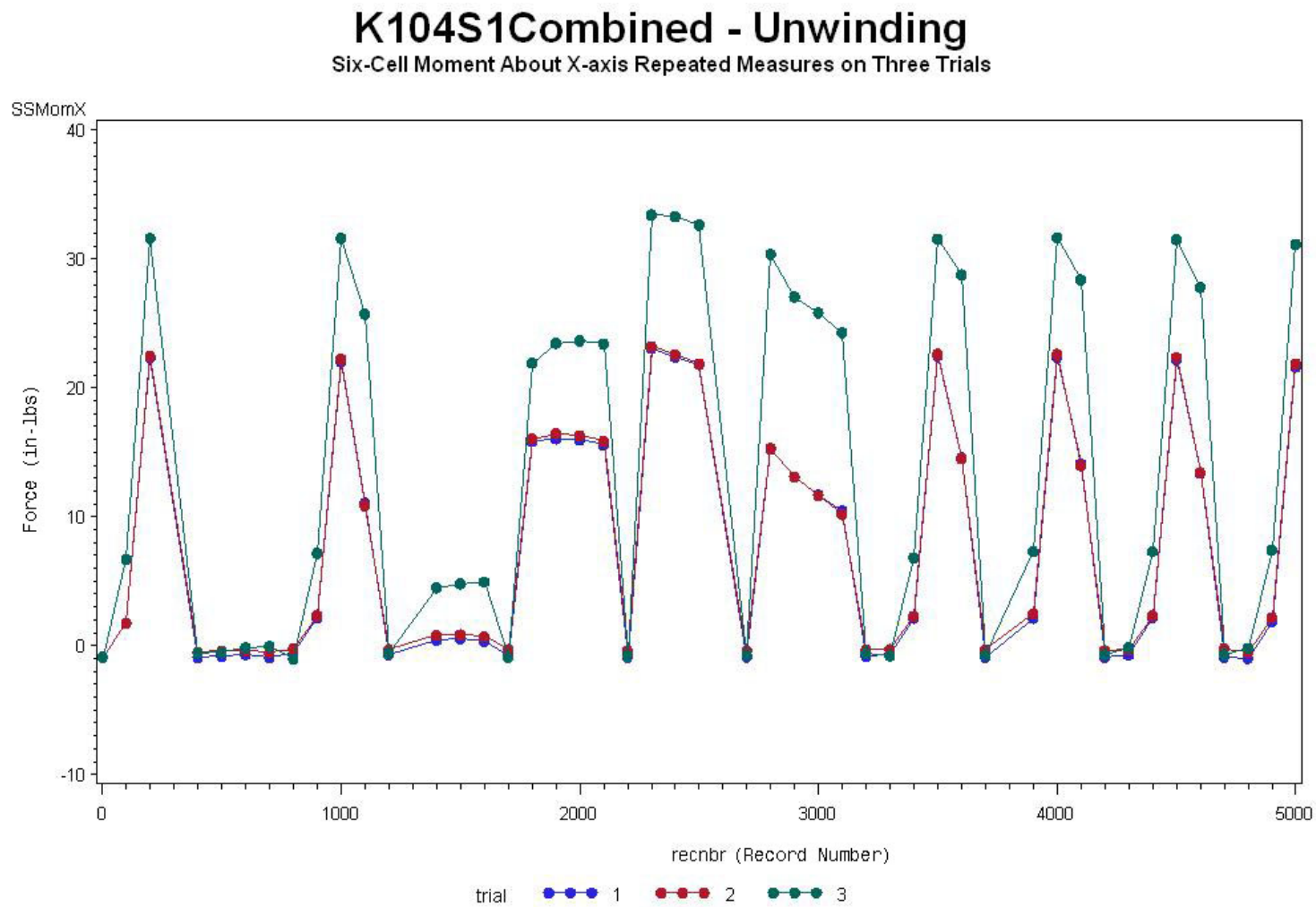
Figure 75: 6 Cell Moment X Load Repeated Measures Analysis on Three Stage I Part 1 Trials on Spring K104
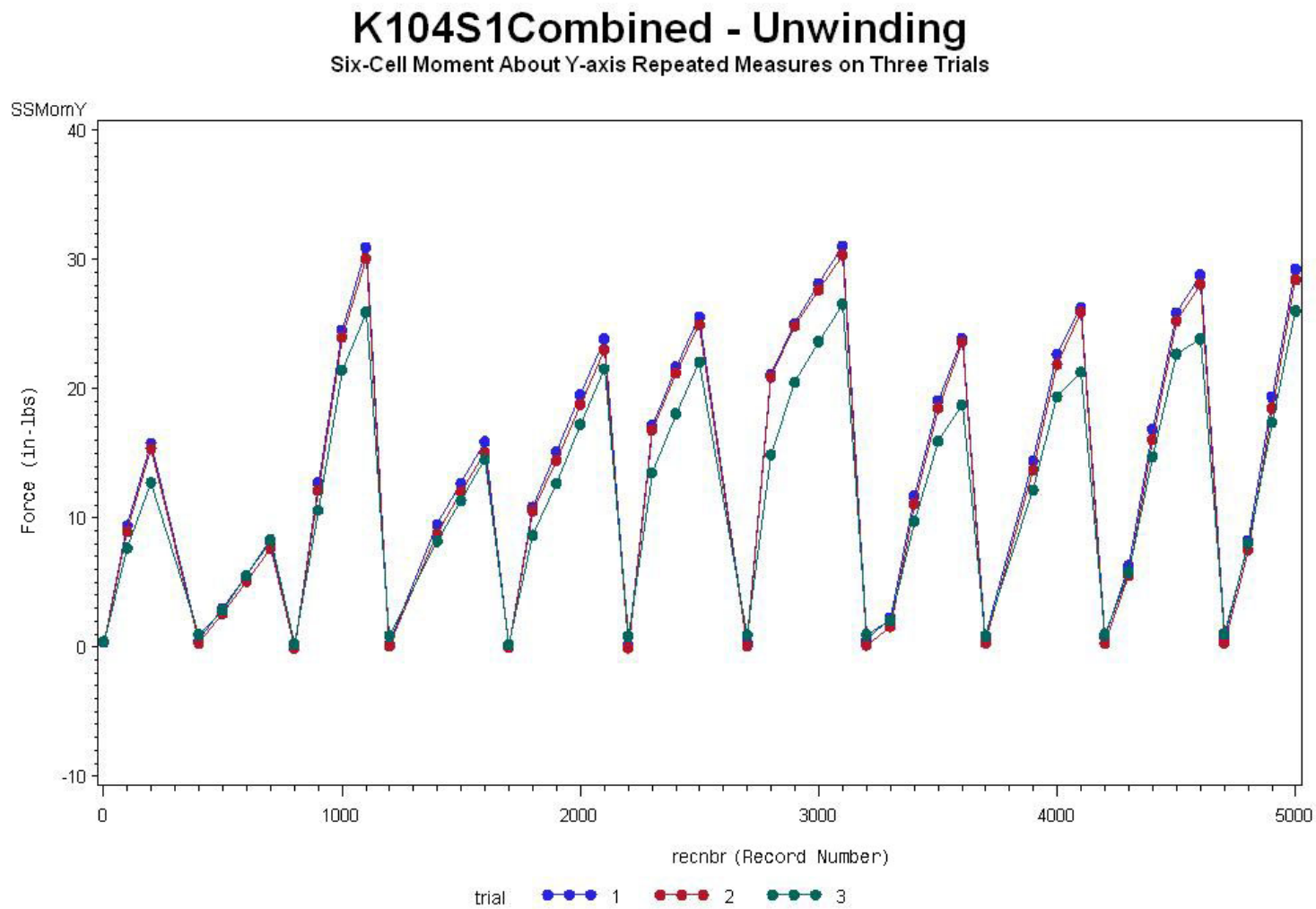
Figure 76: 6 Cell Moment Y Load Repeated Measures Analysis on Three Stage I Part 1 Trials on Spring K104

Evaluation of Stage II Testing Procedure and Preliminary Test Results

The following section includes the results obtained from part 1 of the stage II testing. Both Stage I and Stage II were divided into two parts. Part 1 and part 2 follow the same general test protocol with the exception of the direction of applied torque. In part 1, an unwinding torque is applied, and in part 2 a winding torque is applied to the compression spring. Figure 77 is a three dimensional plot showing the MTS axial load during part 1 of Stage II versus both the MTS axial displacement and MTS torsion angle. The following figures, Figure 78 and Figure 79, are the two dimensional x-z and y-z plots of Figure 77, respectively. The axial displacement is plotted along the x-axis, the torsional angle along the y-axis, and the axial load is along the z-axis.

Figure 80 is the three dimensional plot of the MTS torsional response versus the MTS axial displacement and the MTS torsional angle. Figure 80 is also followed by its x-z and y-z plots, Figure 81 and Figure 82. For these plots, the axial displacement is plotted along the x-axis, the torsional angle along the y-axis, and the torsional load is along the z-axis. The key trends seen from Figure 77 through Figure 82 will be discussed in detail in Chapter 7.

Figure 83 shows a plot of the axial compressive displacement at which the coils of the K104 compression spring began to clash at different shear levels. The shear displacement applied during the stage II testing procedure were 0.375 in, 0.750 in, 1.125 in, and 1.500 in. Each of the points in Figure 83 are plotted at their respective axial displacements where the coils began to clash. The onset of coil clashing was determined to be at the point at which the axial stiffness began to increase beyond the manufacturer's spring constant. In other words, the coil clash point was determined at the point where

the slope increased from the known spring constant to a higher value. The increase in the

slope can be clearly seen in Figure 78 as the axial displacement is applied.

There was no increase in the slope (i.e. the axial stiffness) at the first shear

displacement level (S1). Because of this, the point of clash for the S1 displacement point

was estimated to be beyond 3.6 inches of compression which is past the upper limit of the

axial displacement applied during the testing procedure. A polynomial trend line (see

Figure 83) was plotted through the S4, S3, S2, and S0 points, and the S1 point was then

estimated to lie on the plotted trend line. The estimated S1 point plotted was greater than

3.6 inches of compression, as it should considering coil clash did not occur at the first

shear displacement level with 3.6 inches of compression applied. The S0 point plotted is

the closed length of the K104 compression spring as specified by the manufacturer.

Figure 84 shows how the pure shear load measurements varied for each shear

displacement. The significance of this figure will be elaborated on in the discussion in

Chapter 7.

The results obtained from part 1 of the stage II testing are presented below in

figures 77 through 84. On each figure, the x-axis, y-axis, and z- axis (if applicable) are

clearly labeled. A color legend is provided to the right of each figure. This allows the

various levels of shear displacement applied to be easily distinguished.
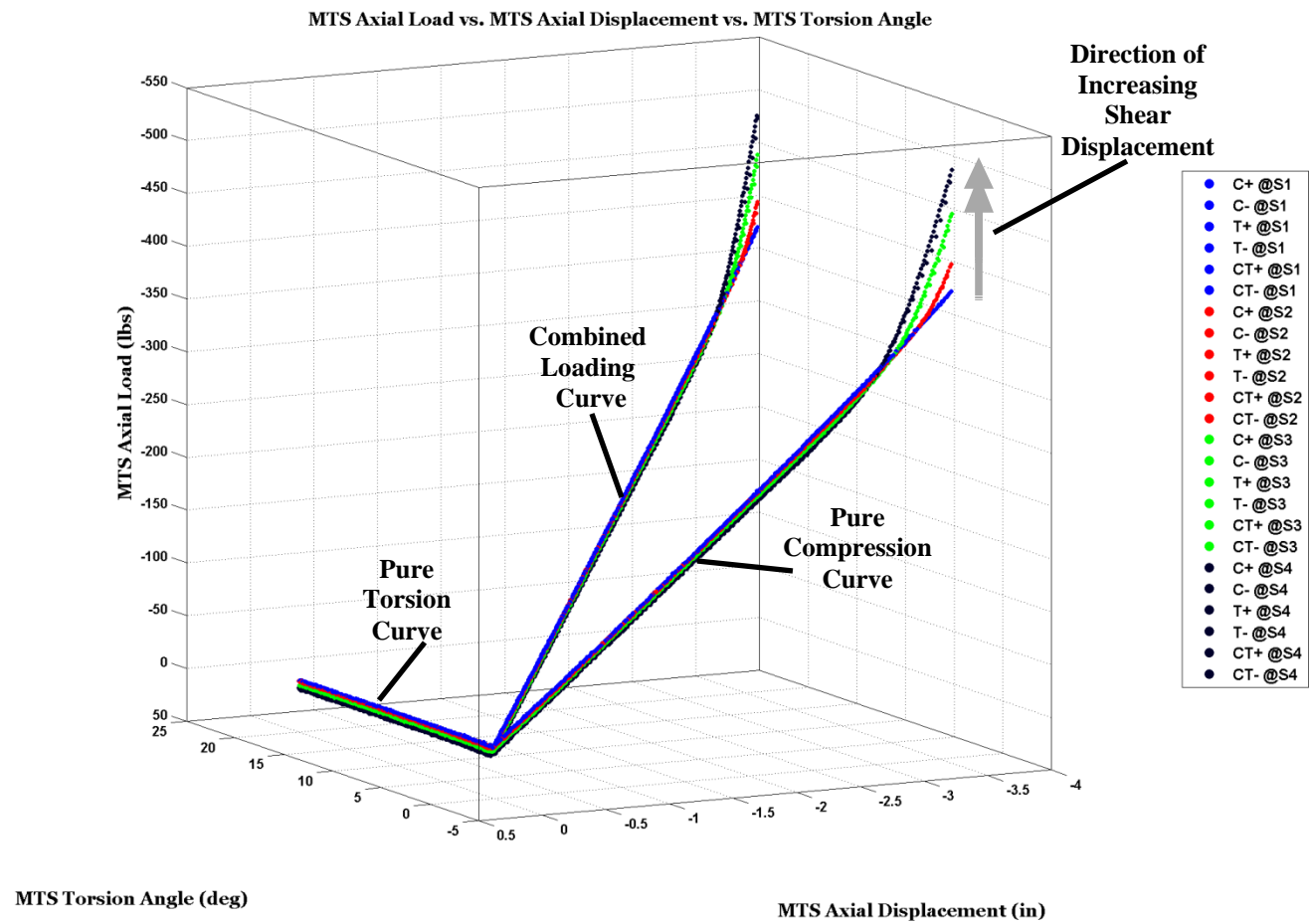
Figure 77: Spring K104 Stage II Axial Load vs. Axial Displacement vs. Torsional Angle
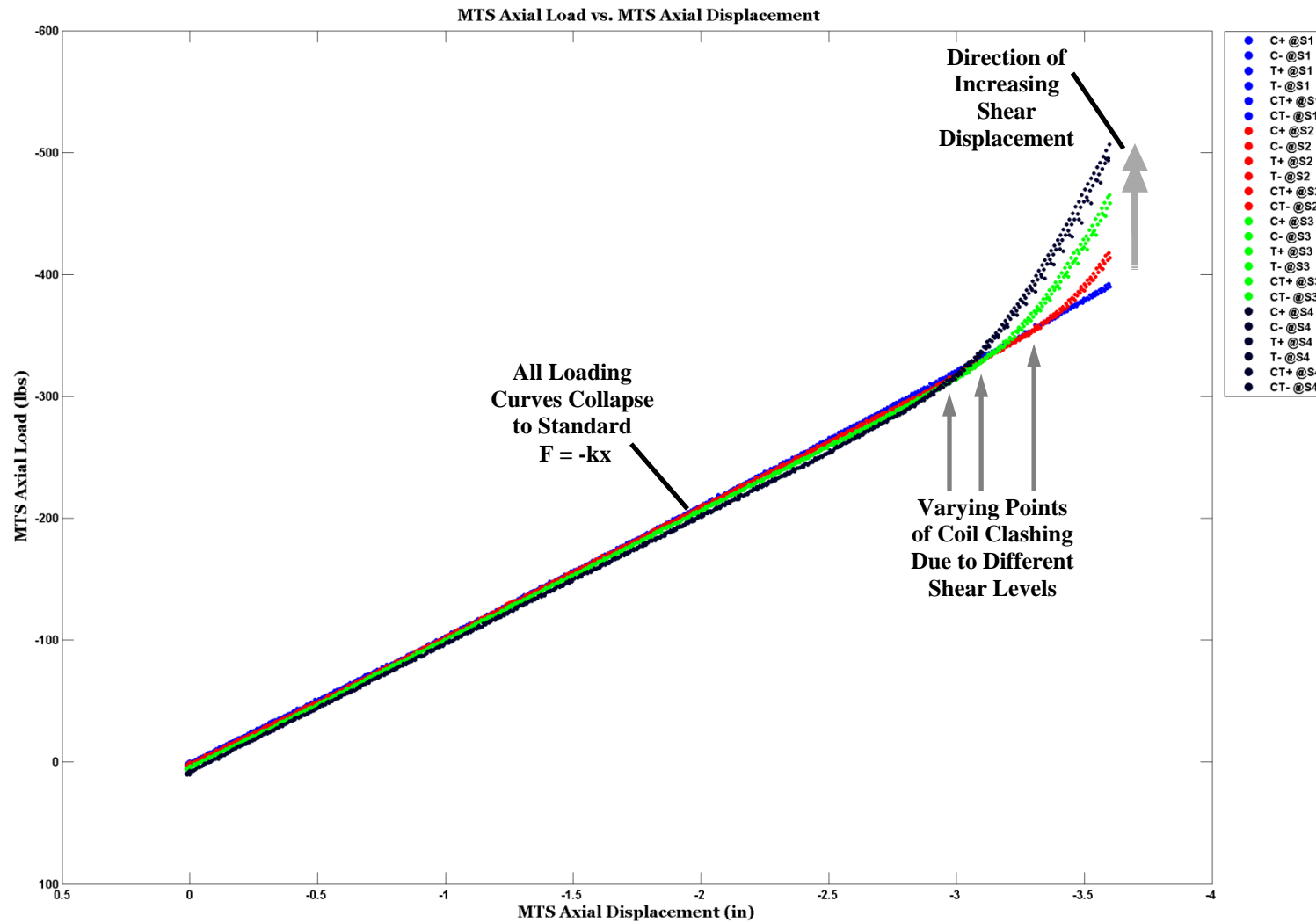
Figure 78: Spring K104 Stage II Axial Load vs. Axial Displacement
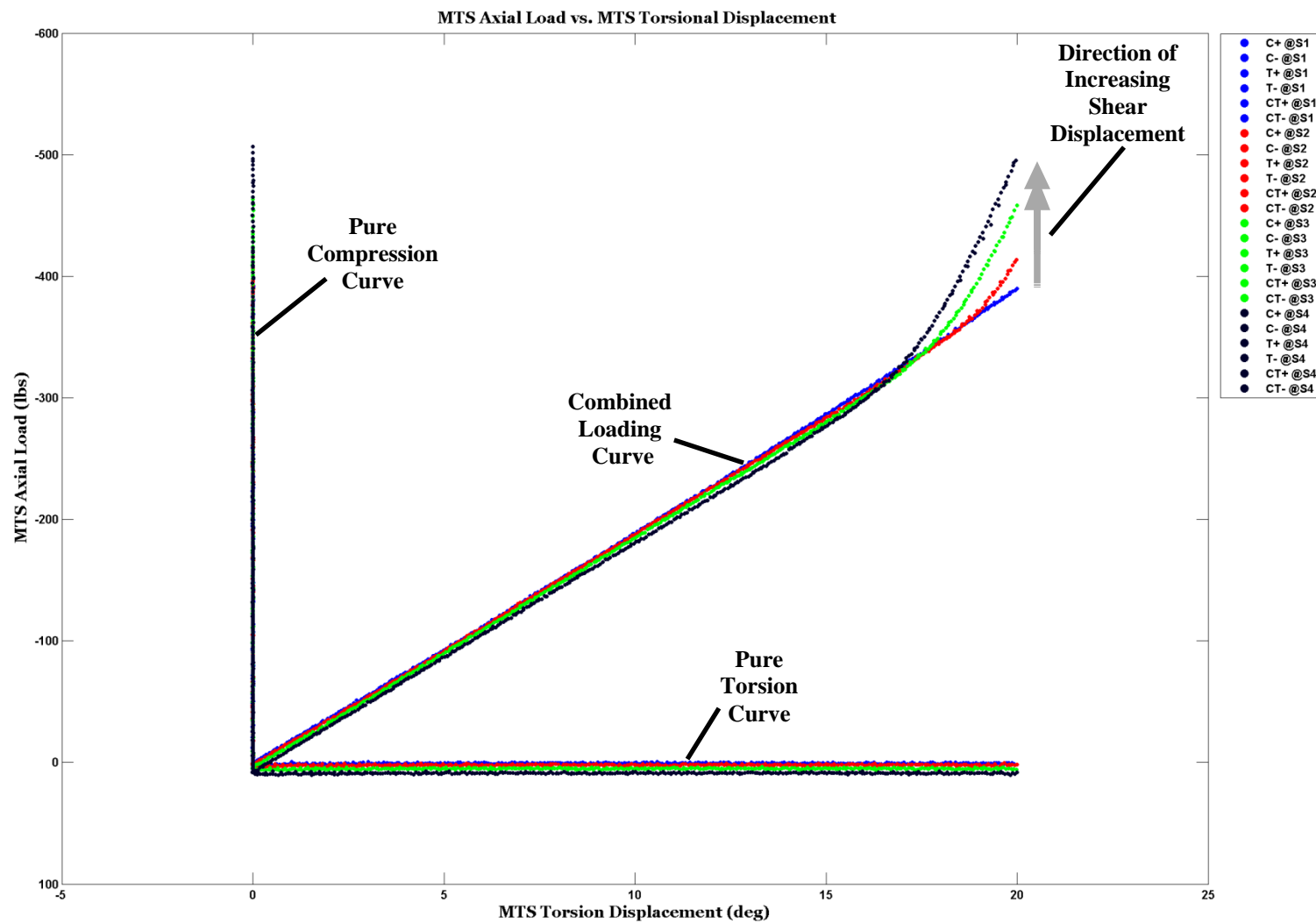
Figure 79: Spring K104 Stage II Axial Load vs. Torsional Angle
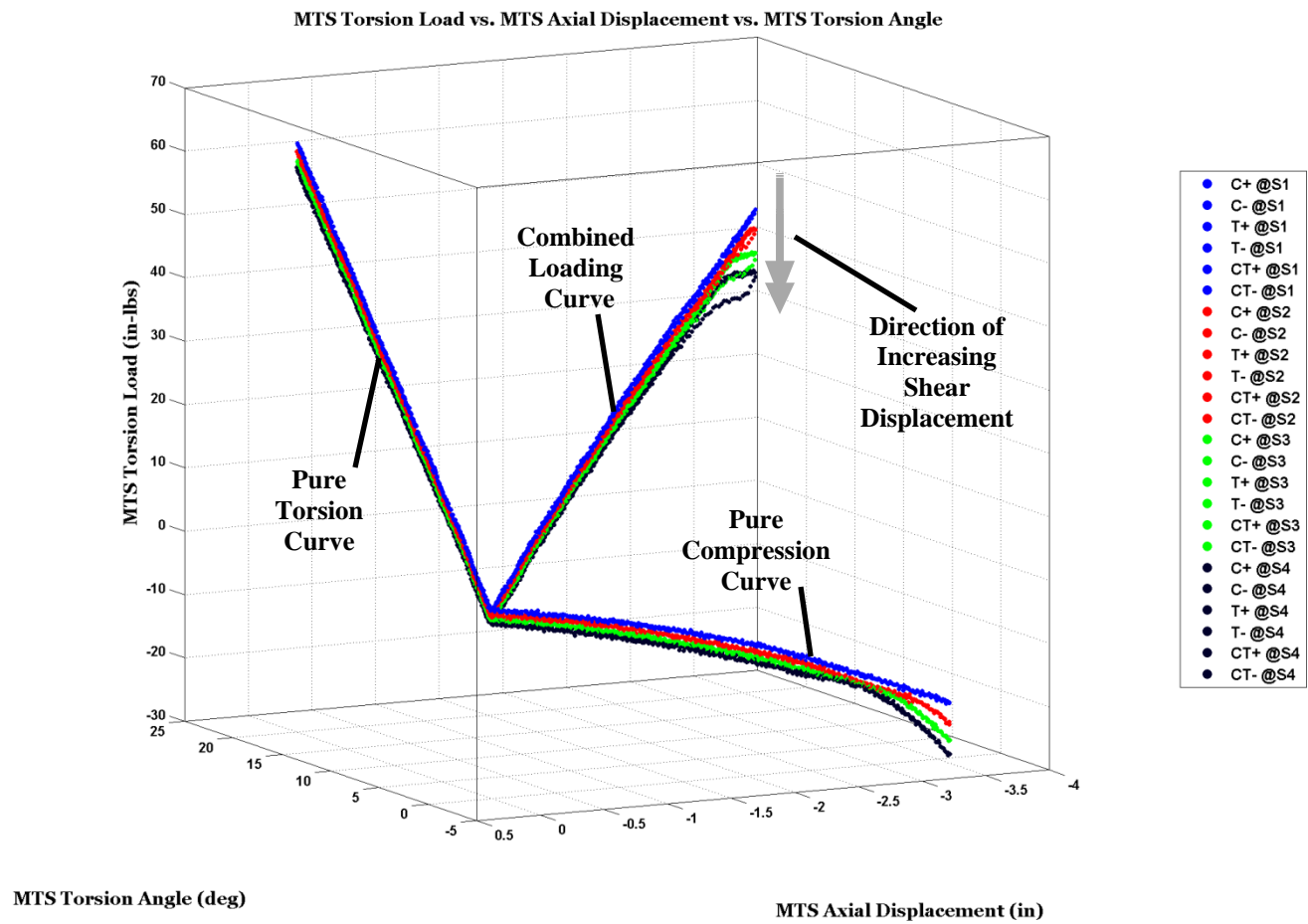
Figure 80: Spring K104 Stage II Torsion Load vs. Axial Displacement vs. Torsional Angle
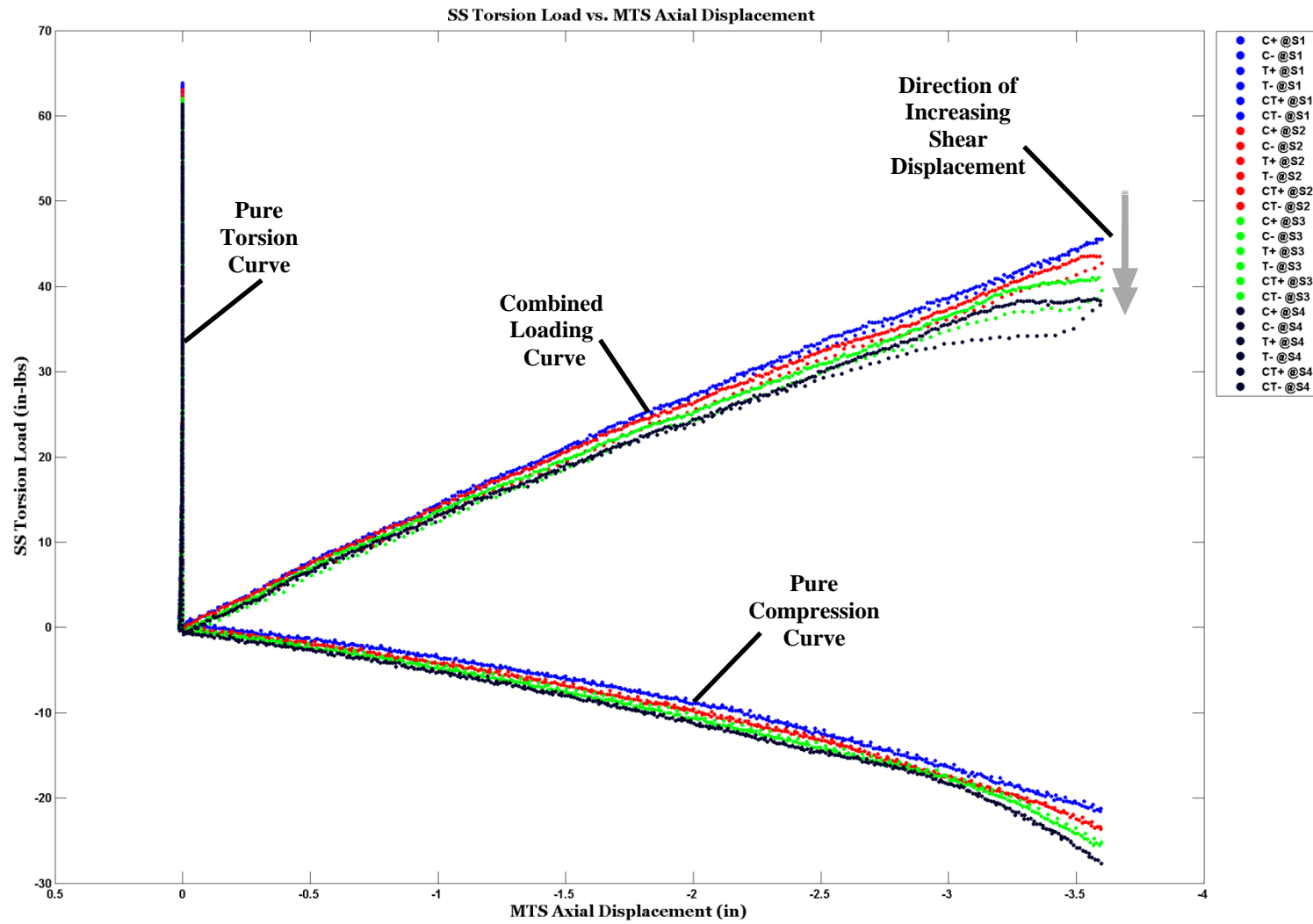
Figure 81: Spring K104 Stage II Torsion Load vs. Axial Displacement
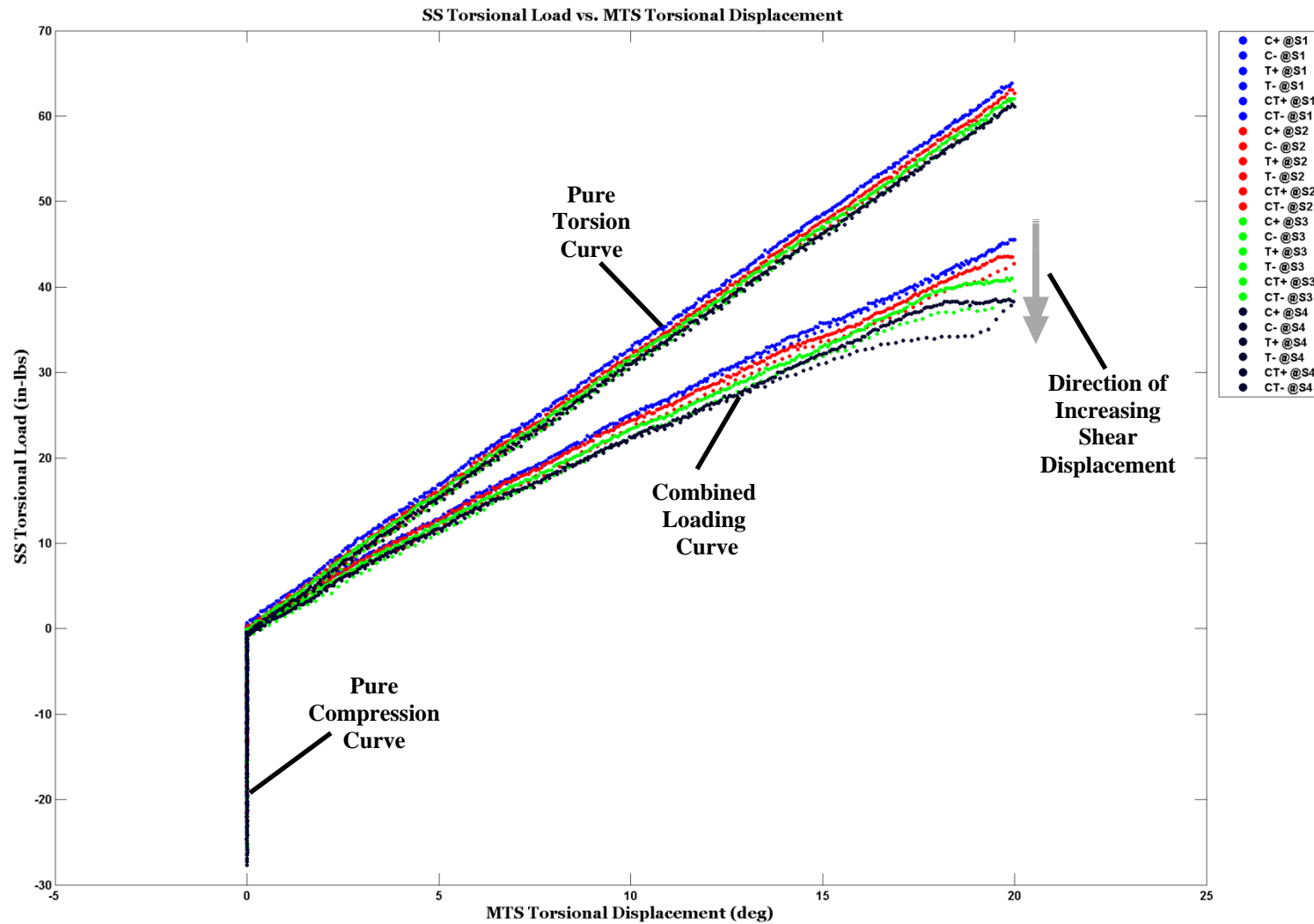
Figure 82: Spring K104 Stage II Torsional Load vs. Torsional Angle
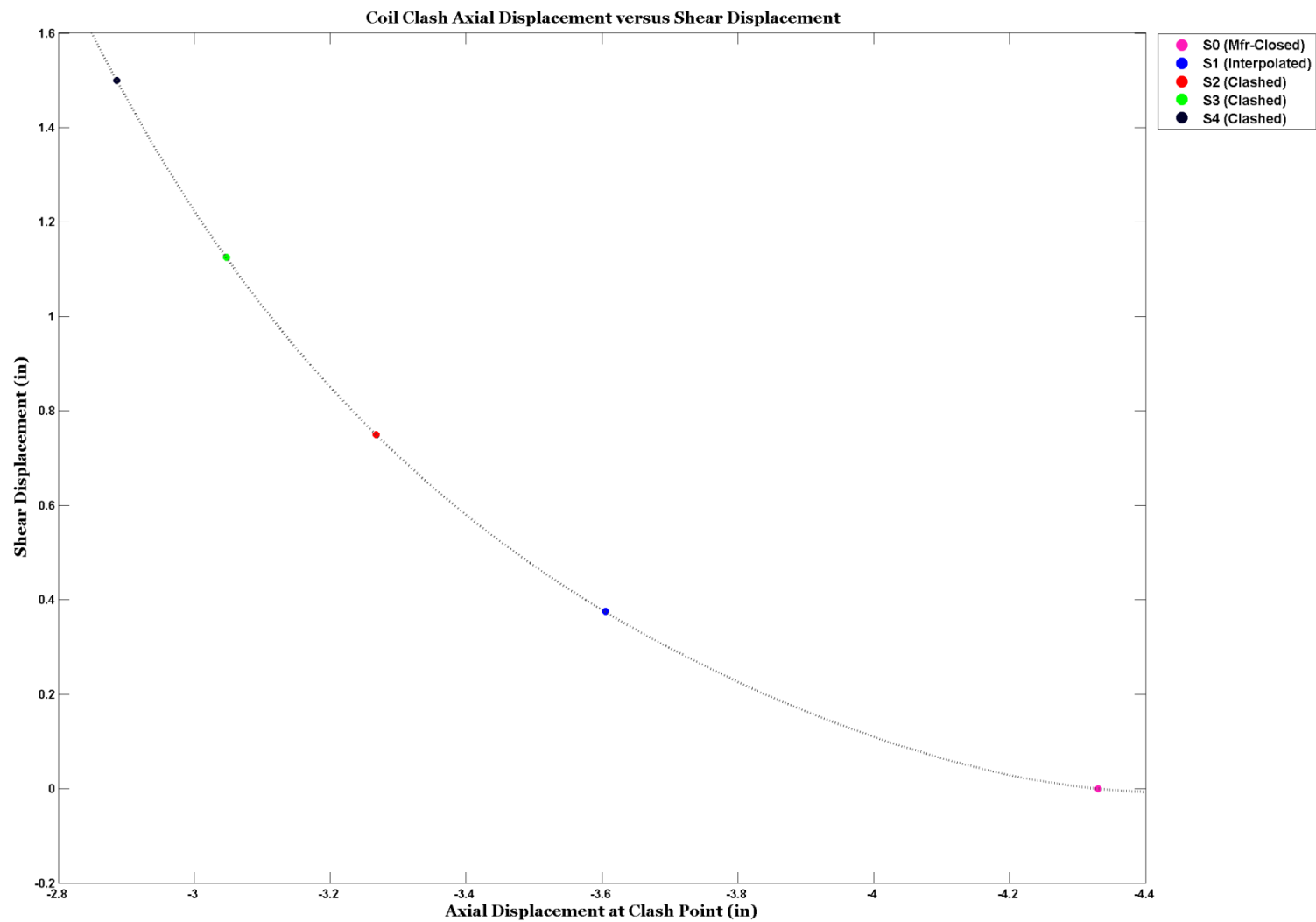
Figure 83: Spring K104 Stage II Shear Displacement vs. Axial Displacement at Coil Clash
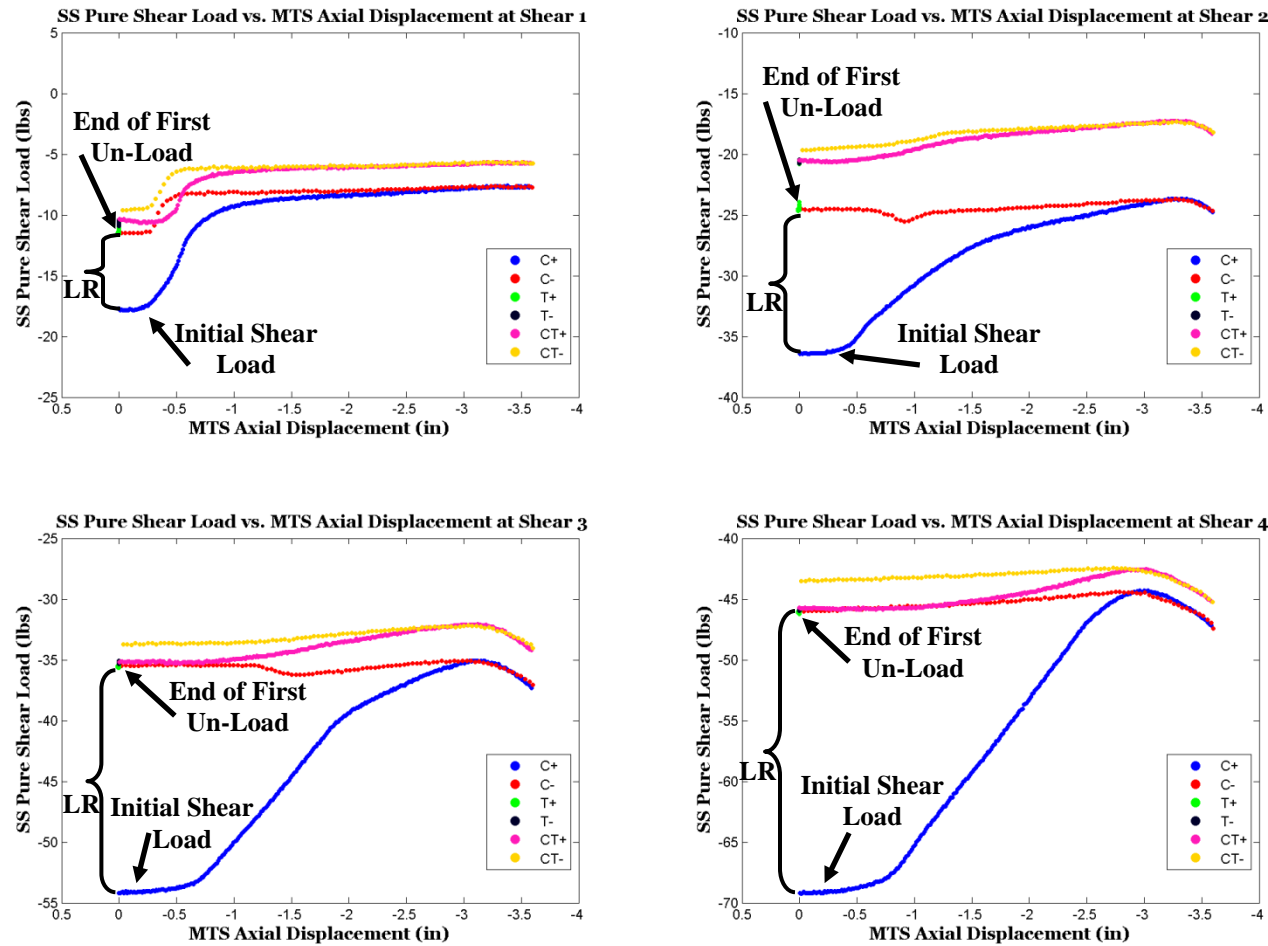
Figure 84: Spring K104 Pure Shear vs. Axial Displacement at Each Shear Level {LR –Load Return Loss}

CHAPTER SEVEN

Discussions and Conclusion

6 Cell –The Custom Six Axis Load Cell

The analysis performed on the raw calibration data for each load axis showed a statistically highly significant linear correlation between the applied load and the output signal for each load channel. These results are summarized in Table 9 in Chapter 6. The root mean square error (RMSE) of each load channel is an estimate of the standard deviation of scatter about the linear model [53]. The standard deviation of scatter about the linear model of the 6 Cell, the RMSE, for each load channel was outstanding (See Table 10). The load measurement error of the 6-Cell for each load channel compared to the calibrated FS load was under 1.5%. It is typically taken in industry that any commercial load cell with load error less than 5% of the full-scale load range is good. The load error of the 6-Cell is less than half of this industry standard. In other words, the 6-Cell's force measurements are outstanding and provide research quality measurements.

The 6 Cell was also validated during the testing process by comparing the force measurements recorded simultaneously by the 6 Cell with the measurements recorded by the MTS load cell. The regression analysis performed on the 6 Cell and the MTS axial loads indicates that the difference in the force measurements is extremely small. The slope of the regression model between the 6 Cell and MTS axial loads was 1.0225. If the slope of the fitted linear model obtained from the regression analysis was equivalent to one it would indicate that the axial force measurements of both the MTS and 6 Cell were statistically the same within the bounds of the 95% confidence interval. This is also true

of the MTS and 6 Cell torsional force measurements, which had a slope of 1.0001. The

RMSE of linear correlation model between the MTS and 6-Cell axial load was 4.6386 lbs

and only 0.6267 in-lbs for the MTS versus 6-Cell torsional load. In short, the 6-Cell's

axial load measurements are within 4.64 lbs of a commercially built and calibrated load

cell. The 6-Cell's torsional load measurements are even better, being within only 0.627

in-lbs of the MTS load cell.

Table 10: Comparison of the RMSE values with the Full-Scale Calibrated Load

6-Cell Channel	Full-Scale Calibrated Load	RMSE	% Error of FS Load
6-Cell Axial Load	500 lbs	3.747 lbs	0.7494%
6-Cell Torsion Load	750 in-lbs	10.169 in-lbs	1.356%
6-Cell Shear X Load	500 lbs	2.0253 lbs	0.4051%
6-Cell Shear Y Load	500 lbs	1.5141 lbs	0.3028%
6-Cell Moment X Load	1890 in-lbs*	7.0189* in-lbs	0.3714%
6-Cell Moment Y Load	1890 in-lbs*	17.387* in-lbs	0.9199%
Transverse S Cell Axial Load	500 lbs	2.4358 lbs	0.4872%
MTS vs. 6-Cell Axial Load	N/A	4.6386 lbs	N/A
MTS vs. 6-Cell Torsion Load	N/A	0.6267 lbs	N/A

* - Denotes values that differ from previous plots. These values have been multiplied by the moment
arm of 3.5 inches to correctly obtain the calibration curve in units of in-lbs.

The results from both the calibration and the validation tests indicate that the

calibration of the 6 Cell was accurate and precise and that the axial and torsional force

measurements of the 6 Cell provided similar output to a professionally constructed and

calibrated load cell. It was therefore assumed that the calibration curves for the

remainder of the loading modes (i.e. shear in the x, shear in the y, moment about the x, and moment about the y) are similarly trustworthy.

The 6 Cell design is simple, efficient, and cost effective. It is possible that the surface finish could be slightly improved reducing some of the noise in the load cell by using higher precision equipment during the construction of the load cell. However, the 6-Cell provided exceptional force measurements, and it is likely that any improvements in noise reduction from using high precision manufacturing tools would only be evident for a significantly smaller load cell design with a very thin wall thickness. By using a full bridge Wheatstone circuit (four gages) design, errors caused by slight misalignments in gage placement were canceled out. Selecting strain gages that have a different strain limit, more specifically, a smaller strain limit for a more strain-sensitive design would improve the design by increasing the load sensitivity. However, the cost of more sensitive strain gages would significantly increase manufacturing costs. For the purposes of most research and the research completed for this thesis, the load error, the RMSE, of the 6-Cell was sufficiently small.

Another design disadvantage was the geometric design of the 6 Cell, a tube, prevented the design from being isotropic. In other words, the design is not capable of providing equal sensitivity for all loading modes. In particular, the 6 Cell is most sensitive to bending loads. The sensitivity to any particular load is determined by the load cell's geometry. For instance, for the 6 Cell the axial stress caused by an axial load of 1000 lbs would be 848.8 lbs/in^2. The bending stress caused by a moment of 1000 in-lbs would be 3184.7 lbs/in^2. Thus the 6 Cell is 3.75 times more sensitive to bending stress than axial stress. The ideal load cell would exhibit approximately equal sensitivity to each load component when an external load is applied. The design process for the 6

Cell did not fully take into account the variable sensitivity to the loads due to the geometry. Because of this, it is likely that the load cell could be optimized to improve the sensitivity differences between each load axis. The sensitivity between each component could be optimized to be closer to equality; however, the bending moment sensitivity will still be greater than the axial, shear, and torsional sensitivities. A more isotropic load cell design would improve the load sensitivity and increase the accuracy of the load cell. On the other hand, isotropic load cells that measure all six load components can be disadvantageous because of the increased design complexity and expense. The 6-Cell design used for this project was efficient, inexpensive, robust, and simple and provided good force measurements.

Analysis of the Testing JIG and Testing Procedure

Design of the Test Jig

The primary goal for the design was to allow the application of shear displacement angular with torsion and axial displacement. The testing jig accomplished these goals; however, some of the limitations and possible solutions will be discussed in the following section.

The testing apparatus that was designed and constructed to allow combined loading tests of compression springs was developed with simplicity and cost in mind. The design was simple to construct and provided an extremely sturdy support frame for mounting and applying shear displacements. However, the simplicity of the design resulted in unanticipated disadvantages when used for the mechanical testing of the compression springs.

As seen in Figure 85 the shear displacement is applied by manually by rotating a threaded rod to displace the dovetail slide. There were a few issues related to applying the shear displacement this way.
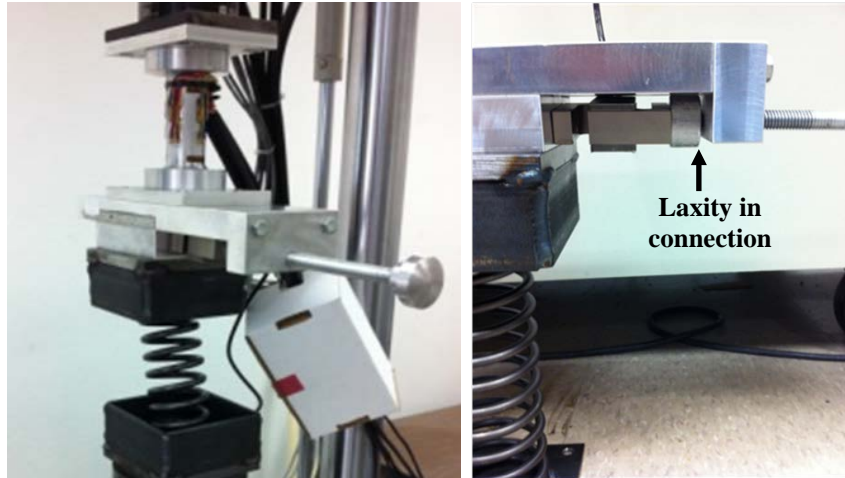
Figure 85: Application of Shear Displacement and Location of Laxity in Shear JIG

The first issue was that during the tests the shear displacement had to be manually applied between each testing phase. This meant that measurements could only be taken at 5 discrete shear intervals rather than along the entire range of application, as was done with the axial and torsional displacements. The test results would be greatly improved if the shear displacement could be applied and removed using an automated actuator. The automation of applying shear displacement would also allow for continuous shear force-displacement curves to be developed. The ability to develop shear force-displacement curves would be beneficial when evaluating the effects of axial and torsional displacements on the shear force response by allowing the user to test the effects of compression on the shear rigidity.

The second issue is that there was a certain level of laxity between the threaded rod and the S–Cell that measured the pure shear force as well as the threaded rod and the

dovetail slide. It is likely that the flexibility between the S–Cell and the threaded rod

introduces error into the pure shear measurements, and is certainly a key factor in another

issue that will be discussed later. The spring was considered a fundamental component

of the shear jig because the spring was required to push back against the shear actuator to

maintain contact between the actuator, S-Cell, and dovetail slide. It was necessary for the

spring to push back against the S–Cell for there to be a viable measurement. It is

uncertain whether or not each spring was capable of providing a sufficient lateral

response to the shear jig because of issues with the jig design. The connection between

the threaded rod and S–Cell needs to be modified to eliminate laxity. If the connection

was rigid and the spring could properly respond to shear displacements, the S–Cell

measurements would be improved.

Validation of Testing Procedure and Testing Jig

The testing procedure and testing jig needed to be robust. The design of the

testing jig was discussed in the previous section. The testing jig provided a sturdy

platform on which to mount a test specimen and to apply axial, angular, and shear

displacements. But in order for the design to be considered truly robust, the test results

need to be repeatable. The results from a repeated measures analysis showed that there

was no statistical significance in the variance of the measured load values for all load

axes. Because of the lack of statistical results showing significance in the variance of the

load measurements over all three trials it was inferred that the test procedure was

repeatable.

The variance seen in the repeated measures results of the S–Cell shown in Figure

72 would seem to be significant. However, the results from the third trail showed

positive readings. Due to the setup of the S–Cell, it is impossible for it to be loaded in

tension. Therefore, the only reason for there to be positive load measurements on the S–

Cell is if the load was not adequately zeroed before the test began.

It should be noted that the repeated measures analysis was performed on only the

stage I test protocol. This is due to issues surrounding the application of the shear

displacement and the ability of the spring to respond correctly once displaced. These

issues will be discussed in detail at the end of the following section.

Stage II Preliminary Test Results

The preliminary stage II test results and an evaluation of the stage II testing

procedure are discussed in this section. The results are considered preliminary because

generalizations regarding only the axial and torsional load responses of a single helical

compression spring are presented. Issues surrounding the reason for why only the axial

and torsional load responses were analyzed will be presented as well as possible solutions

for those issues.

The axial load response behavior of the K104 spring when subjected to combined

loading is presented in Figure 77, Figure 78, and Figure 79 in Chapter 6. The axial force

response of the K104 spring is plotted in Figure 77 against both axial displacement and

torsional angle. Figure 77 illustrates how a torsional displacement up to 20 degrees does

not affect the axial force response of the spring. The pure torsion curve is linear and

causes no change in the axial load. Figure 78 is the 2D axial load versus axial

displacement plot of Figure 77. In Figure 78 the combined loading curve has the same

slope as the pure axial load-displacement curve in this view. This indicates that the

torsional displacement of 20 degrees did not have any effect on the axial load response.

136

This means that a torsional displacement of 20 degrees does not affect the axial stiffness of the K104 spring.

Figure 78 also shows how the shear displacement affects the point at which the spring coils begin to clash. Coil clash is defined as the point when any two adjacent coils come into physical contact with one another. As the amount of shear displacement increases, the amount of compressive displacement possible before coil clash decreases. Figure 79 is the 2D axial load versus torsional angle plot of Figure 77 plots, and also illustrates that a torsional displacement up to 20 degrees does not affect the axial load response. There also appears to be a slight amount of axial load offset as the shear displacement increases. This is clearly seen in Figure 79 in the pure torsion curve. Further testing is required to determine whether or not the shear displacement has an effect on the axial load.

The torsional load response behavior of the K104 spring subjected to combined loading is shown in Figure 80, Figure 81, and Figure 82 in Chapter 6. Figure 80 is the 3D plot that illustrates the torsional load response to both axial and torsional displacements. Figure 81 and Figure 82 are then the torsional load versus axial displacement and torsional load versus torsional angle 2D plots of Figure 80 respectively. The most interesting result seen in these figures is the affect that 3.6 inches of compression has on the torsional load, clearly seen in Figure 81. As illustrated by the pure compression curve, a compressive displacement of 3.6 inches caused a winding torque response of approximately 20 in-lbs in the K104 compression spring. This result is not entirely unexpected. A compressive displacement causes the coil diameter of the spring to enlarge. The change in the coil diameter causes a responsive effect, resulting in the 20 in-lbs winding torque response. The shear displacement again appears to have a minor

137

offset effect on the torsional load as it did with the axial load; however, without further testing it cannot be assumed that a shear displacement affects the torsional load.

It was clearly illustrated in Figure 78 that the amount of shear displacement affected the amount of axial displacement that could be applied before coil clash. Typically, engineers design components that use springs in a manner that will prevent the coils from clashing in this manner. Because of this practice published data regarding the affect of shear displacement on the axial displacement coil clash point could not be found in literature searched using the Academic Search Complete, Engineering Village 2, ScienceDirect, and Web of Science databases. Figure 83 shows that there does appear to be a trend between the amount of shear displacement and the amount of axial displacement before coil collision occurs for the K104 spring. This trend could be fitted by a polynomial equation, and could be verified by further testing. This trend warrants further investigation by analyzing additional springs and looking for a common shear displacement and axial coil clash displacement trend for springs with similar slenderness ratios, spring indices, or critical buckling loads.

Testing JIG Issues and their affect on the Stage II Results

Some of the issues regarding the testing jig design have been discussed already. However, the effect of these issues, additional concerns, and possible solutions need to be discussed. The testing jig successfully allowed the application of shear displacements in combination with axial and torsional displacements. It did not however successfully allow for the measurement of pure shear force. Figure 84 illustrates the inability to properly maintain pure shear force measurements during the stage II testing procedure. In between the plots of each stage II test phase, the pure shear force measured by the S–

138

Cell diminished. The bracketed zones shown in Figure 84 show the amount of load return loss that occurred from the first compression curve at each shear level. The load should return to its initial level once the compression is removed, but this is not the case. Once the load was lost (i.e. could no longer be measured by the S–Cell) it did not return.

There are several reasons for the loss in the shear load after the compression curve was performed. The first issue lies with the connection between the threaded rod and the S–Cell. The laxity between the threaded rod and the S–Cell was previously discussed, and it is partially because of this laxity that there are issues with the pure shear measurements. The testing jig was designed with the assumption that the lateral response of the spring would be sufficient to maintain a stable connection between the S–Cell and the threaded rod. Without a stable connection between the S–Cell and the threaded rod, the load cannot be accurately measured. The only pure shear load reading that can be used from the current stage II data is the initial shear load measurement.

The design of the slide itself caused issues with not only the ability to maintain a stable connection between S–Cell and the threaded rod, but also other issues that affected the bending and shear reading from the 6 Cell. The dovetail slide and slider were designed to be simple, sturdy, and efficient at applying a known shear displacement. The design was simple, cost effective, and provided a sturdy connection between the load cell and the compression spring; however, the design failed to account for the stiction (static friction threshold) between the dovetail slide and the dovetail base.

During the testing of the compression springs, the axial force increased. This increased the static friction threshold between the dovetail slide and base. The dovetail base and slide were lubricated before each test; however, the stiction was still significantly high enough to prevent the lateral response in the spring. For the K104

spring, an axial compressive displacement of just 0.5 inches was enough to prevent the spring from returning to zero shear displacement when the threaded rod was back off from the S–Cell. As a result, the pure shear force measured by the S–Cell did not return to the initial load level and was considered to be untrustworthy.

The ability of the testing jig to transfer the spring's responsive loads correctly to the load cell is also a problem. In particular, the ability of the testing JIG to correctly transfer the shear and moment loads to the 6-Cell is concerning. As shown in Figure 86, when the compression spring was displaced laterally, there was both a shear and moment response. The load cell should ideally read the same initial shear force that the S–Cell is reading, and there should also be a moment about the axis orthogonal to the shear load. However, the shear load for the 6 Cell began each test at zero and did not reach the initial load of the S–Cell until the end of the compression curve. When a compression curve was performed, the moment would also linearly decrease until the moment value changed direction. The graphs of the 6 Cell's shear and moment forces in Stage II can be found in Appendix H.
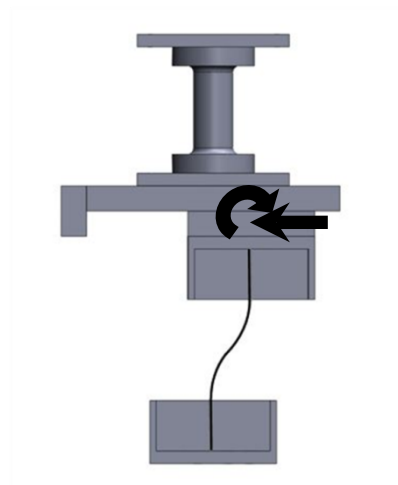
Figure 86: Side view of testing Jig with 1.5 in of shear displacement

The assumption is that, due to the way the dovetail slide is mounted with respect to the 6 Cell and because of the stiction between the dovetail slide and base, the load is not correctly transferred from the end of the spring to the 6 Cell. The moment is artificially high because of the testing JIG setup, and the shear force is affected by the stiction. These various issue together caused the 6 Cell's shear and moment force measurements to be unexpected.

There are several possible solutions for each testing JIG issue that was encountered. The issue with the 6 Cell not experiencing the true load responses of the compression springs could be solved by adjusting the overall testing apparatus setup. Now that the 6 Cell axial and torsional load channels are calibrated and validated against the MTS reading, the 6 Cell can be moved. The 6 Cell could be moved to either end of the helical compression springs. The spring's end plate could be mounted directly to the load cell. This would help ensure that the 6 Cell measures the response forces directly at the end of the spring and thus eliminate any concerns about proper load transfer through additional levels of test jig. With the 6 Cell moved, the spring's response can be measured by the 6 Cell, and the in-line axial and torsional loads could be measured by the MTS load cells.

Modifying the housing that the springs are mounted in to be flat plates with no side walls would allow the spring to be laterally displaced further without colliding with the sidewalls of the mount housings. The mount housings limit the level of shear and compressive displacement. The 1.5 inch maximum of shear displacement was selected partially because at 2 inches of shear displacement the coils of the springs would clash with the sidewall of the housings. The shear displacement was also limited by the ability to manually apply the shear. At shear displacements over 1.5 inches, manual application

of shear displacement was difficult. The use of flat mounting plates would also allow for a complete visualization of the spring's deformation under combined loads. The addition of a micrometer to measure the amount of shear displacement would increase the accuracy of any shear displacement made by hand as well.

The most important changes that need to be completed to the testing jig are the development of another jig to apply the shear displacement and the automation of the shear displacement. The dovetail slide was sturdy but introduced excessive friction forces. The resulting stiction inhibited the lateral response of the compression springs. The most logical solution would to use a roller-slide setup that is rated to withstand the expected compressive and torsional forces. Using a roller setup would greatly decrease the amount of friction greatly reducing the contact surface area. The shear displacement needs to be automated as well. Automating the shear displacement could be achieved with the use of a high precision threaded rod and a servomotor. The servomotor could be controlled by the MTS system through the use of the auxiliary outputs. If the shear displacement was automated, the stage II protocol could easily be modified to mimic the stage I protocol. The modified stage II protocol would provide more data regarding the effects of axial and torsional displacements on the lateral stiffness.

The testing JIG was successful in allowing for the addition of shear displacement, but due to the other issues associated with the design, it was not completely successful. The design concept behind the testing JIG is not the problem, but rather the implementation of the design through the use of a dovetail slide was the problem. The dovetail design introduced too many test issues.

Conclusion

The work completed in this thesis has setup a means of evaluating helical compression springs displaced three-dimensionally. The design and calibration of a cost effective, simple, and effective 6 axis load cell (6-Cell) was presented. The 6-Cell provided research quality force measurements that are comparable to commercial load cells. A new testing apparatus was developed and used to apply axial, torsional, and shear displacements simultaneously to a helical compression spring. Recommendations regarding the design of the testing jig were presented. The testing jig can be modified according to those recommendations to provide a final testing jig configuration that will provide a means to measure the 3D force response of helical compression springs.

Additionally, the testing procedure developed and presented can be modified to allow for a more in-depth analysis on the effects of shear, axial, and torsional displacement on the behavior of helical springs. Mechanical test results of a single helical compression spring (K104) were presented. These results indicated that an angular rotation of ±20 degrees did not have an effect on the axial response of a helical compression spring. It was shown that for the K104 spring a compressive displacement of 3.6 inches did affect the torsional force-response of the spring. For the spring tested, compression induced a winding torque response from the spring. Shear displacement up to 1.5 inches did not affect the axial response of the spring, but did affect the point of coil clash during compression. A reduction in the amount of axial compression that could be applied before two adjacent coils clashed evident, and a possible trend in the amount of shear displacement to axial displacement describing the point of coil clash was seen.

By making the appropriate adjustments recommended in this thesis, more helical compression springs can be mechanically testing. The results from these tests could be

used to validate Wahl's theoretical models for helical spring behavior. The data from the mechanical tests could also be provided to other researcher to validate other models used to describe the response of helical compression springs. Finally, the development of a fast, simple computation model could be developed that could aid in the development of a Stewart platform that utilizes helical compression springs.

APPENDICES

APPENDIX A

Load Cell Construction Procedure

Pre-Construction

1. Make Load Cell Structure. Choose material properties and load cell structure dimensions accordingly with expected loads during use.
2. Place strain gage alignment marks on the load cell structure. It is recommended that latex gloves be used from this point forward to keep the surface of the load cell clean.

Surface Prep

1. Condition load cell surface with Vishay M-Prep Conditioner A. Do not forget to use proper latex gloves during this procedure and all following steps.
2. Sand surface with 400-500 rated grit paper to condition and prepare surface for strain gage adhesive.
3. Neutralize surface with Vishay Neutralizer 5A.
4. Wipe, in a unidirectional motion, the surface dry with a gauze sponge cloth.
5. Re-wet surface with small amount of neutralizer. Then using uncontaminated cotton tips, wipe firmly with a unidirectional motion until surface is dry. Take care to not contaminate surface by wiping with a used cotton tip.
6. Repeat Surface Prep step #5 until cotton tips show no visible signs of dirt/grease or other contaminates.
7. Wipe surface dry with gauze cloth again.
8. Mask off any surface area that will need to remain clean of adhesive in order to place future strain gages.

Gage Placement

1. Remove strain gage from packaging and place the matrix/solder tabs face up on chemically clean glass using a pair of clean tweezers to prevent any oils or contaminants from getting on the strain gage or load cell surface.
2. Using Mylar tape strip cover 25-50% of the gage matrix and all of the solder tabs.
3. At a low angle, peel the tape and strain gage combination off the glass surface.
4. Align the gage carefully with the alignment marks placed on the load cell surface earlier with the indicator marker on the gage.
5. Place the strain gage/tape the strain gage, into position on the load cell surface. It is recommended that the user create a small pull-tab on the tape by folding a small amount of the tap onto itself. This will allow the user to remove the tape easily without risk of damaging gage or load cell surface after adhesive is cured.

6. If building a multi-axis load cell, complete Gage Placement steps #1-#5 for the gage 180 degrees from the first gage placed on the load cell surface.
7. In a similar manner to Gage Placement step #3, peel back the tape with the gage attached until the entire under surface of the strain gage is exposed, yet the tape is still in position and taped to the load cell surface.
8. Apply M-Bond 400 adhesive according to Vishay instructions to the back of the strain gage, without touching tape surface, and to the load cell surface. Apply adhesive to both gages if more than one gage is to be placed at one time.
9. Wait for 10 minutes for the adhesive to begin to dry.
10. Re-tape the gage(s) down and check that the alignment is still within tolerances.

Adhesive/Gage Curing

1. Once the gage(s) is re-taped and alignment is confirmed, take a piece of Teflon film that is larger than the entire strain gage and tape it over the gage(s) to be cured.
2. Place a second piece of Teflon tape over the first. Do NOT tape the second piece down.
3. Place a properly sized piece of silicon padding over the second piece of Teflon tape.
4. Place metal bracket/clamping piece over the silicon pad.
5. Clamp down metal/Teflon/Teflon assemble over the strain gage. Choose an appropriate pressure according to specifications from Vishay M-Bond 400 instructions.
6. Take load cell structure with gage(s) clamped in place and put the load cell into a COLD furnace.
7. For M-Bond 400, heat furnace from COLD to 150 degrees C, approximately 300 degrees F.
8. Once furnace reaches cure temperature of 150 degrees C, begin a one-hour timer.
9. After one hour, turn off furnace and open furnace door.
10. Let load cell cool down to room temperature before any additional work is performed. This may take several hours.
11. Once at room temperature, remove the clamps, metal, and Teflon carefully from over the strain gages.
12. Carefully pull back and remove the tape from over the strain gage. Check that all corners of the gage are firmly glued to the load cell surface.
13. Either tin the solder tabs of the strain gages attached to the load cell surface or use the Mylar tape to cover the solder tabs. This will prevent adhesive from covering the tabs preventing a proper electrical connection once other gages are placed onto the surface.
14. It may be necessary to carefully re-clean the surface of the load cell where other gages are to be placed after gages have been cured onto the surface due to the flow of the adhesive during the curing process. To do so, never apply neutralizer to the surface directly, but rather to the cotton tips or sand paper. Take care to adequately cover gages already cured to prevent damage to the strain gages.

Following Gage Placement

1. If surface was re-cleaned, then mask off any areas that need to remain clear of glue for gage placement later.
2. Return to Gage Placement step #1. Follow procedure accordingly until current gage is properly cured.
3. Repeat process until all strain gages have been placed onto the surface of the load cell, cured, and tinned with solder.

Wiring

1. Using an appropriate wire size, follow the wiring diagrams provided in the appendix.
2. It is recommended that zip-ties are used along with heat shrink to keep the wires from being difficult to deal with and to make trouble-shooting easy.
3. Wire shielding could be included around the wires inside the heat shrink if necessary. This wire shielding would then need to be grounded.

APPENDIX B

Mechanical Horse Specifications

Purpose:

- The mechanical horse shall produce rotational and translational movement that can be used for physical therapy.
-

Performance Specifications:

- The mechanical horse will repeat simulated equine gait cycles with cycle periods that vary down to a minimum of 1.2 seconds.
- Three non-collinear points fixed to the moving riding surface of the mechanical horse will track the three-dimensional movements of corresponding points on the saddle of a therapeutic horse to within a maximum, absolute deviation of 1 cm over a full gait cycle, based on comparison between experimental motion capture data recorded and provided by Dr. Garner from a live horse, and experimental motion capture data recorded from the mechanical horse.
- The mechanical horse will remain upright and stationary when up to 50 lbs of lateral force is applied at the highest point of the saddle.

Design Specifications:

- A maximum of 50 lbs force will be required to move the mechanical horse along the floor.
- The mechanical horse will operate using only one motor.
- The mechanical horse will be powered by U.S. standard 120 V at 60 Hz wall outlet.
- The mechanical horse will have a seat and will be able to accommodate the use of a saddle over the seat.
- The mechanical horse will have adjustable stirrups.
- The mechanical horse will have at least one handle that can be utilized by the user to aid in stability.
- The mechanical horse will be no higher than 4 feet and no longer than 6 feet.
- The mechanical horse will be no wider than 2.5 feet when in transport and 4 feet when stationary and in use.
- The mechanical horse will be able to carry a user load of at least 250 lbs. while meeting the performance specifications.
- The mechanical horse will be equipped with at least one safety mechanism for emergency stop situations.
- To protect the user from accidental exposure to internal moving parts of the mechanical horse, a shielding surface fixed to and moving with the saddle component will overlap a shielding surface fixed to the base structure by at least 10 inches, with the closest gap spanning between the shields being no less than 2 inches at the minimum point, and no more than 6 inches at the maximum point.
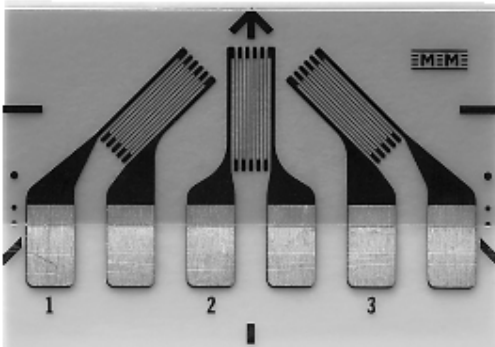
APPENDIX C

Strain Gage Specifications

General Purpose Strain Gages - Rectangular Rosette

GAGE PATTERN DATA

actual size

GAGE DESIGNATION See Note 1	RESISTANCE (OHMS)	OPTIONS AVAILABLE See Note 2
CEA-XX-125UR-120 CEA-XX-125UR-350	120 ± 0.4% 350 ± 0.4%	P2

DESCRIPTION

General-purpose 45° single-plane rosette. Compact geometry. Exposed solder tab area 0.08 x 0.06 in [2.0 x 1.5 mm].

GAGE DIMENSIONS		Legend:	ES – Each Section S – Section (S1 – Sec 1)	CP – Complete Pattern M – Matrix	Inch millimeter

Gage Length	Overall Length	Grid Width	Overall Width	Matrix Length	Matrix Width
0.125 ES	0.300 CP	0.060 ES	0.560 CP	0.42	0.62
3.18 ES	7.62 CP	1.52 ES	14.22 CP	10.7	15.7

GAGE SERIES DATA
See Gage Series data sheet for complete specifications.

Series	Description	Strain Range	Temperature Range
CEA	Universal general-purpose strain gages.	±5%	−100° to +350°F [−75° to +175°C]

Note 1: Insert desired S-T-C number in spaces marked XX.
Note 2: Products with designations and options shown in bold are not RoHS compliant.

Disclaimer

All product specifications and data are subject to change without notice.

Vishay Precision Group, Inc., its affiliates, agents, and employees, and all persons acting on its or their behalf (collectively, "Vishay Precision Group"), disclaim any and all liability for any errors, inaccuracies or incompleteness contained herein or in any other disclosure relating to any product.
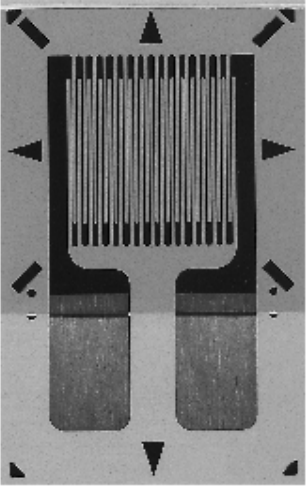
Vishay Precision Group disclaims any and all liability arising out of the use or application of any product described herein or of any information provided herein to the maximum extent permitted by law. The product specifications do not expand or otherwise modify Vishay Precision Group's terms and conditions of purchase, including but not limited to the warranty expressed therein, which apply to these products.

No license, express or implied, by estoppel or otherwise, to any intellectual property rights is granted by this document or by any conduct of Vishay Precision Group.

The products shown herein are not designed for use in medical, life-saving, or life-sustaining applications unless otherwise expressly indicated. Customers using or selling Vishay Precision Group products not expressly indicated for use in such applications do so entirely at their own risk and agree to fully indemnify Vishay Precision Group for any damages arising or resulting from such use or sale. Please contact authorized Vishay Precision Group personnel to obtain written terms and conditions regarding products designed for such applications.

Product names and markings noted herein may be trademarks of their respective owners.

General Purpose Strain Gages - Linear Pattern

GAGE PATTERN DATA

GAGE DESIGNATION See Note 1	RESISTANCE (OHMS)	OPTIONS AVAILABLE See Note 2
CEA-XX-125UW-120	120 ± 0.3%	**P2**
CEA-XX-125UW-350	350 ± 0.3%	**P2**

actual size

DESCRIPTION

General-purpose gage. Exposed solder tab area 0.10 x 0.07 [2.5 x 1.8 mm]. See also 125UN pattern.

GAGE DIMENSIONS — Legend: ES = Each Section, S = Section (S1 = Sec 1), CP = Complete Pattern, M = Matrix — inch / millimeter

Gage Length	Overall Length	Grid Width	Overall Width	Matrix Length	Matrix Width
0.125	0.325	0.180	0.180	0.42	0.27
3.18	8.26	4.57	4.57	10.7	6.9

GAGE SERIES DATA — See Gage Series data sheet for complete specifications.

Series	Description	Strain Range	Temperature Range
CEA	Universal general-purpose strain gages.	±5%	−100° to +350°F [−75° to +175°C]

Note 1: Insert desired S-T-C number in spaces marked XX.
Note 2: Products with designations and options shown in bold are not RoHS compliant.

www.micro-measurements.com   For technical questions, contact: micro-measurements@vishaypg.com   Document Number: 11241
38   Revision: 28-Jan-10

152

Disclaimer

153

S–Cell Manufacturer's Specifications

BSA

Features

- S-Type Load Cell
- Alloy Steel
- Easy to Install, Stable & Reliable
- Suitable for Tension Measurement, Batching Scales and Batching Systems,etc.
- Rated up to IP67
- Equivalent to: Rice Lake RL20000 & Artech 20210

Dimensions

Capacity		A	B	C	D	E	L	M
50 - 300 lb	in	2.32	2.00	1.00	0.65	0.50	2.50	1/4"-28 UNF
	mm	59.0	50.8	25.4	16.5	12.7	63.5	
500 - 1000 lb	in	3.27	2.00	1.00	1.10	0.75	2.50	1/2"-20 UNF
	mm	83.0	50.8	25.4	28.0	19.0	63.5	

1

BSA
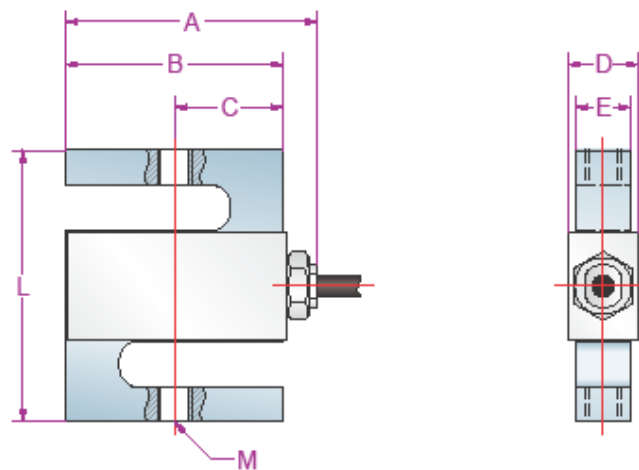
Schematic

Red: + excitation
Black: − excitation
Green: + signal
White: − signal
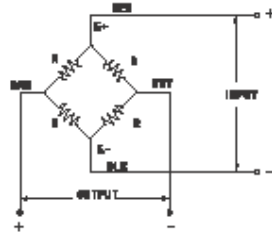
Capacities / Model

50 lb	BSA-50
100 lb	BSA-100
200 lb	BSA-200
500 lb	BSA-500
1,000 lb	BSA-1k

Specifications

Rated Output	3.05mV/V ±1.64%
Zero Balance	± 1% of rated output
Creep after 30 minutes	±0.03% of rated output
Nonlinearity	±0.03% of rated output
Hysteresis	±0.03% of rated output
Repeatability	±0.03% of rated output
Temp. effect on output	≤0.002% of applied output/°C
Temp. effect on zero	≤0.002% of rated output/°C
Safe Temp. Range	-10°C to + 70°C
Temp. Compensated	-10°C to + 50°C
Safe Overload	150%
Input Impedance	387ohm ± 5 ohm
Output Impedance	350 ohm ± 3 ohm
Insulation Resistance	≥5000 M ohm (50V DC)
Rated Excitation	10V DC/AC
Maximum Excitation	15V DC/AC
Cable Length	20 ft (6 m)
Cable Color Code	Red(+E) Black(-E) Green(+S) White(-S)

Version 1.6, 03/12/09

YOUR AUTHORIZED TRANSCELL DEALER IS:

Specifications and features subject to change without notice.

2

VISHAY
PRECISION
GROUP

Instruction Bulletin B-130

Micro-Measurements

M:ME®

Strain Gage Installations with
M-Bond 43-B, 600, and 610 Adhesive Systems

INTRODUCTION

Micro-Measurements M-Bond 43-B, 600, and 610 adhesives are high-performance epoxy resins, formulated specifically for bonding strain gages and special-purpose sensors. When properly cured, these adhesives are useful for temperatures ranging from -452° to +350 °F [-269° to +175 °C] with M-Bond 43-B, and to +700 °F [+370 °C] for short periods with M-Bond 600 and 610. In common with other organic materials, life is limited by oxidation and sublimation effects at elevated temperatures. M-Bond 43-B is particularly recommended for transducer applications up to +250 °F [+120 °C], and M-Bond 610 for transducers up to +450 °F [+230 °C].

For proper results, the procedures and techniques presented in this bulletin should be used with qualified Micro-Measurements installation accessory products (refer to Micro-Measurements Strain Gage Accessories Databook). Accessories used in this procedure are:

CSM Degreaser or	CSP-1 Cotton Applicators
GC-6 Isopropyl Alcohol	MJG-2 Mylar® Tape
Silicon-Carbide Paper	TFE-1 Teflon® Film
M-Prep Conditioner A	HSC-X Spring Clamp
M-Prep Neutralizer 5A	GT-14 Pressure Pads and
GSP-1 Gauze Sponges	Backup Plates

MIXING INSTRUCTIONS

Since M-Bond 43-B is a solvent-thinned, precatalyzed epoxy mixture, it is applied at room temperature directly as received. The M-Bond 600 and 610, on the other hand, are two-component systems. These must be mixed as follows:

1. Resin and curing agent bottles must be at room temperature before opening.

2. Using the disposable plastic funnel, empty contents of bottle labeled "Curing Agent" into bottle of resin labeled "Adhesive". Discard funnel.

3. After tightening the brush cap (included separately), thoroughly mix contents of this "Adhesive" bottle by vigorously shaking it for 10 seconds.

4. Mark bottle with date mixed in space provided on the label.

Allow this freshly mixed adhesive to stand for at least one hour before using.

SURFACE PREPARATION

The extensive subject of surface preparation techniques is covered in Application Note B-129. Metal surface cleaning procedures usually involve solvent degreasing with either CSM Degreaser or GC-6 Isopropyl Alcohol, abrading, and cleaning with M-Prep Conditioner A, followed by application of M-Prep Neutralizer 5A. When practical, these preparation procedures should be applied to an area significantly larger than that occupied by the gage. Surfaces should be free from pits and irregularities. Porous surfaces may be precoated with a filled epoxy, such as M-Bond GA-61, which is then cured and abraded.

SHELF LIFE AND POT LIFE

At room temperature, M-Bond 600 has a minimum storage life of three months, while M-Bond 43-B and M-Bond 610 will last a minimum of nine months.

Once opened and mixed, M-Bond 600 and 610 have room-temperature pot lives of two weeks and six weeks, respectively. Since M-Bond 43-B is supplied already mixed, its pot life is about the same as its shelf life when kept in a tightly closed container.

These periods of adhesive usefulness can be increased by refrigeration at +30° to +40 °F [0° to +5 °C]. Check individual adhesive kit labels for details. Never open a refrigerated bottle until it has reached room temperature.

GAGE INSTALLATION

The basic steps for bonding gages using M-Bond 43-B, 600, and 610 adhesives are given on the following pages.

HANDLING PRECAUTIONS

Epoxy resins and hardeners may cause dermatitis or other allergic reactions, particularly in sensitive persons. The user is cautioned to: (1) avoid contact with either the resin or hardener; (2) avoid prolonged or repeated breathing of the vapors; and (3) use these materials only in well-ventilated areas. If skin contact occurs, thoroughly wash the contaminated area with soap and water immediately. In case of eye contact, flush immediately and secure medical attention.
Rubber gloves and aprons are recommended, and care should be taken not to contaminate working surfaces, tools, container handles, etc. Spills should be cleaned up immediately. For additional health and safety information, consult the Material Safety Data Sheet, which is available upon request.

Strain Gage Installations with M-Bond 43-B, 600, and 610 Adhesive Systems

Document No.:11130   1 of 4   Revision 28-Jun-10
Micro-Measurements   micro-measurements@vishaypg.com   www.micro-measurements.com

156

Instruction Bulletin B-130

VISHAY
PRECISION
GROUP

Micro-Measurements

M:M®

Step 1

Thoroughly degrease the gaging area with solvent, such as CSM Degreaser or GC-6 Isopropyl Alcohol. The former is preferred, but there are some materials (e.g., titanium and many plastics) that react with CSM. In these cases, GC-6 Isopropyl Alcohol should be considered. All degreasing should be done with uncontaminated solvents-thus the use of "one-way" containers, such as aerosol cans, is highly advisable.

Step 2

Preliminary dry abrading with 220- or 320-grit silicon-carbide paper is generally required if there is any surface scale or oxide. Final abrading is done by using 320- or 400-grit silicon-carbide paper on surfaces thoroughly wetted with M-Prep Conditioner A; this is followed by wiping dry with a gauze sponge.

With a 4H pencil (on aluminum) or a ballpoint pen (on steel), burnish (do not scribe) whatever alignment marks are needed on the specimen. Repeatedly apply Conditioner A and scrub with cotton-tipped applicators until a clean tip is no longer discolored. Remove all residue and Conditioner by again slowly wiping through with a gauze sponge. Never allow any solution to dry on the surface because this invariably leaves a contaminating film and reduces chances of a good bond.

Step 3

Now apply a liberal amount of M-Prep Neutralizer 5A and scrub with a cotton-tipped applicator. With a single, slow wiping motion of a gauze sponge, carefully dry this surface. Do not wipe back and forth because this may allow contaminants to be redeposited on the cleaned surface.

Step 4
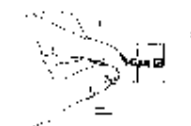
Remove a gage from its mylar envelope with tweezers, making certain not to touch any exposed foil. Place the gage, bonding side down, onto a chemically clean glass plate or empty gage box. If a solder terminal is to be incorporated, position it next to the gage. While holding the gage in position with a mylar envelope, place a short length of MJG-2 mylar tape down over about half of the gage tabs and the entire terminals.

Step 5

Remove the gage/tape/terminal assembly by peeling tape at a shallow angle (about 30°) and transferring it onto the specimen. Make sure gage alignment marks coincide with specimen layout lines. If misalignment does occur, lift the end of the tape at a shallow angle until assembly is free. Realign and replace.
Use of a pair of tweezers often facilitates this handling.

Strain Gage Installations with M-Bond 43-B, 600, and 610 Adhesive Systems

Document No.:11130
Micro-Measurements
2 of 4
micro-measurements@vishaypg.com
Revision 28-Jun-10
www.micro-measurements.com

157

Note: A "hot-tack" method of positioning can be used, which eliminates need for taping. This method is explained after Step 9.

Step 6

Now, by lifting at a shallow angle, peel back one end of the taped assembly so as to raise both gage and terminal. By curling this mylar tape back upon itself, it will remain in position, ready to be accurately repositioned after application of adhesive.

Coat the gage backing, terminal, and specimen surface with a thin layer of adhesive. Also coat the foil side of open-faced gages. Do not allow the adhesive applicator to touch the tape mastic. Permit adhesive to air-dry, by solvent evaporation, for 5 to 30 minutes at +75°F [+24°C] and 50% relative humidity. Longer air-drying times are required at lower temperatures and/or higher humidities. *Note: An additional drying step with 43-B is beneficial for large gages. Place the unclamped installation in an oven for 30 minutes at +175°F [+85°C] following the air-dry step above.*

Step 7

Return the gage/terminal assembly to its original position over the layout marks. Use only enough pressure to allow the assembly to be tacked down. Overlay the gage/ terminal area with a piece of thin Teflon sheet (TFE-1). If necessary, anchor the Teflon in position across one end with a piece of mylar tape.

Cut a 3/32-in [2.5-mm] thick silicone gum pad and a metal backup plate (GT-14) to a size slightly larger than the gage/terminal areas, and carefully center these. Larger pads may restrict proper spreading of adhesive, and entrap residual solvents during cure process.

Note: Steps 6, 7, and 8 must be completed within 30 minutes with M-Bond 600, 4 hours with M-Bond 610, and 24 hours with M-Bond 43-B.

Step 8

Either spring clamps or deadweight can be used to apply pressure during the curing cycle. For transducers, 40 to 50 psi [275 to 350 kN/m2] is recommended and 10 to 70 psi [70 to 480 kN/m2] for general work. Place the clamped gage/specimen into a cool oven and raise temperature to the desired during level at a rate of 5° to 20°F [3° to 11°C] per minute. Air bubbles trapped in the adhesive, uneven gluelines, and high adhesive film stresses often result from starting with a hot oven. Time-versus-temperature recommendations for curing each adhesive are given on the next page.

Step 9

Upon completion of the curing cycle, allow oven temperature to drop to at least 100°F [55°C] before removing the specimen. Remove clamping pieces and mylar tape. It is advisable to wash off the entire gage area with either RSK Rosin Solvent or toluene. This should remove all residual mastic and other contamination. Blot dry with a gauze sponge.

"Hot-Tack" Method of Gage Installation
This procedure eliminates all need for taping to prevent movement of the gage during mounting, and is especially suited to M-Bond 43-B and M-Bond 600.

1. After completing the preceding Steps 1, 2, and 3, remove a gage from its mylar envelope using clean tweezers.
2. Coat the bonding side of gage and gaging area of the specimen with adhesive, and set each aside to air-dry for at least 15 minutes. M-Bond 43-B may dry for up to 24 hours.

Strain Gage Installations with M-Bond 43-B, 600, and 610 Adhesive Systems

Document No.:11130   3 of 4   Revision 28-Jun-10
Micro-Measurements   micro-measurements@vishaypg.com   www.micro-measurements.com

158

3. Using tweezers, position gage onto the specimen. A properly cleaned dental probe may help.

4. To anchor the gage, use a 15- to 25-watt soldering iron with a new conical tip. This is usually done by hot-tack-setting the adhesive at two spots (such as opposite gage-alignment marks) while temporarily holding the gage down with a mylar envelope. A little experimentation may be required to learn the correct iron temperature and hot tip contact time. These depend upon type of adhesive used and thermal conductivity of the base material.

5. If the gage is open-faced, apply a thin coating of adhesive to its face and allow to dry for at least five minutes before overlaying with a Teflon sheet (as described in Step 7). Proceed with Steps 8 and 9.

RECOMMENDED CURE SCHEDULE
It should be noted that the following curves represent a range of time-versus-temperature; however, the upper limits of both time and temperature should be employed whenever possible, while keeping in mind the possible effect on the heat treat condition of the substrate material.

M-Bond 43-B: 2 hours at +375°F [+190°C], or as an alternate cure for aluminum alloy transducers 2 ½ hours @ +300°F [+150°C].

M-Bond 600: Cure at temperature for time period specified by graph below.
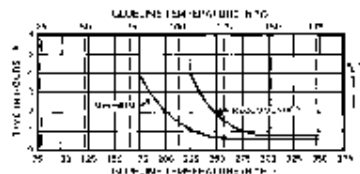
M-Bond 610: Cure at temperature for time period specified by graph below.
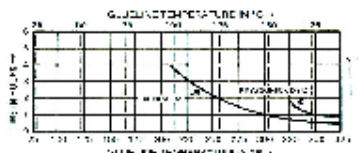
POSTCURING
Postcures with the clamping fixture removed are usually required for stable transducer applications. Postcuring can be done following Step 9 above, or after wiring the transducer (subject to temperature limits of solder and wire insulation).

M-Bond 43-B: 2 hours at +400°F [+205°C], or as an alternate postcure for aluminum alloy transducers 2 ½ hours @ +350°F [+175°C].

M-Bond 600: 1 to 2 hours at 50°F [30°C] above maximum operating or curing temperature, whichever is greater.

M-Bond 610: 2 hours at 50° to 75°F [30° to 40°C] above maximum operating or curing temperature, whichever is greater.

FINAL INSTALLATION PROCEDURES
1. Refer to Strain Gage Accessories Databook to select an appropriate solder, and attach leadwires. Be sure to remove solder flux with Rosin Solvent. Gage tabs and terminals can be cleaned prior to soldering by light abrading with pumice to remove the adhesive film. This pumicing is not required with gages having integral leads (Options L and LE) or pre-attached solder dots. See Application Note TT-606, "*Soldering Techniques for Lead Attachment to Strain Gages with Solder Dots*." General soldering instructions are discussed in Application Note TT-609, "*Strain Gage Soldering Techniques*."

2. Select and apply protective coatings according to recommendations given in Strain Gage Accessories Databook.

ELONGATION CAPABILITIES
M-Bond 43-B:
1% at -452°F [-269°C]; 4% at +75°F [+24°C]; 2% at +300°F [+150°C].

M-Bond 600 & 610:
1% at -452°F [-269°C]; 3% from room temperature to 500°F [+260°C].

Mylar and Teflon are Registered Trademarks of DuPont.

Strain Gage Installations with M-Bond 43-B, 600, and 610 Adhesive Systems

Document No.:11130
Micro-Measurements

4 of 4
micro-measurements@vishaypg.com

Revision 28-Jun-10
www.micro-measurements.com

159

APPENDIX F

Spring Manufacturer's Specifications

This Appendix contains the manufacturer's specifications for the K104 spring. The manufacture specifications are presented in table format in order of increasing spring constant. The manufacture drawings follow in the same order.

Table F.5: Manufacture Specifications for Spring K104

SPRING K104

Type	Compression Springs
Material	Steel
Steel Type	Spring-Tempered Steel
System of Measurement	Inch
Outside Diameter	2-11/16"
Wire Size	.312"
Overall Length	8"
Compressed Length	3.67"
Ends	Closed and Ground
Wire Type	Round Wire
Load	445 lbs.
Deflection at Load	4.33"
Rate	104.3 lbs./inch
Specifications Met	Not Rated

2 11/16"

0.312
Wire Diameter

8"

McMASTER-CARR CAD.
http://www.mcmaster.com
© 2005 McMaster-Carr Supply Company

PART
NUMBER 96485K205

Spring-Tempered Steel
Compression Spring

Unless otherwise specified, dimensions are in inches. Information in this drawing is provided for reference only.
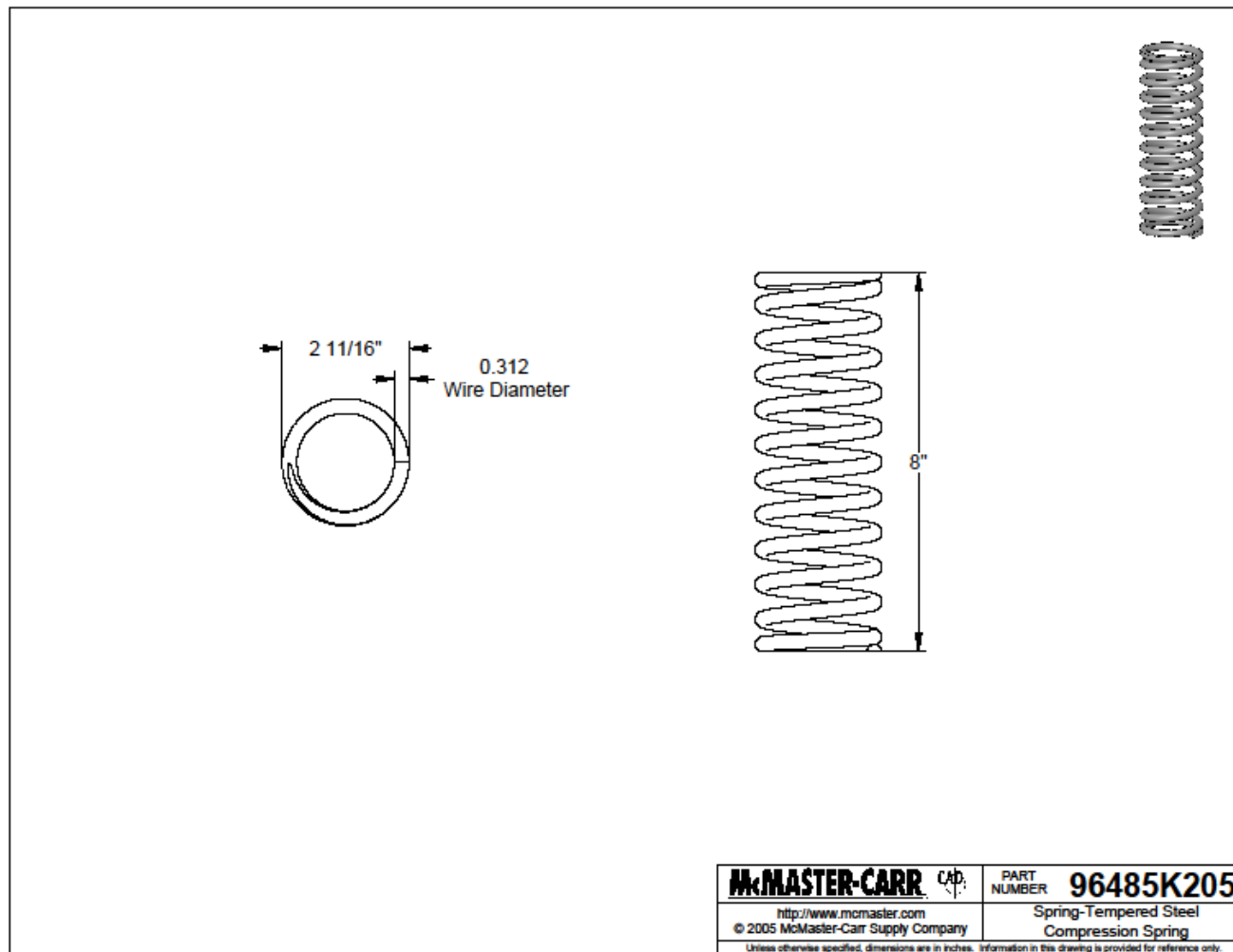
Figure F.5: Manufacture Drawing for Spring K104

Stage I Test Preliminary Plots

The following figures present the preliminary plots used to analysis the testing jig and behavior of the K104 compression spring. Only the plots that present either axial or torsional results were used. The plots containing the shear and bending loads were not used due effects of the testing jig design.

SPRING K104

STAGE I PART 1
(Un-winding Torque)
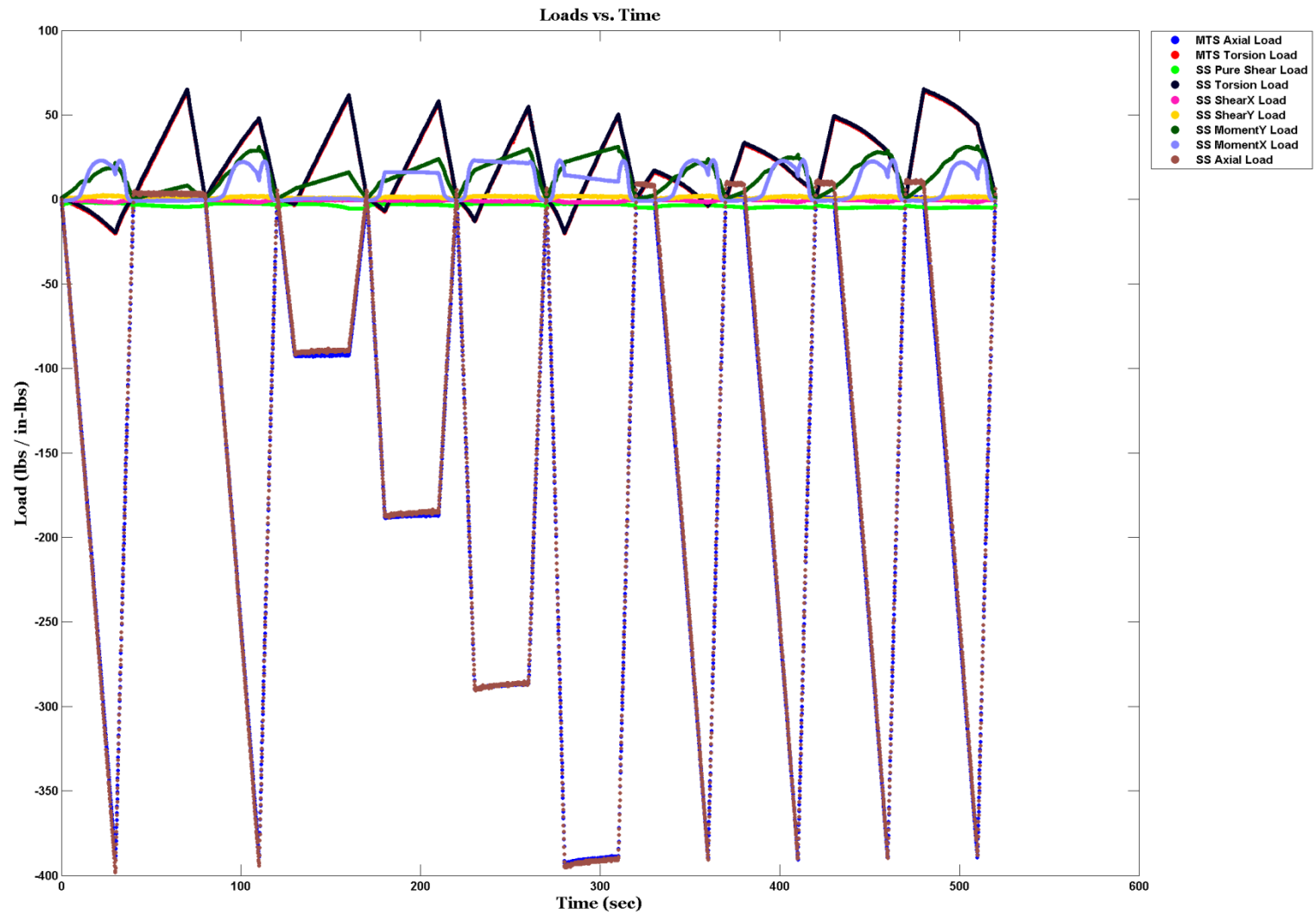
Figure G.1: Spring K104 Part 1 of Stage I – All 6 Cell and MTS Loads vs. Time
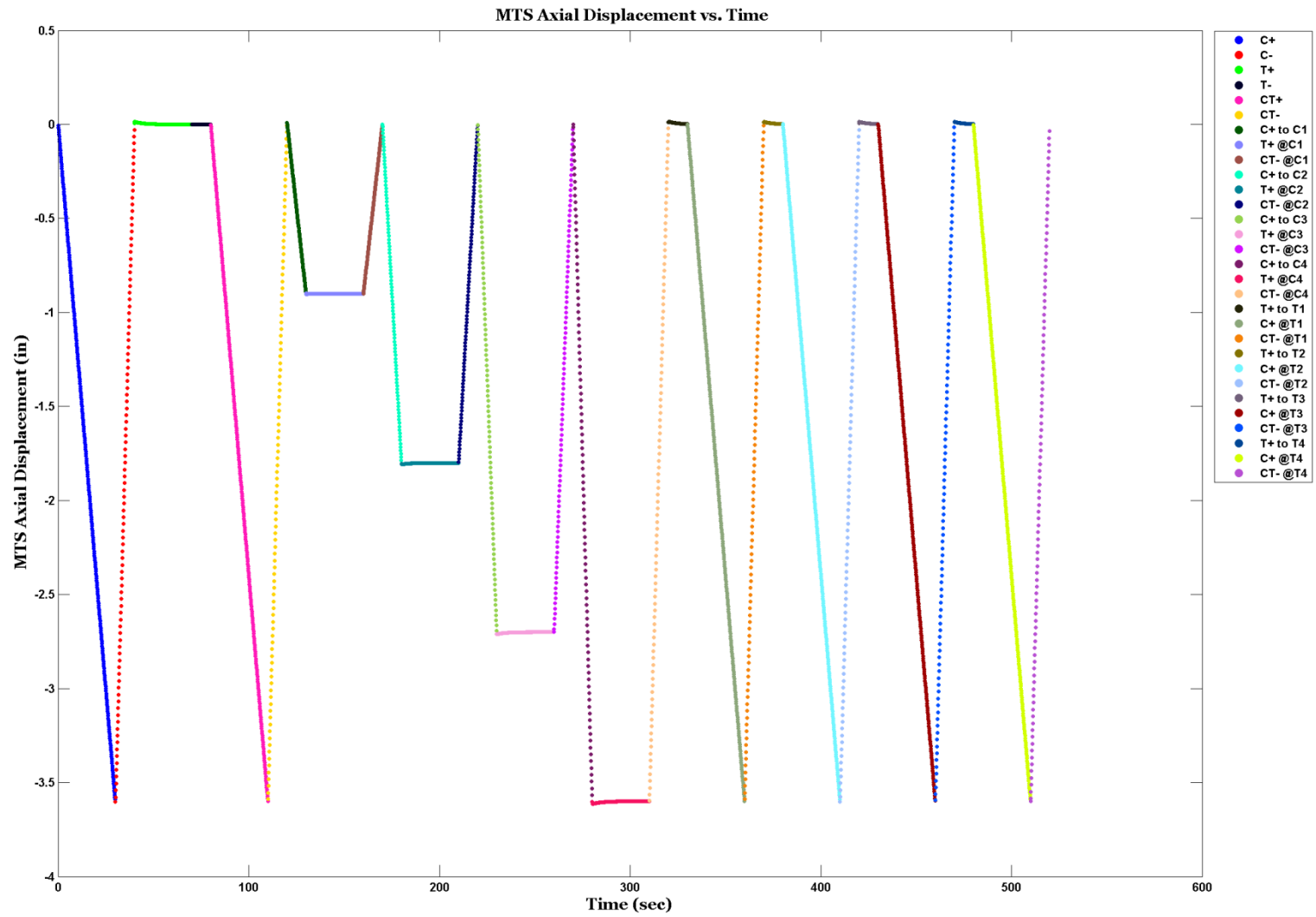
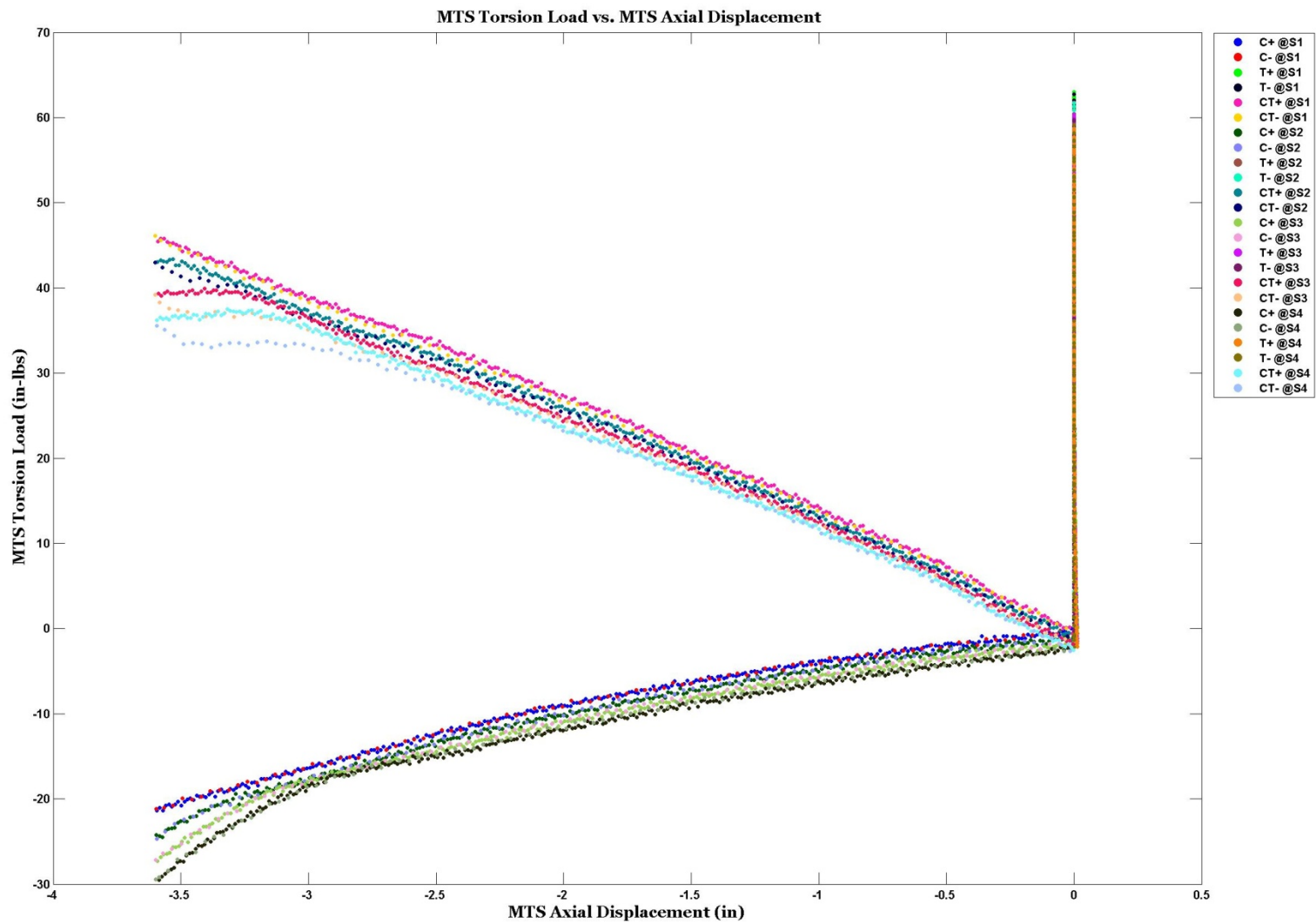Figure G.2: Spring K104 Part 1 of Stage I – MTS Axial Displacement vs. Time
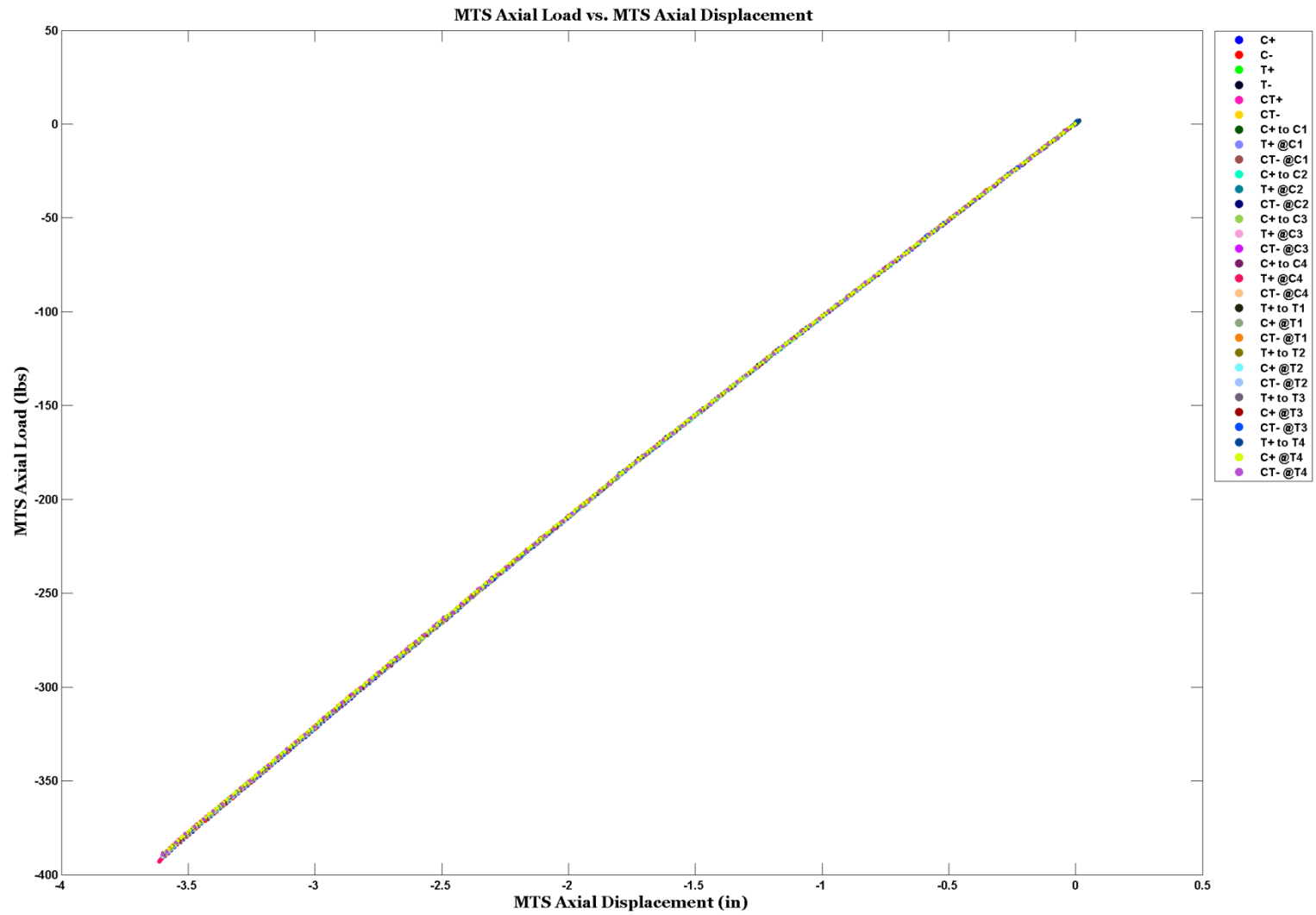
Figure G.3: Spring K104 Part 1 of Stage I – MTS Axial Load vs. MTS Axial Displacement
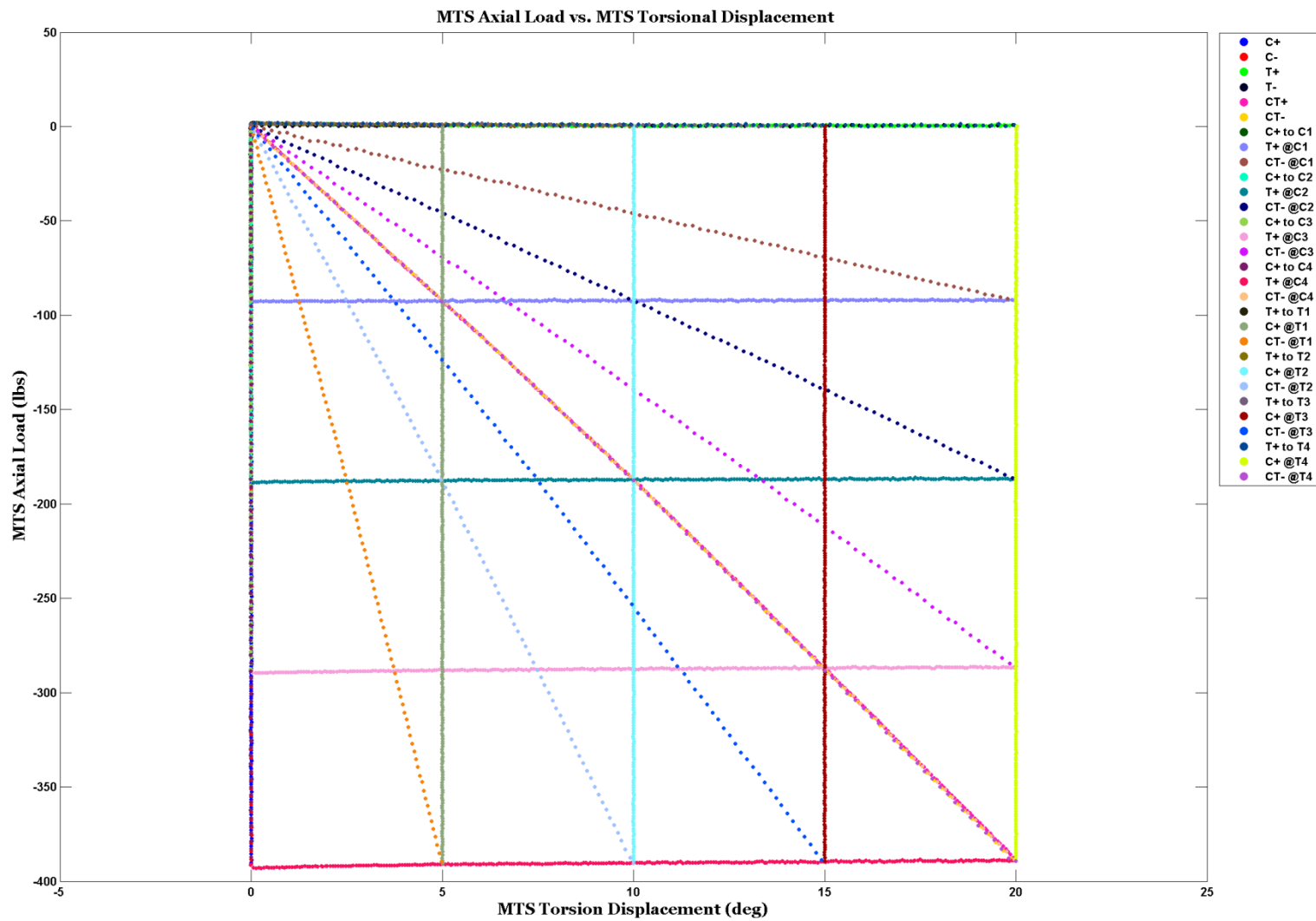
Figure G.4: Spring K104 Part 1 of Stage I – MTS Axial Load vs. MTS Torsional Displacement
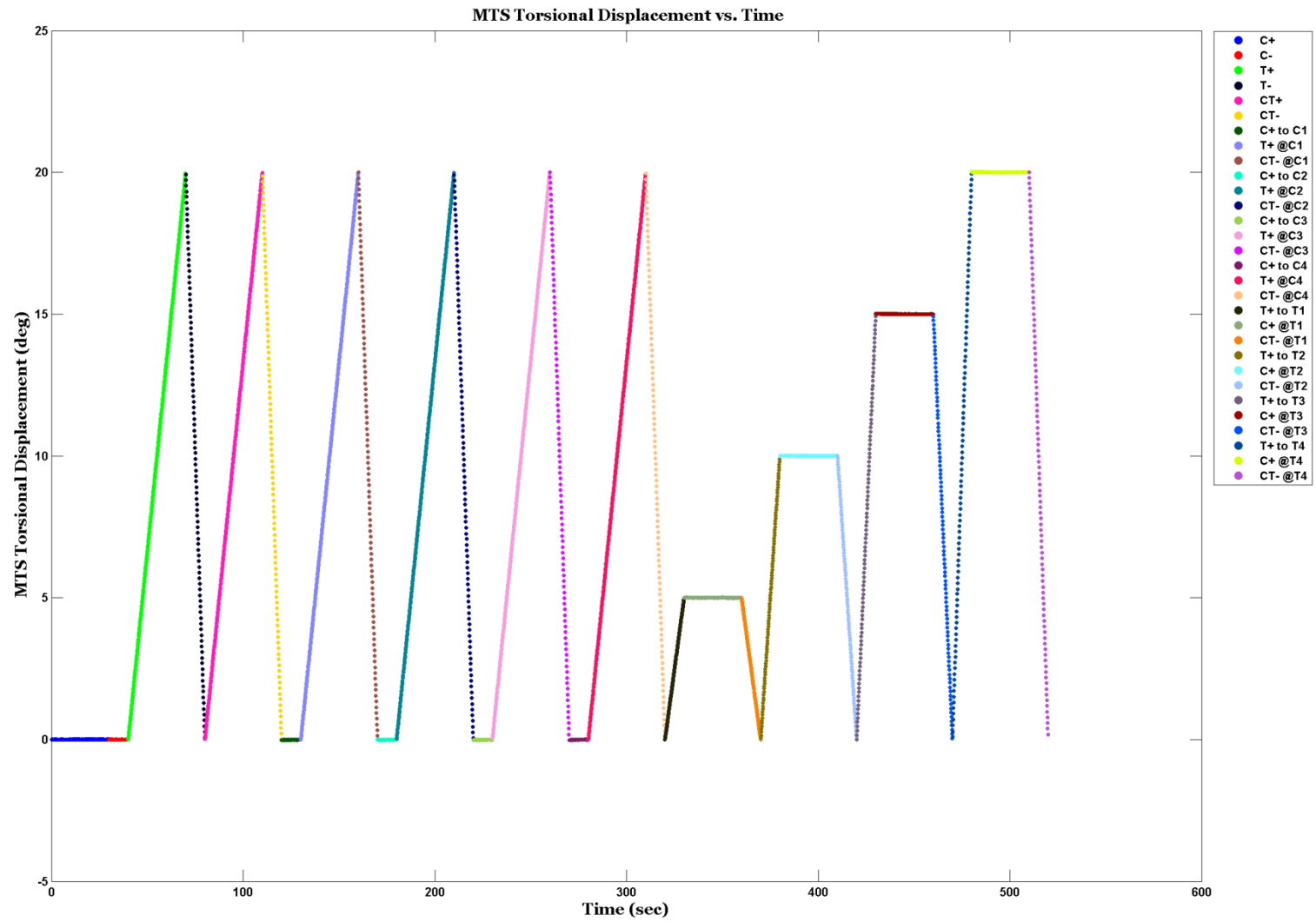
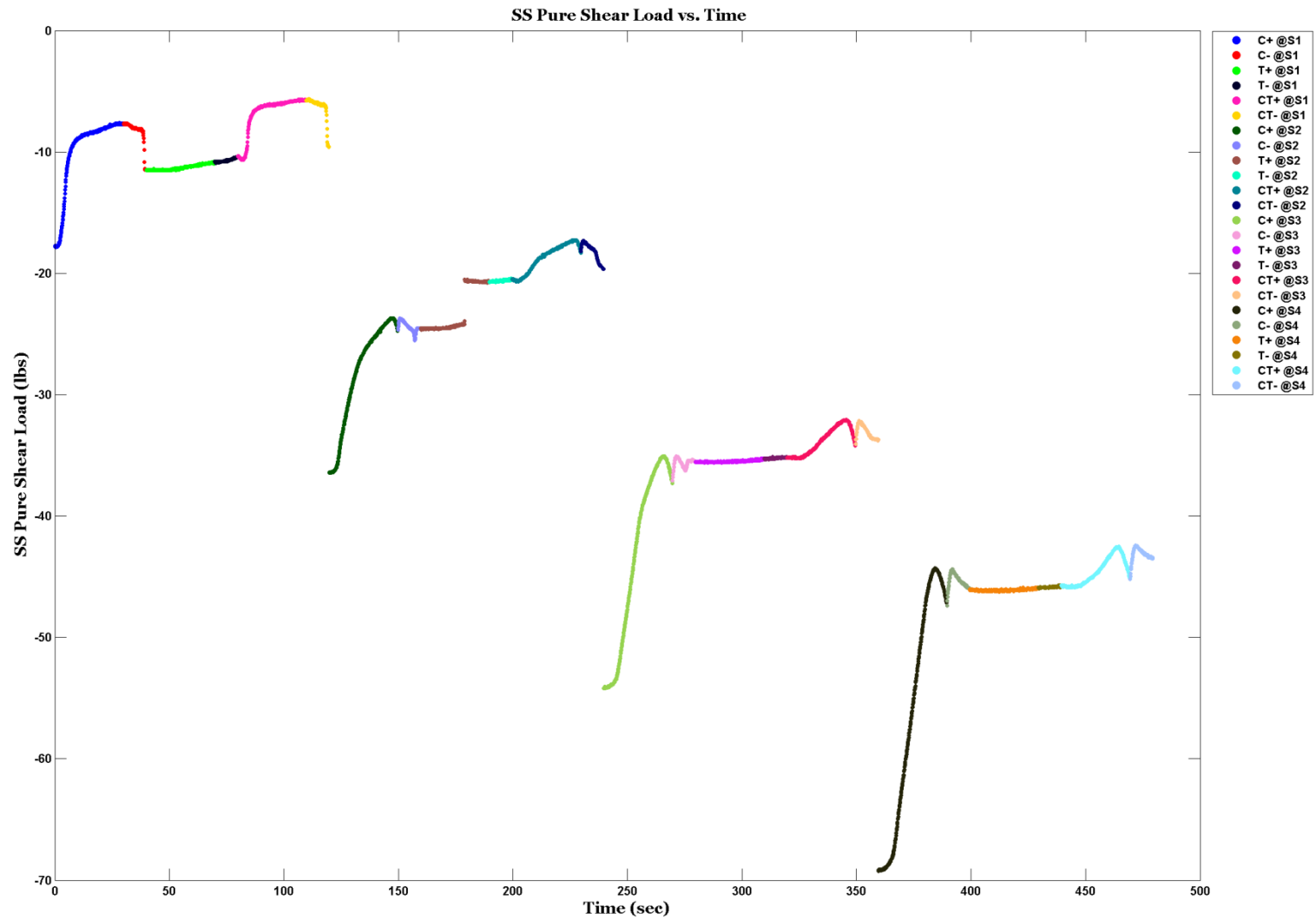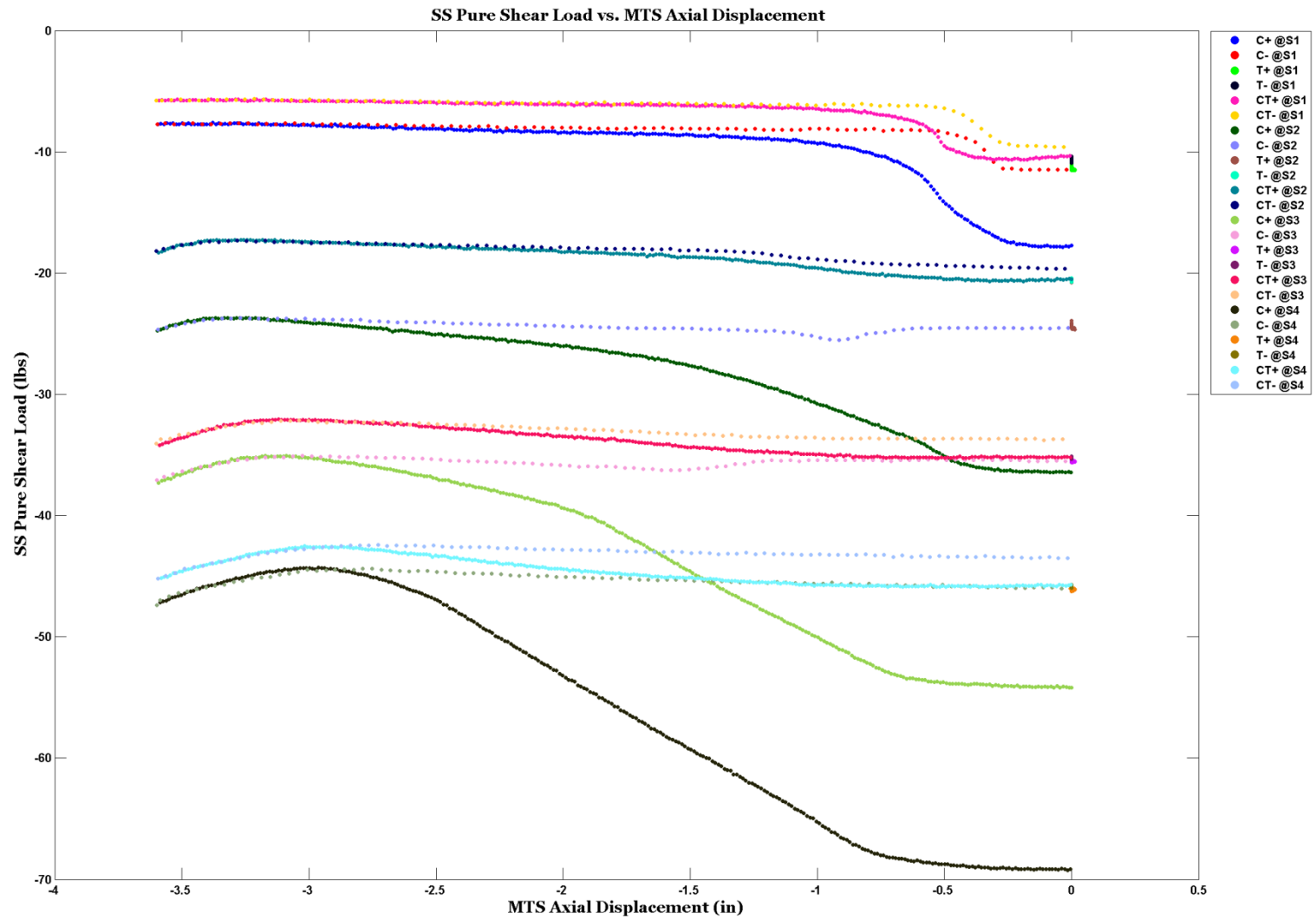Figure G.5: Spring K104 Part 1 of Stage I – MTS Torsional Displacement vs. Time
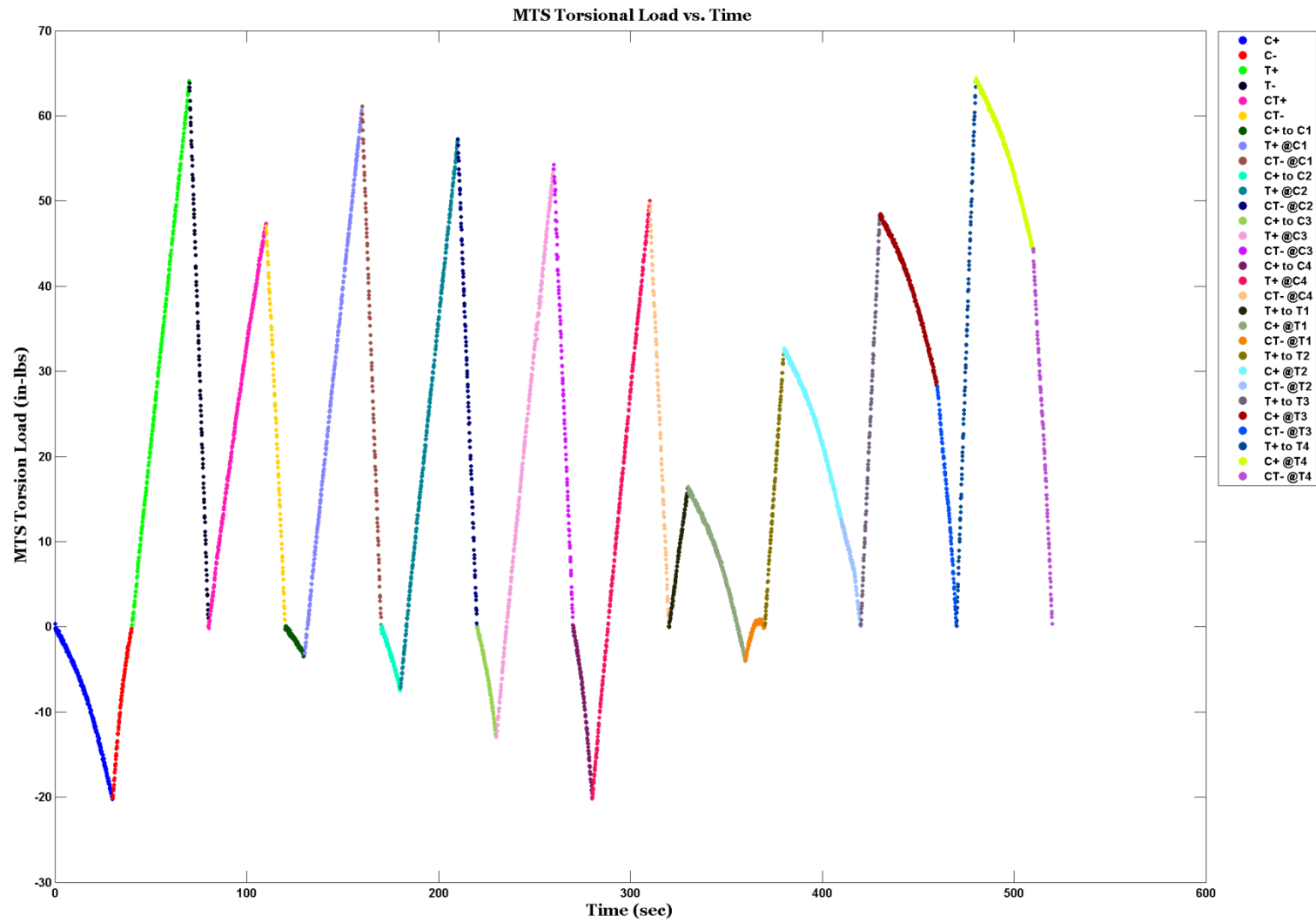
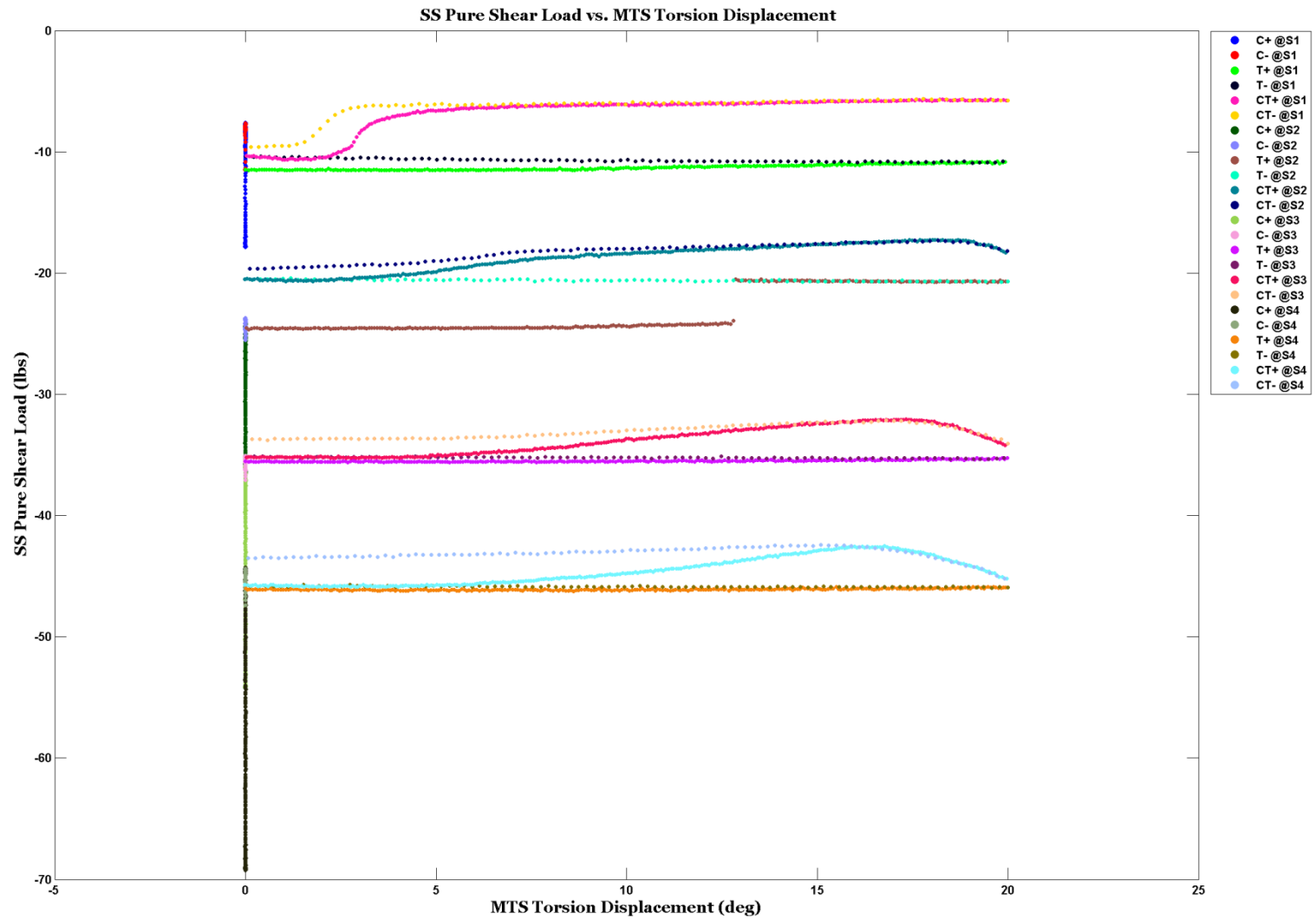Figure G.6: Spring K104 Part 1 of Stage I – MTS Torsional Load vs. Time
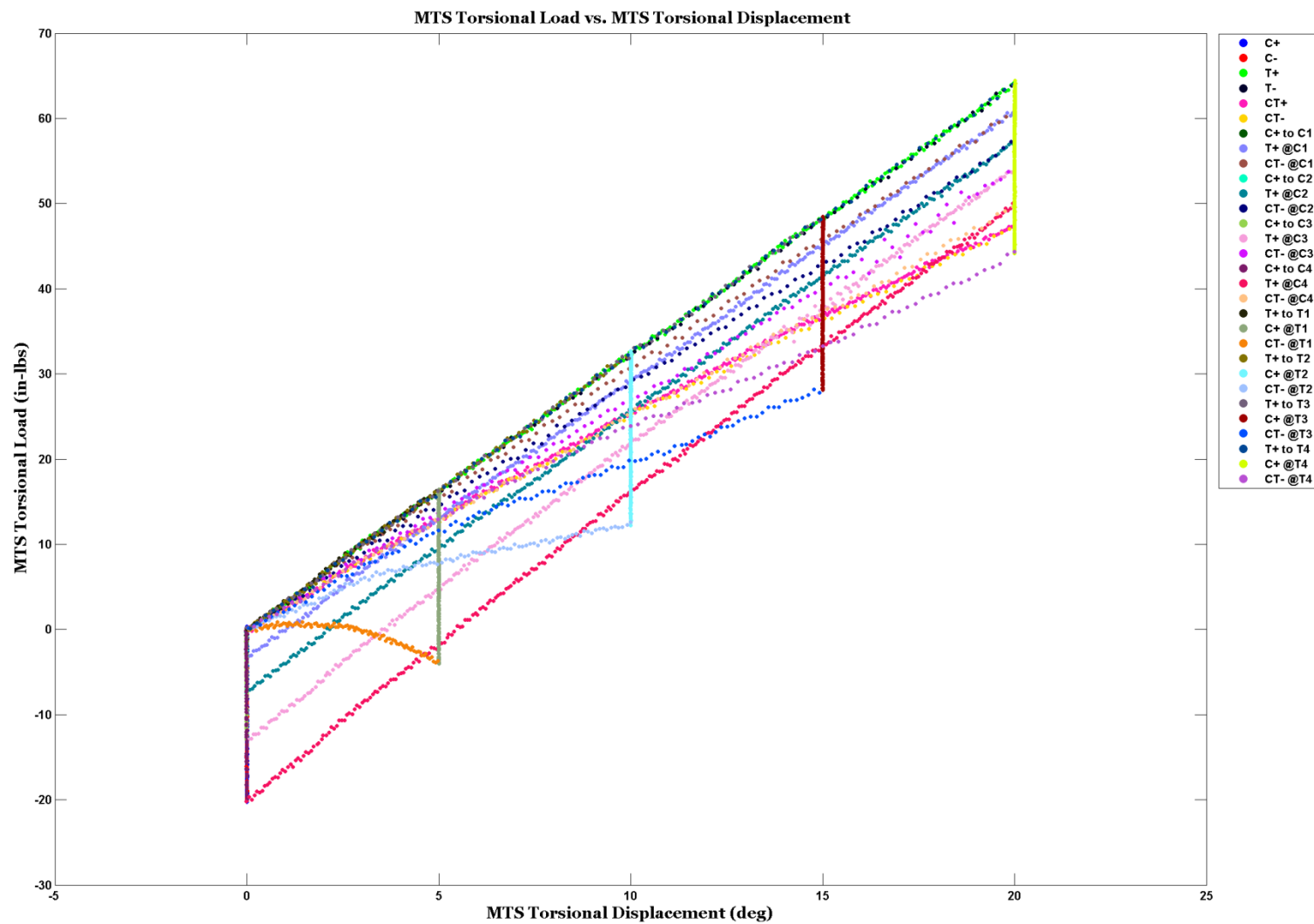
Figure G.7: Spring K104 Part 1 of Stage I – MTS Torsional Load vs. MTS Torsional Displacement
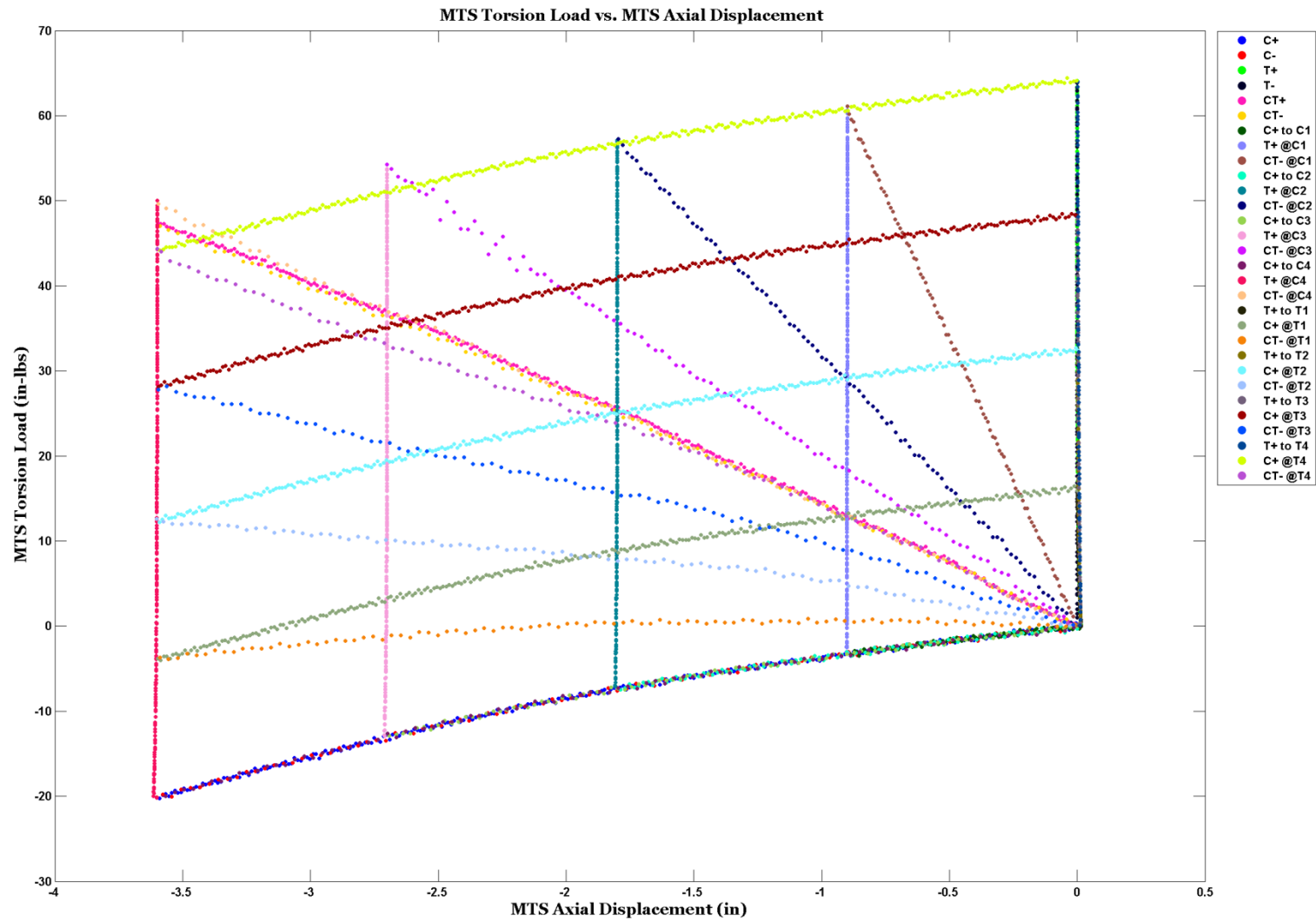
Figure G.8: Spring K104 Part 1 of Stage I – MTS Torsion Load vs. MTS Axial Displacement
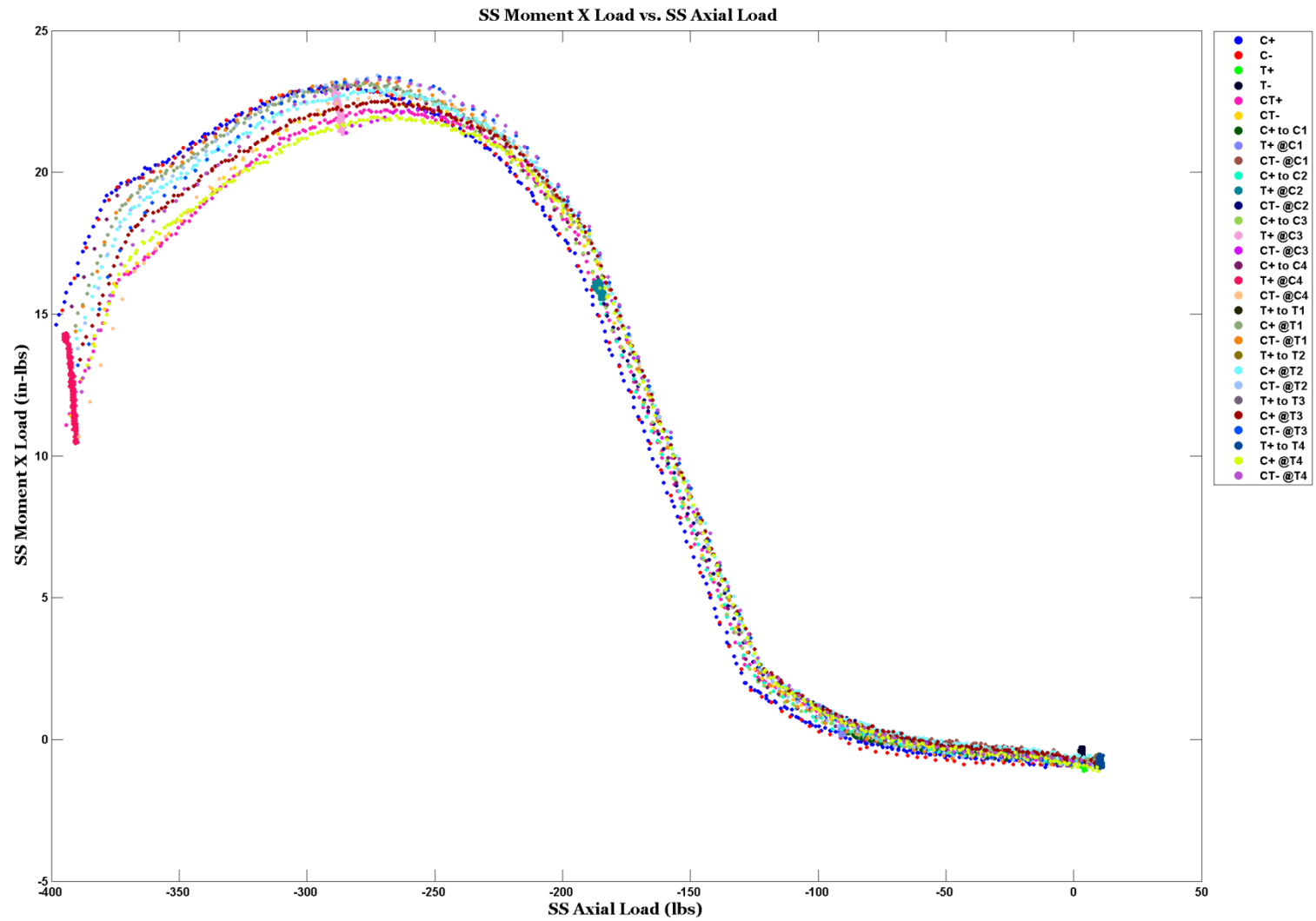
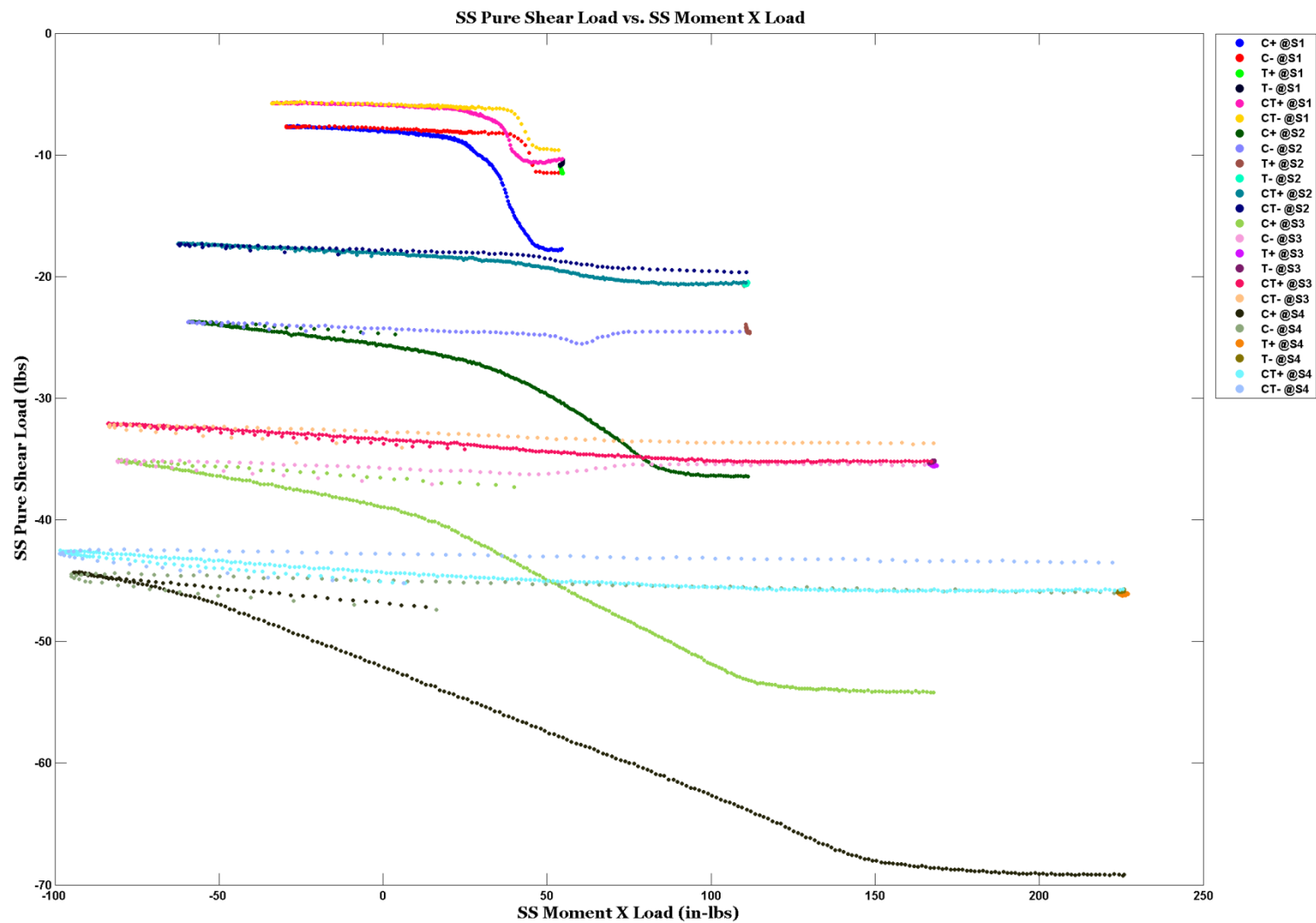Figure G.9: Spring K104 Part 1 of Stage I 6 – Cell Moment X Load vs. 6-Cell Axial Load
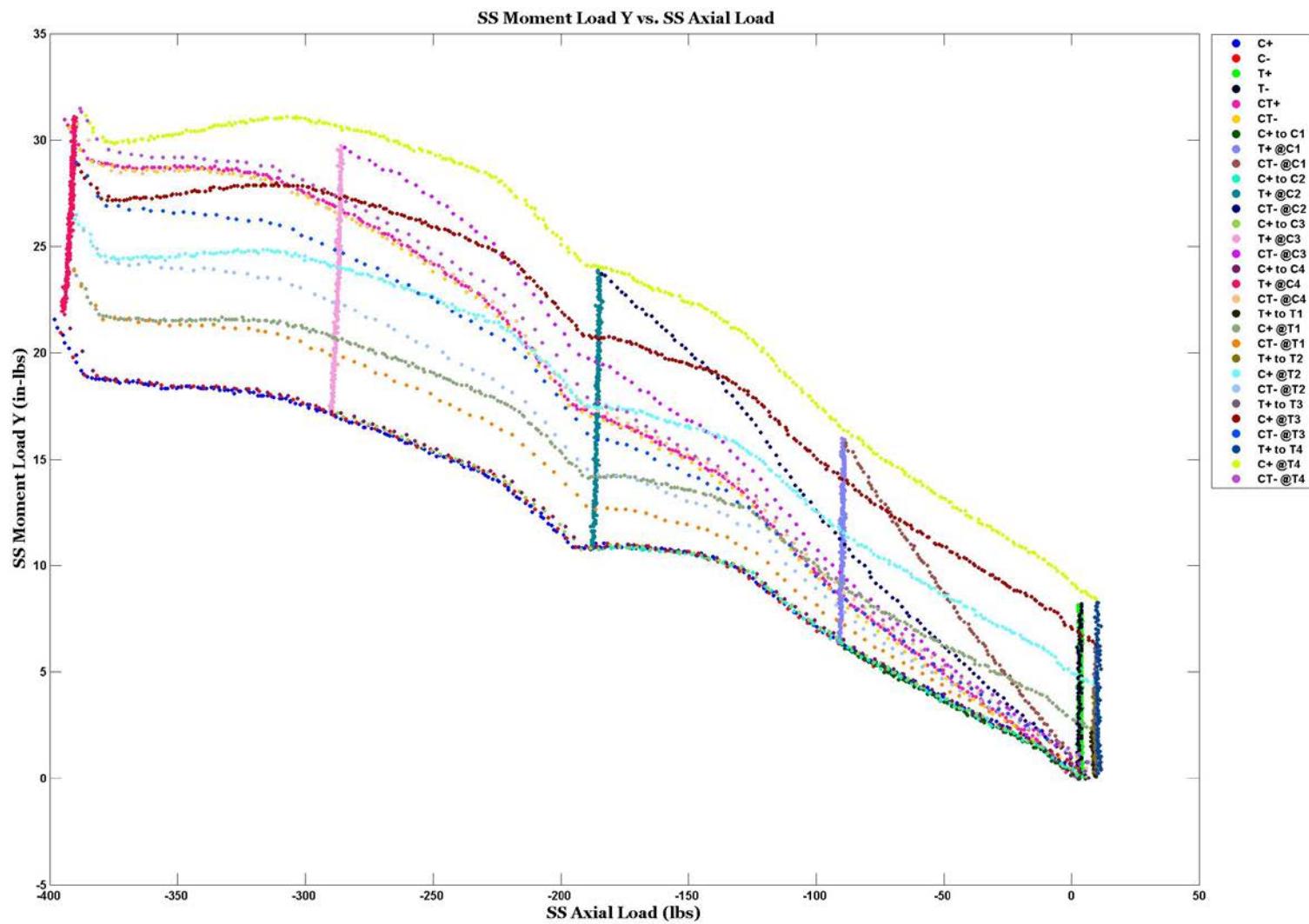
Figure G.10: Spring K104 Part 1 of Stage I 6 – Cell Moment Y Load vs. 6-Cell Axial Load
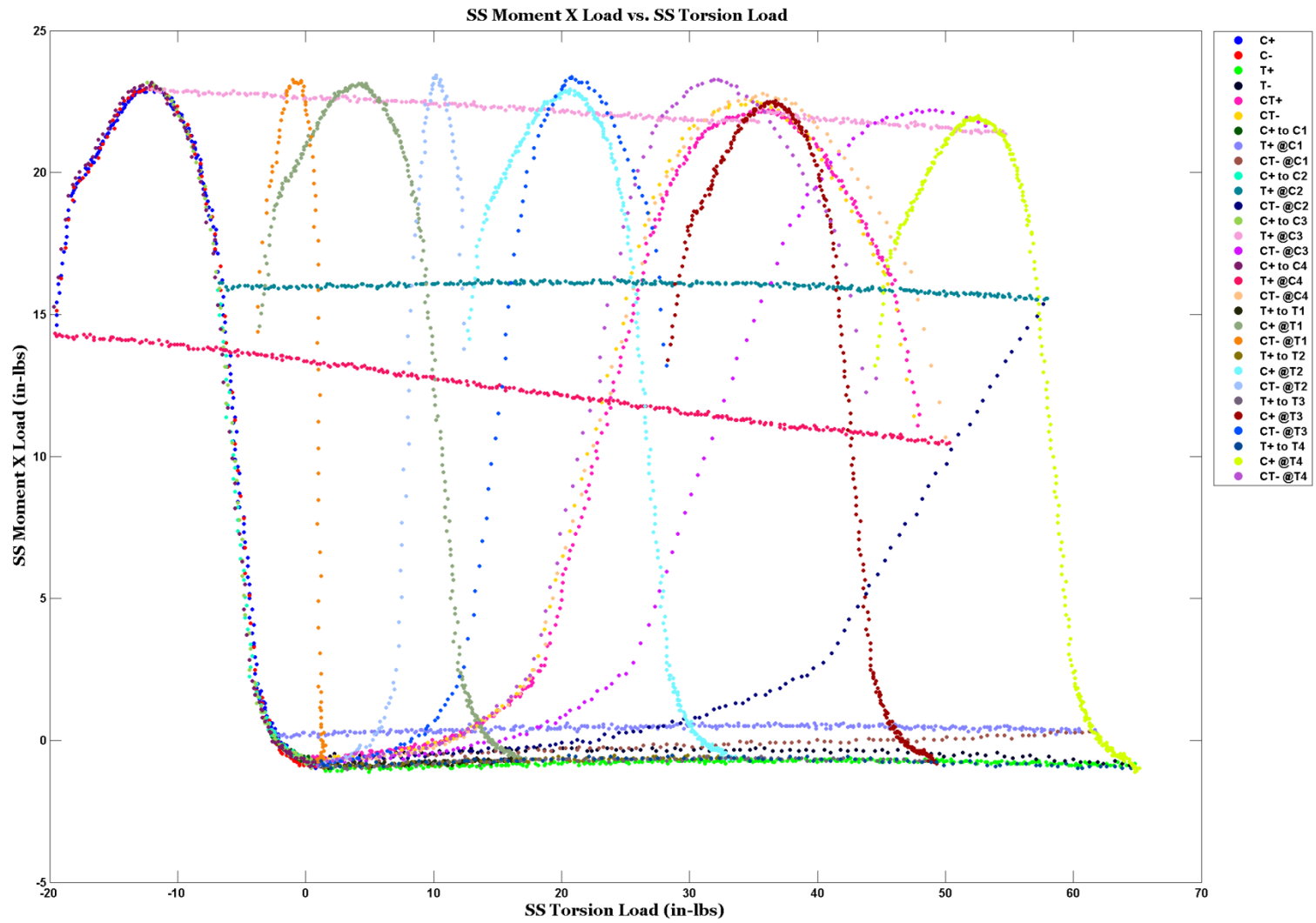
Figure G.11: Spring K104 Part 1 of Stage I – 6-Cell Moment X Load vs. 6-Cell Torsion Load
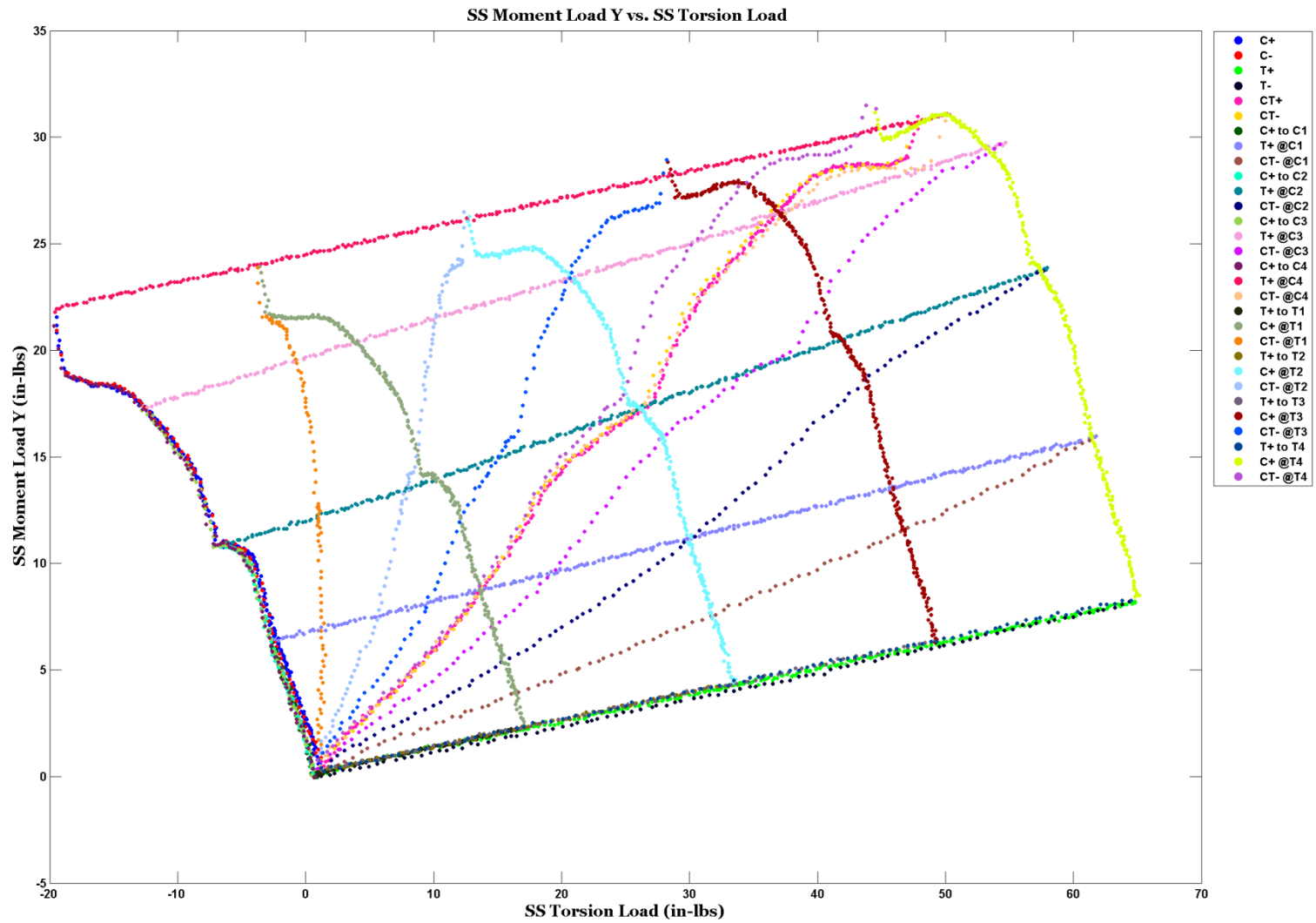
Figure G.12: Spring K104 Part 1 of Stage I K104 Part 1 of Stage I – 6-Cell Moment Y Load vs. 6-Cell Torsion Load

SPRING K104

STAGE I PART 2
(Winding Torque)
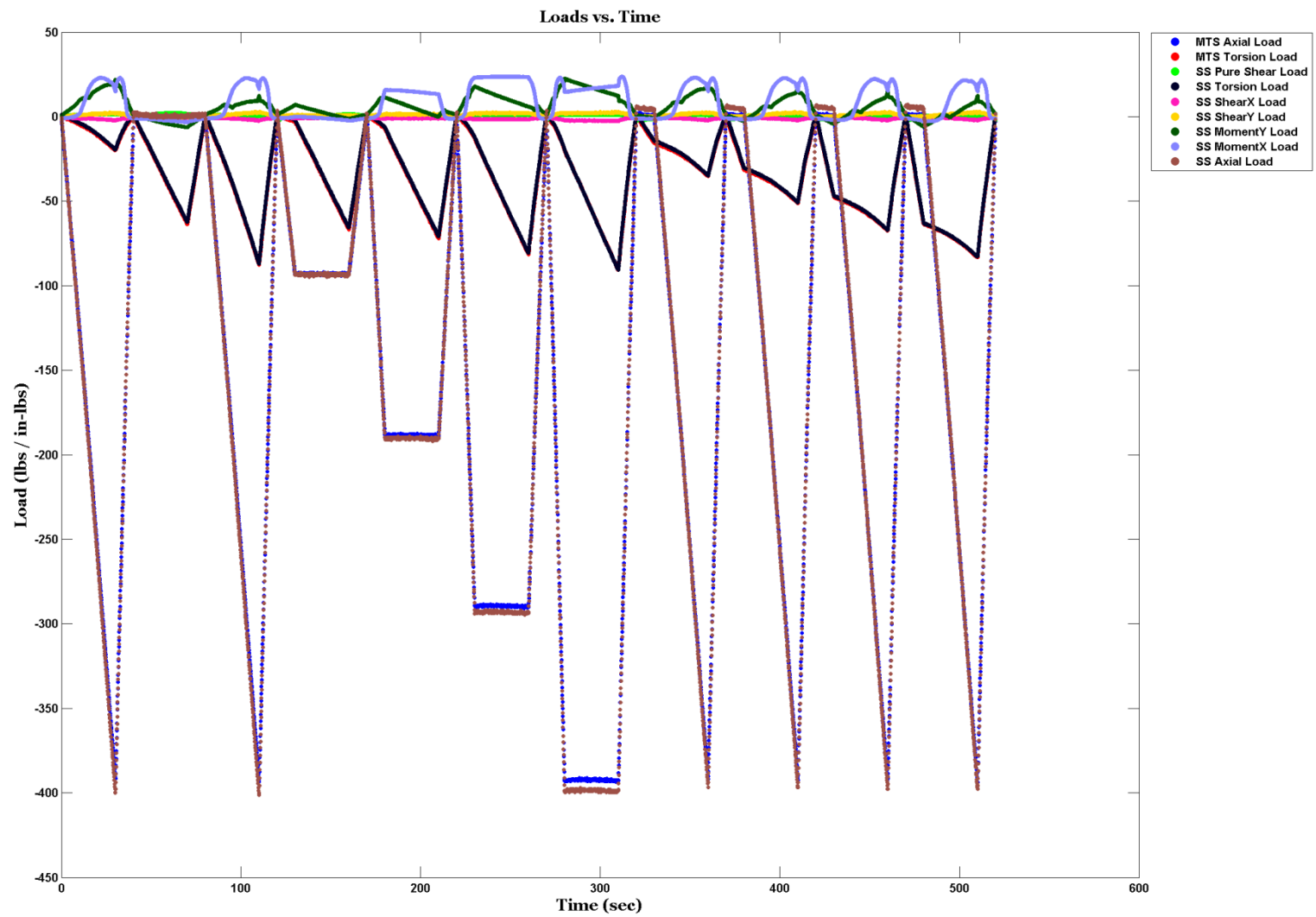
Figure G.13: Spring K104 Part 2 of Stage I – All 6 Cell and MTS Loads versus Time
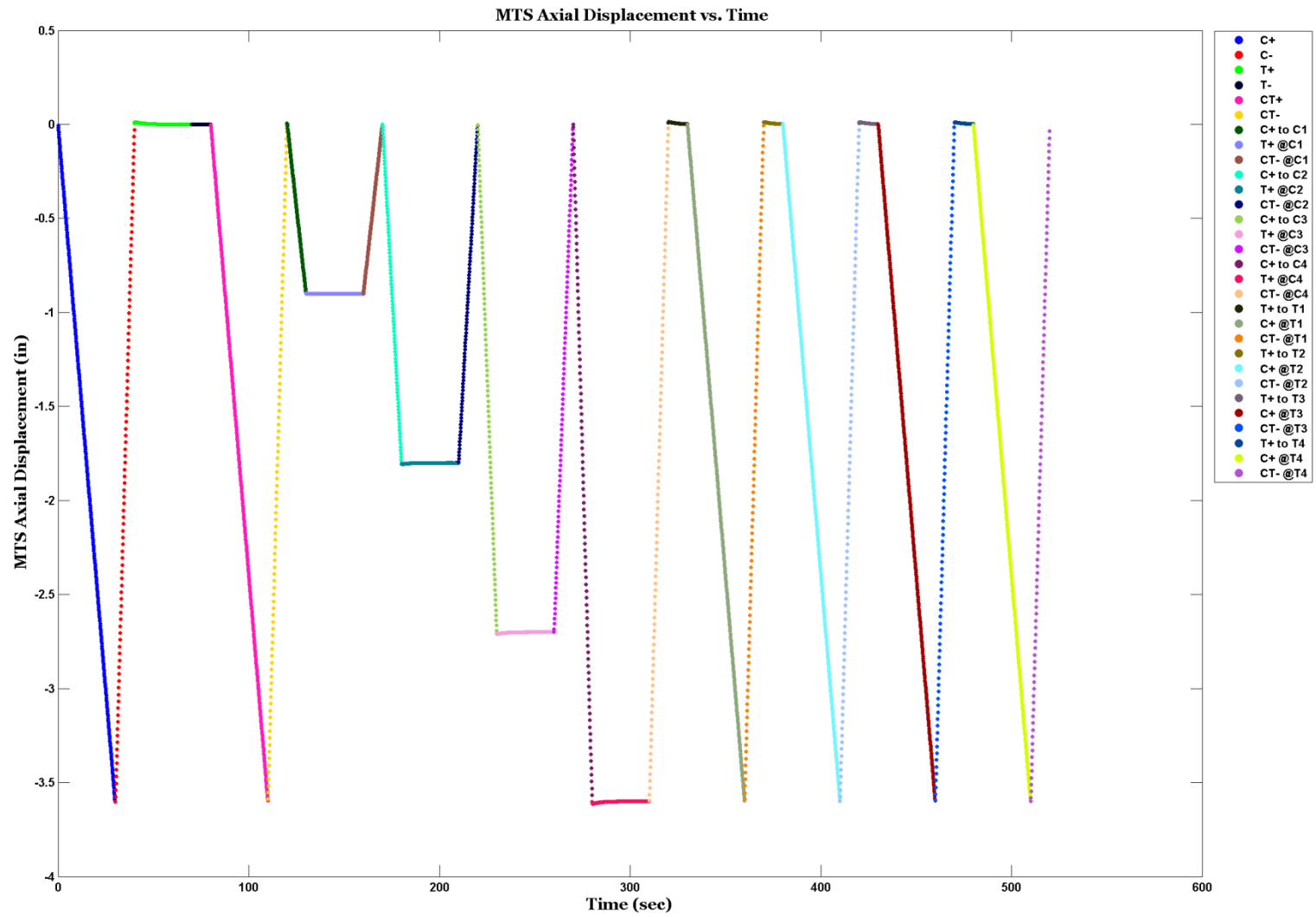
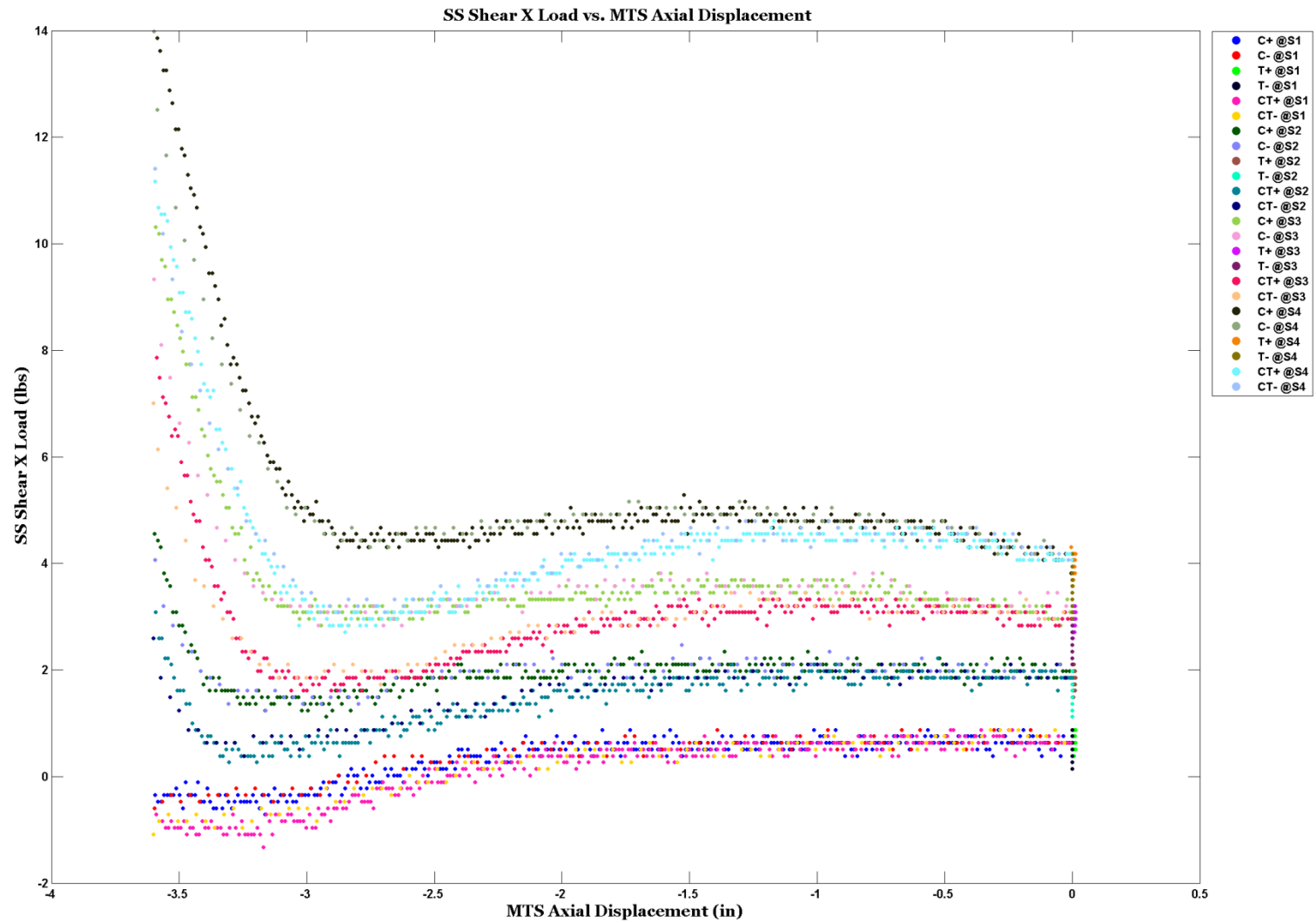Figure G.14: Spring K104 Part 2 of Stage I – MTS Axial Displacement versus Time
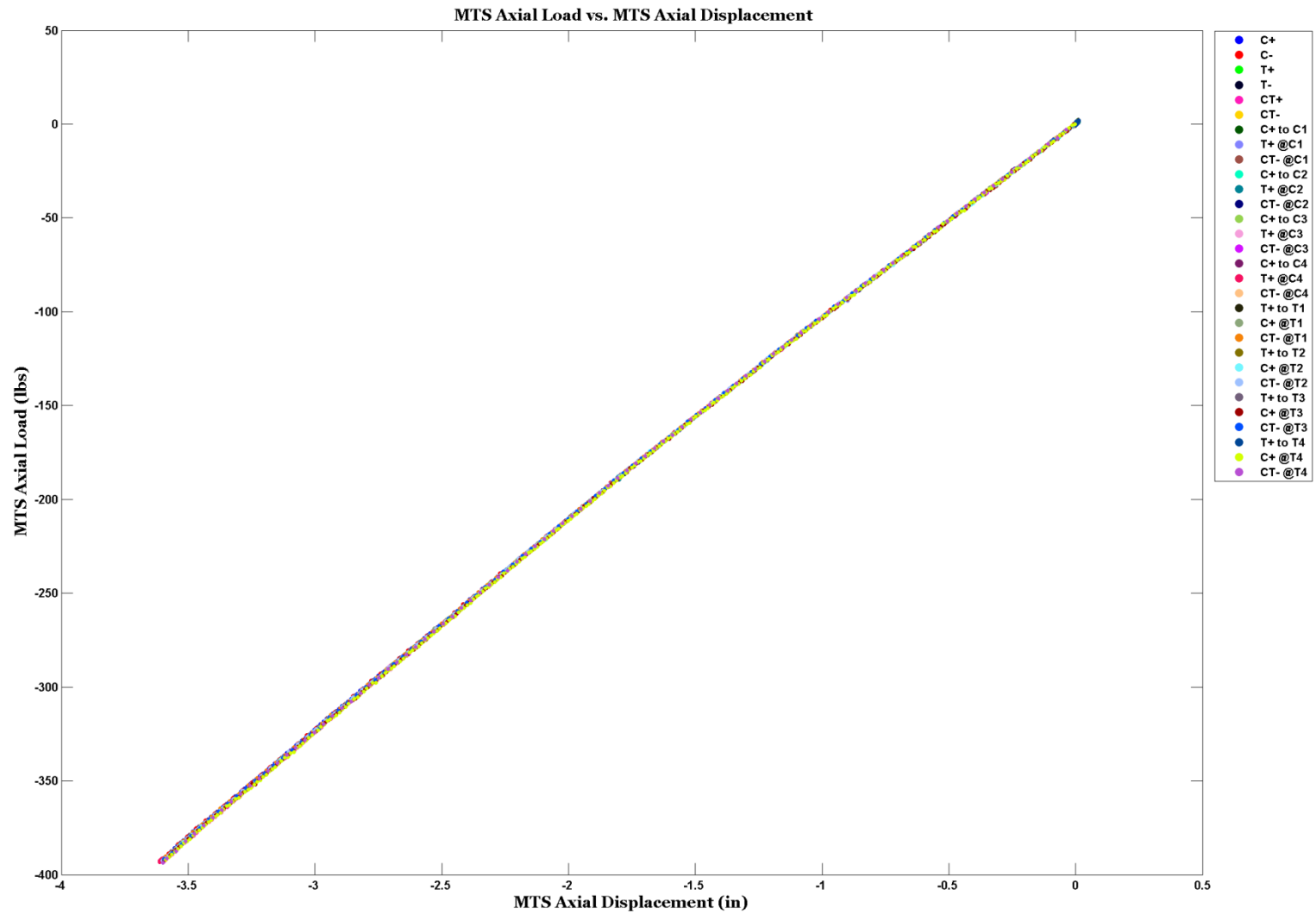
Figure G.15: Spring K104 Part 2 of Stage I – MTS Axial Load vs. MTS Axial Displacement
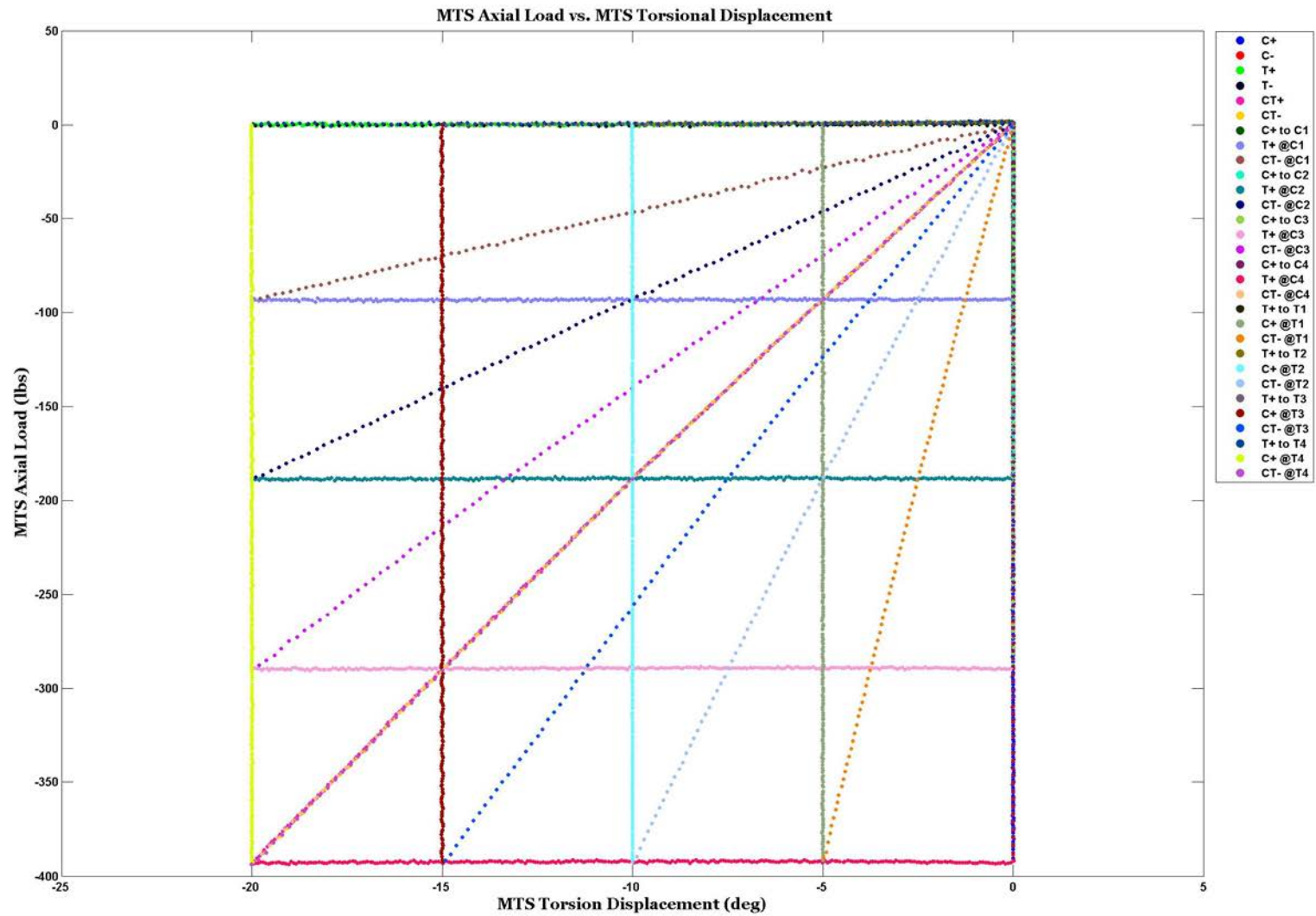
Figure G.16: Spring K104 Part 2 of Stage I – MTS Torsional Load vs. MTS Torsional Displacement
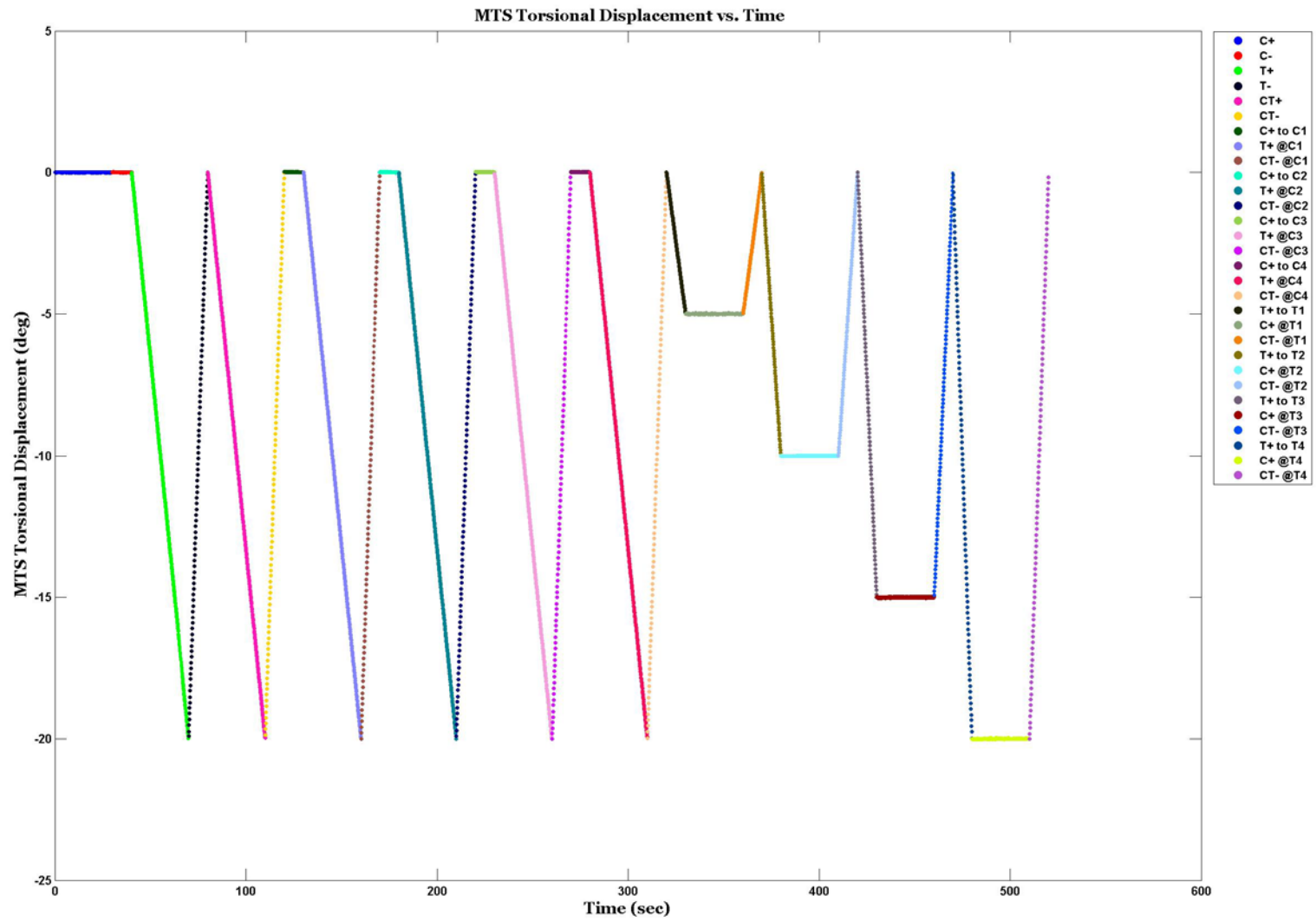
Figure G.17: Spring K104 Part 2 of Stage I – MTS Torsional Displacement vs. Time
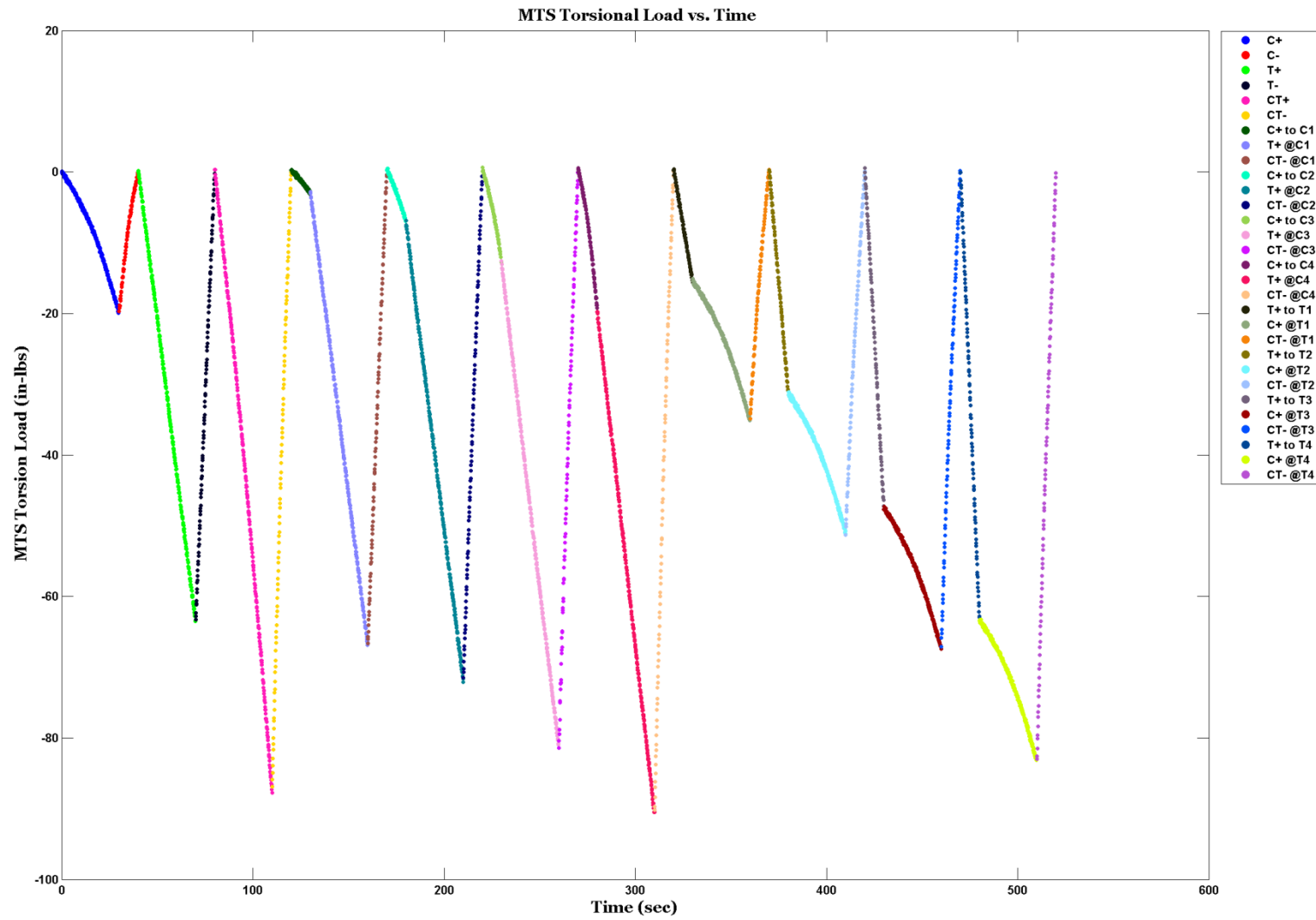
Figure G.18: Spring K104 Part 2 of Stage I – MTS Torsional Displacement vs. Time
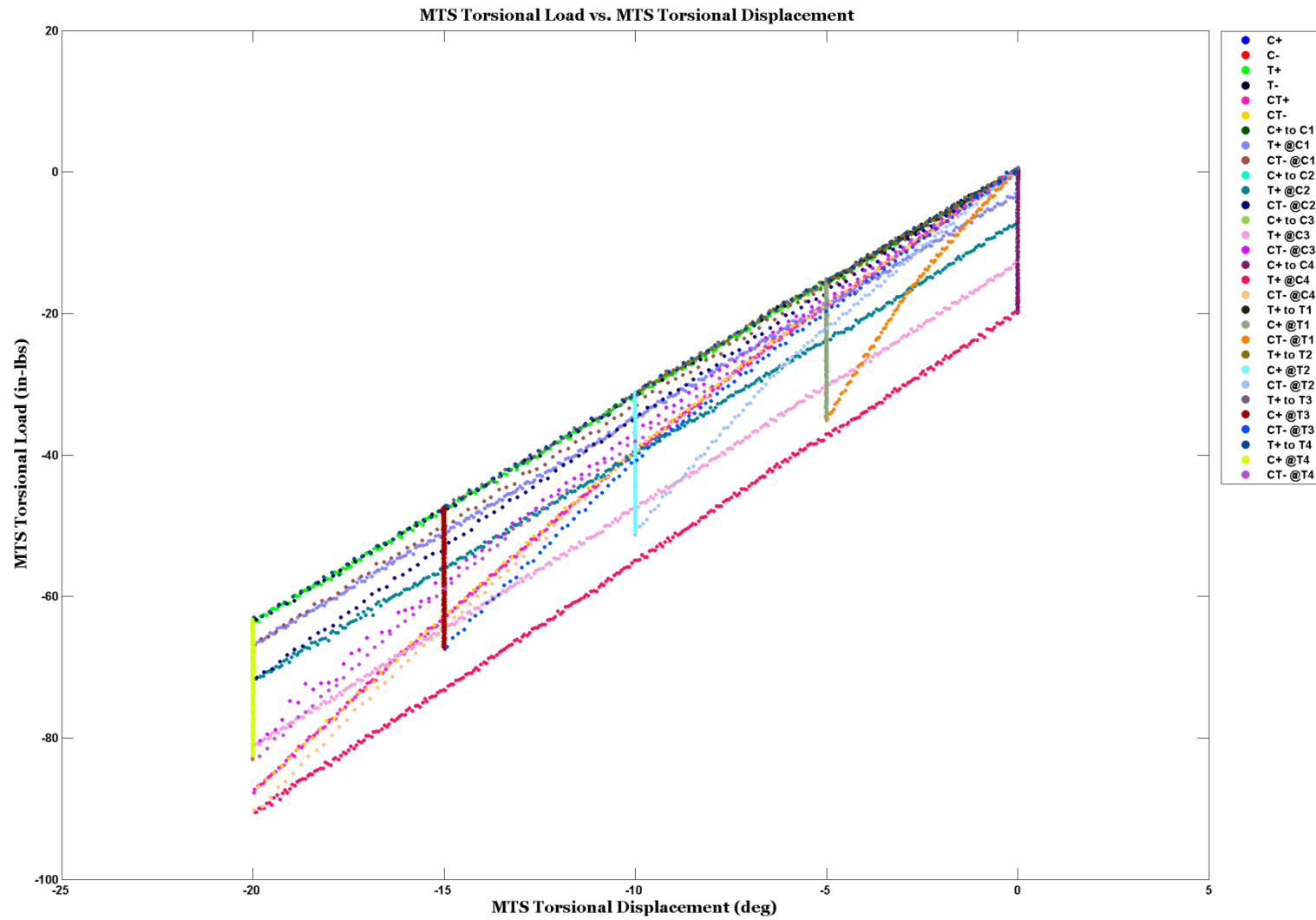
Figure G.19: Spring K104 Part 2 of Stage I – MTS Torsional Load vs. MTS Torsional Displacement
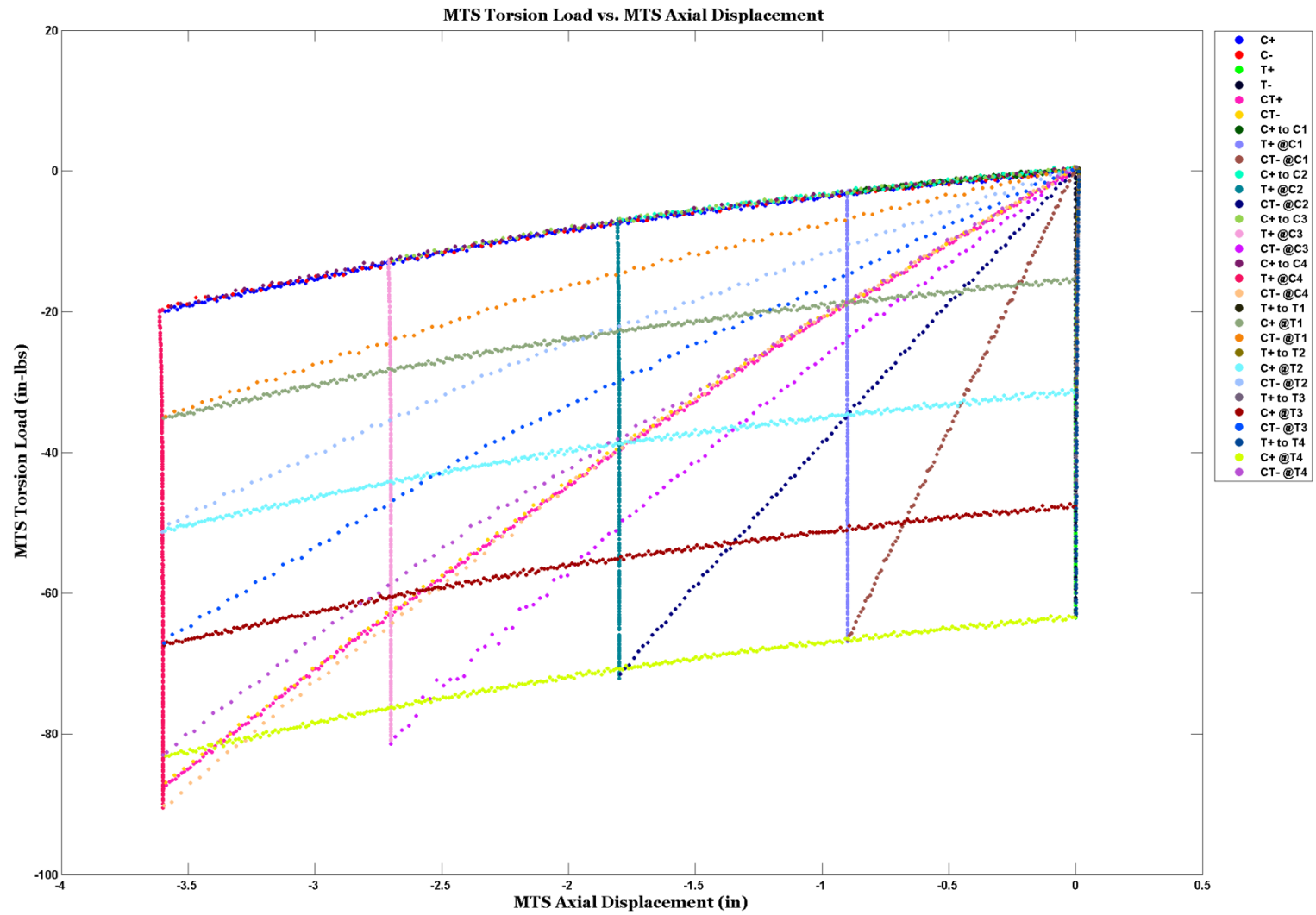
Figure G.20: Spring K104 Part 2 of Stage I – MTS Torsion Load vs. MTS Axial Displacement
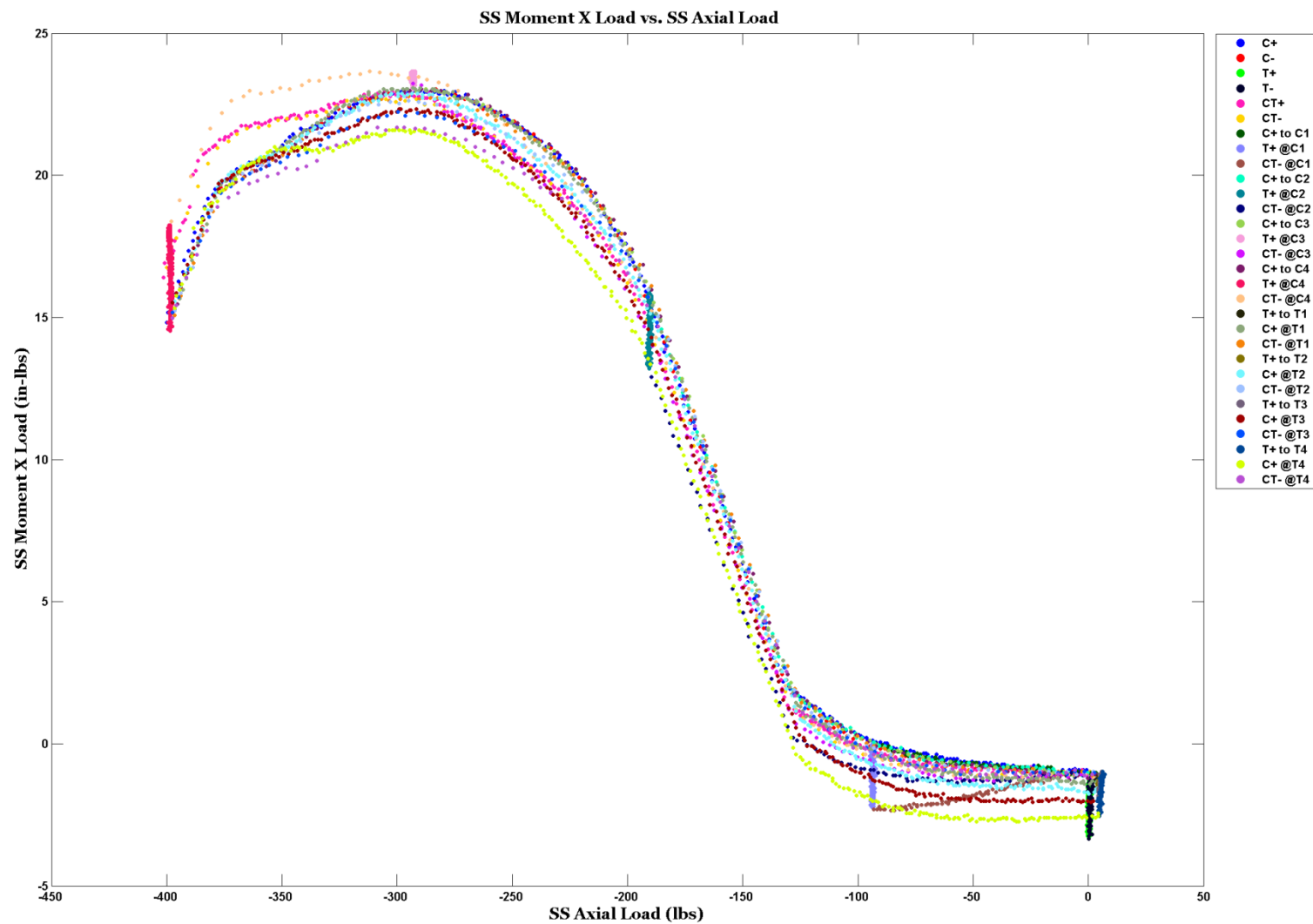
Figure G.21: Spring K104 Part 2 of Stage I 6 – Cell Moment X Load vs. 6-Cell Axial Load
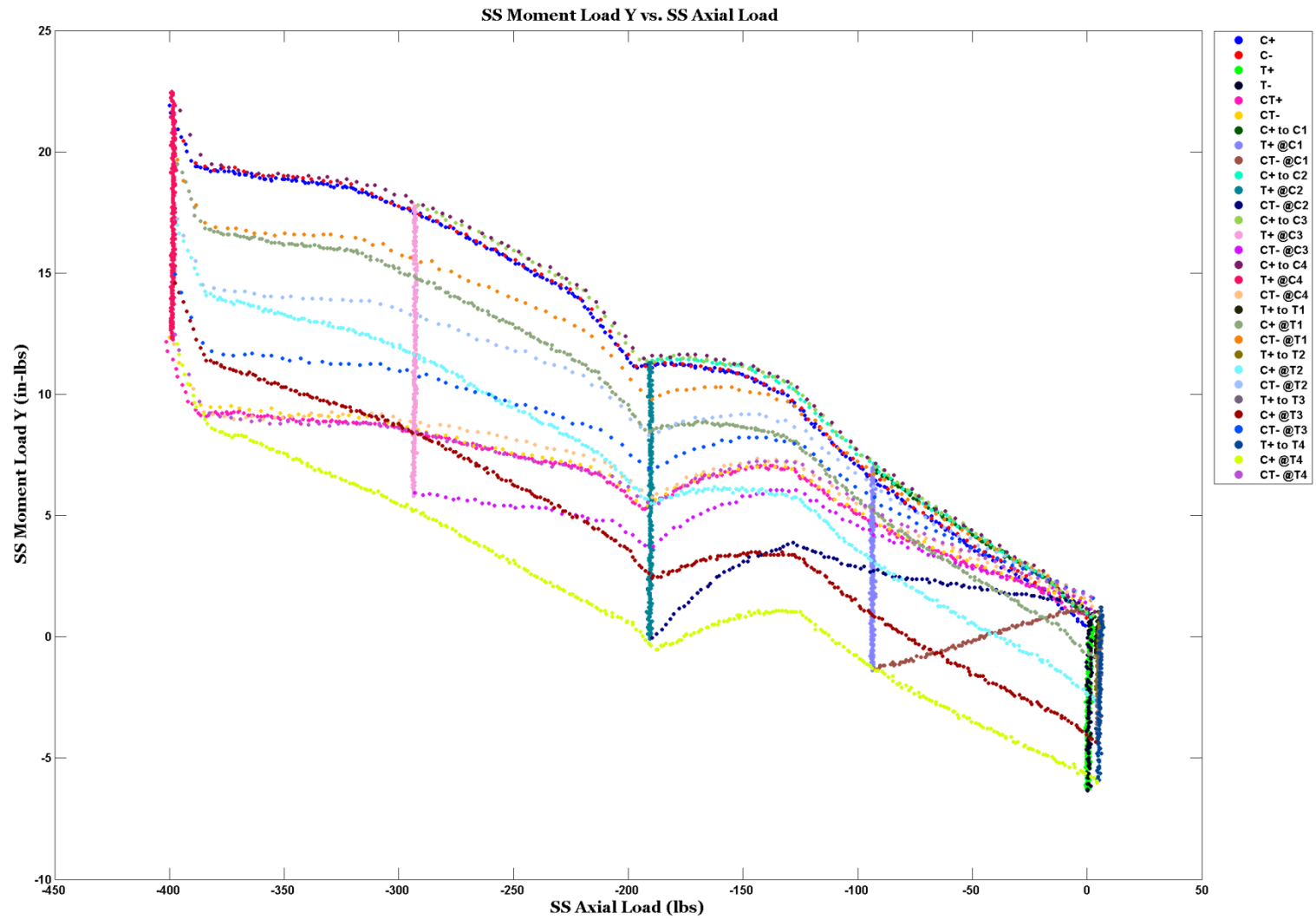
Figure G.22: Spring K104 Part 2 of Stage I 6 – Cell Moment Y Load vs. 6-Cell Axial Load
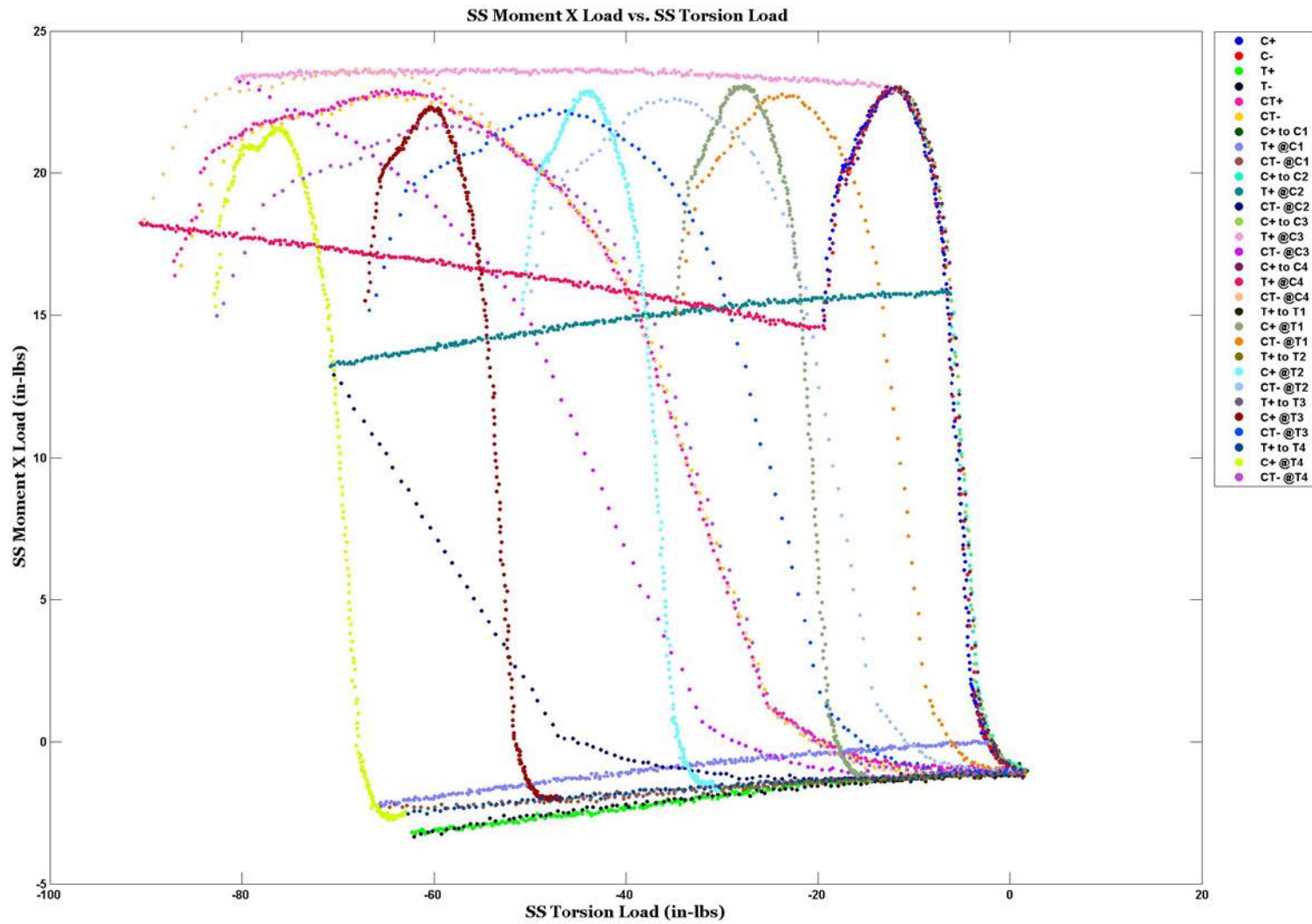
Figure G.23: Spring K104 Part 2 of Stage I – 6-Cell Moment X Load vs. 6-Cell Torsion Load
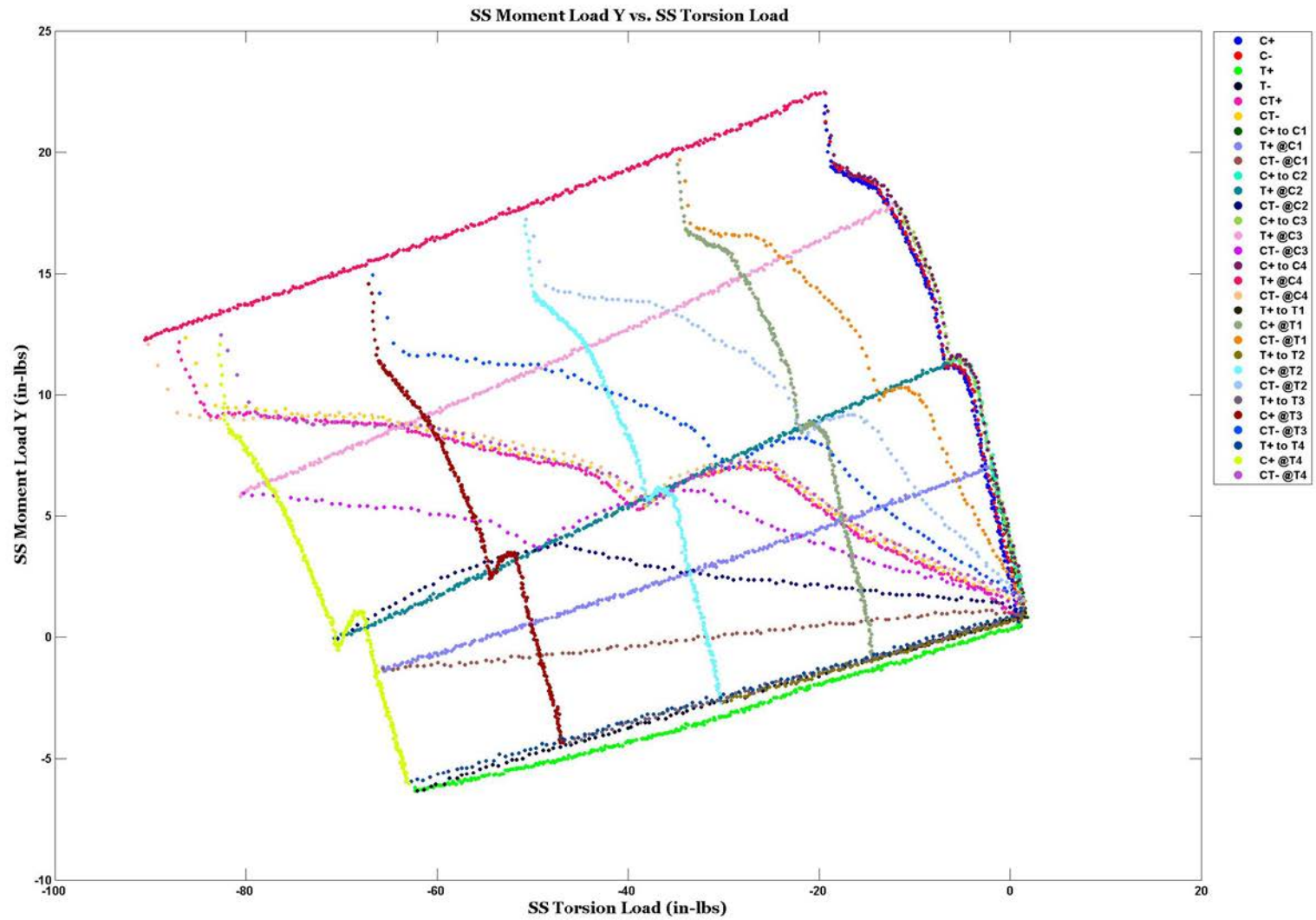
Figure G24: Spring K104 Part 2 of Stage I – 6-Cell Moment Y Load vs. 6-Cell Torsion Load

Stage II Test Preliminary Plots

The following figures present the preliminary plots used to analysis the testing jig and behavior of the K104 compression spring. Only the plots that present either axial or torsional results were used. The plots containing the shear and bending loads were not used due effects of the testing jig design. For the following Stage II plot, only the Part 1 (unwinding torque) plots are provided.

SPRING K104

STAGE II PART 1
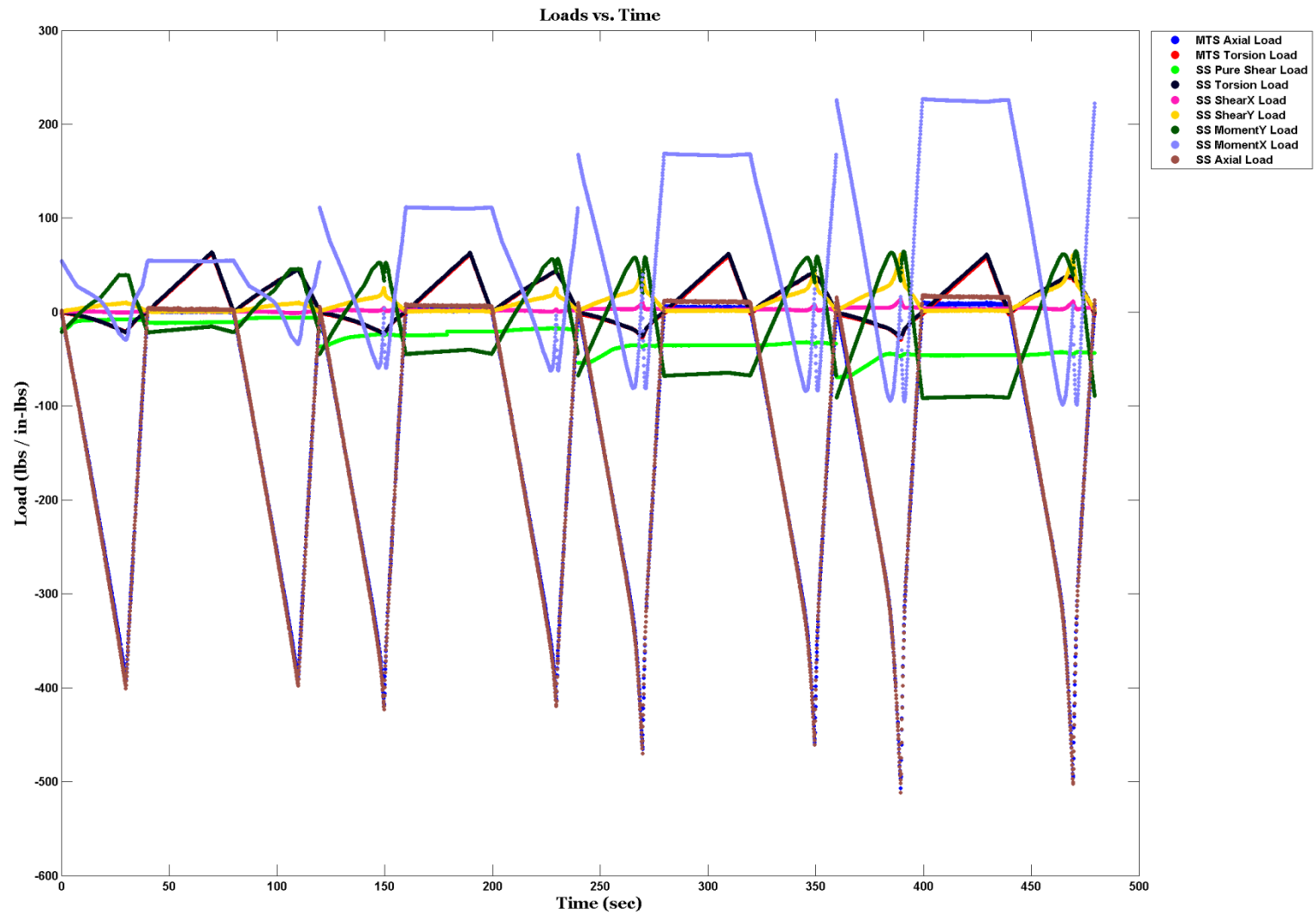
Figure H.1: Spring K104 Part 1 of Stage II – All 6 Cell and MTS Loads vs. Time
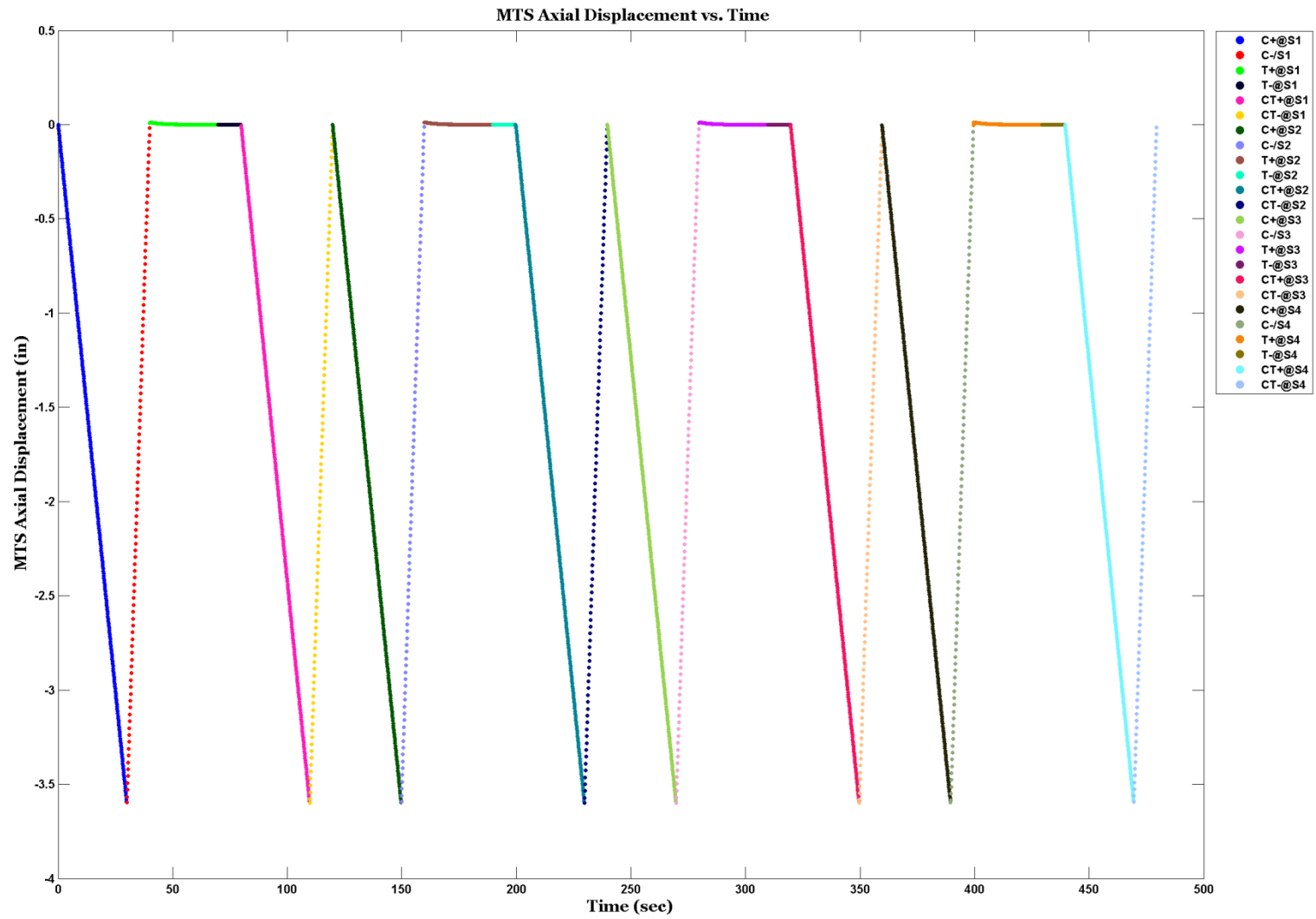
Figure H.2: Spring K104 Part 1 of Stage II – MTS Axial Displacement vs. Time
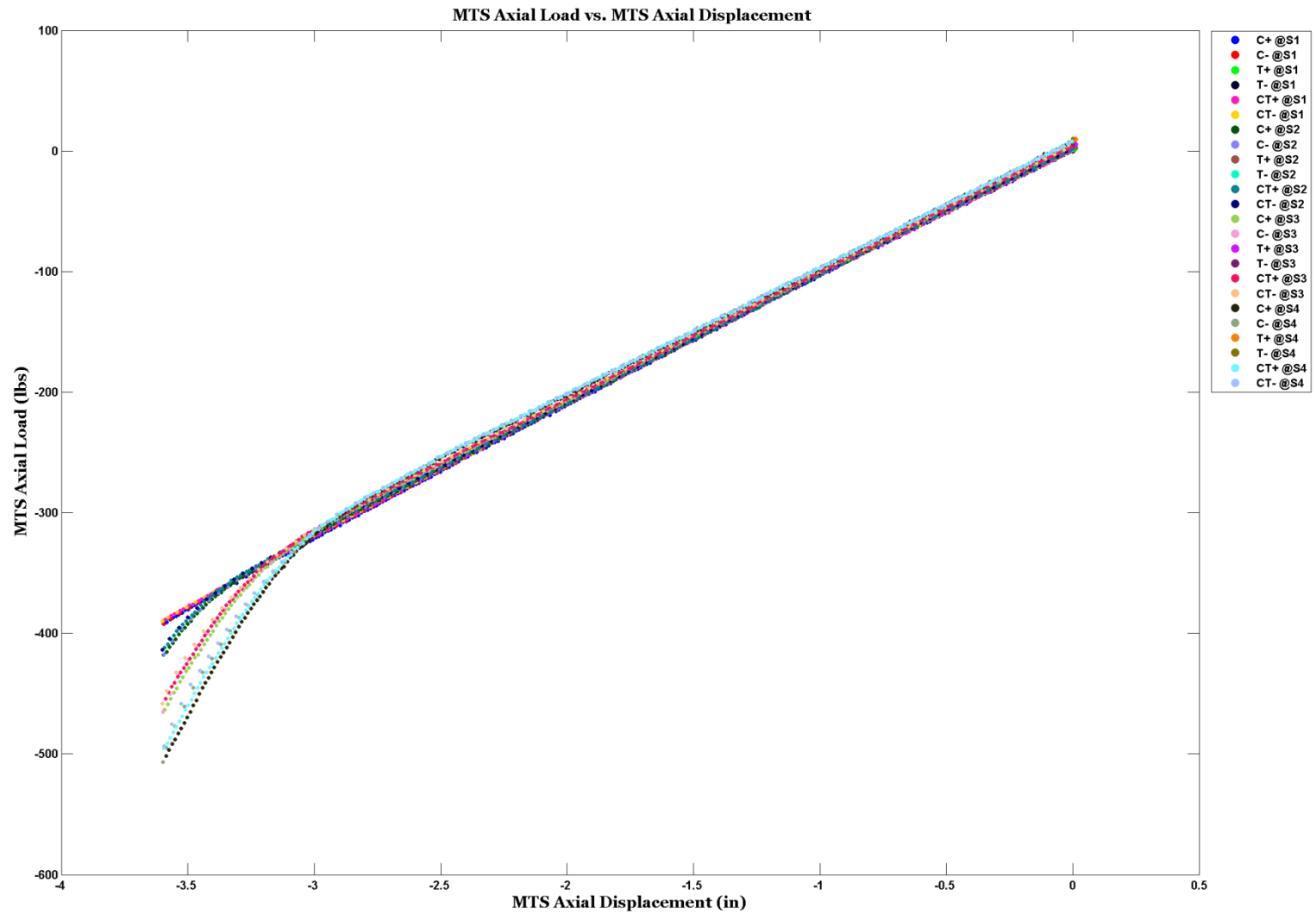
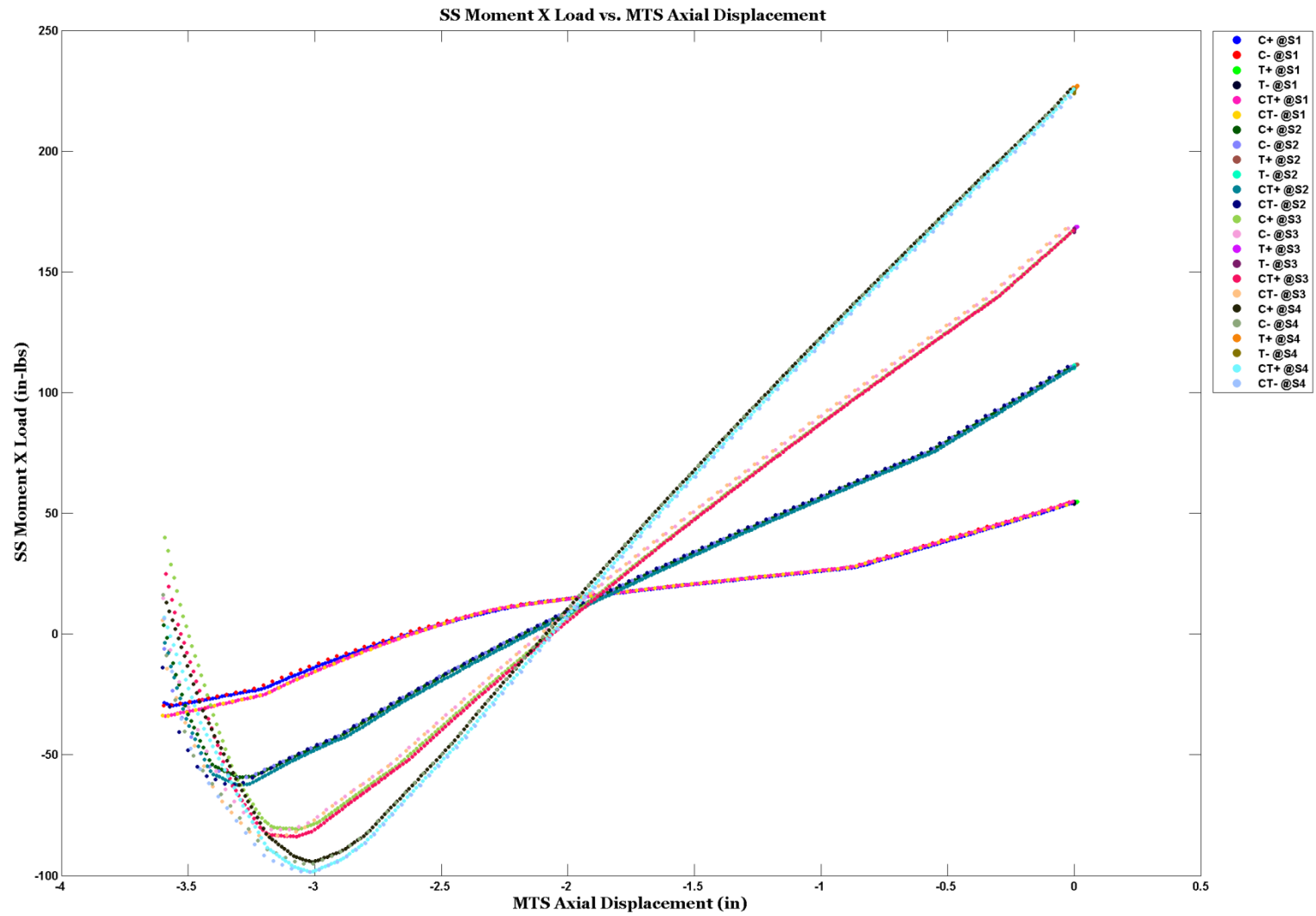Figure H.3: Spring K104 Part 1 of Stage II – MTS Axial Load vs. MTS Axial Displacment
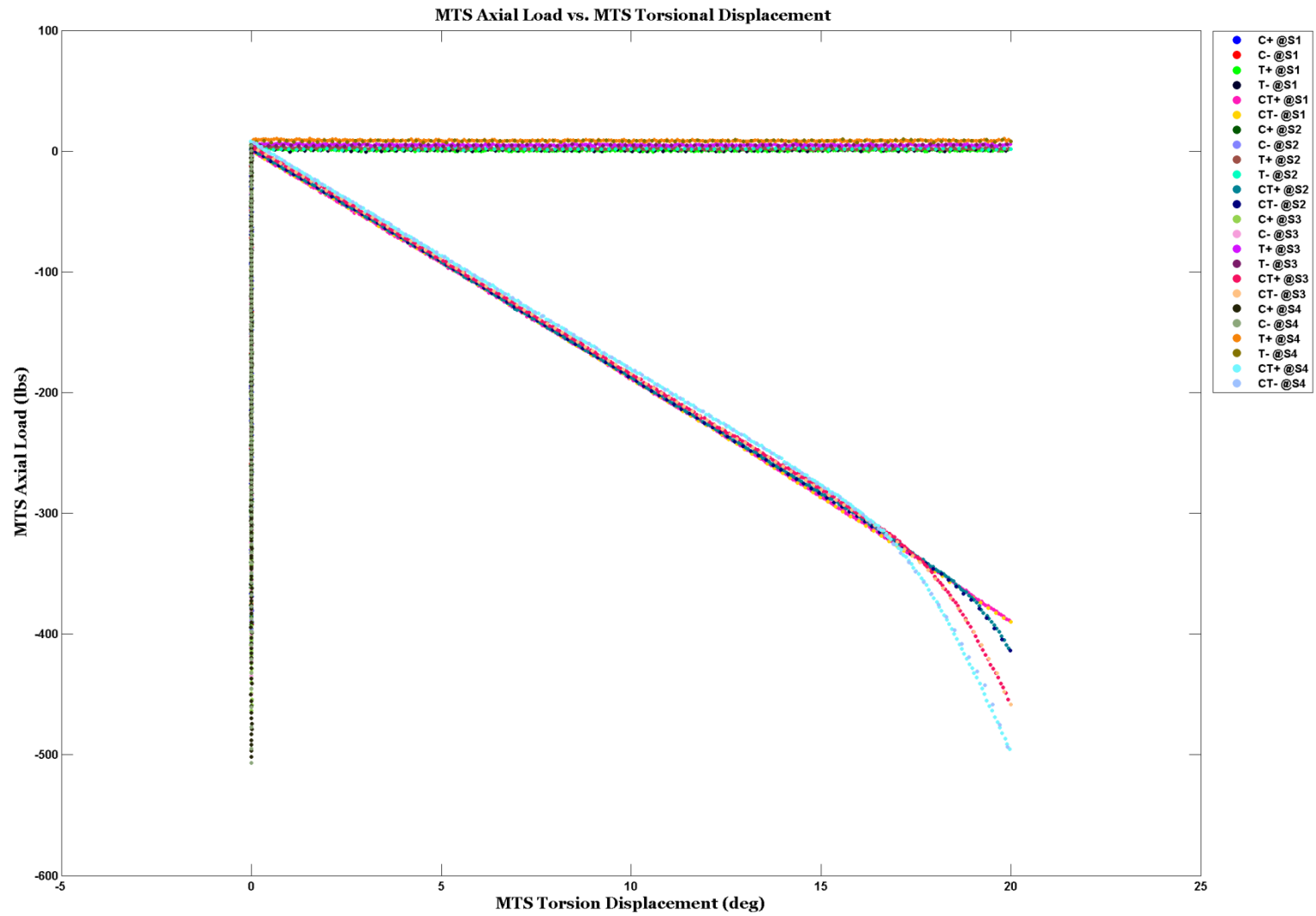
Figure H.4: Spring K104 Part 1 of Stage II – MTS Axial Load vs. MTS Torsional Displacement
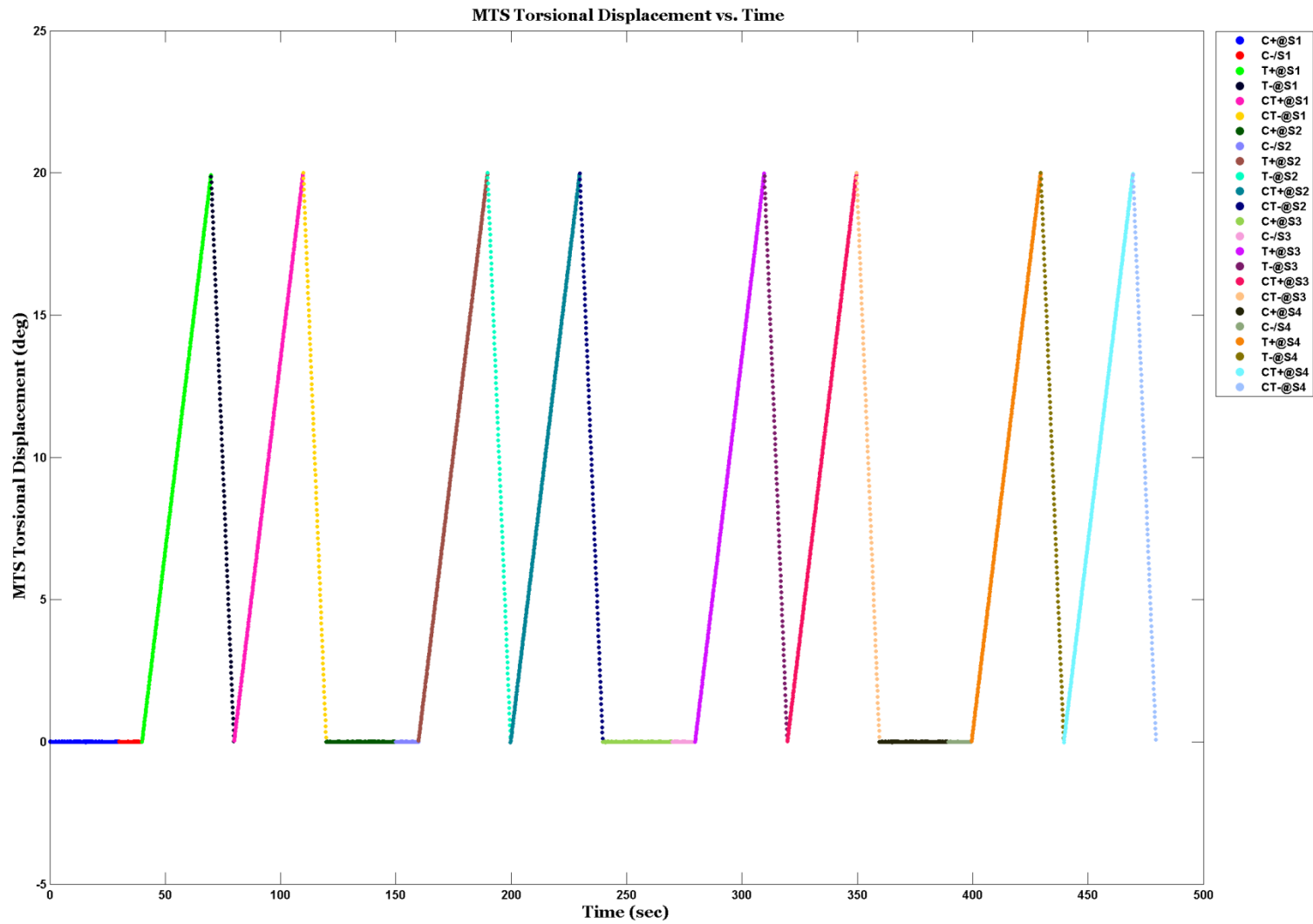
Figure H.5: Spring K104 Part 1 of Stage II – MTS Torsional Displacement vs. Time
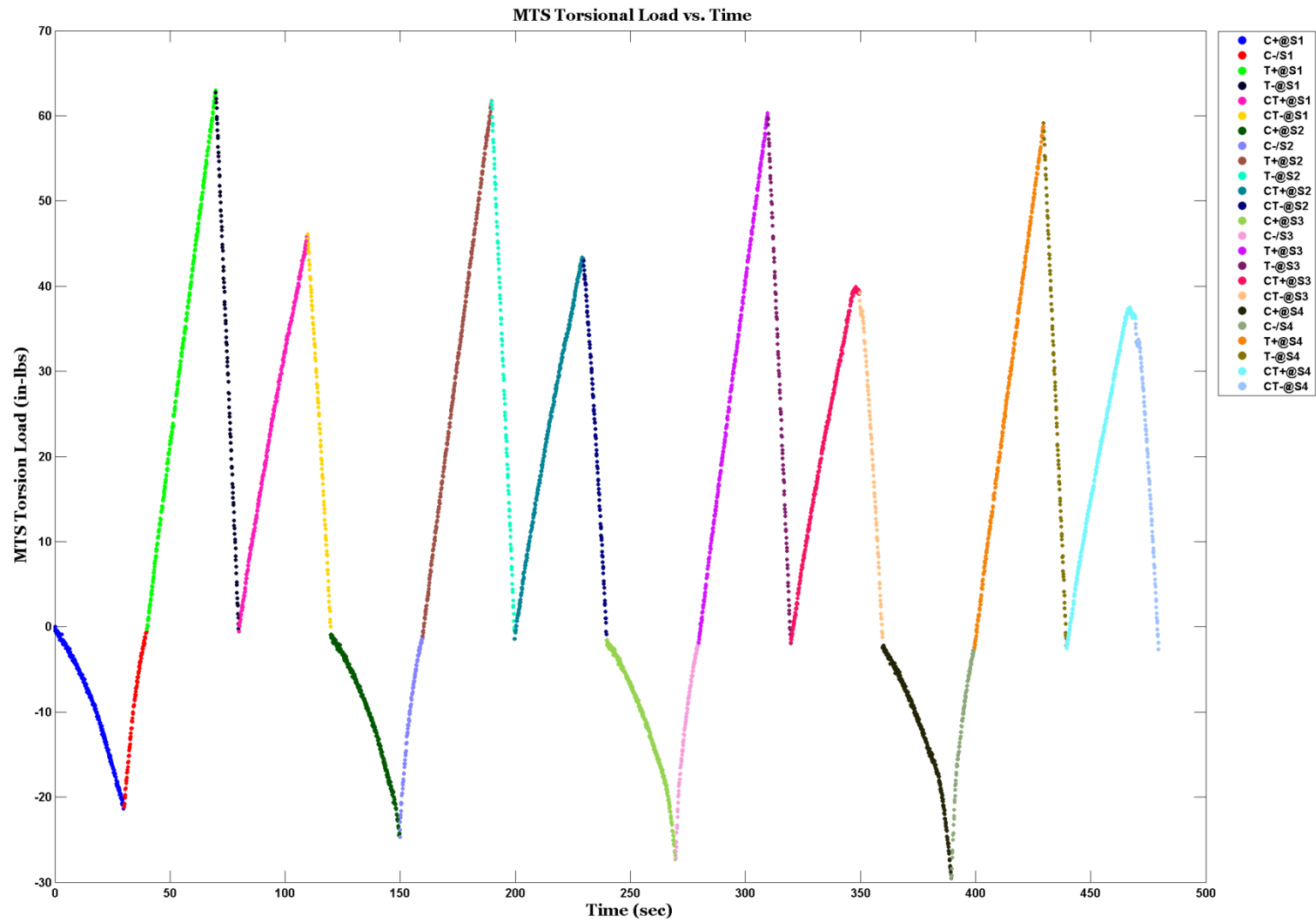
Figure H.6: Spring K104 Part 1 of Stage II – MTS Torsional Load vs. Time
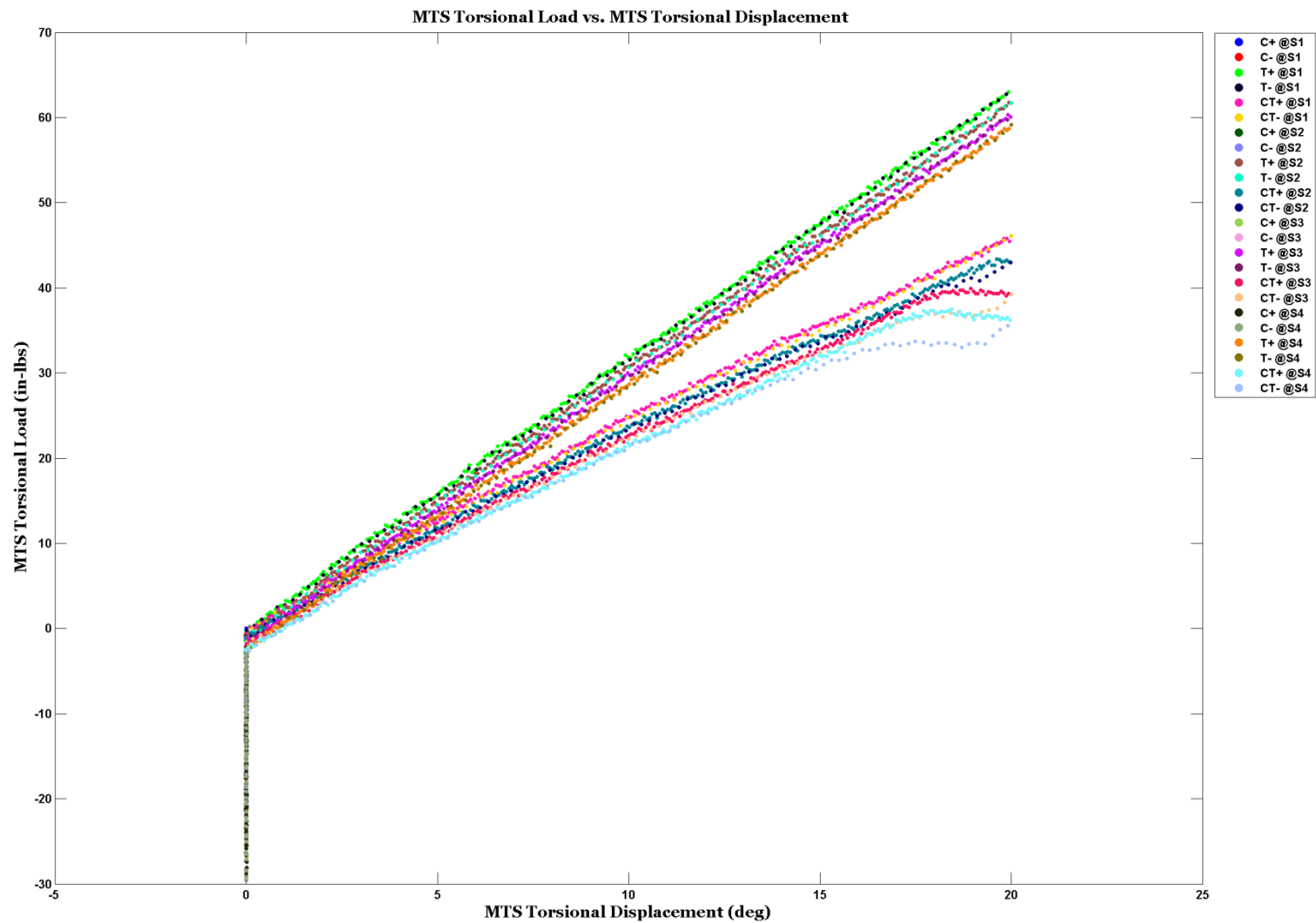
Figure H.7: Spring K104 Part 1 of Stage II – MTS Torsional Load vs. MTS Torsional Displacement

Figure H.8: Spring K104 Part 1 of Stage II – MTS Torsion Load vs. MTS Axial Displacement

Figure H.9: Spring K104 Part 1 of Stage II – 6-Cell Pure Shear Load vs. Time

Figure H.10: Spring K104 Part 1 of Stage II – 6-Cell Pure Shear Load vs. MTS Axial Displacement

Figure H.11: Spring K104 Part 1 of Stage II – 6-Cell Pure Shear Load vs. MTS Torsion Displacement

Figure H.12: Spring K104 Part 1 of Stage II – 6-Cell Pure Shear Load vs. 6-Cell Moment X Load
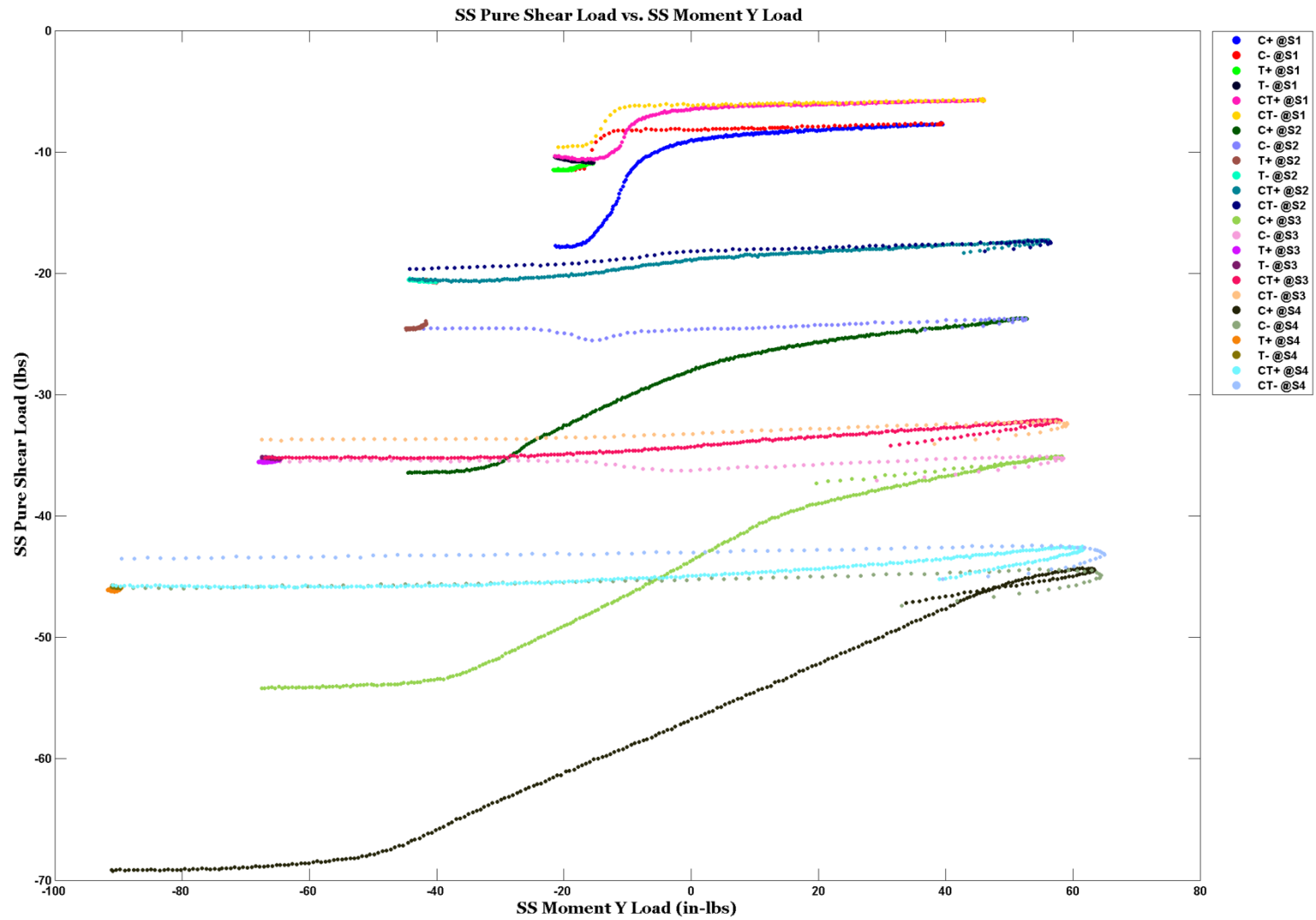
Figure H.13: Spring K104 Part 1 of Stage II – 6-Cell Pure Shear Load vs. 6-Cell Moment Y Load
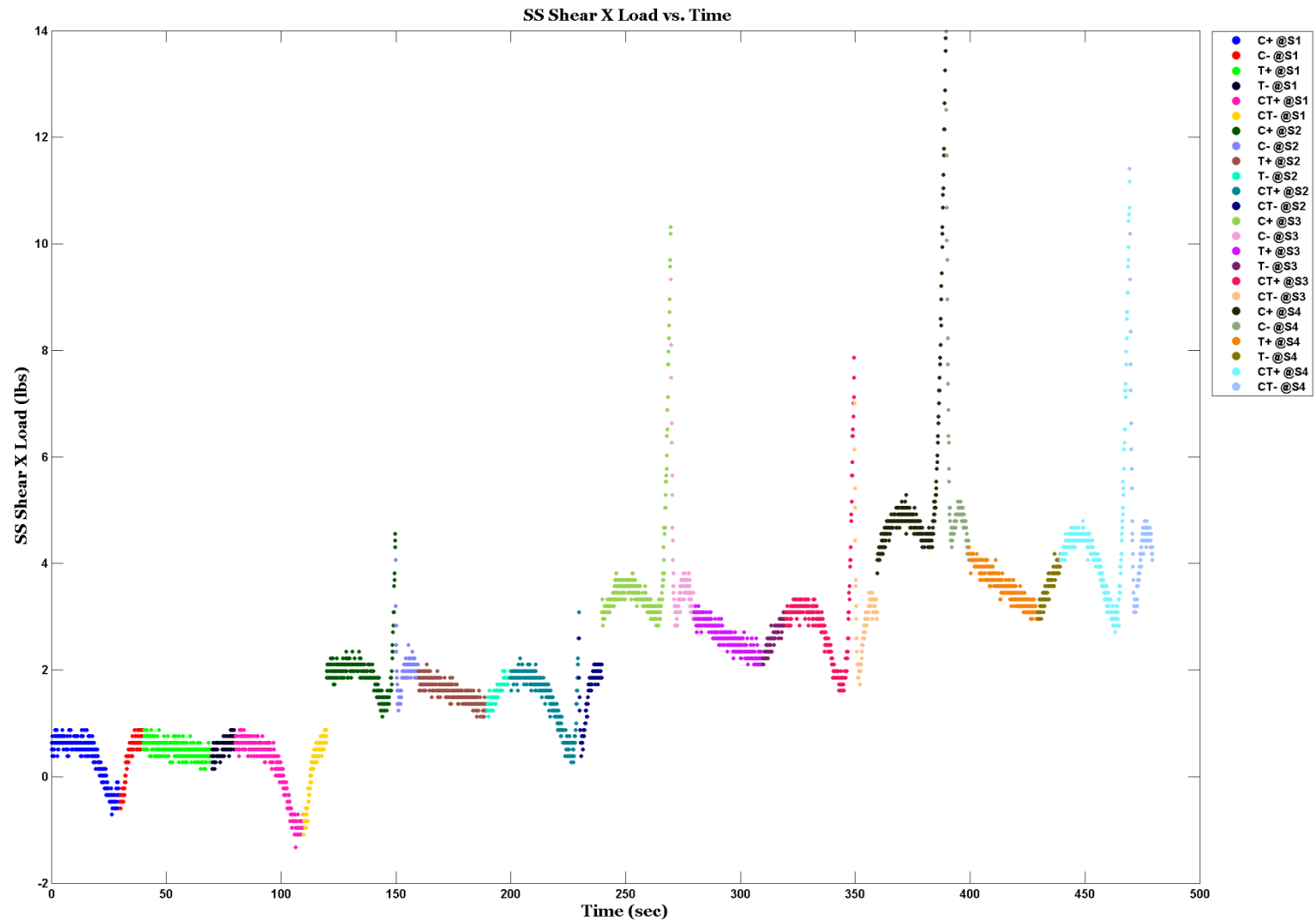
Figure H.14: Spring K104 Part 1 of Stage II – 6-Cell Shear X Load vs. Time

Figure H.15: Spring K104 Part 1 of Stage II – 6-Cell Shear X Load vs. MTS Axial Displacement
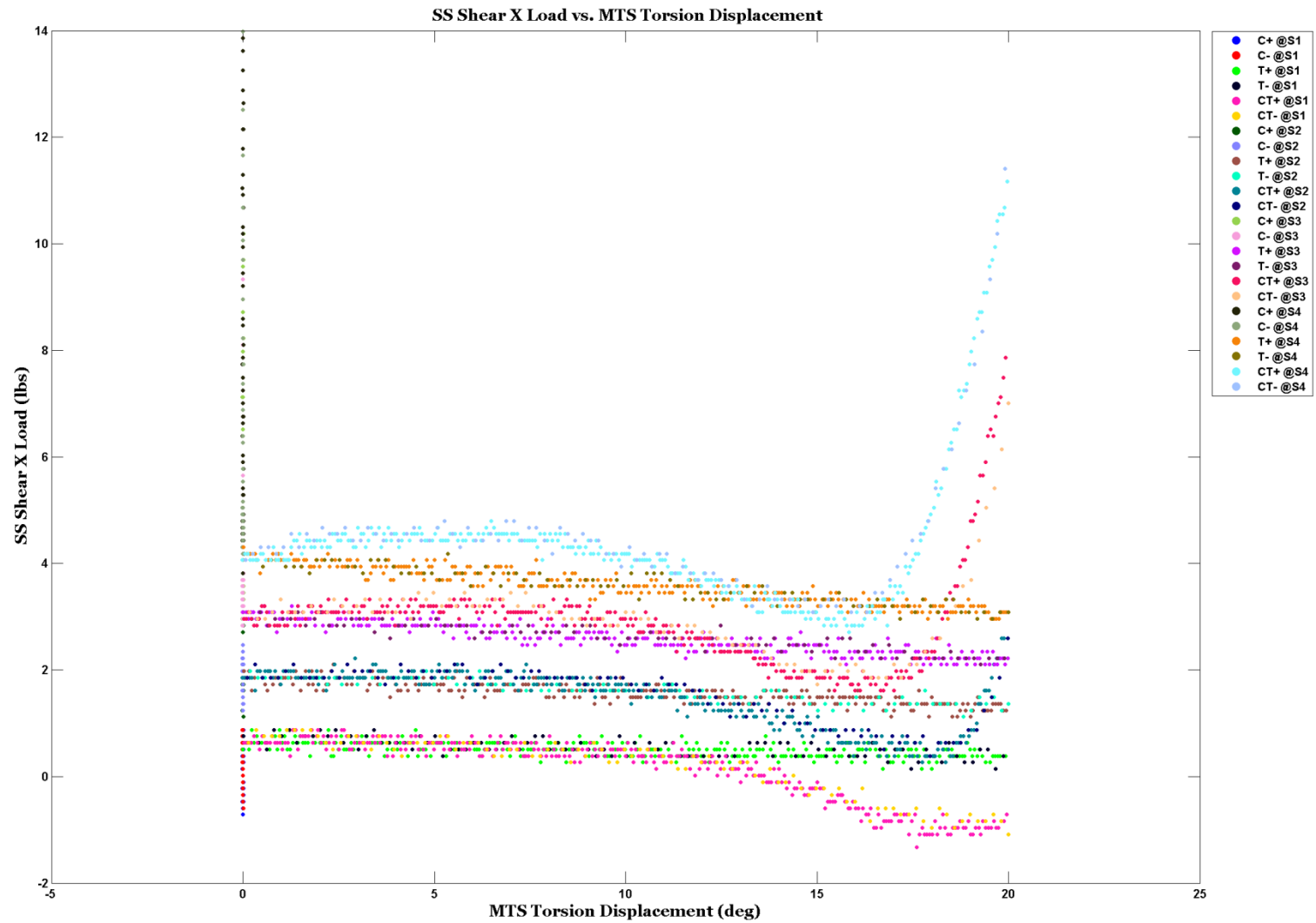
Figure H.16: Spring K104 Part 1 of Stage II – 6-Cell Shear X Load vs. MTS Torsion Displacement
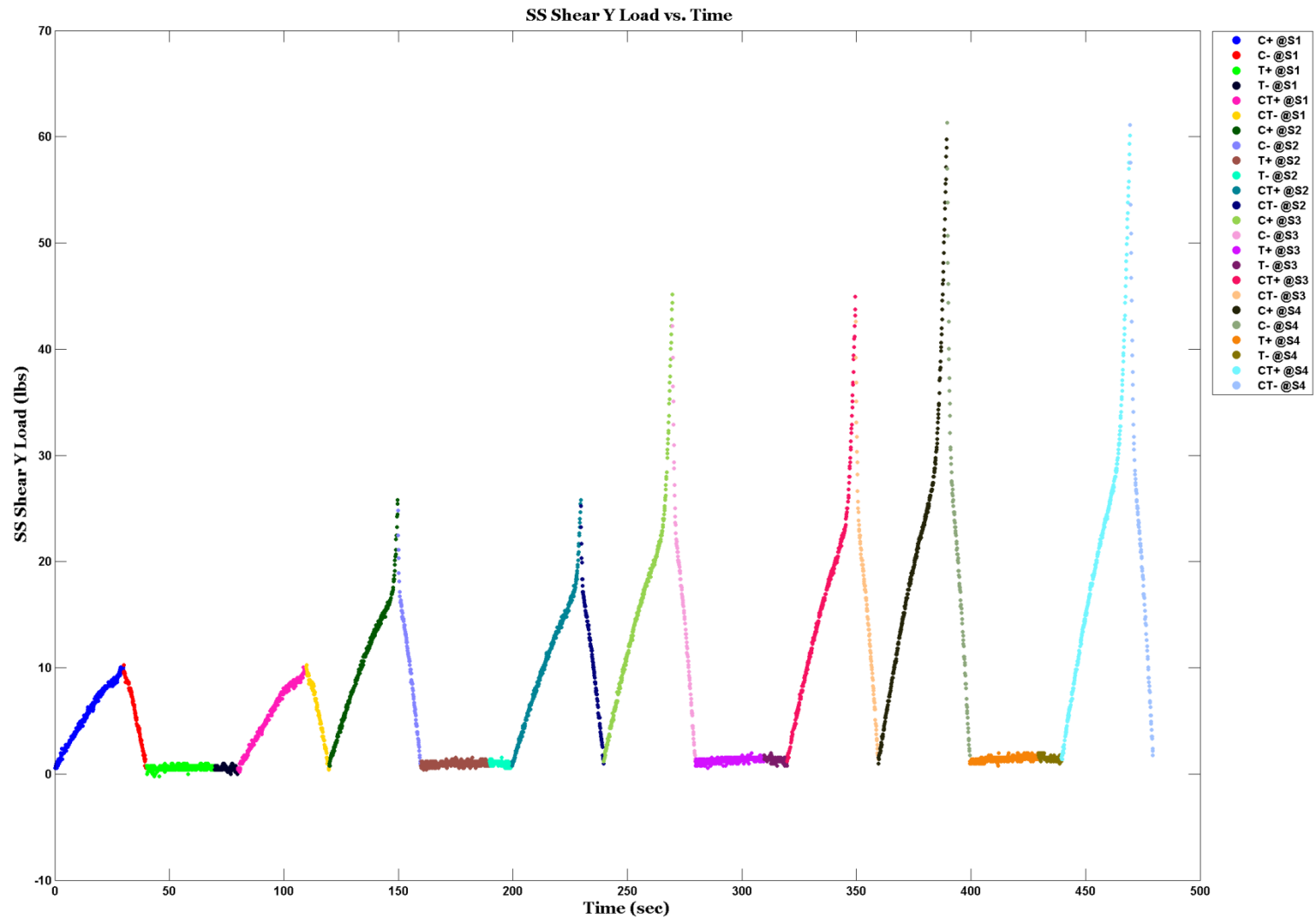
Figure H.17: Spring K104 Part 1 of Stage II – 6-Cell Shear Y Load vs. Time
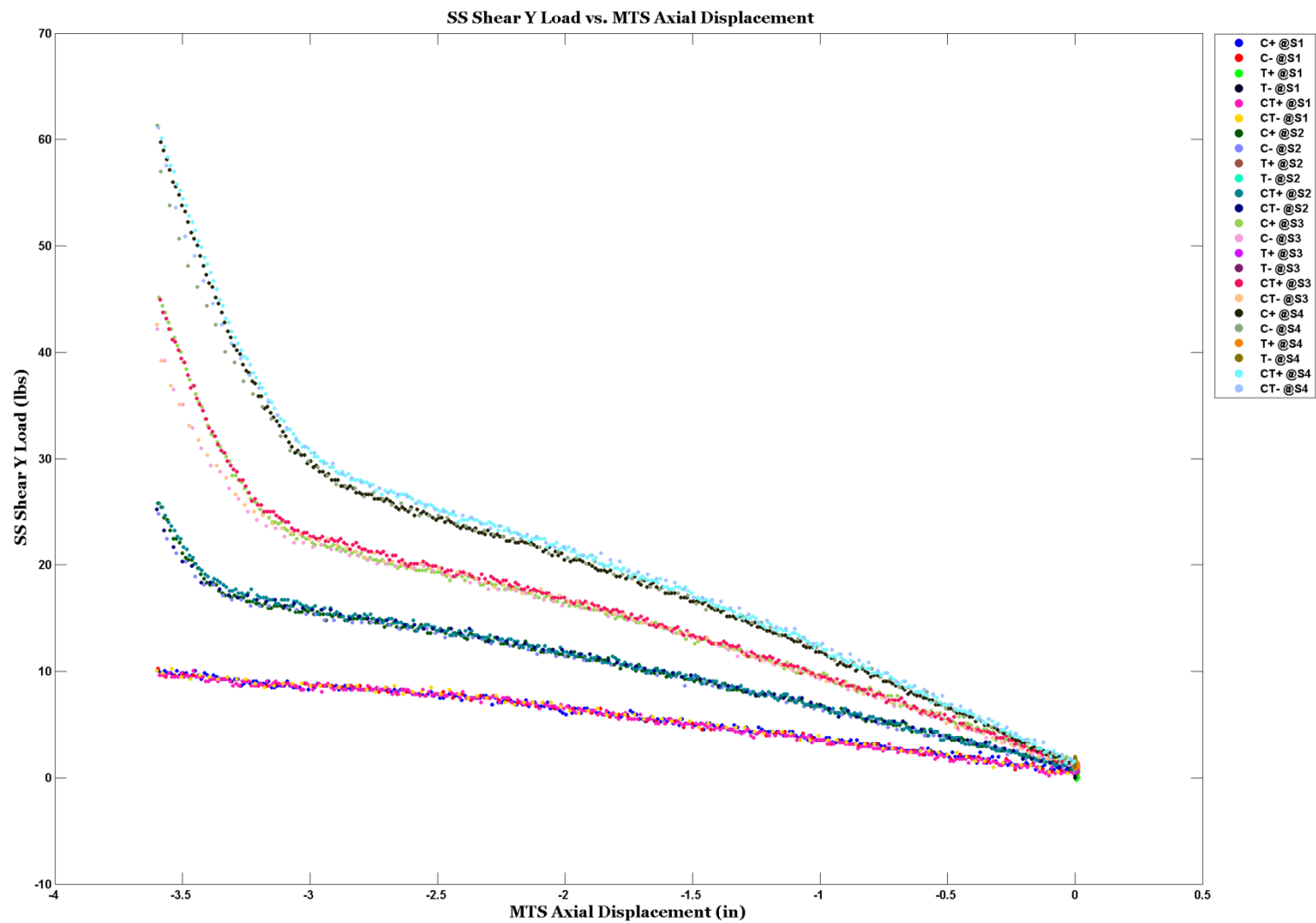
Figure H.18: Spring K104 Part 1 of Stage II – 6-Cell Shear Y Load vs. MTS Axial Displacement
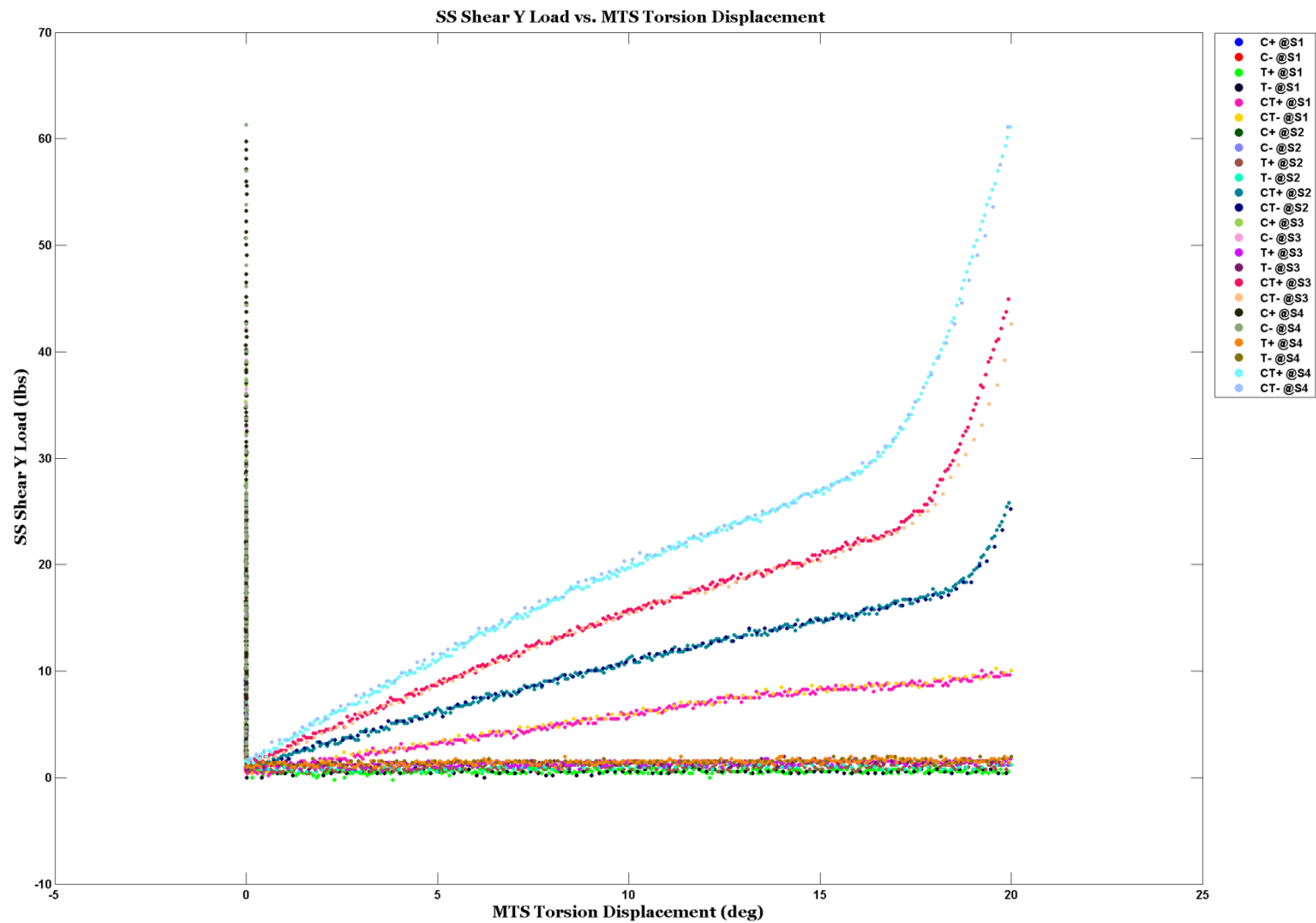
Figure H.19: Spring K104 Part 1 of Stage II – 6-Cell Shear Y Load vs. MTS Torsion Displacement

Figure H.20: Spring K104 Part 1 of Stage II – 6-Cell Moment X Load vs. MTS Axial Displacement
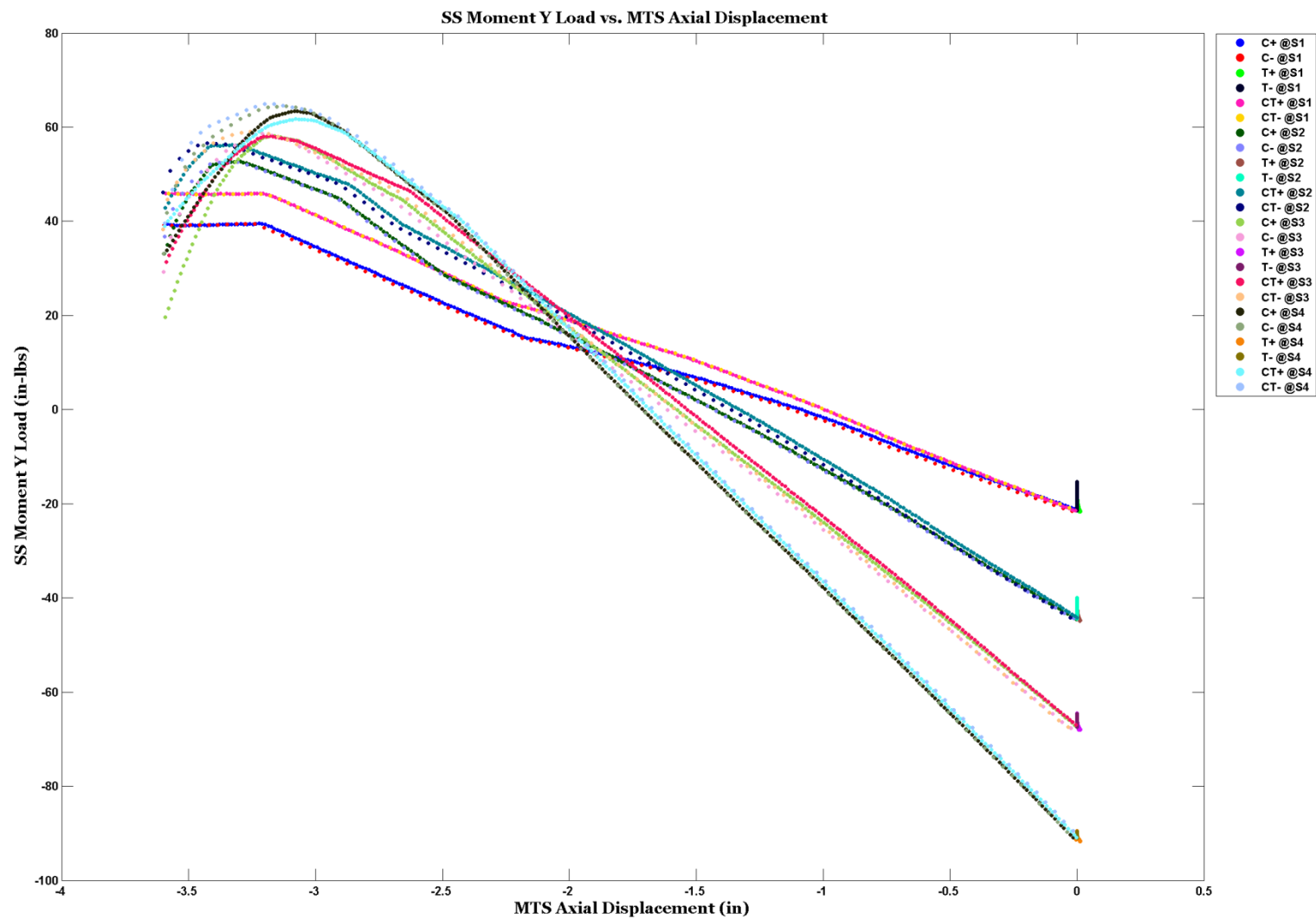
Figure H.21: Spring K104 Part 1 of Stage II – 6-Cell Moment Y Load vs. MTS Axial Displacement

APPENDIX I

MTS and StrainSmart Test Procedure for Compression Spring Testing

- Turn on the MTS hydraulics and pump power
- Manually return the crosshead to both zero displacement and rotation
- Run at least a thirty minute warm-up cycle for the hydraulic system
    - o Warm-up procedure used was to apply a cyclic displacement of the axial displacement at 95% of the full scale range using the built in function generator
    - o Optional: Consult the MTS Manual for a standard warm-up procedure

- Turn on StrainSmart 5100B Scanners
- Open StrainSmart project "Custom 6 Axis Load Cell Transducer Assigned"
- Connect 6–Cell's six D-sub connectors to StrainSmart strain gage cards on back of scanners
- Adjust "channel assignments" in StrainSmart to match the channel number each load channel was connected to (else check assignments first and connect D-subs accordingly)
- Place StrainSmart into "Online State" – Activate GUI button at bottom left of StrainSmart window (zeroing channels and arming tests cannot be completed until this step is completed)
- Zero/Calibrate 6-Cell in StrainSmart
- Stop MTS warm-up procedure
- Mount testing Jig to MTS crosshead
- Move MTS bulk crosshead to elevated position to allow enough room to mount compression spring
- Zero both the 6–Cell and MTS load channels
- Mount the spring to the Jig connected to MTS crosshead
- Place MTS crosshead/actuator at zero displacement (highest position to allow maximum compressive displacement)
- Lower MTS bulk crosshead until spring is almost touching bottom mount housing
- Bolt compression spring down into the mount housing (this causes a tensile load which is read by the MTS load cell)
- Lower MTS bulk crosshead until load returns to zero
- Tighten four bolts on the MTS bulk crosshead after MTS axial load is back to zero
- Zero both 6–Cell and MTS load cells once again
- Select the correct test protocol to be ran in the MTS multipurpose testware
- Name specimen on MTS software to unique identifier
- Name test on StrainSmart to same unique identifier
- Start MTS program (program will only start time and prepare live graphs, data collection and commands have not started)
- Adjust the MTS graphs to personal preferences

- Arm StrainSmart test
- Open StrainSmart online display and view all six loads plus the sync signal in Strip Chart View
- Run StrainSmart test
- Wait 5 to 10 seconds
- Activate Synchronization signal for both StrainSmart and MTS (sync should be connected to MTS Auxillary Channel 1 input)
- Remove sync signal from StrainSmart Strip Chart viewport and rescale axes
- Once MTS test protocol is completed, stop StrainSmart test
- Export (name.xls) and Save StrainSmart test to flash drive
- Locate Specimen on MTS computer and copy test data to flash drive
- Repeat at least three times per spring for each test protocol

Additional Info on Stage II protocol

- Once first sync signal is activated for MTS and StrainSmart systems, a GUI button will appear on MTS command window
- Manually apply shear displacement to maximum deflection and return to zero displacement
- Go to MTS computer and click the GUI button that says "S1 Curve completed"
- MTS program is now paused
- Move shear displacement to S1 level
- Activate sync signal on both MTS and StrainSmart systems (this continues MTS program and provides additional data alignment info)
- Program will pause again once S1 curve are completed
- Move to S2 position manually
- Activate sync signal once again
- Repeat until all shear displacement static points are completed
- Export and save data as usual

Shut down MTS once spring and test jigs are removed

Circuit Diagrams for 6–Cell Build and Gage Placement

Torsion :

P+

TA2   TA5

TA1   AT①   AT③   TA6

TD2   TC5

TD①   DT①   CT②   TC6

TD1   Yellow wire   S-
w/ red
S+   stripes

TD6   DT③   CT①   TC1

TD5   BT③   BT①   TC2

TB6   TB1   BlK

Bro   TB5   TB2

P-

Connectors Labeled, T✱

$\underline{\underline{S_x}}$:

P+

XB2   XB5

BX①   BX③

XB1   XB6

S+   S−

XD2   DX①   DX②   XD5

XD1   XD6

P−

$\underline{\underline{S_y}}$:

P+

XA2   XA5

AX①   AX③

XA1   XA6

S+   S−

XC2   CX①   CX②   XC5

XC1   XC6

P−

214

$M_x:$

P+
MA4
MC3
AM②
CM②
MA3
MC4
S+
S-
MC2
MA1
CM①
AM①
MC1
MA2
P-

$M_Y:$

P+
MB4
MD3
BM②
DM②
MB3
MD4
S+
S-
MD2
MB1
DM①
BM①
MD1
MB2
P-
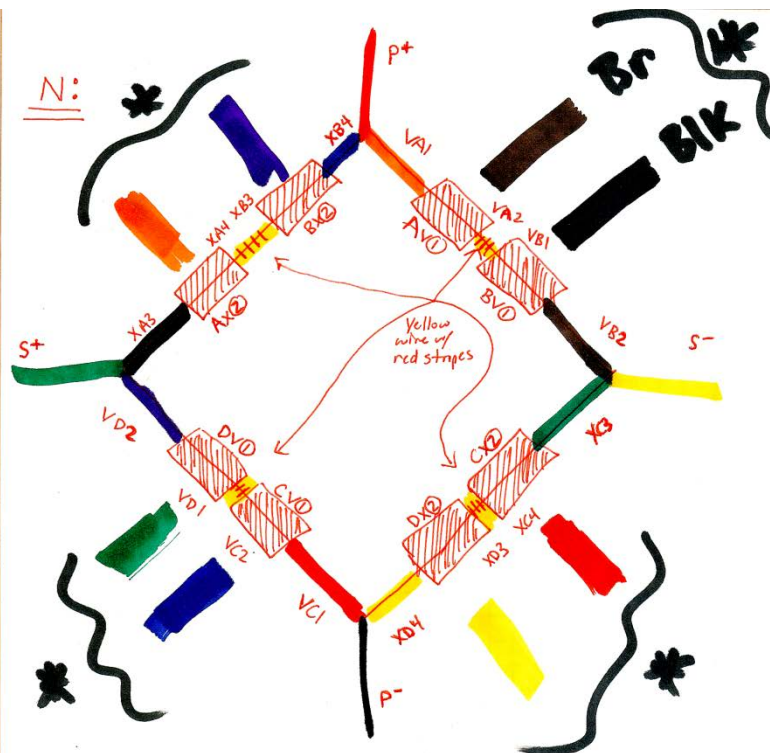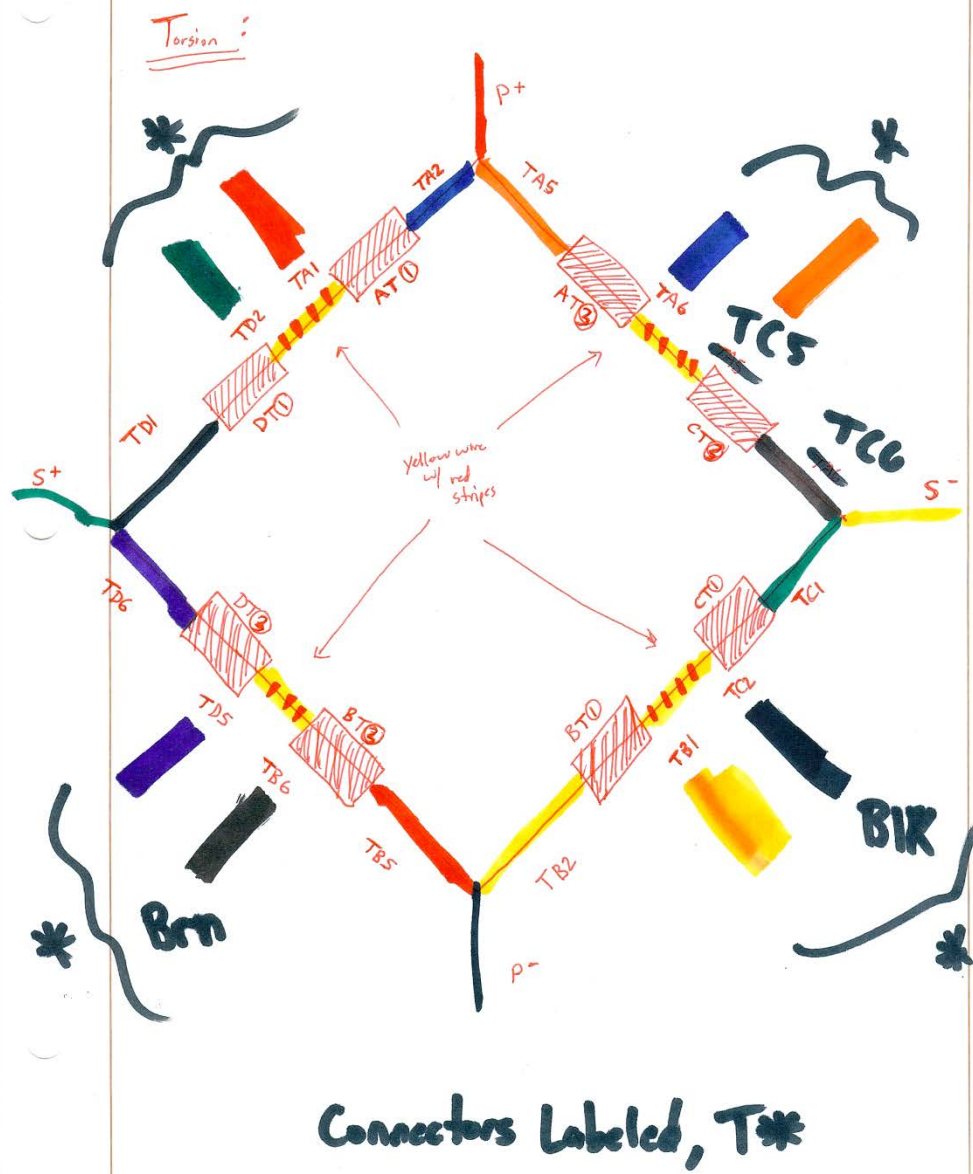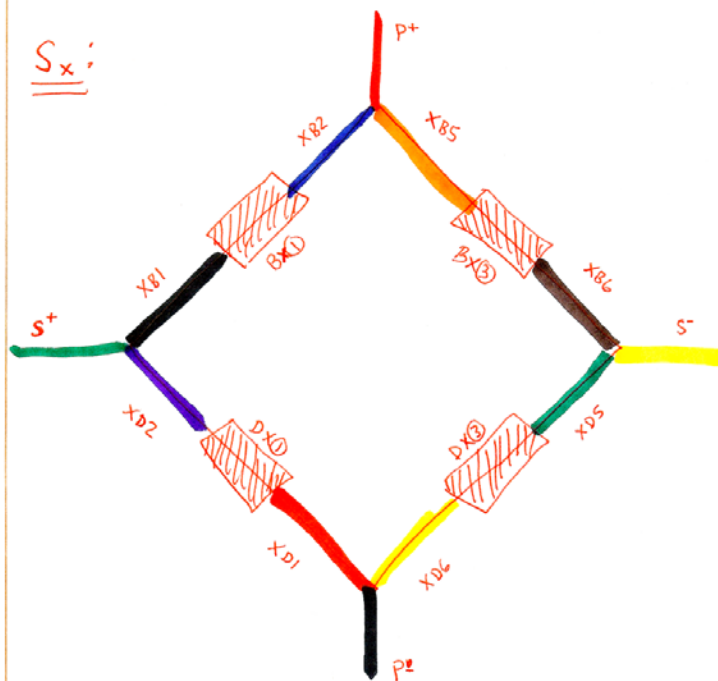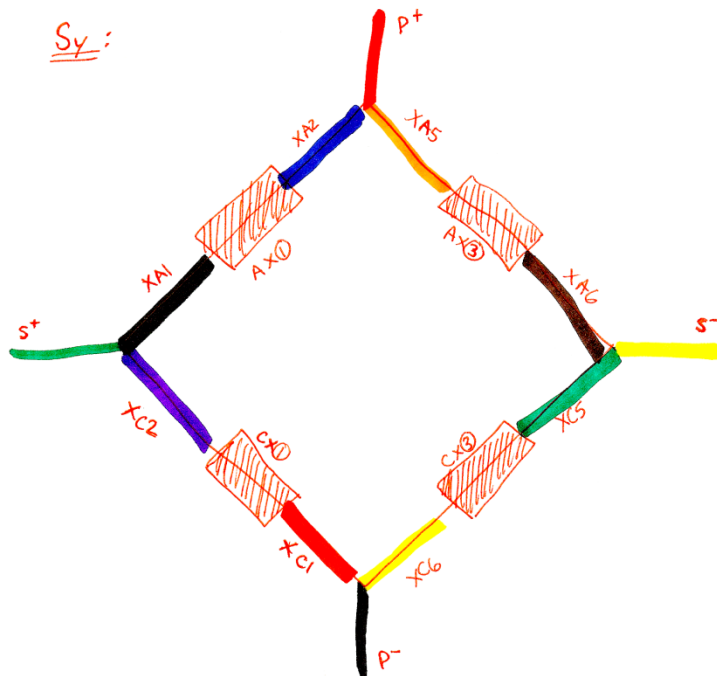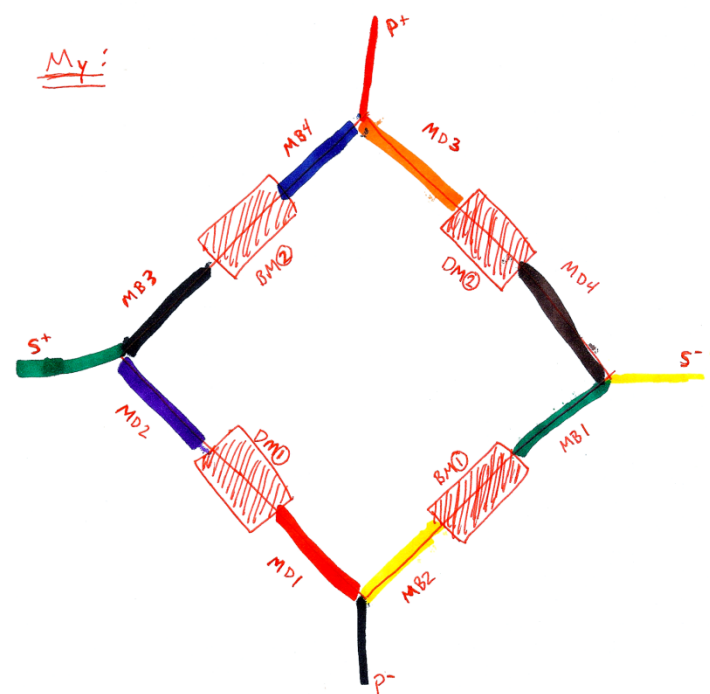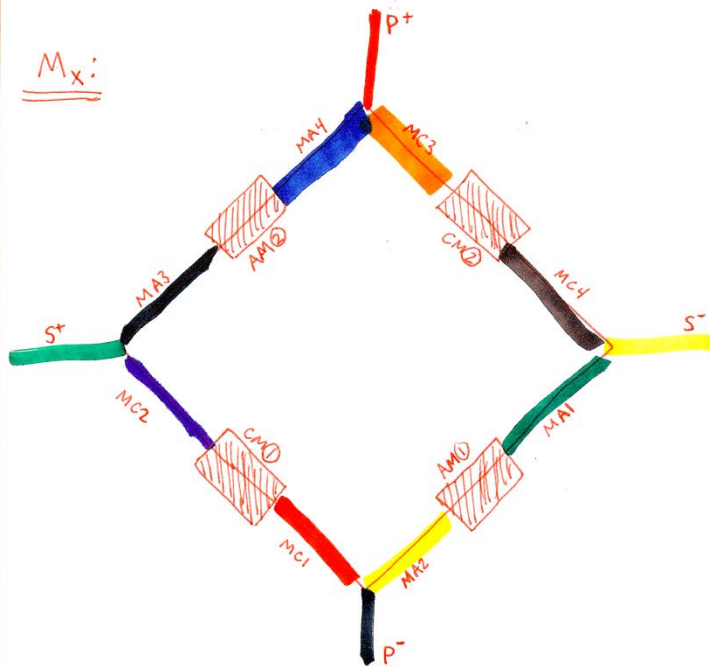
CONNECTOR BOARD
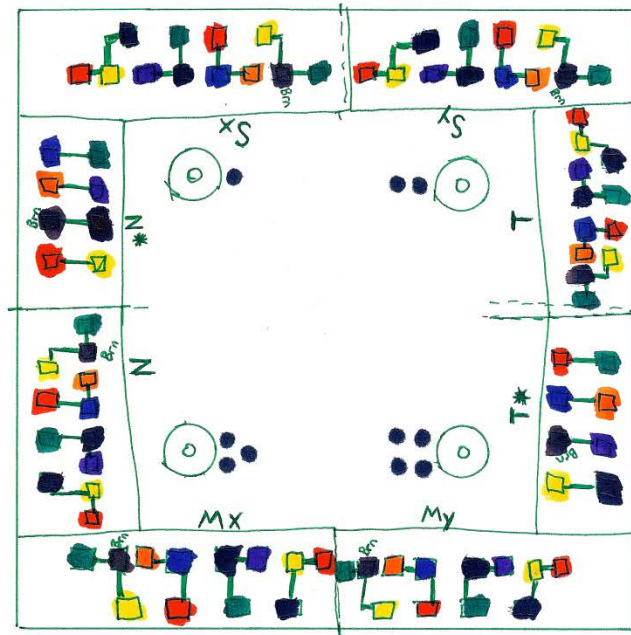
Output Connections:

S^-: [yellow box] : White Insulated Wire

P^+: [red box] : Red Insulated wire

S^+: [green box] : Green Insulated wire

P^-: [dark blue box] : Yellow Insulated wire/with Black Marker Tips
or White

216

A   B   C   D

AIIC

X: Axial Shear

T: Torsion

V: Axial Forces

M: Moment

① ② ③ A1 A2 A3 A4 A5 A6
① ② ③ B1 B2 B3 B4 B5 B6
① ② ③ C1 C2 C3 C4 C5 C6
① ② ③ D1 D2 D3 D4 D5 D6

① ② ③ A1 A2 A3 A4 A5 A6
① ② ③ B1 B2 B3 B4 B5 B6
① ② ③ C1 C2 C3 C4 C5 C6
① ② ③ D1 D2 D3 D4 D5 D6

① A1 A2
① B1 B2
① C1 C2
① D1 D2

① ② A1 A2 A3 A4
① ② B1 B2 B3 B4
① ② C1 C2 C3 C4
① ② D1 D2 D3 D4
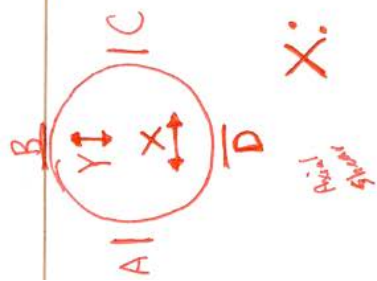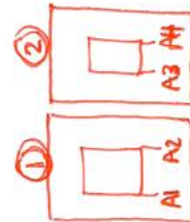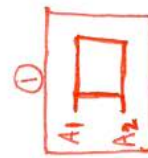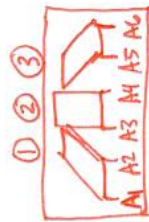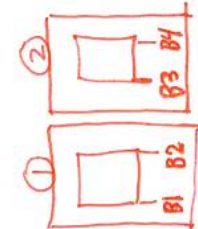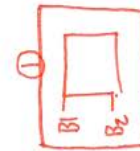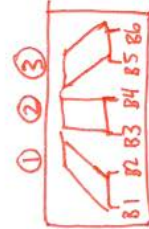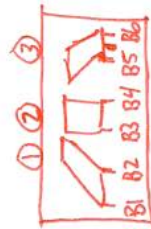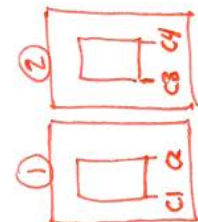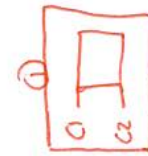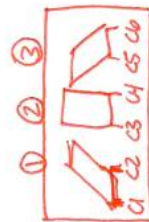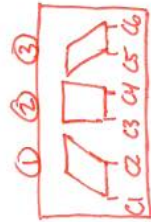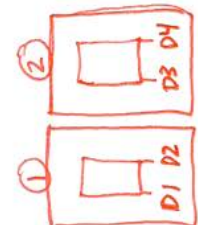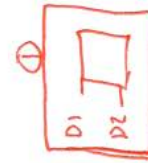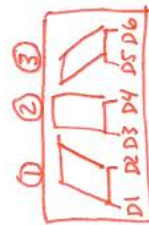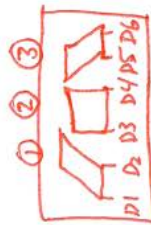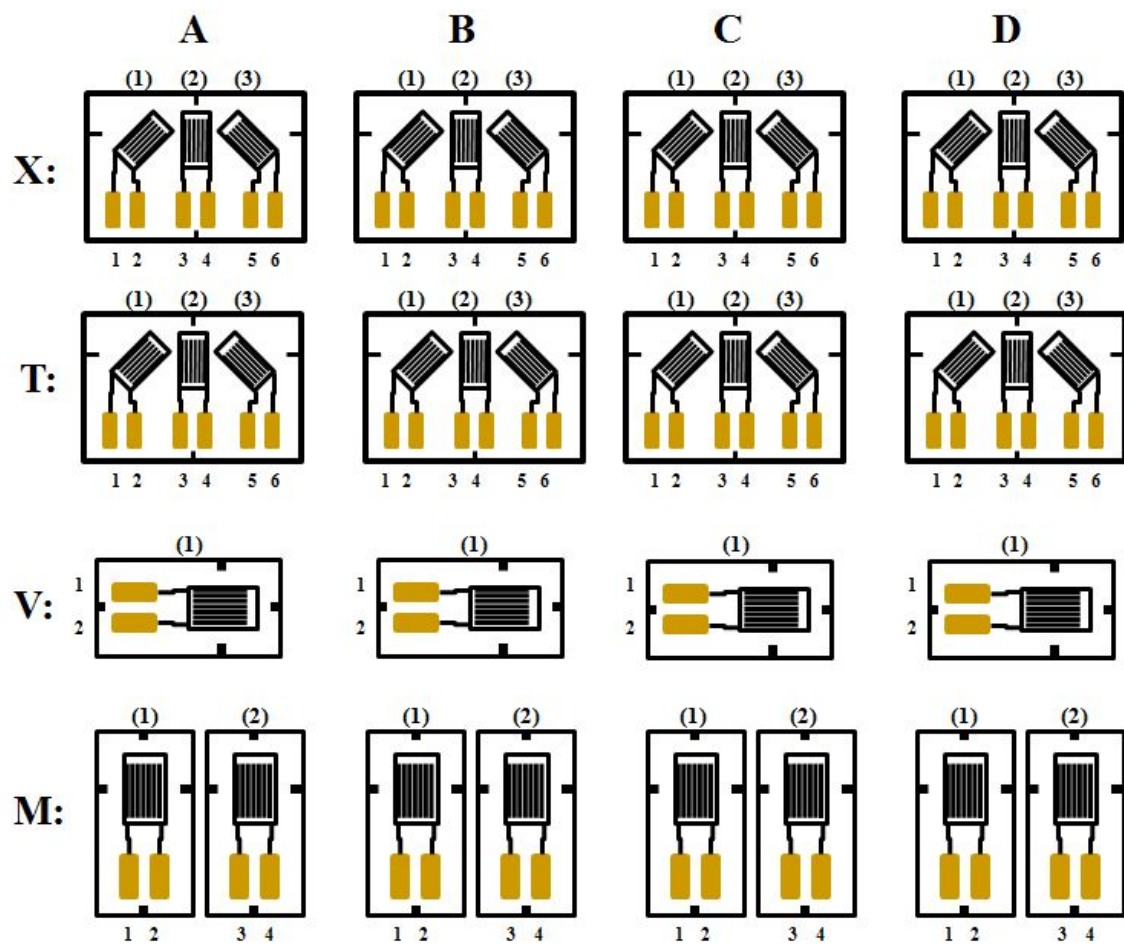
APPENDIX K

Load Cell and Jig Design Drawings

Ø2.125

Ø3.250

7 - I or F Ø Holes
Taped for 5/16" Bolts

5/16-18 Tapped Hole

.750

.750

.850

.400

3.000

5.000

R.250

.250

3.250

SECTION E-E
SCALE 1 : 1.25

220

2 x ⌀0.2570 for 5/16 -18 Counter Sunk

4.0000

0.5000

0.5000

2.0000

1.5000

2.0000

0.5000

1/2-20 Tapped Hole

1.0000

2.0000

⌀0.3125 Threaded

0.5000

1.0000

4.0000

221

	NAME	DATE
DRAWN		
CHECKED		
APPROVED		

<COMPANY NAME>

TITLE:

SIZE **B**   DWG. NO.   Dovetail Connector   REV

SCALE: 1:1   SHEET 1 OF 1

2x ⌀0.2570 for 5/16-18

3.0000

1.0000

0.5000

0.5000

4.0000

3.0000

1.0000

4.0000

3.0000

4 x ⌀0.2570 Threaded Holes (5/16 - 18)

0.9709

3.0000

0.5000

⌀0.2570

1.0000

0.9709

1.3750

4.00

10.0000

1.0000

222

	NAME	DATE
DRAWN		
CHECKED		
APPROVED		

<COMPANY NAME>

TITLE:

SIZE **B**   DWG. NO. Dovetail Runner   REV

SCALE: 1:2   SHEET 1 OF 1

5.00000

1.00000

2.86400

4.00000

1.18600

4 x ⌀0.27559 Tapped Hole for M8-1.00" Bolt

⌀0.19000 :: #10-24 Tapped Hole for Set-Screw
(Can be different size. TBD during build)

⌀0.50000 Hole 1" Deep

5.00000

1.35000

1.00000

0.35000

4.00000

1.51457

1.51457

1.00000

0.35000

1.37500

223

<COMPANY NAME>

TITLE:

	NAME	DATE
DRAWN		
CHECKED		
APPROVED		

SIZE **B**

DWG. NO. Dovetail Slide

REV

SCALE: 1:1   SHEET 1 OF 1

4 x Ø0.3125 Through Hole Counter Sunk on Opposing Side

6.0000

1.0000

1.0000

0.5000

4.0000

2.0000

2.1250

3.0000

4.0000

4.0000

0.5000

0.5000

8 x Ø0.3125 Through-Hole Counter-Sunk

5.0000

4 x Ø0.2010 for 1/4" Threaded Hole

0.5000

6.0000

<COMPANY NAME>

TITLE:

	NAME	DATE
DRAWN		
CHECKED		
APPROVED		

SIZE **B** DWG. NO. Load cell to head   REV

SCALE: 1:2   SHEET 1 OF 1

0.25000

8 x ⌀0.31496 Through Hole w/ Counter-Sink (M8 Bolts)

8 Holes are about a 3.1" diameter center

4.50000

5.00000

2.50000

5.00000

<COMPANY NAME>

TITLE:

	NAME	DATE
DRAWN		
CHECKED		
APPROVED		

SIZE **B** | DWG. NO. Large Dyncast Holder | REV

SCALE: 1:2 | SHEET 1 OF 1

APPENDIX L

Repeated Measures Analysis
(Part 2, Winding Torque)

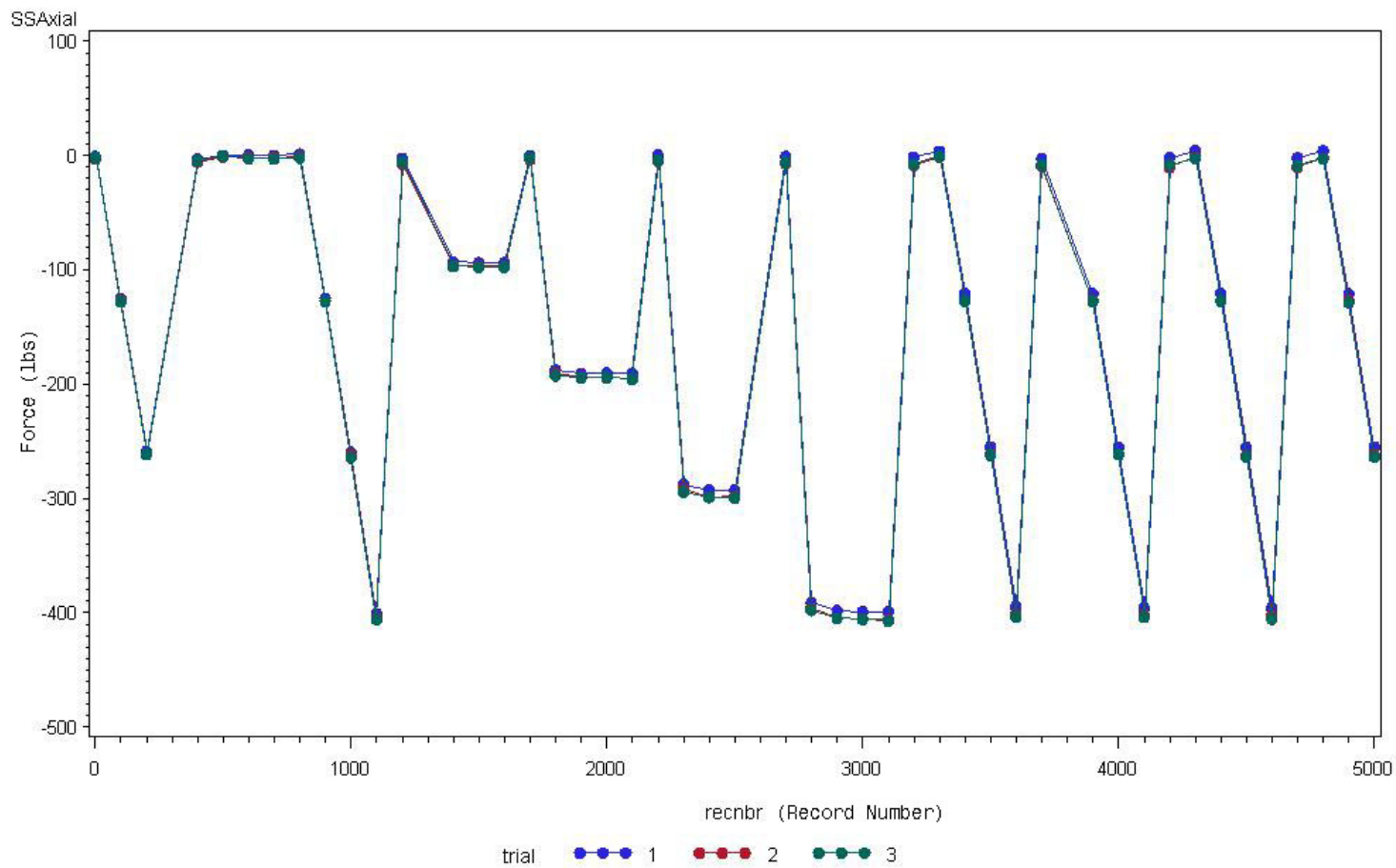Figure L.1: MTS Axial Load Repeated Measures Analysis on Three Stage I Part 2 Trials on Spring K104

Figure L.2: 6 Cell Axial Load Repeated Measures Analysis on Three Stage I Part 2 Trials on Spring K104
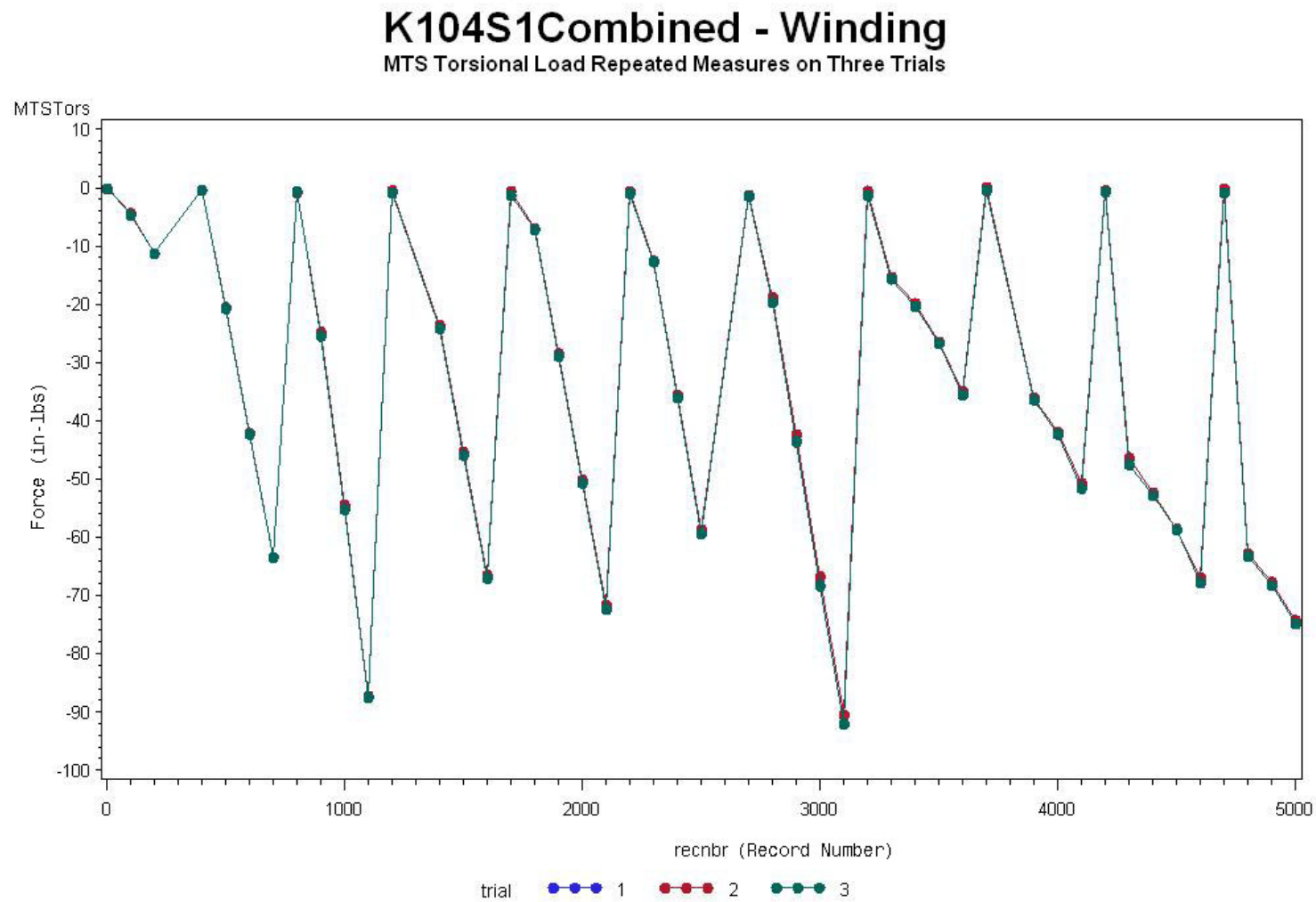
Figure L.3: MTS Torsional Load Repeated Measures Analysis on Three Stage I Part 2 Trials on Spring K104
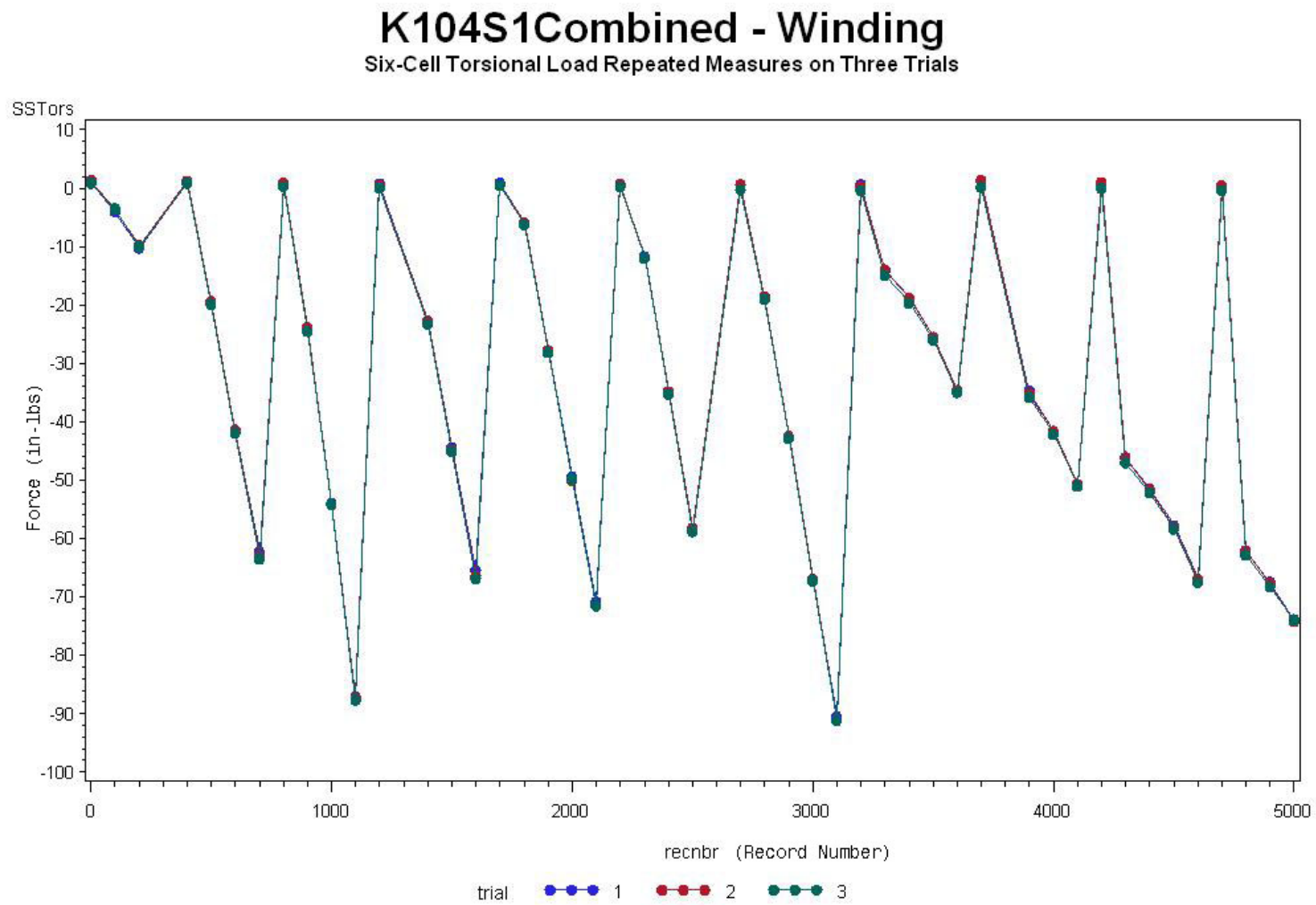
Figure L.4: 6 Cell Torsional Load Repeated Measures Analysis on Three Stage I Part 2 Trials on Spring K104
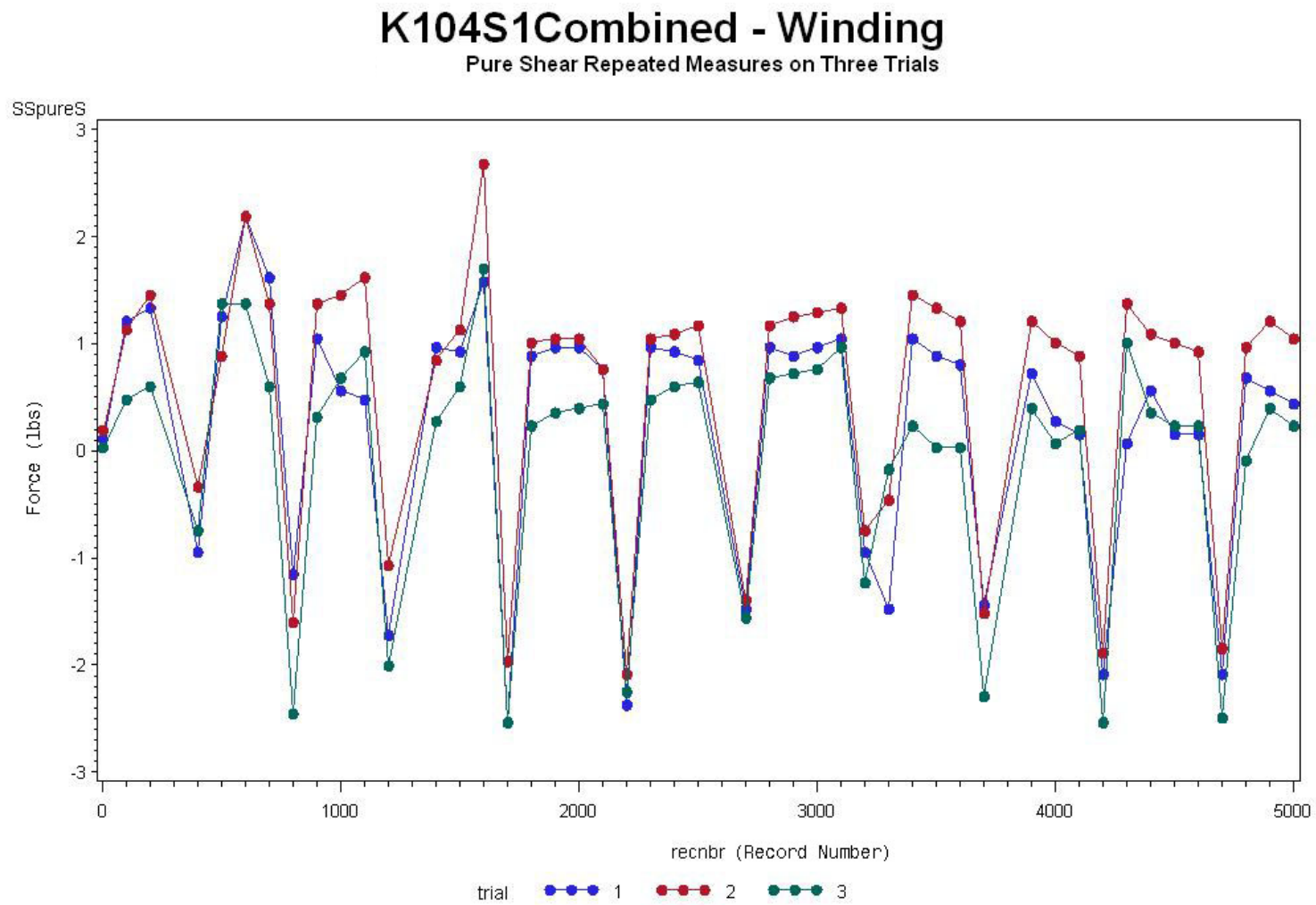
Figure L.5: S-Cell Pure Shear Load Repeated Measures Analysis on Three Stage I Part 2 Trials on Spring K104
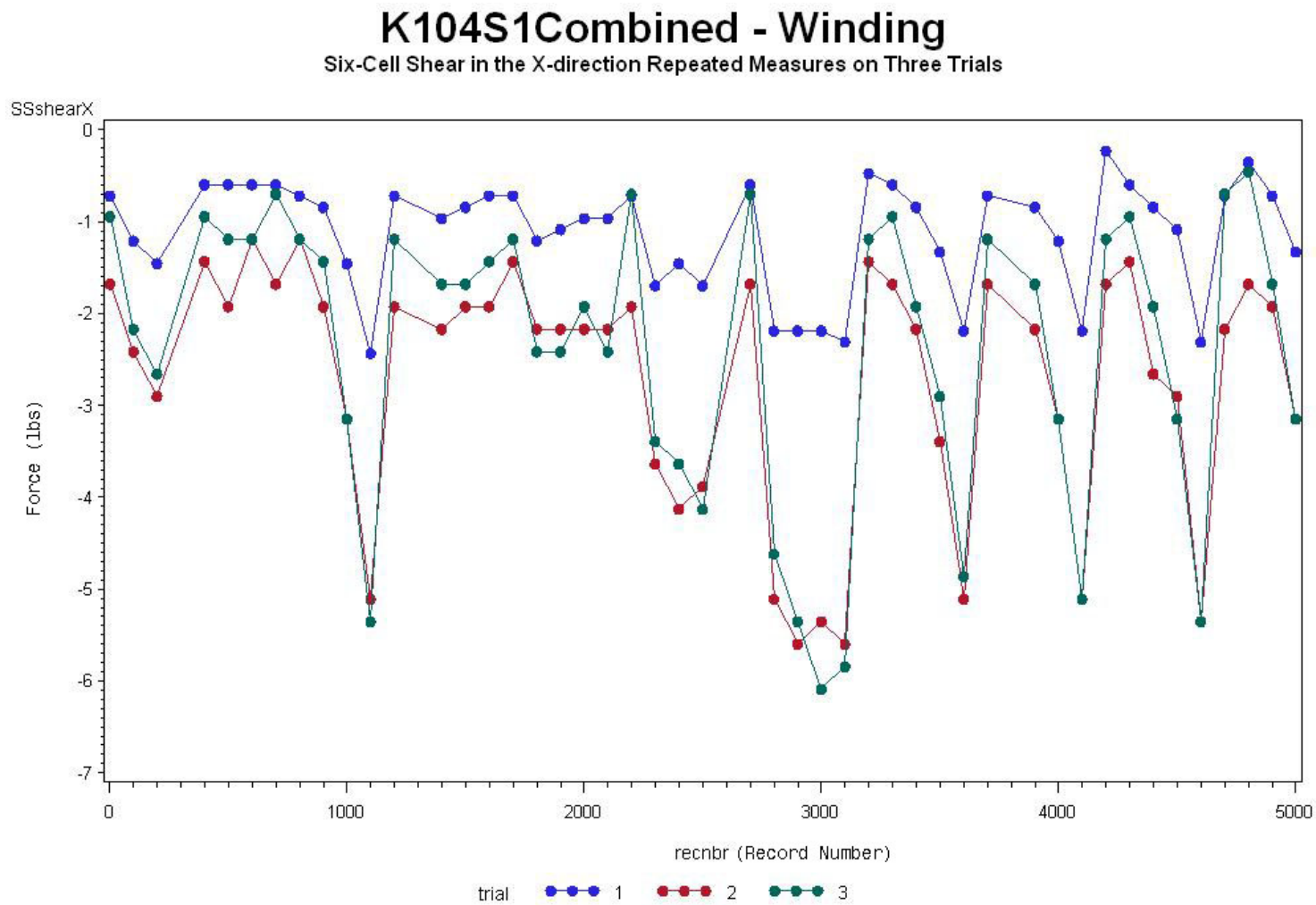
Figure L.6: 6 Cell Shear X Load Repeated Measures Analysis on Three Stage I Part 2 Trials on Spring K104
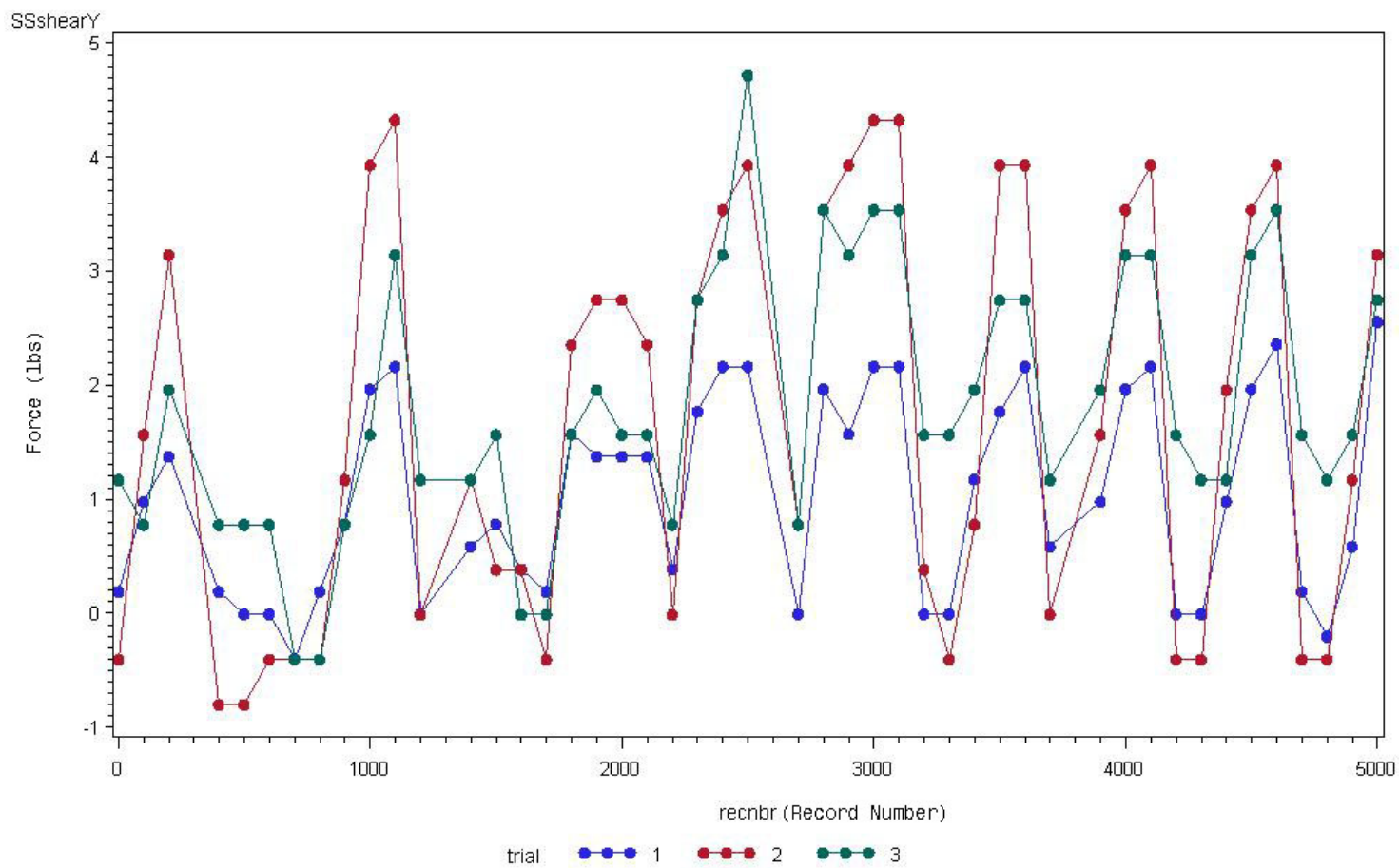
Figure L.7: 6 Cell Shear Y Load Repeated Measures Analysis on Three Stage I Part 2 Trials on Spring K104
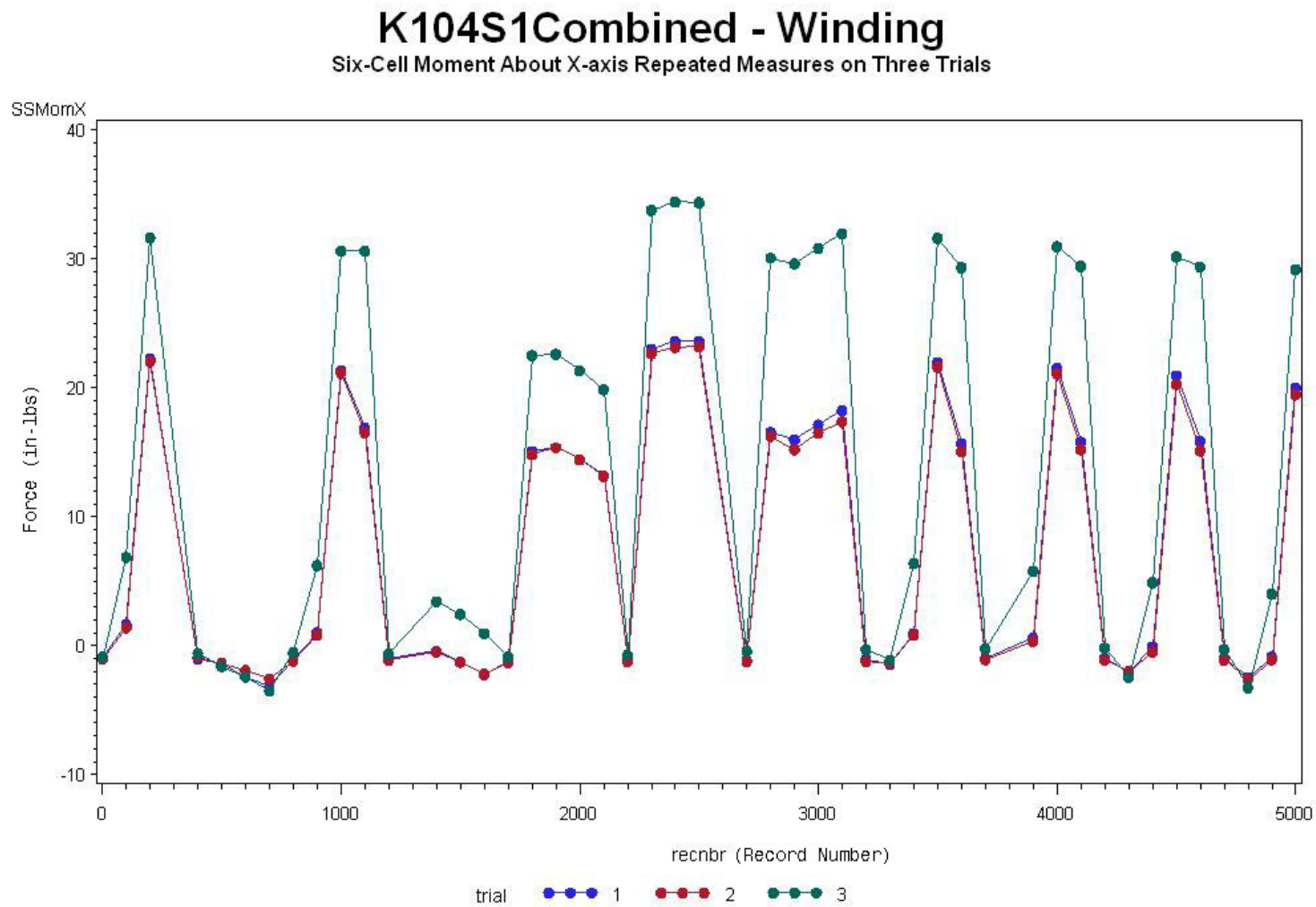
Figure L.8: 6 Cell Moment X Load Repeated Measures Analysis on Three Stage I part 2 Trials on Spring K104
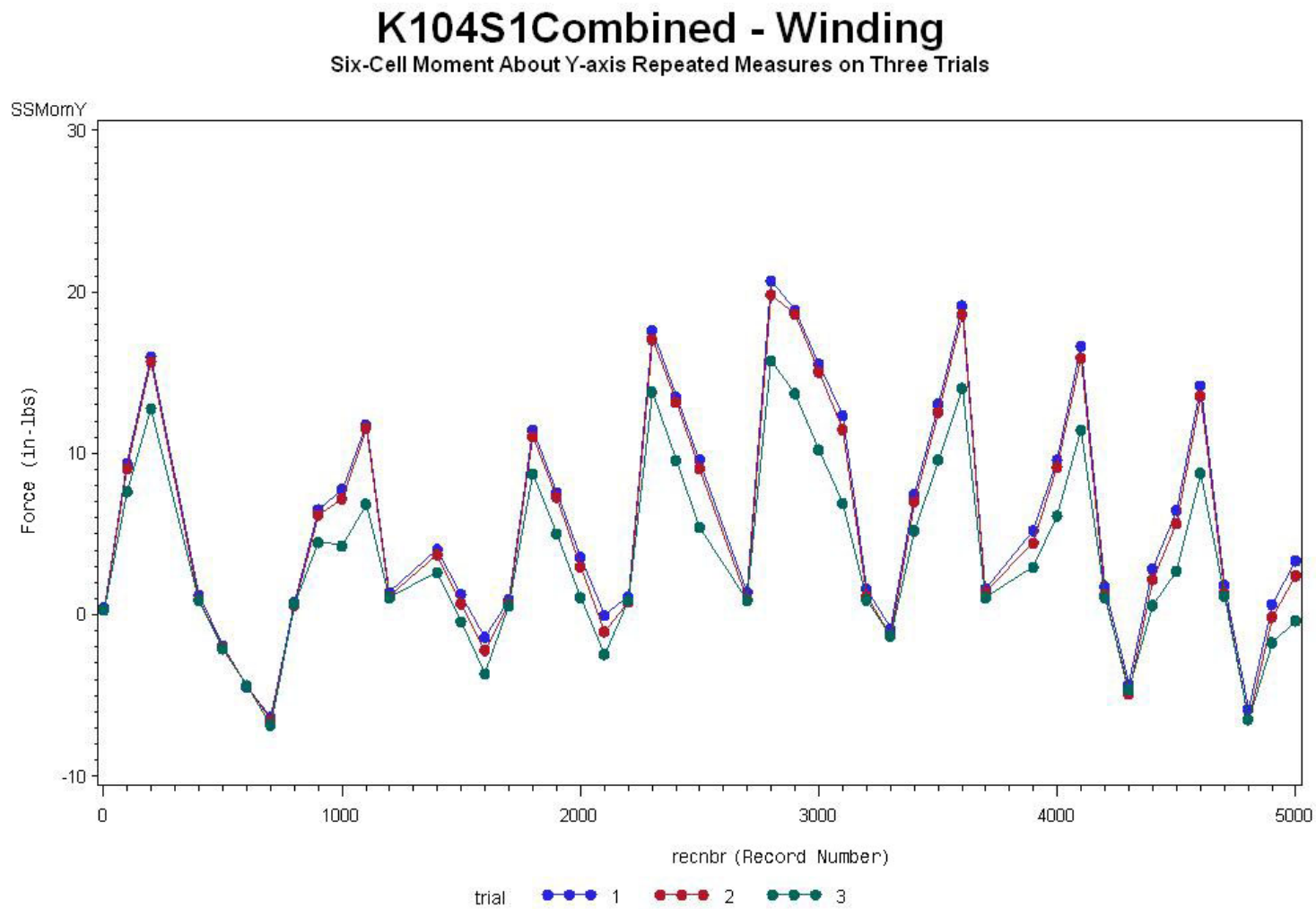
Figure L.9: 6 Cell Moment Y Load Repeated Measures Analysis on Three Stage I Part 2 Trials on Spring K104

REFERENCES

[1] Wikipedia contributors, 2011, "Spring (Device)," 2011(04/28). Available from: http://en.wikipedia.org/wiki/Spring_(device).

[2] Wikipedia contributors, 2011, "Spring Rider," 2011(04/28). Available from: http://en.wikipedia.org/wiki/Spring_rider.

[3] Wahl, A.M., 1963, "Mechanical Springs,".

[4] Tabarrok, B., and Xiong, Y., 1992, "A Spatially Curved and Twisted Rod Element for Buckling Analysis," International Journal of Solids and Structures, 29(23) pp. 3011-3023.

[5] Juvinall, R.C., and Marshek, K.M., 2006, "Fundamentals of Machine Component Design," John Wiley & Sons, Inc., Hoboken, NJ, pp. 832.

[6] Becker, L. E., and Cleghorn, W. L., 1992, "On the Buckling of Helical Compression Springs," International Journal of Mechanical Sciences, 34(4) pp. 275-282.

[7] Burdick, W. E., Chaplin, F. S., and Sheppard, W. L., 1939, "Deflection of Helical Springs Under Transverse Loading," Trans. of ASME, 61pp. 623-632.

[8] Dengler, K., 2008, "A Look at the Many Uses of Springs," The International Magazine of Spring Manufacture: Springs, 47(3) pp. 22-25.

[9] Chonajcki, C., 2008, "A History of Springs," The International Magazine of Spring Manufacture: Springs, 47(3) pp. 26-30.

[10] Mashinostroeniya, V., 1975, "Comparison of Characteristics of Transverse Stiffness of Cylindrical Helical Springs," Russian Engineering Journal, 55(8) pp. 30-32.

[11] Satoh, T., Kunoh, T., and Mizuno, M., 1988, "Buckling of Coiled Springs by Combined Torsion and Axial Deflection," JSME International, 31(1) pp. 56-62.

[12] Chassie, G. G., Becker, L. E., and Cleghorn, W. L., 1997, "On the Buckling of Helical Springs Under Combined Compression and Torsion," International Journal of Mechanical Sciences, 39(6) pp. 697-704.

[13] Jiang, W. G., and Henshall, J. L., 2000, "Novel Finite Element Model for Helical Springs," Finite Elements in Analysis and Design, 35(4) pp. 363-377.

[14] Dasgupta, B., and Mruthyunjaya, T. S., 2000, "The Stewart Platform Manipulator: A Review," Mechanism and Machine Theory, 35(1) pp. 15-40.

[15] Stewart, D., 1966, "A Platform with Six Degrees of Freedom," Proc Instn Mech Engrs, 180(15) pp. 371-378.

[16] Ben-Horin, R., Shoham, M., and Djerassi, S., 1998, "Kinematics, Dynamics and Construction of a Planarly Actuated Parallel Robot," Robotics and Computer Integrated Manufacturing, 14(2) pp. 163-172.

[17] Wikipedia contributors, 2011, "Flight Simulator," 2011(04/28). Available from: http://en.wikipedia.org/wiki/Flight_simulation.

[18] Lexus, 2011, "The Pursuit Continues in Advancing Technology," 2011(04/28). Available from: http://www.lexus.com/tomorrow/?siteid=Lexus_More_Sites_Nav#sites.

[19] Taylor, J. C., 2002, "Correction of General Deformity with the Taylor Spatial Frame Fixator," pp. 1-26.

[20] Wapler, M., Urban, V., Weisener, T., "A Stewart Platform for Precision Surgery." Transactions of the Institute of Measurement & Control, 25(4) pp. 329.

[21] Wendlandt, J. M., and Sastry, S. S., 1994, "Design and control of a simplified Stewart platform for endoscopy," Decision and Control, 1994., Proceedings of the 33rd IEEE Conference on, Anonymous 1, pp. 357-362 vol.1.

[22] Yao, J., Hou, Y., Wang, H., 2008, "Isotropic Design of Stewart Platform-Based Force Sensor," Lecture Notes in Computer Science (Including Subseries Lecture Notes in Artificial Intelligence and Lecture Notes in Bioinformatics), 5315 LNAI(PART 2) pp. 723-732.

[23] Yao, J., Hou, Y., Wang, H., 2011, "Spatially Isotropic Configuration of Stewart Platform-Based Force Sensor," Mechanism & Machine Theory, 46pp. 142-155.

[24] Zhenlin, J., Feng, G., and Xiaohui, Z., 2003, "Design and Analysis of a Novel Isotropic Six-Component force/torque Sensor," Sensors and Actuators A: Physical, 109(1-2) pp. 17-20.

[25] Dwarakanath, T. A., Dasgupta, B., and Mruthyunjaya, T. S., 2001, "Design and Development of a Stewart Platform Based force–torque Sensor," Mechatronics, 11(7) pp. 793-809.

[26] Benoit, H. D., 2011, "Designing, Constructing, and Testing a Second-Generation Prototype Mechanical Hippotherapy Horse,".

[27] NARHA, 2011, "The North American Riding for the Handicapped Association " 2011(02/09) .

[28] Meregillano, G., 2004, "Hippotherapy," Phys Med Rehabil Clin N Am, 15pp. 843-854.

[29] Sterba, J. A., Rogers, B., France, A., 2002, "Horseback Riding in Children with Cerebral Palsy: Effect on Gross Motor Function." Developmental Medicine and Child Neurology, 44(5) pp. 301-308.

[30] Benda, W., McGibbon, N. H., and Grant, K. L., 2003, "Improvements in Muscle Symmetry in Children with Cerebral Palsy After Equine-Assisted Therapy (Hippotherapy)." Journal of Alternative and Complementary Medicine (New York, N.Y.), 9(6) pp. 817-825.

[31] Bertoti, D. B., 1988, "Effect of Therapeutic Horseback Riding on Posture in Children with Cerebral Palsy." Physical Therapy, 68(10) pp. 1505.

[32] AHA, 2007, "American Hippotherapy Association, Inc." 2011(02/09) .

[33] Hammer, A., Nilsagård, Y., Forsberg, A., 2005, "Evaluation of Therapeutic Riding (Sweden)/hippotherapy (United States). A Single-Subject Experimental Design Study Replicated in Eleven Patients with Multiple Sclerosis," Physiotherapy Theory and Practice, 21(1) pp. 51-77.

[34] Heine, B., 1997, "Introduction to Hippotherapy," NARHA Strides, 3(2) .

[35] MacPhail, H. E. A., Edwards, J., Golding, J., 1998, "Trunk Postural Reactions in Children with and without Cerebral Palsy during Therapeutic Horseback Riding," Pediatric Physical Therapy, 10(4) .

[36] Riede, D., 1987, "The Relationship between Man and Horse with Reference to Medicine Throughout the Ages," People-Animals-Enviroment, 5(2) pp. 26-28.

[37] Pena, C., 2008, "The Origins of Cybex Space," Cabinet Magazine, (29). Available from: http://www.cabinetmagazine.org/issues/29/pena.php.

[38] Leila, 2010, "Horse in the House?" 2011(05/16). Available from: http://www.sidesaddlegirl.co.uk/2010/09/horse-in-house.html .

[39] Wooden Horse Corporation, "Equicizer," 2010(12/05) .

[40] Garner, B. A., 2009, "How Realistic Are The Motion Patterns of Horse Simulator Exercise Devices?" Annual Conference of the Lone Star Therapeutic Equestrian Network (LSTEN), Anonymous .

[41] Human Touch, 2011, "Effortless Exercise - iJoy Ride and Board by Human Touch," 2011.

[42] Benoit, H. D., Kelley, J. D., White, J. D., 2010, "Design of a Therapeutic Mechanical Horse," ASME 2010 Summer Bioengineering Conference, Anonymous .

[43] Omega Engineering Inc., 2011, "Introduction to Load Cells," 2011(04/28). Available from: http://www.omega.com/prodinfo/loadcells.html.

[44] Omega Engineering Inc., 2011, "Technical Reference: Positioning Strain Gages," 2011(04/28). Available from: http://www.omega.com/techref/pdf/Positioning_Strain_Gages.pdf.

[45] Vishay Precision Group, I., 2011, "Technical Notes: Strain Gage Selection (TN-505)," 2011(04/28).

[46] Wikipedia contributors, 2011, "Strain Gage," 2011(04/27). Available from: http://en.wikipedia.org/wiki/Strain_gauge.

[47] eFunda, I., 2011, "Strain Gage: Materials," 2011(04/28). Available from: http://www.efunda.com/designstandards/sensors/strain_gages/strain_gage_selection_matl.cfm.

[48] Eibeck, P., and Muramatsu, B., 2000, "Vibrating Beam Experiment Instructional Courseware: Types of Strain Gages," 2011(04/05).

[49] RDP Group, 2011, "How it Works - Strain Gauge Load Cell," 2011. Available from: http://www.rdpe.com/us/hiw-sglc.htm

[50] Futek Advanced Sensor Technology, Inc., 2011, "Sensor Applications for Load Cells," 2011(04/14). Available from: http://www.futek.com/apps_load.aspx.

[51] Reinhorn, A. M., and Bracci, J. M., 1992, "Multi Axis Load Cell, Design and Construction,".

[52] Vishay Micro-Measurements, 2003, "Systen 5000, Model 5100B Scanner Instruction Manual," pp. 1-17.

[53] Schlotzhauer, S.D., and Littell, R.C., 1997, "SAS System for Elementary Statistical Analysis,"pp. 281-334.